



**HAL**  
open science

# Growth kinetics of individual carbon nanotubes studied by in situ optical microscopy

Vladimir Pimonov

► **To cite this version:**

Vladimir Pimonov. Growth kinetics of individual carbon nanotubes studied by in situ optical microscopy. Electronics. Université Montpellier, 2021. English. NNT : 2021MONTTS101 . tel-03615720

**HAL Id: tel-03615720**

**<https://theses.hal.science/tel-03615720>**

Submitted on 21 Mar 2022

**HAL** is a multi-disciplinary open access archive for the deposit and dissemination of scientific research documents, whether they are published or not. The documents may come from teaching and research institutions in France or abroad, or from public or private research centers.

L'archive ouverte pluridisciplinaire **HAL**, est destinée au dépôt et à la diffusion de documents scientifiques de niveau recherche, publiés ou non, émanant des établissements d'enseignement et de recherche français ou étrangers, des laboratoires publics ou privés.

# THÈSE POUR OBTENIR LE GRADE DE DOCTEUR DE L'UNIVERSITÉ DE MONTPELLIER

En Physique

École doctorale I2S

Unité de recherche Laboratoire Charles Coulomb

## Growth kinetics of individual carbon nanotubes studied by *in situ* optical microscopy

Présentée par Vladimir PIMONOV

Le 6 Décembre 2021

Sous la direction de Vincent JOURDAIN

Devant le jury composé de

Mme Catherine JOURNET, Professeure, Université Claude Bernard Lyon 1

M. Benji MARUYAMA, Principal Materials Research Engineer, US Air Force Research Laboratory

M. Jean-Louis BANTIGNIES, Professeur, Université de Montpellier

Mme Sofie CAMBRÉ, Research professor, University of Antwerp

Mme Annick LOISEAU, Directrice de recherche, ONERA

M. Vincent JOURDAIN, Professeur, Université de Montpellier

Rapporteure

Rapporteur

Examinateur

Examinatrice

Examinatrice

Directeur de thèse



UNIVERSITÉ  
DE MONTPELLIER







# Contents

Acknowledgements .....	5
Introduction .....	6
Chapter 1. Literature overview .....	8
1.1 CNT structure.....	8
1.1.1 Crystal structure.....	8
1.1.2 Defects .....	10
1.1.3 Electronic structure.....	11
1.2 Carbon nanotube growth.....	15
1.2.1 Synthesis methods .....	15
1.2.2 Parameters influencing the growth selectivity.....	17
1.2.3 Growth mechanism.....	18
1.3 Growth selectivity .....	20
1.3.1 Selectivity models.....	21
1.3.2 Experimental kinetic measurements .....	27
1.4 Open questions from the literature.....	33
Chapter 2. Experimental approach.....	36
2.1 Homodyne polarization microscopy .....	36
2.2 Raman spectroscopy .....	38
2.3 Scanning electron microscopy .....	42
Chapter 3. Materials and methods.....	44
3.1 Substrates and catalysts.....	44
3.2 CNT synthesis .....	45
3.3 Optical imaging.....	45
3.4 Raman measurements .....	46

3.5	Sample treatment with photoresist.....	47
3.6	Scanning electron microscopy .....	47
Chapter 4.	Raman spectroscopy of CNTs grown on monocrystalline quartz.....	48
4.1	Raman features of horizontally aligned CNTs grown on quartz .....	48
4.2	Wall number, chirality and diameter assignment.....	54
4.2.1	Identifying cases incompatible with individual SWCNTs .....	55
4.2.2	Chirality assignment .....	59
4.3	Conclusion .....	63
Chapter 5.	In situ optical imaging: video processing and analysis .....	66
5.1	Video processing.....	66
5.1.1	Alignment .....	67
5.1.2	Correction of illumination irregularities .....	68
5.1.3	Noise filtration and edge enhancement.....	72
5.2	AI recognition .....	73
5.2.1	Principle of neural networks.....	74
5.2.2	Core model.....	80
5.2.3	Segment assignment and tracking .....	82
5.2.4	Human-supervised kinetic extraction .....	87
5.3	Conclusion .....	89
Chapter 6.	Growth kinetics of individual carbon nanotubes.....	92
6.1	Types of kinetic behavior.....	93
6.1.1	Linear growth.....	93
6.1.2	Broken-line kinetics .....	95
6.2	Ethanol pressure dependence .....	97
6.2.1	Types of growth kinetics .....	97
6.2.2	Reaction order.....	101
6.3	Temperature dependence .....	102
6.3.1	Growth kinetics.....	102

6.3.2	Activation energies .....	106
6.4	Other catalysts .....	108
6.5	Conclusion .....	110
Chapter 7.	Etching and pauses .....	112
7.1	Pressure dependence .....	113
7.1.1	Growth kinetics.....	114
7.1.1	Reaction kinetics.....	117
7.2	Temperature dependence .....	117
7.2.1	Growth kinetics.....	118
7.2.1	Reaction kinetics.....	119
7.2.2	Pause behavior .....	121
7.3	Conclusion .....	121
Chapter 8.	Discussion .....	122
Conclusion.....		126
Résumé étendu en français.....		128
References .....	<b>Ошибка! Закладка не определена.</b>	

# Acknowledgements

First of all, I would like to express my gratitude to my scientific advisor Vincent Jourdain, who has guided and inspired me with his patience and interest in science over the past three years. Discussions and debates with him have proven to be fertile ground for developing my perception of myself as a scientist and strengthening my confidence in my chosen path.

I am also grateful to my previous supervisor, Roshal Sergey Bernardovich, for motivating me to follow my desires and challenges, which planted the seed of my desire to become a scientist.

My colleagues, past and present, Huy Nam Tran, Leonard Monniello, Saïd Tahir, David Maurin and Thierry Michel have also made important contributions to this work, creating the conditions for my research.

Special thanks to Nathalie Job and Christophe Bichara for inspiring conversations at the “SFEC 2021 colloque”, and to Mariyka El for her incredible ability to inspire and motivate.

Equally important contributions were the coffee that kept me going, the sweets that kept my dopamine levels up while I worked, and the 2019 Coronavirus outbreak, without which I would not have had as much free time at my disposal to invest in learning programming and data analysis.

# Introduction

Scientific knowledge constantly progresses and technology is always in search of greater performance, lower cost, and miniaturization of size. While the use of silicon as the basis for electronic devices is now reaching its limits due to physical limitations, new materials with comparable or superior properties are entering the scene. Nanomaterials are of particular interest because of their intrinsically small size and because their properties can be tailored by slight modifications of size, shape or crystal structure.

Among them, carbon nanotubes (CNTs) are a promising substitute for modern materials in electronic and optical devices due to their exceptional properties which have already been demonstrated in theory (1) and practice (2). They were discovered by Sumio Iijima in 1991 during electron microscopy observations. This discovery has led to countless research efforts to study and control the structure and properties of these new objects as well as to develop their potential applications in fields as vast and diverse as microelectronics, energy storage and production, biological imaging or material reinforcement. The synthesis of CNTs in particular has made great progress from the initial methods of electric arc and laser ablation, which were not very selective, difficult to scale and costly in energy, to more sophisticated and varied methods of catalytic chemical vapor deposition assisted by catalyst nanoparticles.

However, for the transition to mass use of CNTs, it is first necessary to solve the problem of obtaining nanotubes with tailored structures and properties such as diameter, helical angle and conductivity type. There are two ways to accomplish this task: post-synthesis sorting (3–5) and selective synthesis (6, 7). The second approach is preferable for implementation in production because it does not require adding extra steps in the device fabrication process. However, to date, successes in selective synthesis are sparse especially because a deeper understanding of chiral selectivity mechanisms and its dependence on synthesis conditions is missing.

The selective synthesis of CNTs falls into the general category of selective crystal growth and one may therefore expect kinetic selectivity as in the case of 2D and 3D crystals whose growth rate depends on the crystal face or crystal edge. However, CNTs are very special crystals. They are one-dimensional crystals whose crystal structure, also known as chirality in the nanotube field, can totally change if a few topological defects are introduced during the course of growth. Their unit cell is also quite peculiar since it is conceptually a short ribbon of graphene rolled up into a tubular shape. The

fact that CNTs are 1D crystals with an open circular edge raises several questions of importance for their growth kinetics and selectivity.

First, one may wonder about the actual structure of the CNT edge during growth: does it adopt a stable configuration slightly evolving between close configurations? Or does it randomly fluctuate between all possible configurations? Second, one may ask whether and how the edge influences the nanotube growth rate as it is generally the case in crystal growth? Third, the question of whether and how the edge structure depends on the nanotube chirality and the catalyst particle it is connected to is still open despite its important implications for the energetics, kinetics and selectivity of growth. Shedding light on these questions is crucially important for the development of chirality selective synthesis techniques based on kinetics.

The present thesis manuscript details the results of my experimental work on this problem. As described hereafter, my approach was primarily based on a new method of optical microscopy, named homodyne polarization microscopy, which allowed me to image long CNTs during their growth and to measure their kinetics at the individual level. These observations led to the discovery of previously unknown stochastic processes, namely growth rate switches, growth pauses and switches between growth and shrinkage. To correlate these observations with the nanotube structure, I also performed a large-scale characterization of individual CNTs by Raman spectroscopy in the particular but important case of horizontally aligned CNT arrays grown on monocrystal quartz substrate.

The plan of this manuscript is the following. In the first chapter will be presented a state of the art on selective CNT synthesis which will lead me to highlight some important and still open questions in the field. The second chapter is dedicated to describing my experimental approach which combined *in situ* optical imaging, Raman spectroscopy and Scanning Electron Microscopy. The third chapter is devoted to detailing the materials and methods used throughout my research work. The fourth chapter is devoted to describing the results of my Raman investigations of individual CNTs and providing an interpretation to the peculiar Raman signatures of individual CNTs grown on monocrystalline quartz. The fifth chapter describes the methods I developed for processing and analyzing *in situ* optical microscopy data. The sixth chapter is devoted to describing the growth behaviors of individual CNTs and studying their dependence on the main growth parameters, temperature and precursor pressure. The seventh chapter is devoted to the description of the stochastic processes of shrinkage and pauses. Finally, in chapter 8, I discuss the possible mechanisms behind the stochastic processes of growth rate switches and shrinkage evidenced during the course of my PhD work.

# Chapter 1.

## Literature overview

In this chapter will be reviewed the current state of the art on carbon nanotube structure and synthesis methods as well as growth models and their experimental validation.

### 1.1 CNT structure

#### 1.1.1 Crystal structure

Before describing the structure of carbon nanotubes, it is necessary to mention that nanotubes are not a single type of molecules, but a whole class of nanostructures, differing in their structural parameters and properties.

At the atomic level, carbon nanotubes represent a quasi-one-dimensional tubular crystal with hexagonal motif made of a rolled sheet of  $sp^2$ -hybridized carbon atoms (Figure 1).

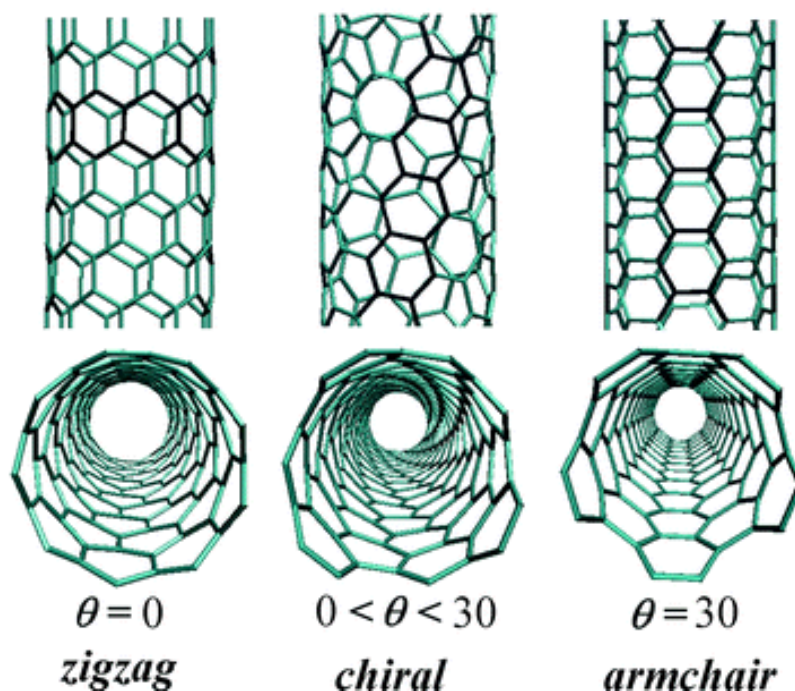


Figure 1 — Different types of carbon nanotubes. Adapted from (8). See Table 1 for element designations.

More clearly the structure can be depicted by folding of graphene sheet into a seamless cylinder along the chosen direction, which is determined by the so-called chiral vector (Figure 2). This vector is expressed through the sum of graphene translation vectors multiplied by the integer indices.

$$\mathbf{C}_h = n\mathbf{a}_1 + m\mathbf{a}_2 \quad (1)$$

The numbers  $(n, m)$  are called Hamada indices (9) after Noriaki Hamada who first proposed such a notation and unambiguously describe nanotube characteristics (Table 1). Depending on the values of these indices, nanotubes are also divided into three groups: zigzag  $(n, 0)$ , armchair  $(n, n)$  and chiral  $(n, m)$  (Figure 2). It is worth noting that for the chiral CNTs exist two enantiomers: left- and right-handed (10). By convention when  $n$  is larger than  $m$  nanotubes are right-handed or S and when  $m$  is larger than  $n$  the CNTs are left-handed or R (10–12). Note however that in most works the distinction between right- and left-handed CNTs is not made and that the convention  $0 \leq m \leq n$  is used when the CNT handedness is not considered (13).

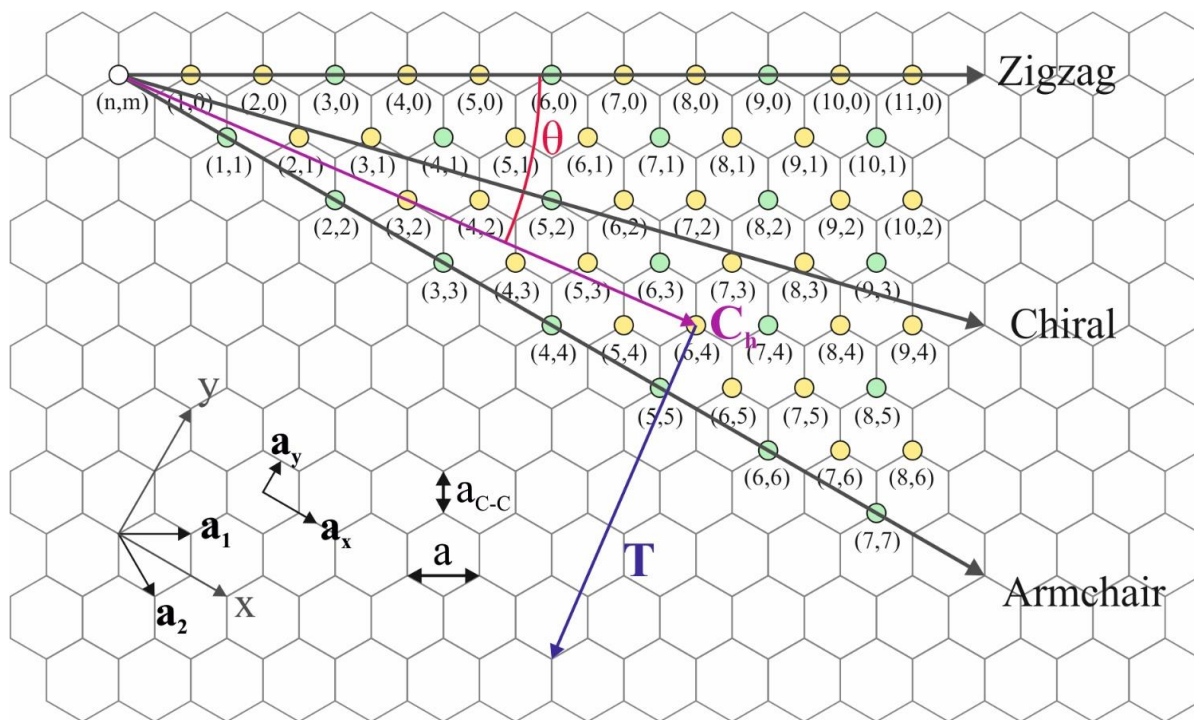


Figure 2 — Nanotube's indices on graphene hexagonal lattice. See Table 1 for element designations.

The number of walls in a single nanotube may vary from one for single-walled (SW) CNTs to several tens for multi-walled (MW) CNTs (14) with the interlayer distance approximately corresponding to that of bulk graphite. A chiral angle relationship between consecutive layers was reported by some groups. (15, 16).

Table 1 — Geometrical parameters of carbon nanotubes (13)

Parameter	Name	Formula	Comment
$a$	Length of unit vectors	$a = \sqrt{3}a_{C-C} = 0.246 \text{ nm}$	$a_{C-C} = 0.142 \text{ nm}$
$\mathbf{a}_1, \mathbf{a}_2$	Graphene translation unit vectors	$\left(\frac{\sqrt{3}}{2}, \frac{1}{2}\right)a, \left(\frac{\sqrt{3}}{2}, -\frac{1}{2}\right)a$	x, y coordinates
$\mathbf{C}_h$	Chiral vector of CNT	$\mathbf{C}_h = n\mathbf{a}_1 + m\mathbf{a}_2$	$0 \leq m \leq n$
$C_h$	Chiral vector length	$C_h =  \mathbf{C}_h  = a\sqrt{n^2 + m^2 + nm}$	
$d_t$	Nanotube diameter	$d_t = \frac{C_h}{\pi}$	
$\theta$	Chiral angle of nanotube	$\tan \theta = \frac{\sqrt{m}}{2n + m}$ $\sin \theta = \frac{\sqrt{3}m}{2\sqrt{n^2 + m^2 + nm}}$ $\cos \theta = \frac{2n + m}{2\sqrt{n^2 + m^2 + nm}}$	$-\frac{\pi}{6} \leq \theta \leq \frac{\pi}{6}$
$d$	gcd( $n, m$ ) (grand common divisor)		$1 \leq d \leq n$
$d_R$	gcd( $2n + m, 2m + n$ )	$d_R = \begin{cases} d, & \text{if } (n - m) \bar{\propto} 3d^* \\ 3d, & \text{if } (n - m) \propto 3d \end{cases}$	$1 \leq d_R \leq 3n$
$N$	Number of hexagons in unit cell of CNT	$N = \frac{2(n^2 + m^2 + nm)}{d_R}$	
$\mathbf{T}$	CNT translation vector	$\mathbf{T} = t_1\mathbf{a}_1 + t_2\mathbf{a}_2$	
$t_1, t_2$		$t_1 = \frac{2m+n}{d_R}, t_2 = \frac{2n+m}{d_R}$	gcd( $t_1, t_2$ ) = 1
$T$	Length of translation vector	$T =  \mathbf{T}  = \frac{\sqrt{3}C_h}{d_R}$	

\*  $\bar{\propto}$  : non proportional to.

### 1.1.2 Defects

The growth of CNTs may be accompanied by the incorporation of defects that disrupt their ideal crystal structure (17, 18). In addition to the standard point defects of crystal structures such as vacancies and adatoms (18), pentagonal and heptagonal defects can also occur in nanotubes (18, 19).

Pentagons play an important role in nanotube formation (20, 21). They introduce a positive curvature into the hexagonal periodic structure assembled from sp<sup>2</sup>-hybridized carbon atoms, thus

contributing to the formation of the CNT cap (22). According to Euler's theorem, six pentagons are necessary for this purpose.

Further incorporation of single pentagons into the CNT structure, can result in a conical structure with subsequent growth termination, whereas single heptagons, introducing a negative curvature, lead to an increase of the CNT diameter (23, 24) (Figure 3 (a, b)). More complex configurations are also possible, such as 5-7 couples, which lead to a change of the nanotube chirality (18) (Figure 3 (c-e)) or even double 7-5-5-7 couples called Stone-Wales defects (25) (Figure 3 (f-h)).

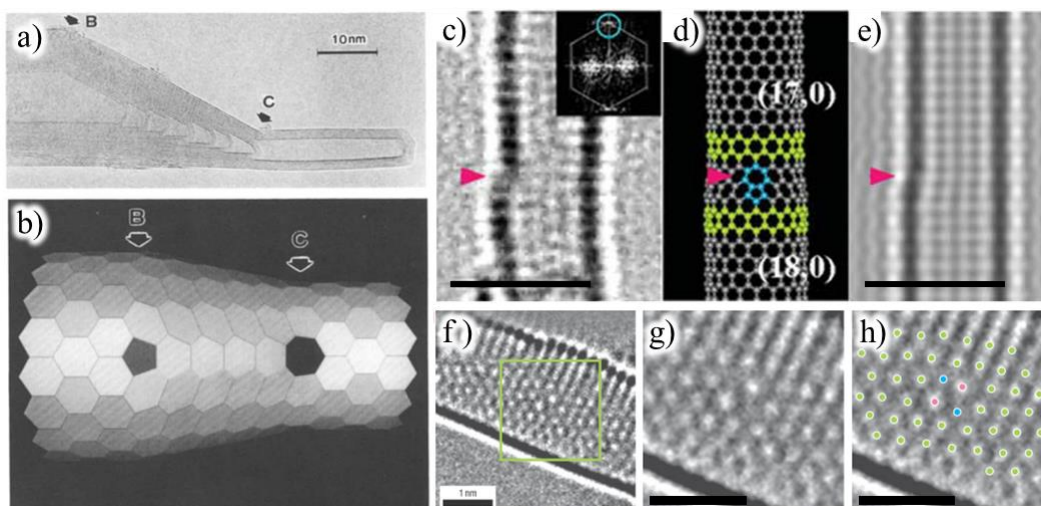


Figure 3 — Different types of defects in carbon nanotubes. CNT end a) with one 5-defect in position B and one 7-defect in position C and b) model of their modification of the CNT structure.

c) HR-TEM image of CNT structure change, d) atomic visualization of 5-7 couple leading to structure change from (18,0) to (17,0) and e) HR-TEM simulation of such defects (scale bar 2 nm).

f) HR-TEM image of CNT with pair of 5-7 defects described by the Stone-Wales model, g) magnified image of the inset of the area with these defects and h) marking of hexagons (green dots), pentagons (blue dots) and heptagons (red dots) in this image (scale bar 1 nm). a,b) adapted from (23), c–e) adapted from (18), f-h) adapted from (19).

### 1.1.3 Electronic structure

In addition to their large diversity in atomic structures, CNTs also manifest unique electronic properties originating from their one-dimensional structure. But it is worth mentioning first what is meant by the dimensionality of materials. The dimensions of 3D or bulk materials exceed the de Broglie wavelength of electrons in all three dimensions (which depends on the material but is in the order of 10 nm for a typical metal) (13). However, 2D materials have only two such dimensions, 1D materials have one such dimension and in 0D materials (such as molecules or quantum dots) all three dimensions have sizes comparable to or lower than the de Broglie wavelength of electrons. These

limitations are also reflected in the density of electronic states, which can be written in the general form (26):

$$D(E) = \left(\frac{L}{2\pi}\right)^d \int \frac{d\mathbf{k}^2 \delta(\mathbf{k}(E)-\mathbf{k})}{|\nabla_{\mathbf{k}}(E)|} \quad (2)$$

where  $d$  is the dimensionality of the material,  $L$  is the material size,  $E$  is the electron energy,  $\mathbf{k}$  is the electron wave vector and  $\nabla_{\mathbf{k}}$  is the gradient or nabla operator. In cases where the gradient is zero in the electron density of states, kinks called van Hove singularities (VHS) occur. These singularities are characteristic features of dimensionality; for one-dimensional systems such as nanotubes, they appear as sharp peaks with a descending tail (Figure 4).

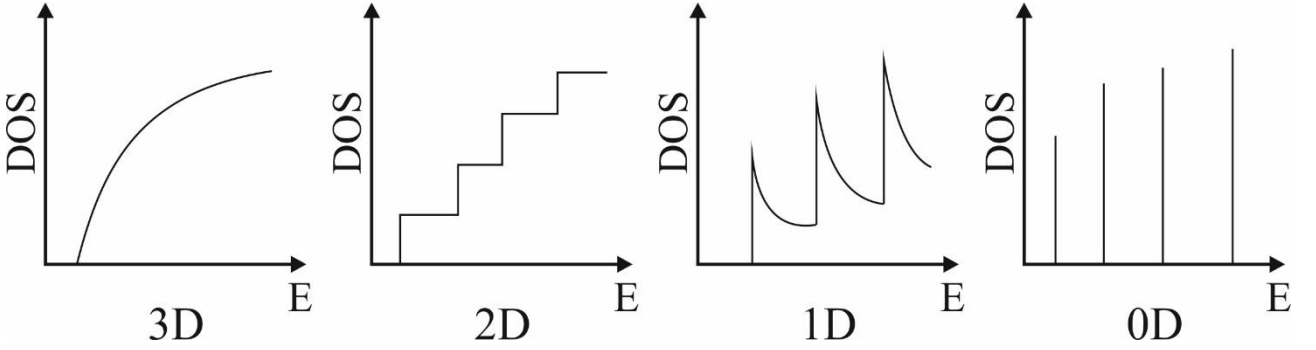


Figure 4 — Typical electronic density of states plots for materials of different dimensionalities.

Electronic structure of the nanotubes can be derived from the electronic structure of graphene by using a zone folding scheme (13, 27). This approach allows to model the electronic structure of lower-dimensional materials from its higher-dimensional form by imposing boundary conditions on the electronic wave functions in the first Brillouin zone. The fact that the 1D unit cell of a CNT is made of a finite size graphene nanoribbon imposes boundary conditions on the wave vector perpendicular to the CNT axis (*i.e.* along the nanotube circumference defined by chirality vector  $\mathbf{C}_h$ ):

$$\mathbf{C}_h * \mathbf{k} = 2\pi N \quad (3)$$

where  $\mathbf{k}$  is the wave vector of graphene reciprocal space perpendicular to CNT axis and  $N$  is the number of hexagons in the nanotube unit cell (Table 1). Since graphene is a semimetal or semiconductor with zero band gap closing at  $\mathbf{K}$ - and  $\mathbf{K}'$ -point of the first Brillouin zone, the nanotube will have metallic properties in case one of the allowed states (or cutting lines) crosses the  $\mathbf{K}$ -point of graphene and semiconducting in all other cases (Figure 5). In the plot of electronic density of states of CNTs each of the cutting line will correspond to a van Hove singularity (Figure 5 (b)), except for the lowest one that crosses the  $\mathbf{K}$ -point in the case of a metallic CNT.

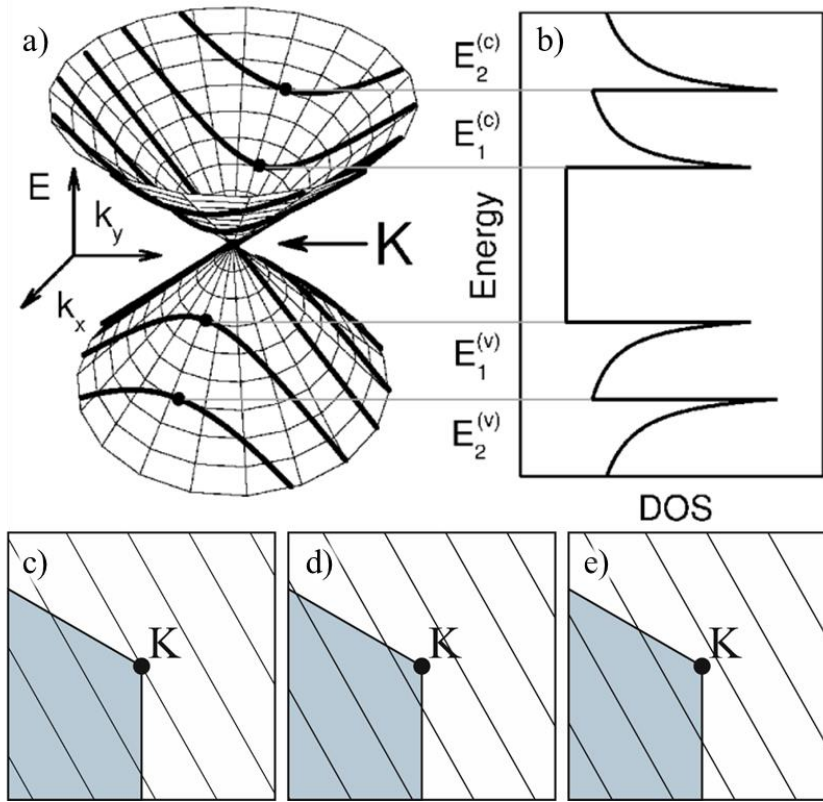


Figure 5 — a) 2D band structure of graphene near the K-point of the first Brillouin zone and its transformation into 1D electronic DOS of CNT b) by applying the method of cutting lines. Typical arrangement of cutting lines near the K-point for CNTs of c) metallic type ( $2n + m = 3l$ ), d) type-2 semiconductor ( $2n + m = 3l + 2$ ) and e) type-1 semiconductor ( $2n + m = 3l + 1$ ). Adapted from (13).

This approach provides a simplified picture of the electronic structure of carbon nanotubes. However, its applicability is limited to individual single-walled nanotubes of relatively large diameters ( $> 1.2$  nm (28)) because it does not take into account curvature effects of the nanotubes which affects electronic structure (29). These effects affect the hybridization of  $\sigma$  and  $\pi$  orbitals and modify the electronic structure (13, 30). In the case of multi-walled or bundled CNTs, the van der Waals interaction between walls also comes into effect, which also modifies the electronic structure (13, 31–33).

On Figure 5 (b) the gap between VHS with the same numbers (e.g.  $E_1^{(c)}$  and  $E_1^{(v)}$ ) corresponds to the energy of resonant optical transitions (13). These energies are the fingerprints of nanotubes and are unique for each pair of indices. Kataura *et al.* calculated a table of resonant optical transitions named after him (Figure 6) (34). Later works proposed more advanced modelling (tight binding calculations of the dielectric response of CNTs) in order to calculate more accurate values (35). Moreover, experimental comparisons were also made for nanotubes on substrate (36) and for suspended ones (37). The Kataura plot is widely used for the structure assignment of single walled

carbon nanotubes (SWCNTs) studied by optical absorption (38) and Raman spectroscopy (39), as well as photoluminescence (40).

The structural diversity of SWCNTs raises the question of their growth mechanisms and the possibilities of controlling the structure at the stage of the synthesis. In the next part, the currently available models describing the process of CNT growth as well as the synthesis methods and parameters affecting its selectivity are discussed.

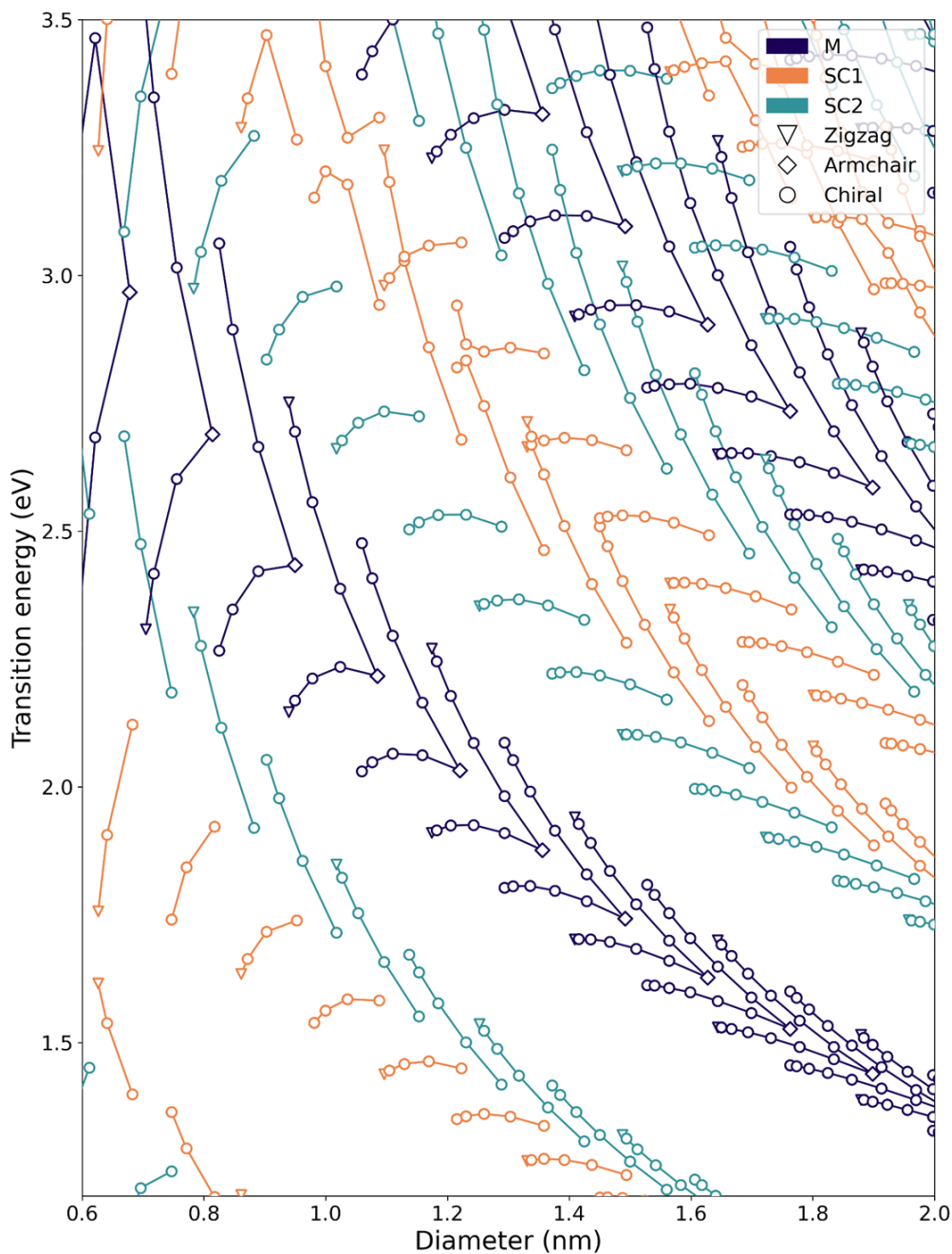


Figure 6 — Theoretical Kataura plot (41, 42) adjusted after experimental studies of SWCNTs on substrate.

## 1.2 Carbon nanotube growth

In practice, carbon nanotubes are not obtained by rolling graphene sheets but are directly grown as a seamless cylinder. Most often used methods of synthesis involve the formation of reactive carbon atoms followed by their condensation as nanotubes.

### 1.2.1 Synthesis methods

To date, there are mostly three groups of methods for synthesizing carbon nanotubes: laser ablation, arc discharge, and chemical vapor deposition (CVD) (Figure 7).

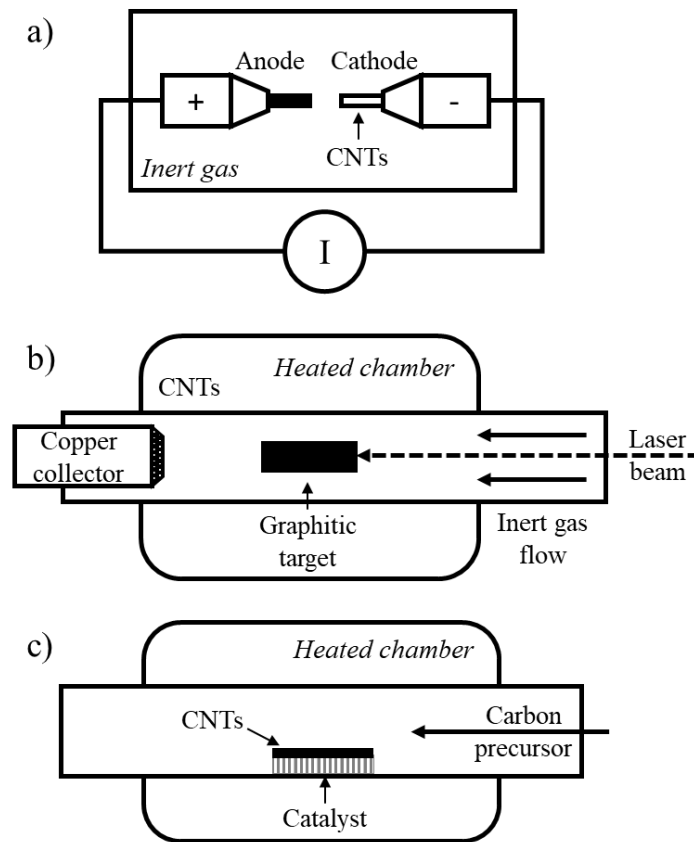


Figure 7 — Schemes of methods of nanotube synthesis: a) arc discharge, b) laser ablation and c) chemical vapor deposition.

#### 1.2.1.1 Arc discharge and laser ablation

These were the first methods (14, 43–45) used for CNT synthesis. Both of them are based on the evaporation of a graphite target in an inert gas atmosphere followed by the condensation and deposition of the as-formed carbon nanostructures on a collector.

In the case of arc-discharge synthesis, the graphite anode is evaporated and the carbon nanostructures condensate when leaving the plasma and are deposited on the cathode (Figure 7 (a)).

The synthesis typically takes place at a current of 50-120 A and a voltage of 20-30 V, and the plasma temperature can reach 3000 °C (46).

In laser ablation synthesis, the graphite target is placed in a furnace heated to a temperature of 1000-1500 °C (43, 47) and is evaporated by a laser beam in a flow of inert gas, which transfers the carbon nanostructures formed during cooling in the gas phase on a water-cooled collector (48) (Figure 7 (b)).

These methods made it possible to produce nanotubes in a few grams quantities (45, 48). However, they cannot be easily scaled up to increase the production, and the structure and properties of the synthesized nanotubes cannot be precisely controlled, making these methods unsuitable for industrial applications. Moreover, synthesis by these methods requires high energy consumption, which also increases the cost of as-produced nanotubes.

### **1.2.1.2 Chemical vapor deposition**

Nowadays, the most widely used method for the synthesis of carbon nanotubes is chemical vapor deposition (49). This method can be easily scaled up for industrial production (50), and also has a large number of controllable parameters, the tuning of which allows to influence the CNT features (51).

The classical process of CNT synthesis proceeds as follows (Figure 7 (c)): a sample with catalyst nanoparticles is placed in the reaction chamber. The chamber is then heated to operating temperatures (600-1000 °C (51)) in an inert gas atmosphere. Then, a gaseous or vapor carbon precursor is fed into the system and its catalytic decomposition releases carbon atoms that assemble into nanotubes under the catalytic and template effects of the particle (50).

The CVD process can be modified in a variety of ways (52). The above described method is called synthesis in fixed bed reactor (53, 54) and, due to its simplicity, it is the most common.

For industrial production of CNTs, the synthesis in fluidized bed reactor is most commonly used (55). The main difference from the fixed bed reactor is that the catalyst in the reaction chamber is arranged so that gas flow passes through nanoparticles, stirring them in the process and thus ensuring more efficient interaction between catalyst and precursor (56).

There are two other CVD variations in which the interaction between the catalyst and precursor is higher due to the absence of contact between catalyst nanoparticles and substrate during CNT growth: floating catalyst (FC) (57–59) and aerosol-assisted (AA) CVD (60, 61). The main difference between them is in the catalyst fabrication method. In the FC-CVD case it can be nanoparticles (57, 58) or even gaseous metal-bearing catalyst precursor (59) that are fed into the chamber together with the carrier gas and carbon precursor. Then, growth occurs during the flight of the nanoparticles through the reaction chamber. After that, synthesized CNTs are collected on a

substrate. In the case of AA-CVD, a catalyst consisting of metal-bearing molecules such as ferrocene (60, 61) is fed into the chamber in the form of an aerosol by a nebulizer together with the precursor and carrier gas.

Combined synthesis methods such as plasma-enhanced (PE) (62–65) and laser-assisted (LA) CVD (66–68) also exist. CNT synthesis by these methods causes less damage to the substrate (65), which makes it promising for local nanotube synthesis directly on devices (66, 68). However, these methods display a major drawback compared with their predecessors: the difficulty to scale up the synthesis.

In addition to the variety of CVD modification and its simplicity, its popularity is also due to a variety of parameters (such as temperature, pressure, catalyst, reagent composition) which can be tuned to influence the final product (69).

### 1.2.2 Parameters influencing the growth selectivity

Before describing the effect of synthesis parameters on the resulting nanotubes it is worth discussing what is meant by selectivity and how this concept evolved over time. One of the first steps in the development of selective synthesis methods was the synthesis of single-walled CNTs (49, 70). Nowadays, attention is focused on the development of synthesis protocols allowing to obtain nanotubes of a certain metallicity (71–73) or even certain chirality (74, 75). All these results were obtained by tuning the synthesis conditions and parameters, which is the focus of this chapter.

The catalyst plays a key role in the CVD synthesis of CNTs. Different metals (Fe, Ni, Co) (76) or their combinations (CoMo, FeRu, WCo) (77–81) can be used as catalysts due to their high catalytic activity. However, non-metallic catalysts (*e.g.* SiO<sub>2</sub> nanoparticles) were also reported for CNT synthesis (82). A number of works reports that some catalysts (*e.g.* FeCu, CoSO<sub>4</sub>/SiO<sub>2</sub>, WCo) allows the synthesis of nanotubes in a narrow chirality range (74, 75) or even to obtain more than 90 % of CNTs with one chirality (*e.g.* (12,6) nanotubes grown on W<sub>6</sub>Co<sub>7</sub> solid substrate (83)).

One possible mechanism for this type of selectivity may be the templating effect. It was proposed that such catalysts can promote epitaxial growth of carbon nanotubes due to a correspondence between the edge structure of CNTs and the crystal structure of the catalyst nanoparticles (83).

Carbon precursors are also important components of nanotube synthesis. In CVD, a large number of different precursors can be used (*e.g.* CO, C<sub>2</sub>H<sub>5</sub>OH, C<sub>2</sub>H<sub>4</sub>) (84–86). Some researchers have reported the possibility of synthesizing CNTs in a narrow chirality range using particular precursors such as CO (87, 88).

There are two possible mechanisms for this type of selectivity: preferential nucleation of certain types of nanotubes, or the action of radicals occurring as by-products of catalytic

decomposition of the precursor and inhibiting or suppressing the growth of CNTs of a particular chirality were reported (88).

The synthesis of CNTs in some types of CVD reactors requires use of a support or substrate for the catalyst particles. A large number of different materials can fulfill this role (86, 89). Some supports can influence the features of the synthesized CNTs. Thus, monocrystalline quartz (90–92), sapphire (93, 94) and MgO (95) can promote the growth of CNTs in the plane of the substrate aligned along specific crystallographic axes. Moreover, a change in the chiral distribution depending on the sapphire plane used has also been reported (93).

The mechanism of such selectivity is also not clear. However, it may be based on the strong interaction between the nanotube wall and the substrate surface (96), which can promote the growth of only CNTs whose structure matches the pattern of the substrate crystallographic direction.

Synthesis conditions such as temperature and pressure also play an important role in selective CNT synthesis. According to a number of studies, with increasing temperature, the distribution of CNT diameters broadens and shifts toward larger sizes (87, 93, 97). As the pressure increases, the distribution of CNT diameters tends toward smaller sizes (98). This type of selectivity can be the result of two mechanisms, kinetic (affecting growth of carbon nanotubes) and thermodynamic (affecting the tube-catalyst interface), but this question is still debated.

### **1.2.3 Growth mechanism**

In general, the nanotube growth process can be divided in several steps (Figure 8). It generally starts with the metal reduction which leads to catalyst nanoparticle activation. The catalyst particle promotes the decomposition of precursor molecules and the formation of a nanoscale carbon cap by the reticulation of new carbon atoms and the formations of hexagonal and pentagonal rings. After the addition of the 6<sup>th</sup> pentagon, cap formation is completed, and the chirality of the future CNT is determined by the cap structure (20, 21). From this point, the nanotube elongation phase begins by introducing new carbon atoms at the interface between the open end of the CNT and the catalyst nanoparticle, with possible incorporation of defects. Growth termination can be caused by various reasons, such as catalyst encapsulation or catalyst ripening.

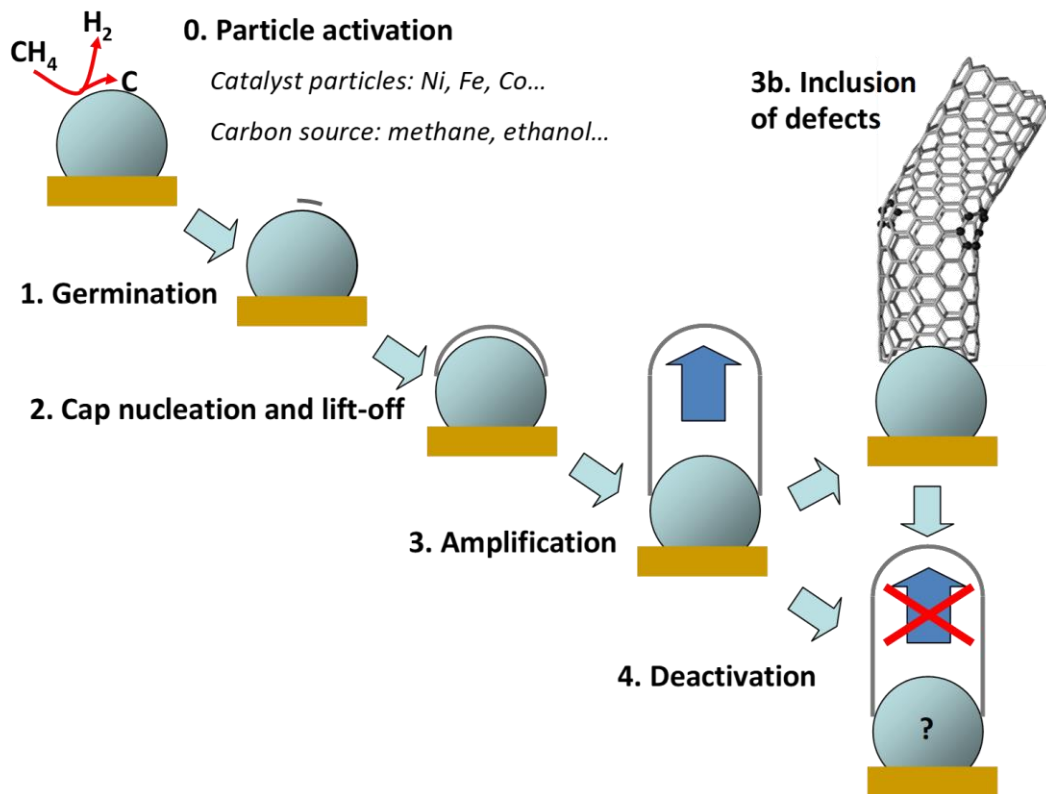


Figure 8 — General scheme of CNT growth by chemical vapor deposition (CVD).

This general description leaves open a large number of questions such as the state (liquid or solid), crystal phase, chemical composition of catalyst particle, localization of the catalyst and tube-particle diameter ratio.

Depending on the catalyst state, two growth mechanisms are distinguished: vapor-liquid-solid (VLS) (99, 100) and vapor-solid-solid (VSS) (101–103) (Figure 9 (a, b)). The difference between them arises from the difference in the physical state of the catalyst (liquid droplets for VLS and solid crystal structures in VSS). In the case of VLS mechanism, carbon atoms dissolve into the catalyst particle and form a liquid metastable carbide solution at saturation from which the nanotube begins to form and grow. The VSS mechanism involves diffusion of carbon atoms on the nanoparticle surface with subsequent incorporation into the nanotube structure (102, 104).

Depending on catalyst-substrate interactions, it is also possible to distinguish two types of nanotube growth: base- and tip-growth (Figure 9 (c, d)). In the first case, the catalyst nanoparticle remains tightly fixed on the substrate while the nanotube tip moves away from it during growth. In the case of tip-growth mechanism, the catalyst particle is detached from the substrate and moves together with the end of the nanotube during its growth (105, 106).

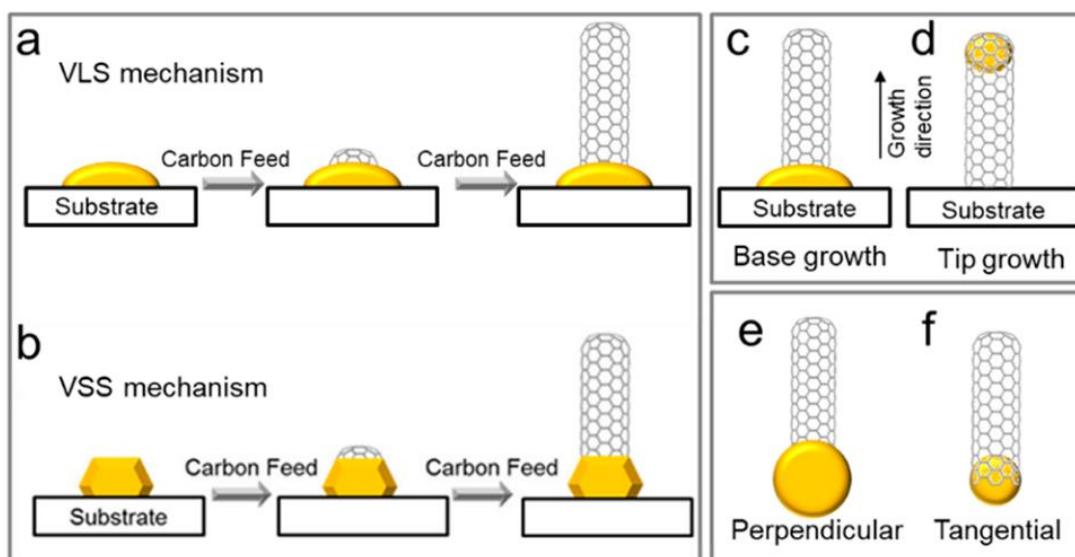


Figure 9 — Illustration of CNT growth mechanisms and modes: a) vapor-liquid-solid mechanism b) Vapor-solid-solid mechanism, c) base growth and d) tip growth modes, e) perpendicular and f) tangential growth modes (adapted from (107) – c, d, (108) – a, b, e, f).

The nanotube-catalyst diameter ratio also plays an important role. Depending on it, there are two configurations of nanotube growth: tangential and perpendicular (109–111) (Figure 9 (e, f)). In the first case, the size of the catalyst particle is comparable to the nanotube diameter. In the second case, however, the nanoparticle size far exceeds the diameter of the CNT, causing it to grow perpendicular to the catalyst surface, which modifies the interaction between carbon and metal orbitals during growth.

### 1.3 Growth selectivity

On one side, a large number of tunable parameters is advantageous in the development of selective growth methods. On the other side, it is a source of complexity and variability since testing and controlling all possible combinations can take a large amount of time. One promising way in solving this problem is the development of automated experimentation systems with the usage of artificial intelligence (AI) (112, 113), which are programmed to find the optimal conditions for synthesizing nanotubes with the required properties by tuning synthesis parameter of series of successive experiments. Another promising approach is aimed at studying the kinetics of nanotube growth to develop a rational understanding of the mechanisms governing it.

### 1.3.1 Selectivity models

#### 1.3.1.1 Epitaxial models

One of the first approaches describing chiral selectivity of CNTs addressed the possible correspondence between the crystal structure of the catalyst and the edge of the formed nanotube. Since the chirality of the nascent CNT is determined by its cap (20), several works assumed that the nanotube structure is determined at the nucleation stage and that epitaxial nanotube growth is observed in the case of solid metal catalysts (114–117).

In the seminal work of Reich *et al.* was shown that if the location of the CNT edge atoms formed on a solid Ni(111) surface matches with certain lattice points (Figure 10 (a, b, e)), the formation energy can decrease compared to the free-standing nanotube (Figure 10 (i)) (114). In the model were defined three particular types of sites on catalyst surface: stable low energy X and H-sites which are between two and three metal atoms, respectively, and energy costly T-sites which are located right upon the catalyst atoms (Figure 10 (a-h)). Thus, if the nanotubes edge atoms are settled on the stable sites their edge energy can be reduced, which can promote their nucleation (Figure 10 (i)) (114). This first modeling attempt however has some drawbacks: in reality, the surface of metal catalyst nanoparticles in CVD is not flat but rounded or faceted, and a surface reconstruction occurs that is additionally impacted by the dissolution of carbon atoms.

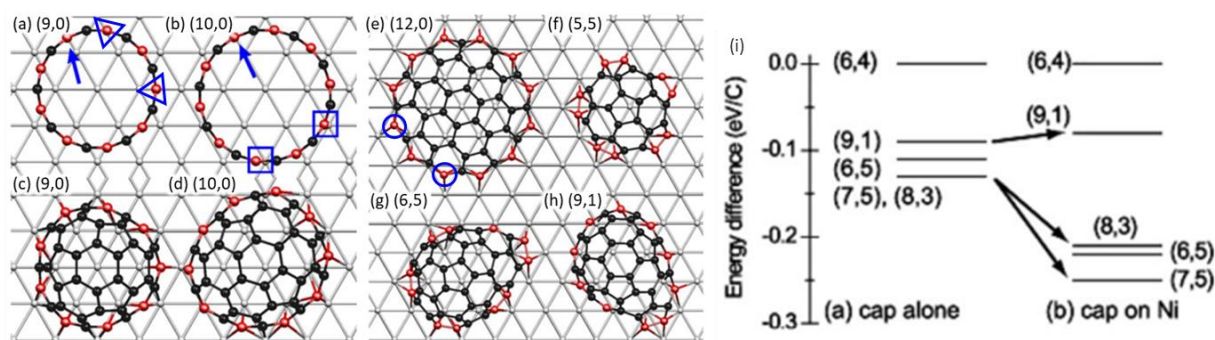


Figure 10 — a–h) Carbon nanotube caps (red, black dots) relaxed on Ni(111) (grey dots). Red dots correspond to CNT edge atoms in contact with Ni surface. Blue triangles and circles highlights examples of stable X and H sites, respectively, while blue squares highlights examples of energy costly T-sites. i) Edge energies of different nanotubes caps alone and relaxed on Ni. Match of CNT edge atoms with X-and H-sites of Ni(111) surface leads to reduction, with T-sites to increase of edge energy. Adapted from (114).

Still, the epitaxial growth model was used to describe the chiral selectivity of CNTs, formed on other metallic (116) and bimetallic catalysts (117). Strategies for directed synthesis of carbon nanotubes based on this concept were also developed (83, 118).

Later modeling works however reported that, within nanotubes of approximately comparable diameters, no cap conformation provides an energy advantage to a certain chirality during nucleation; however, formation of larger diameter nanotubes can be promoted due to a larger number of possible cap configurations (119). Moreover, the tube-catalyst interface was shown to have a very weak influence on the distribution of pentagons in the cap (120). Therefore, different selectivity models were needed.

### 1.3.1.2 Kinetic selectivity models based on edge structure

Yakobson *et al.* suggested that chiral selectivity is controlled by growth rate depending on CNT edge structure (121, 122), similar to dislocation growth process in 2D and 3D crystals. Further development of this work by the same team led to the creation of a more comprehensive model of nanotube growth (123), which combined the kinetic selectivity and thermodynamics of CNT nucleation. In this model, the abundance of nanotubes is described by the following equation:

$$A(\chi, d) = N(\chi, d)R(\chi, d) \quad (4)$$

where  $N(\chi, d)$  — the nucleation probability, and  $R(\chi, d)$  — the growth rate of nanotubes of a certain chirality ( $\chi$ ) and diameter ( $d$ ). This equation can be explained in the framework of simple continuum model (121) (Figure 11 (a-e)) where carbon nanotube is represented as a thin hollow cylinder.

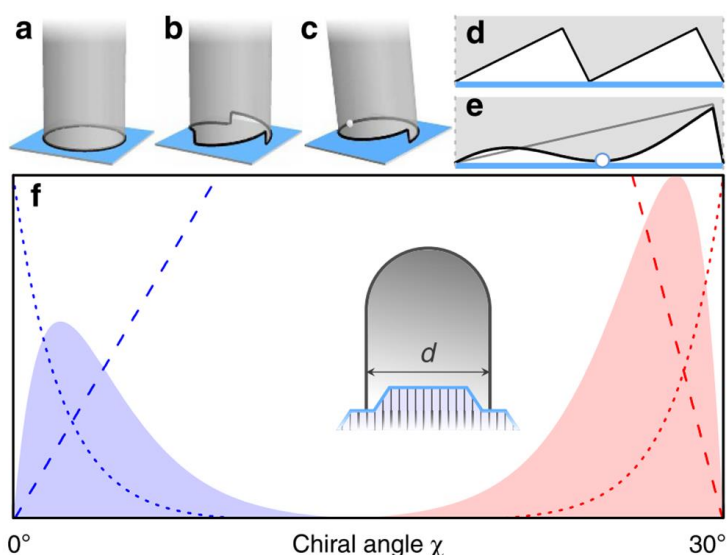


Figure 11 — Continuum representation of a) achiral, b) chiral with multiple kinks and c) near achiral (single kink) CNTs on a flat surface. Unfolding of the edges of CNTs with d) two kinks and e) one kink showing CNT tilt reducing tube-substrate energy. f) Abundance of nanotubes (filled areas) as a function of chiral angle. It is calculated as the product of nucleation probability (dotted

lines) and growth rate (dashed lines) for near zigzag (blue) and armchair (red) angles. Adapted from (123).

The steps at the nanotube-catalyst interface correspond to the so-called dislocations or kinks characteristic of chiral tubes. Full contact between solid catalyst surface and nanotube edge is characteristic of achiral CNTs. Since there are two types of such CNTs (zigzag and armchair) the authors of (123) made a transition from chiral angle  $\chi$  to the angle of deviation from the achiral direction  $x$ , which is  $x = \chi$  near-zigzag direction and  $x = 30^\circ - \chi = \chi^-$  for near-armchair directions. The absence of gap between the catalyst and CNT edge means that interface energy (the barrier that carbon atoms need to overcome to embed themselves in the nanotube structure) is minimal (Figure 11 (a)). Therefore, the nucleation probability of the CNTs is highest near achiral directions and minimal in the middle area of chiral angles ( $\chi = 15^\circ$ ). This behavior can be described by the following expression:

$$N(\chi, d) \propto e^{G^*/k_B T} \propto e^{-\pi d(\gamma + \gamma' \cdot x)/k_B T} \propto e^{-\beta \cdot x} \quad (5)$$

where  $G^*$  is the free energy of critical nucleus depending on ‘elastic’ energy of cap by itself and contact interface between the  $sp^2$  carbon lattice and the metal catalyst,  $(\gamma + \gamma' \cdot x)$  is the edge energy corresponding to gap between catalyst particle and CNT edge. As follows from the equation 5, the probability of nucleation decreases rapidly with the chiral angle deviation  $x$  and is minimal for chiral angles close to  $\chi = 15^\circ$ .

In turn, the term corresponding to the growth rate  $R(\chi, d)$  for solid catalyst surfaces depends on the number of kinks at the nanotube edge. It is minimal for near achiral directions because kink creation breaks the ideal tube-catalyst contact, and, as a result is energetically expensive. This term reaches its maximum at  $\chi = 19.1^\circ$  — the magic angle corresponding to nanotubes  $(2m, m)$  whose edges have the highest number of kinks (124).

$$R(\chi, d) \propto \pi d e^{-\frac{2C}{d^2 k_B T} \left( x + e^{-\frac{E}{k_B T}} \right)} \propto x \quad (6)$$

where  $C = 3,9 \text{ eV} \cdot \text{\AA}$  is the bending rigidity of graphene per atom (125). Thus, the kinetic term is proportional to the number of kinks, determined by CNT edge geometry. However, the difference between the models of (123) and (121) is that the temperature-imposed kinks  $e^{-\frac{E}{k_B T}}$  were taken into account, as well as energy penalty due to nanotube curvature ( $\sim \frac{1}{d^2}$ ). Therefore, nanotube abundance expression transforms into:

$$A(x) = N(x)R(x) \sim x e^{-x}$$

Its distribution is shown in Figure 11 (f) and all calculations are made for equal interface energies and growth barriers for both directions, zigzag and armchair.

Atomic calculations performed for the case of nanotubes grown on Ni(111) surface showed preferential growth of near-armchair CNTs of  $(n, n - 1)$  type (Figure 12). However, it was noted that this result can be influenced, up to reverse distribution with preferred growth of near-zigzag CNTs, by choice of catalyst whose surfaces favor their growth.

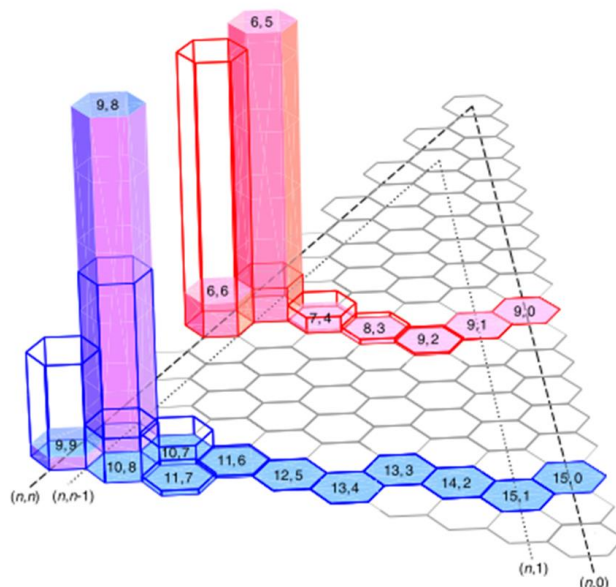


Figure 12 — CNT distributions based on the atomic calculations for two sets of diameters ( $d \approx 0.8$  nm (red) and  $d \approx 1.2$  nm (blue)) on solid (filled areas) and liquid catalyst (empty bars). Adapted from (123).

This model predicts the possibility of selective synthesis only in the case of CNTs grown on solid catalysts, since the liquid catalyst can adjust its structure to the nanotube edge (123) and thus compensate influence of the nucleation term, and at the same time reduce energy of kink formation of armchair CNTs down to zero (121). Therefore, nanotube abundance would depend only on chiral angle with the maximum at armchair region. An important hypothesis of these models is that the nanotube edge is assumed to make a  $90^\circ$  angle with the nanotube axis since this edge has the shortest length. However, this assumption neglects the interface energy and entropy.

### 1.3.1.3 Edge configuration entropy models

Latter works of Bichara *et al.* developed the idea of changes of configuration of the CNT edge during growth (122) and took into account the possible combinations of zigzag and armchair sites along it (126). A main hypothesis of the model proposed in (126) is that the number of carbon dangling bonds on the CNT edge is equal to  $n + m$ , of which  $2m$  of armchair sites (because these sites are always formed in pairs) and  $(n - m)$  of zigzag sites. In this model the edge is cut almost perpendicular to the axis of the nanotube, that is, it has the minimal length.

The total free energy of CNT (equation 7) includes four  $(n, m)$ -dependent terms: interfacial energy (first two terms), curvature energy (third term) and configurational entropy (fourth term):

$$F(n, m, T) = 2mE_{int}^A + (n - m)E_{int}^Z + \frac{4\alpha}{3d_{CC}^2} \frac{(n+m)}{(n^2+nm+m^2)} - k_B T \ln \frac{n!}{m!(n-m)!} \quad (7)$$

where  $E_{int}^{A,Z}$  is the interfacial energy of (A) armchair and (Z) zigzag sites (which have to be positive to promote nanotube growth),  $\alpha$  is the per atom bending rigidity of carbon nanotube (127),  $d_{CC} = 1.42 \text{ \AA}$  is the C-C bond distance. Thus, taking into account not only the number of active sites, but also the number of possible configurations depending on the temperature, the authors were able to build three-dimensional phase diagrams and found that only achiral CNTs are stable in the absence of the configuration entropy term ( $T = 0 \text{ K}$ ), while chiral CNTs are the most abundant in all other cases (Figure 13 (a, b))

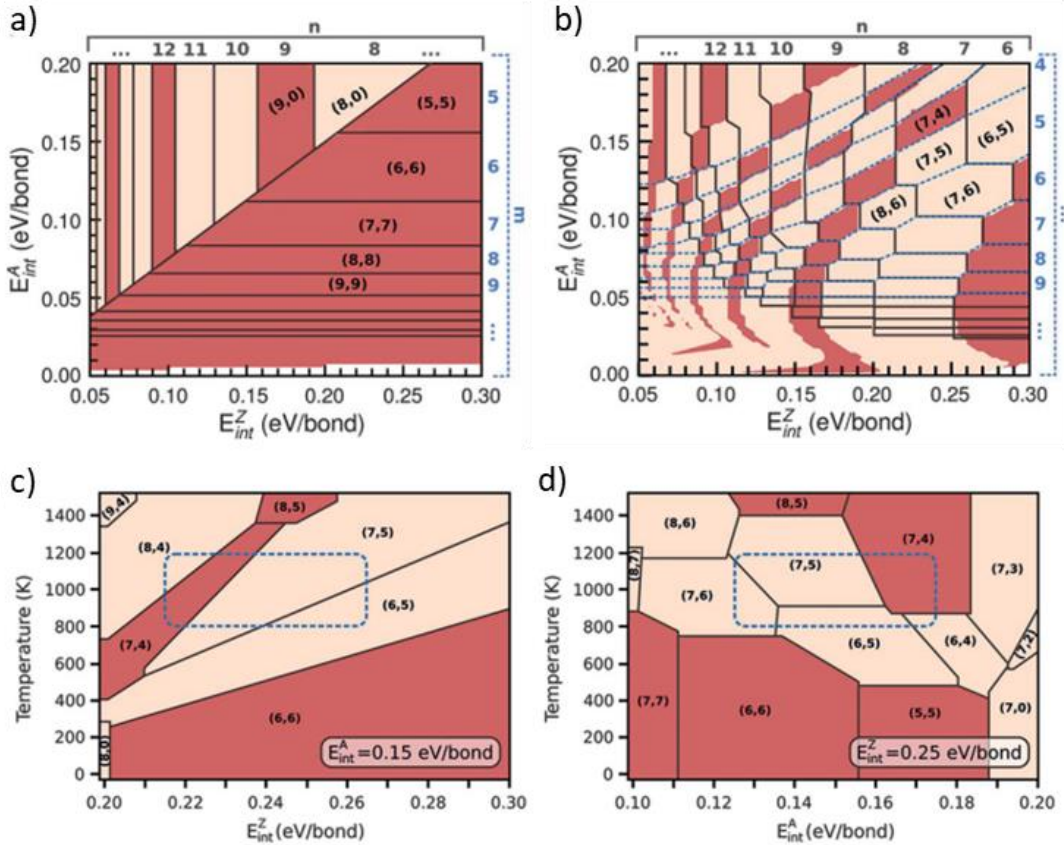


Figure 13 — Chirality maps. a) Ground states ( $T = 0 \text{ K}$ ), b) map at  $T = 1000 \text{ K}$ . Phase diagrams calculated for constant value of c)  $E_{int}^A$  and d)  $E_{int}^Z$ , blue dashed rectangle corresponds to experimental data (74). Adapted from (126).

The following work of Yakobson *et al.* was focused on the mixing term, responsible for all possible configurations of armchair and zigzag sites at the CNT edge (128) as well as on its changes due to the interaction of the nanotube with the catalyst (Figure 14) (128, 129). Authors concluded,

that tube-catalyst contact can influence the edge energy of the CNT, thus favoring a certain segregation of armchair and zigzag sites.

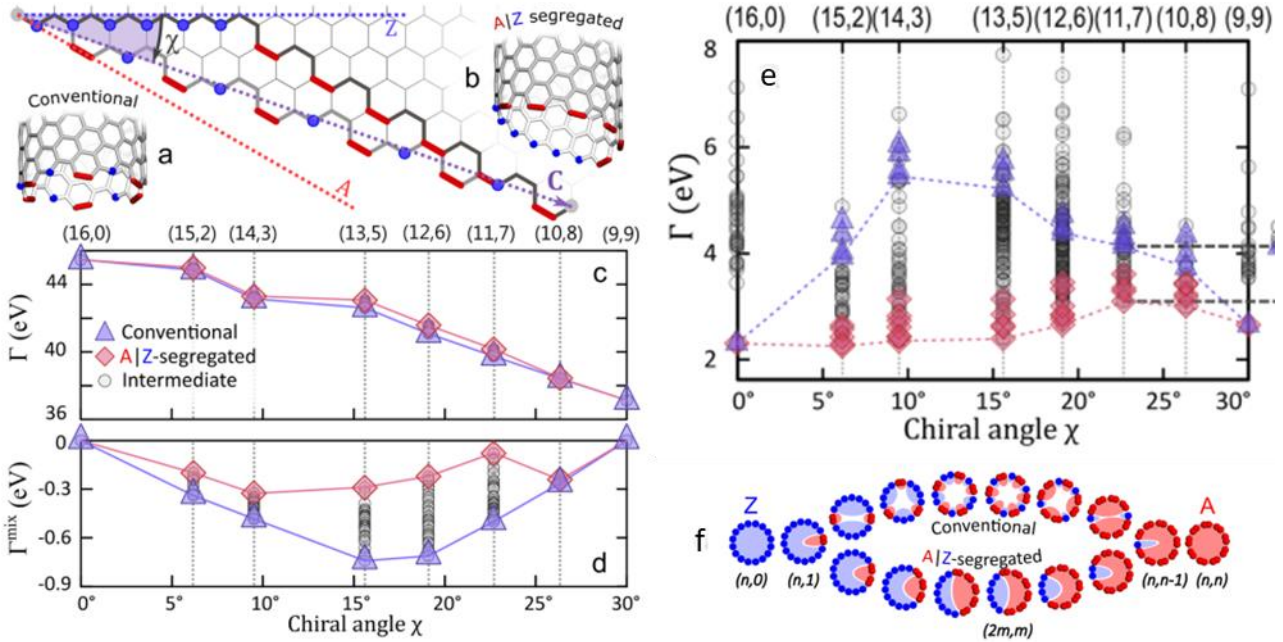


Figure 14 — Two boundary cases a) fully mixed and b) fully A|Z separated zigzag and armchair sites, and c) the plot of the total interface energy of the CNTs and d) the part corresponding to the mixing term for the free standing CNTs. e) Interface energy of the CNT on the solid  $\text{Co}_7\text{W}_6(003)$  W-substrate as a function of chiral angle. f) Schematic representation of fully mixed and A|Z separated sites for nanotubes of different chirality. Adapted from (128).

The most recent work of Bichara *et al.* considers the possibility of formation of more complex oblique tube-catalyst interfaces (Figure 15) (130). The number of edge atoms, as before (126, 128, 129), equal  $n + m$ , however, number of zigzag  $N_Z$  and armchair  $N_A$  sites in this model can vary (up to  $N_Z = n + m - 2$  and  $N_A = 2$ ), satisfying the condition:

$$2 N_A + N_Z = n + m$$

During the simulations, the possibility of both addition and removal of atoms was also taken into account, which allowed to model not only CNT growth, but also shrinkage. Thus, this model complements previous work of Bichara *et al.* (126) and proposes a more comprehensive view on growth selectivity.

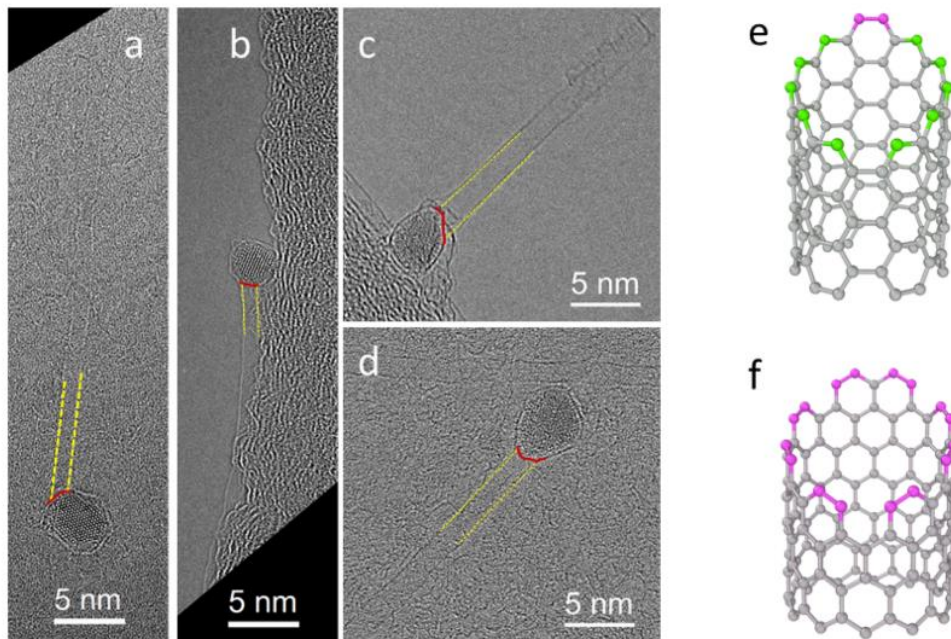


Figure 15 — a-d) HR-TEM images CNTs (yellow dashed lines) on the catalyst, showing oblique interfaces (red curves). e) oblique interface of armchair (6,6) CNT, containing  $n + m = 12$  edge atoms with  $2n - 2 = 10$  zigzag (green) and two armchair (pink) atoms. f) oblique interface of zigzag (12,0) CNT containing 16 edge atoms (which makes such configuration energetically disadvantageous). Adapted from (130).

### 1.3.2 Experimental kinetic measurements

In order to verify these models, numerous approaches were developed and tested to observe the nucleation and elongation of CNTs in real time, as well as to measure their growth kinetics during or after the synthesis.

#### 1.3.2.1 Vertically aligned CNT arrays kinetic measurements

The first methods that allowed to access CNT growth kinetics were focused on vertically aligned (VA) CNT forests (131–133).

Futaba *et al.* grew nanotube forests on similarly prepared substrates during different times, after which their heights were measured (131). Meshot *et al.* used a displacement sensor to *in-situ* record the VACNT height by tracking movements of  $\text{Si}_3\text{N}_4$ -covered cap mounted on the substrate with the catalyst substrate and pushed up by growing CNTs (Figure 16 (a)) (132). Einarsson *et al.* determined the thickness of the layer of synthesized nanotubes based on the evolution of its optical absorbance (Figure 16 (d, e)) (133).

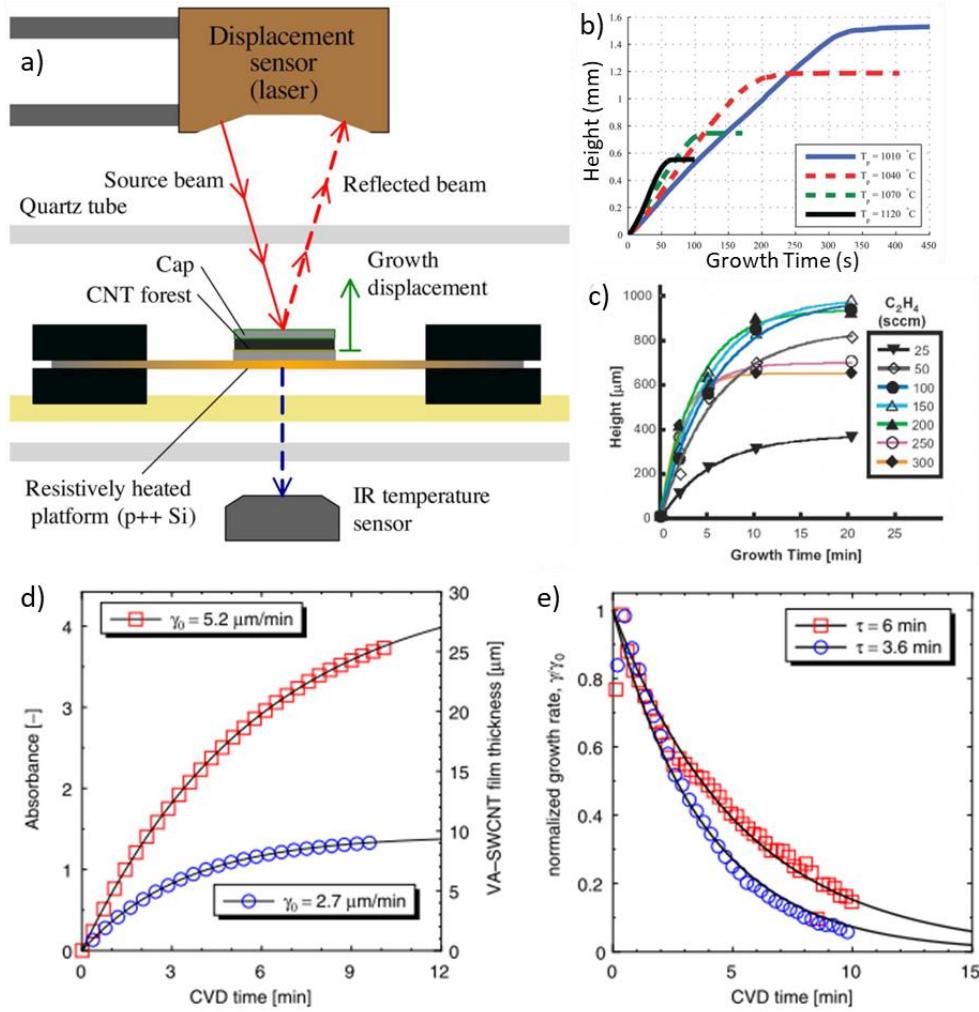


Figure 16 — a) Schematic of the setup for in-situ measurement of the VACNT forests height and b) the kinetic curves for different temperatures measured on it. c) the kinetic curves for different carbon precursor pressures. d) the absorbance and e) the growth rate as a function of synthesis time. Adapted from (a,b) – (132), (c) – (131), (d,e) – (133).

All these methods allow to measure the sample-averaged CNT growth kinetics (Figure 16 (b, c)), which, according to (131, 133) could be described by exponential decay law:

$$H(t) = \beta\tau_0(1 - e^{-t/\tau_0}) \quad (8)$$

where  $\beta$  is the initial growth growth rate, and  $\tau_0$  is the characteristic catalyst lifetime.

The main drawback of this method, which later methods tried to overcome, is the impossibility to access growth kinetics of individual CNTs.

### 1.3.2.2 In-situ Raman spectroscopy

The kinetics can also be measured by indirect methods, such as *in-situ* Raman. In this case, not the length of the CNT itself, but the intensity of its Raman signal is measured. In the works (134,

135) the growth rate was extracted from the curve of the G-band area evolution as a function of time which followed the same exponential decay law as mentioned in previous section. Moreover, the authors of (135) reported measurements of the growth kinetics of individual nanotubes and its linear dependence on the chiral angle with the higher growth rates for CNTs with near-armchair structures (Figure 17 (c-e)). This results are in a good agreement with predictions made by the dislocation theory (121).

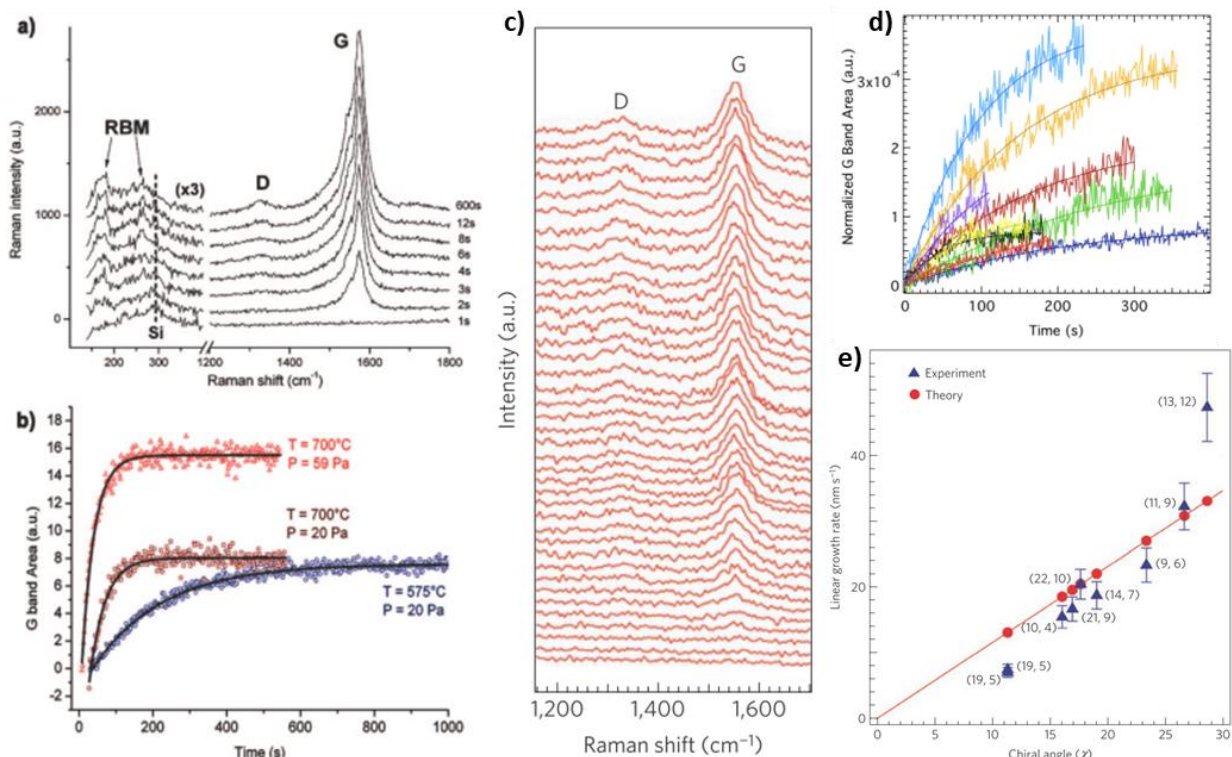


Figure 17 — a) Time evolution of the Raman spectra of the sample and b) the plots of the G-band area as a function of time for different synthesis conditions. c) Time evolution of the D and G-band spectra of the individual CNTs measured via In-situ Raman d) G-band area as a function of time for several individual CNTs and e) the plot of the initial growth rate as a function of chiral angle.

Adapted from (a,b) – (134), (c-e) – (135).

The main drawback of this method for individual kinetic measurements is its low throughput. The statistics of (135) included only 9 nanotubes.

### 1.3.2.3 In-situ transmission electron microscopy

In-situ TEM allows to image the process of the nanotube nucleation and growth by carbon integration at the interface with the catalyst (136). Moreover, it allows to determine the catalyst state during the synthesis (Figure 18). However, the method is not suitable for measuring growth kinetics due to the small imaging area and unrealistic synthesis conditions (electron irradiation, low pressure).

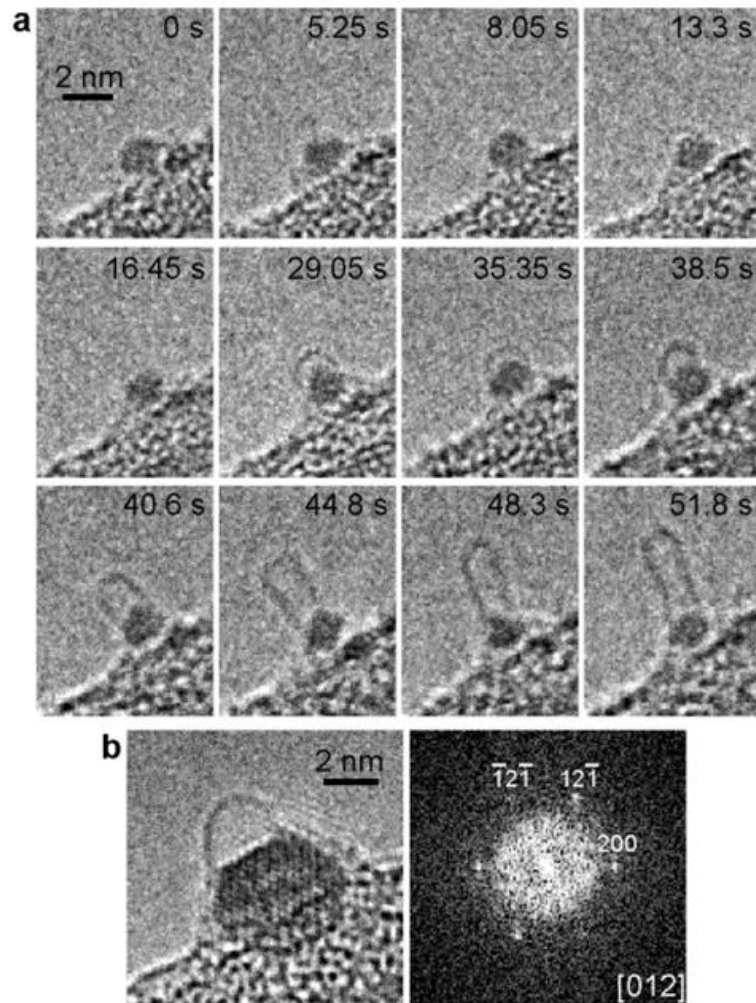


Figure 18 — a) Snapshots of the nucleation and growth process of the nanotube, taken with In-situ TEM. b) Snapshot of carbon cap with nanoparticle (left) and its reciprocal space (right) identified as Fe-carbide. Adapted from (136).

### 1.3.2.4 *In-situ* field emission microscopy

Marchand *et al.* (137) used field emission microscopy to measure the CNT growth kinetics. To do so, nanotubes were grown on a tungsten needle inside a field emission microscope (Figure 19 (top)). As the nanotubes grew longer, they dominated the field emission pattern and by adjusting imaging parameters (such as voltage) it was possible to highlight only CNT signal. Subsequent video analysis provided access to the growth kinetics (Figure 19 (Bottom)).

Marchand *et al.* reported the linear growth of individual nanotubes, sometimes accompanied by a stepwise rotation of the FEM pattern, as well as the occurrence of various incidents such as rotation reversal (Figure 20) (137). These latter observations were attributed to the rotational growth of nanotubes predicted by dislocation theory (121). The main drawbacks of this method are the

unrealistic growth conditions and the low experimental throughput. The overall statistics of measured kinetics included only a few CNTs.

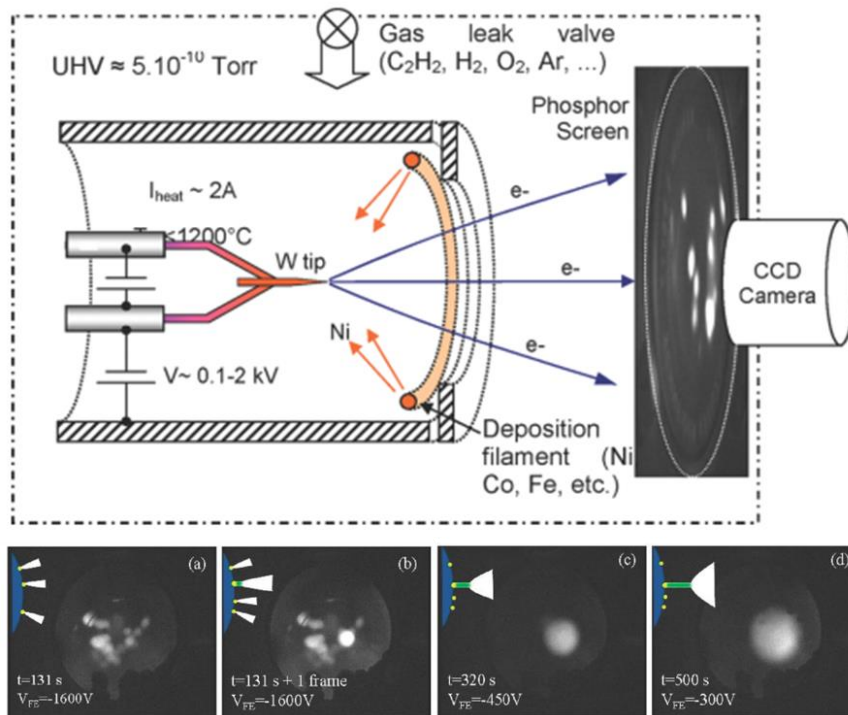


Figure 19 — Top: experimental setup for FEM observations of CNT growth.

Bottom: FEM pattern evolution during nanotube growth. a) FEM signal from Ni nanoparticles, b) sudden appearance of the CNT (bright white spot), c) d) FEM pattern enlargement during nanotube growth (voltage was decreased to avoid oversaturation and to reduce emission of Ni nanoparticles)

Adapted from (137).

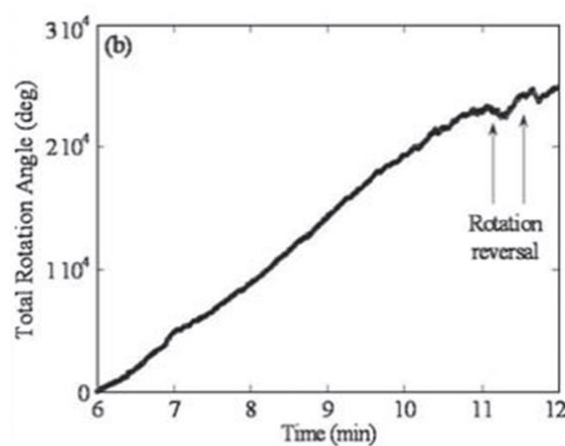


Figure 20 — Rotation angle of nanotube during the synthesis. Adapted from (137).

### 1.3.2.5 Isotope labelling

There are also a number of methods based on labelling of the nanotubes during their growth at certain moments of time (138, 139). After synthesis, such samples are characterized by some method (Scanning electron microscopy (SEM), optical microscopy, Raman) and the distance between the marks are correlated with a time scale, which provides data on the growth kinetics.

The most recent variation of this approach allows to measure the growth kinetics of individual single-walled CNTs with time resolution down to about one minute (139). For this purpose, at certain moments of CVD synthesis, the ethanol used as a precursor was diluted with ethanol containing isotope  $^{13}\text{C}$ , creating labels along the CNTs. Their positions were then determined via Raman mapping after synthesis (Figure 21 (a)).

Using this method, S. Maruyama *et al.* observed that individual CNTs grew at constant rate all over their lifetimes. Moreover, it was found that nanotubes of the same chirality can grow with different growth rates. Also they evidenced growth rate changes when modifying *in situ* the synthesis temperature (Figure 22). Further use of this approach allowed a more detailed study of the behavior of nanotubes in synthesis with interruptions in the carbon precursor feed or with its replacement with etchants (140).

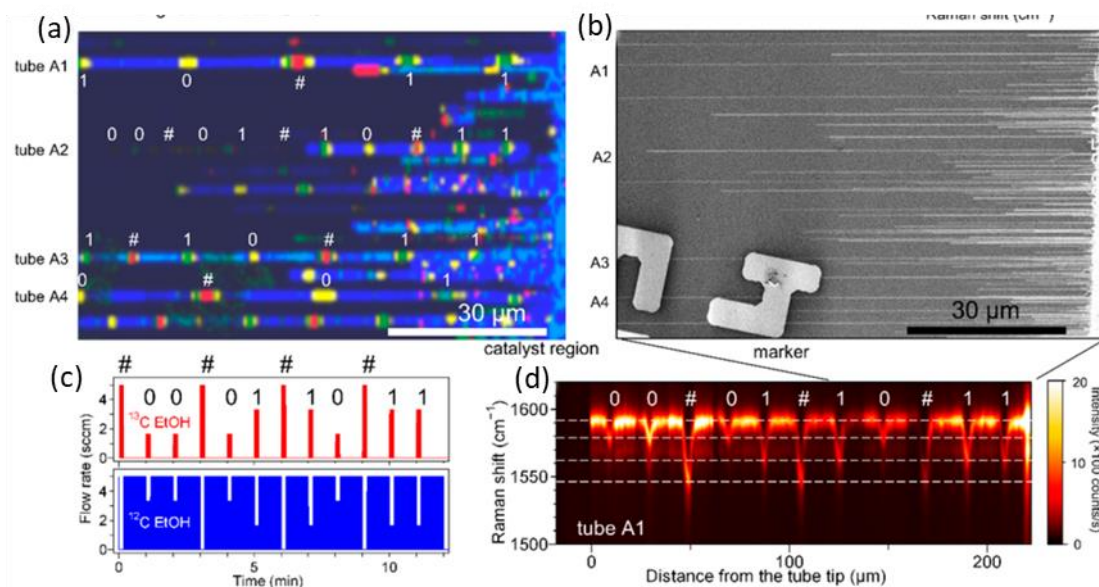


Figure 21 — a) Raman map of the synthesized nanotubes with different labels along them and b) SEM image of the same area. c) Flow rates of  $^{12}\text{C}$  and  $^{13}\text{C}$  ethanol with carrier gas during synthesis. d) Raman intensity map along A1 nanotube. Adapted from (139).

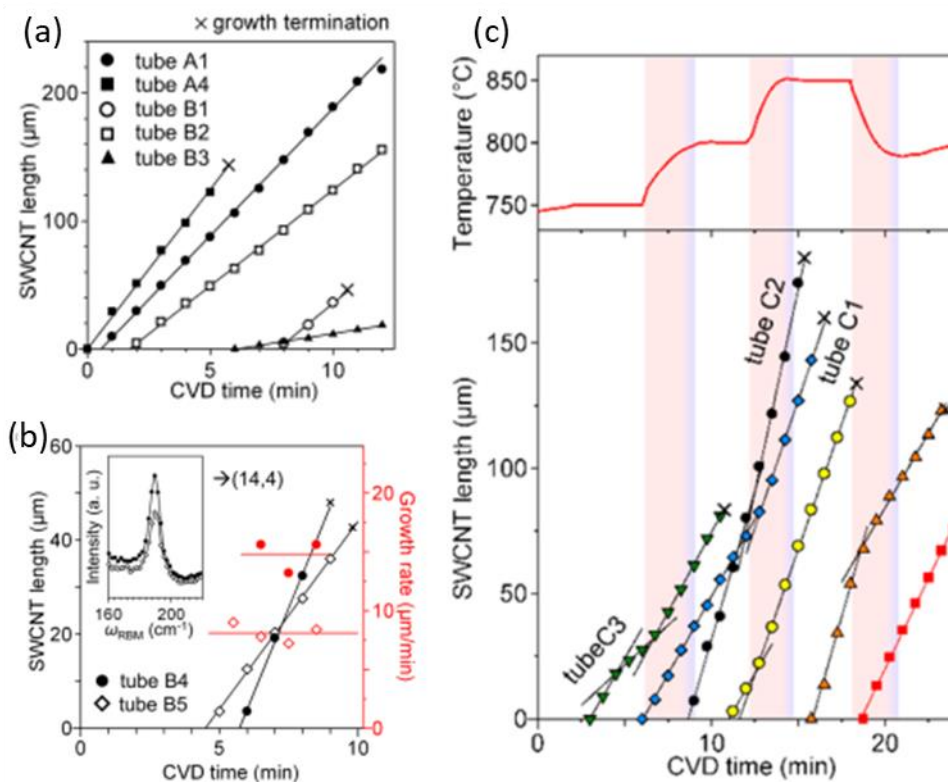


Figure 22 — Plots of CNTs length as a function of synthesis time for a) different nanotubes and b) for nanotubes of the same chirality (Raman spectra of both CNTs in the inset). c) Temporal evolution of the growth rates of the CNTs (bottom) as a function of temperature changes (top) during the synthesis. Adapted from (139).

This method has a relatively high throughput, which allowed to measure the kinetics of 44 CNTs. However, its time resolution of about 1 minute does not allow to access the kinetics of rapid processes, which may occur on shorter time intervals.

#### 1.4 Open questions from the literature

Following this literature analysis, a few important questions regarding CNT growth kinetics that are still debated or simply need to be answered should be highlighted.

- Is the growth of nanotubes at the individual scale constant, as reported by Koyano *et al.* (140) and Marchand *et al.* (137), or exponentially decaying, as reported by Rao *et al.* (135)? Answering this question would allow to understand if catalyst deactivation (*e.g.* progressive encapsulation or ripening) plays the key role in CNT growth termination, or if it is played by other catastrophic events such as the integration of topological defects (causing CNT closure or detachment) or the sudden removal of the catalyst particle. In each case, the solutions to synthesize longer CNTs will be different. For instance, in case of catalyst encapsulation, reactivation of the

particles by carbon coating removal may be considered while for avoiding the integration of catastrophic topological defects, adjustment of the growth conditions (temperature, precursor pressure, gas contaminants) would be more important.

- Does the growth rate of nanotubes depend on their chirality or their metallicity? If so, in which way? Major applications envisaged for carbon nanotubes lie in microelectronics (e.g. metallic CNTs for connecting wires, semiconducting CNTs for field-effect transistors) for which control of the metallicity is crucial, sometimes with an extreme degree of purity. Thus, answering this question is crucial for the development of selective methods of CNT synthesis based on kinetic selectivity. Shedding the light on the influence of chirality on the growth rate may also lead to novel types of chirality selection methods possibly with higher controllability and reproducibility.

- What is the structure of nanotube edge during growth, how does it evolve during carbon addition and how does it influence the growth kinetics? The edge or face structure does affect growth rate in case of 2D and 3D crystals. Since carbon nanotubes can be viewed as 1D crystals with circular edge, their growth rate should depend on the edge structure. Answering these questions may notably help to develop selective synthesis methods based on catalyst templates or growth conditions allowing to stabilize specific edge structures and therefore promote specific chiralities.

- How synthesis conditions (e.g. temperature, pressure, catalyst type, gas phase composition) affect the growth kinetics at the individual nanotube level? Analysis of the temperature and pressure influences can provide important information about the chemical processes governing the growth kinetics.

Although not all these questions were directly addressed during my PhD, they represented the principal source of motivation for my doctoral research work which is described in detail in the rest of the manuscript.



# Chapter 2.

## Experimental approach

To address these questions, I mainly used the combination of three techniques which allowed me to measure the growth kinetics of individual nanotubes, as well as to determine their structure and metallicity in appropriate cases.

First of all, I used homodyne polarization microscopy, which allows to image nanotubes during their synthesis under real growth conditions, that is on the substrate and at atmospheric pressure. Moreover, this setup allows to image a large number of nanotubes per experiment. In addition to high throughput, the setup has high temporal (down to 25 ms) and spatial (down to 1  $\mu\text{m}$ ) resolutions and localization accuracy as good as 0.3  $\mu\text{m}$ , which is crucial for precise kinetic measurements.

Further analysis included the use of scanning electron microscopy, which is necessary to precisely localize the CNTs on the substrate, as well as assess their metallicity, and Raman spectroscopy which allows to determine the metallicity and, in appropriate cases, the chirality of nanotubes.

### 2.1 Homodyne polarization microscopy

This constitutes the main method of this work: it was developed quite recently and is based on the strong optical anisotropy of carbon nanotubes (*141–143*).

Either a tunable (*141*) or a supercontinuum (white) laser (*142, 143*) can be used as a light source. A supercontinuum source allowing to excite nanotubes in the whole visible spectrum was used during my work. The system also uses a polarizer and analyzer in crossed configuration, which is needed to strongly reduce the substrate reflection (Figure 23). The nanotubes are oriented at about 45 ° with respect to the axes of the crossed polarizers, which allows the signal from CNTs to pass through analyzer with little loss compared with that of reflected light. The weak field scattered by the nanotube is then amplified by interferential coupling with the remaining field reflected from the substrate. This process is called homodyning, and the technique is thus called homodyne polarization microscopy.

For the case of an ideal optical system, the contrast of the nanotube can be described by the following equation:

$$C = \frac{I-I_0}{I_0} = \frac{(1+r)^4|A|^2}{4r^2\delta^2} + \frac{(1+r)^2\text{Im}(A)}{r\delta} \quad (9)$$

where  $I$  is the intensity measured at the position of the CNT, and  $I_0$  is the intensity measured beside the CNT (typically a few microns away). The first term of equation 9 is related to scattering and describes what would be measured in a Rayleigh scattering experiment. The second term describes the interference between the field reflected by the substrate and the scattered field of the CNT, and  $r$  is the substrate reflection coefficient. As visible in the equation, the lower the reflection, the higher the contrast.  $\delta$  is the small angular deviation between the polarizers from an angle of perfectly  $90^\circ$ . This deviation can be positive or negative, hence the nanotube contrast can be positive or negative (Figure 23 (d)).  $A$  is proportional to the nanotube susceptibility which describes the optical response of the nanotube to the incident field: its real part is proportional to the nanotube scattering coefficient and its imaginary part to its absorption coefficient. This complex constant depends on the geometrical parameters of the CNT and on its localization in the illuminated area.

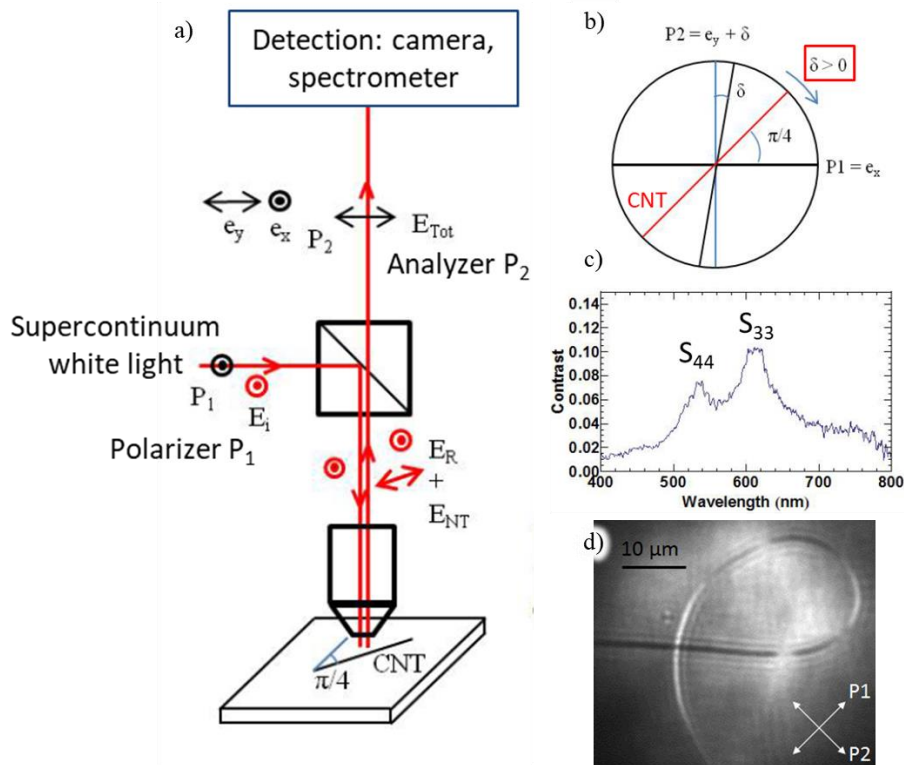


Figure 23 — a) Schematic of the homodyne polarization setup. b) Positions of polarizer (P1), analyzer (P2) and nanotube (CNT) in the setup. c) Absorption spectrum of a nanotube with highlighted transitions and d) image of a CNT demonstrating change of contrast from dark to bright when changing its orientation regarding two crossed polarizers (P1 and P2). Adapted from (143).

As one might notice, the above equation diverges for  $\delta = 0$ , thus corresponding to infinite contrast. In the real case, this never happens due to the depolarization caused by the optics (143). In practice the optimal contrast can be obtained at small but non-zero values of  $\delta$ . A careful beam engineering (in terms of width, aperture, and axis) is also necessary to preserve the ratio of polarization extinction small enough for the extraction of the CNT signal. The polarization extinction ratio is the intensity ratio between the parallel polarizers and the crossed polarizers configurations.

This technique thus allows one to measure the optical absorption spectrum of individual CNTs on substrate and to image them (Figure 23 (c, d), respectively).

## 2.2 Raman spectroscopy

Raman spectroscopy is widely used to characterize various  $sp^2$ -carbon materials such as fullerenes (144), graphene sheets (145), graphene nanoribbons (146), nanotubes (145, 147–149) and other carbonaceous materials (150).

The first-order Raman scattering process can be described by three steps (151) (Figure 24 (a1, a2)):

1. When a photon is absorbed by a material, its energy is transferred to an electron which is excited from its initial level to a higher energy level with the formation of an electron-hole pair.
2. Scattering of the excited electron causes either phonon formation (Stokes scattering) or phonon annihilation (anti-Stokes scattering).
3. Relaxation of the electron to its background level causes the emission of a photon. The energy of the emitted photon differs from the energy of the incident photon by the energy of the phonon.

If the excited electron energy level before or after phonon scattering corresponds to a real electronic state, such a transition is called resonant; if not, the electron is said to be excited to a virtual (unstable) state and the transition is called non-resonant. Thus, there are two types of Raman scattering: resonant and non-resonant. The resonance can either be with the energy of the incident photon (equal to the laser energy) or of the scattered photon (equal to the difference between the laser energy and the phonon energy). Resonant Raman scattering can be orders of magnitude more intense than non-resonant one.

This simplified description neglects the coulombic interaction between electrons and holes: in the case of CNTs, excitonic effects caused by the strong electron-hole interactions come into play and a precise description must involve transitions between excitonic levels caused by photon and phonon scatterings.

Phonons in this process correspond to collective vibrations of atoms in the crystal lattice, but not all of them have the symmetry necessary for being Raman active. In the case of carbon nanotubes, the number of Raman active modes is 8 for achiral CNTs and 14 for chiral ones (152). However, some of them have low intensity and are almost undetectable in experimental spectra, and some are degenerate (*i.e.*, their vibrational frequencies are the same) (153). Moreover, some modes such as the D and 2D bands cannot be derived from such symmetry considerations: their occurrence can be explained by higher-order scattering which involves additional scattering events by phonons or defects (154) (Figure 24).

In our work, we used resonance Raman spectroscopy to characterize nanotubes. Here, the energy of the incident or scattered photon corresponds to the energy of an optical transition of the nanotube (energy difference between two symmetrical van Hove singularities (Figure 5 (b))) because the Raman spectrum of CNTs is dominated by resonant contributions (145).

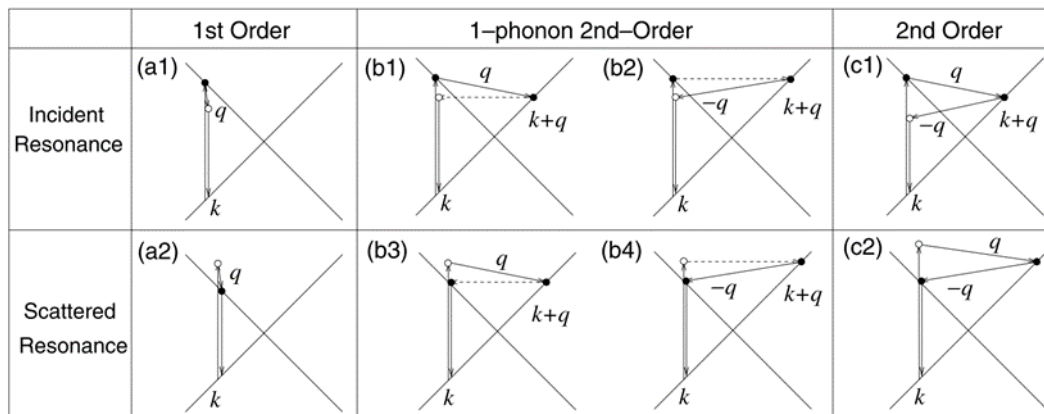


Figure 24 — Schematic of resonance transitions of 1<sup>st</sup> and 2<sup>nd</sup> orders in graphene. Adapted from (154).

A typical nanotube spectrum (Figure 25) has three regions with characteristic features: the radial breathing mode (RBM) region in the range of 100–400 cm<sup>-1</sup> for CNTs with diameters of ~ 0.6–2 nm (149), D and G modes region (1300–1800 cm<sup>-1</sup>) and 2D (or G') region (2400–2800 cm<sup>-1</sup>).

The RBM corresponds to the in-phase vibration of atoms perpendicular to the nanotube surface (Figure 25 (b)). An important feature is its strong dependence on the CNT diameter  $d$ , which can be described by the following equation (28):

$$\omega_{\text{RBM}} = \frac{227}{d} \sqrt{1 + C_e \cdot d^2} \quad (10)$$

where  $C_e$  is the interaction constant of the CNT with the environment (145). Thus, knowing the nanotube diameter and the used laser energy, it is possible to determine the nanotube chirality using a Kataura plot adapted to the nanotube environment (Figure 6).

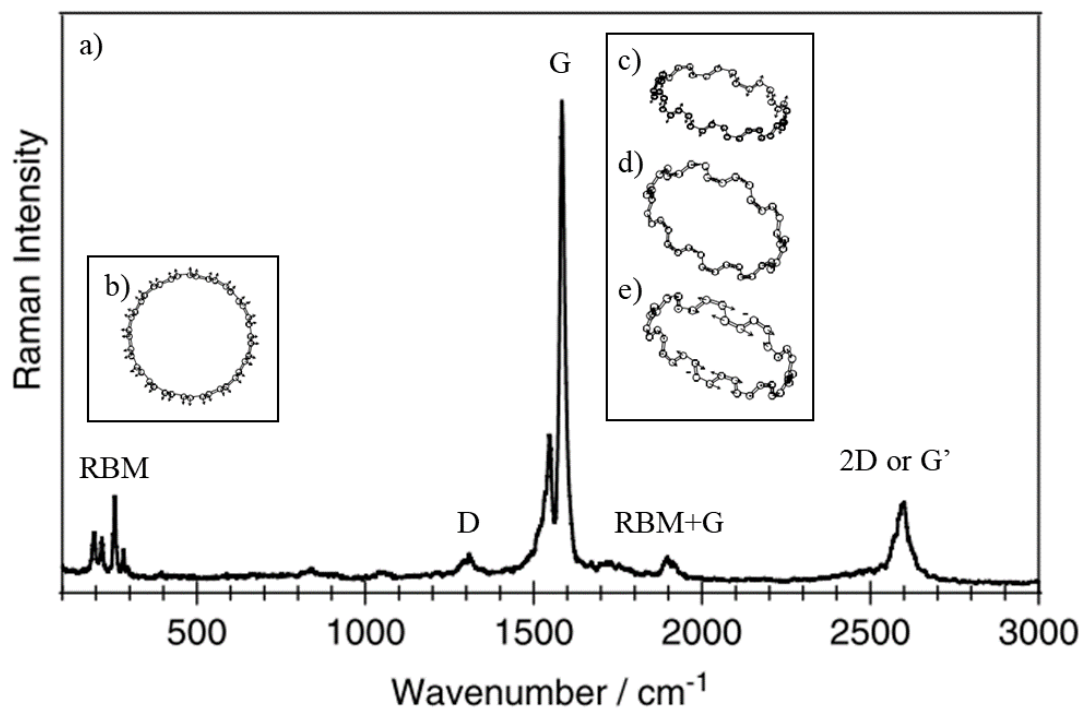


Figure 25 — a) Typical Raman spectrum of CNTs. Atomic vibrations in a nanotube (10,10) corresponding to b) radial breathing mode, c-e) G-mode (for doubly degenerate c) and e) modes, only one variation of vibrations is indicated). Adapted: a) from (155), b-e) from (153).

The G-band, which is in the mid-wavenumber region, comes from degenerate tangential modes of graphene with frequencies around  $1580\text{-}1590\text{ cm}^{-1}$ , corresponding to the anti-phase vibrations of atoms in the plane of graphene sheet (in-plane longitudinal optical (iLO), in-plane transverse optical (iTO)) (156). In the case of free-standing nanotubes, the G-band includes one peak for achiral CNTs and two peaks for chiral ones ( $G^-$  and  $G^+$ ), to which may correspond up to six degenerated vibrations of LO and TO types (Figure 25 (c-e)) (156). The G-band split for chiral CNTs originates from the nanotube curvature making tangential modes non-equivalent in the axial and circumferential directions (39, 148).

The shape of this mode makes it possible to distinguish between metallic and semiconducting nanotubes. G-bands of the latter consist of one or two narrow peaks for achiral and chiral CNTs, respectively. For metallic CNTs, the LO mode is broadened because of electron-phonon interactions, (13, 157) (Figure 26).

Both RBM and G modes arise from first-order transitions (Figure 24) and their frequencies can be described within the framework of symmetry analysis of atomic vibrations in the nanotube crystal lattice (13, 152, 156). Two other characteristic modes of graphene and CNTs, D and 2D, require double resonance theory using single and double-phonon transitions, respectively, to describe them (Figure 24 (b1-c2)) (154, 158).

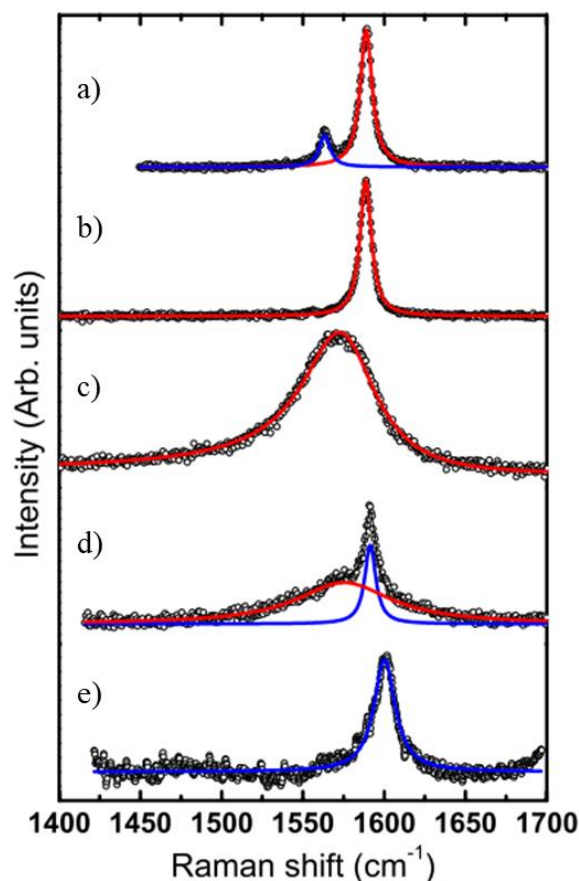


Figure 26 — Different typical G-band shapes for nanotubes a) (11,10) (semiconducting chiral), b) (25,0) (semiconducting achiral), c) (24,0) (metallic achiral (zigzag)), d) (19,6) (metallic chiral) e) (10,10) (metallic achiral (armchair)). Blue and red fitting curves corresponds to TO and LO vibrations, respectively. Adapted from (39).

The D-band arises from the elastic scattering of photo-excited electrons by defects (13, 154). Its characteristic wavenumber is typically between 1200 and 1400  $\text{cm}^{-1}$  and depends on the laser energy (*i.e.* the mode is dispersive). It can be used to estimate the defect density of nanotubes or the percentage of defective carbonaceous by-products, by measuring the intensity ratio of the D and G-bands, since G-band intensity is independent of defects (at sufficiently low defect density) (154).

The second overtone of D-band is called 2D or G'-mode: it arises from two-phonon scattering and can occur even in defect-free nanotubes (13, 154). It is also a dispersive mode due its double resonance nature. In theory, its dependence on the electronic structure can be used to assess strain and doping, and distinguish them in carbon nanomaterials (159).

### 2.3 Scanning electron microscopy

Electron microscopy is a standard characterization technique for micro- and nano-objects. It is based on the quantum nature of electrons (160) and the dependence of their wavelength on an accelerating potential (161), which allows to overcome the diffraction limit of optical microscopy (162).

A SEM includes an electron gun emitting electrons that are accelerated by an anode and focused by an electronic lens system. The sample is scanned point by point by the electron beam using scanning coils. The inelastic scattering of electrons by the sample results in secondary electrons which are captured by a specific detector and used to obtain information on the sample topography, composition, and surface charge (163). Back-scattered electrons resulting from the elastic scattering of incident electrons can also be used for SEM imaging.

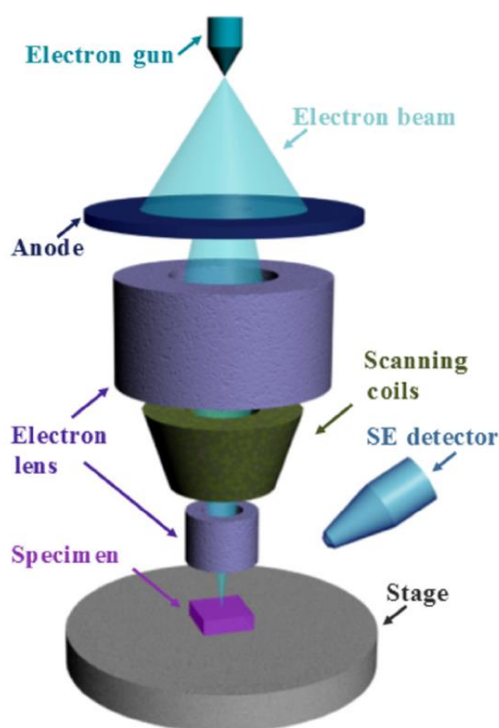


Figure 27 — Schematic of SEM. Adapted from (163).

When studying CNTs, SEM can not only provide information on their location, but can also be used to distinguish between metallic and semiconducting CNTs based on their SEM contrast (163–165). The difference of contrast is caused by the difference of charge carrier mobilities (Figure 28 (d, e)) between M and SC SWCNTs which impacts the local charge density of the substrate beneath the nanotube, hence the local charge contrast. The absolute value of the contrast also depends on the type of substrate and the acceleration potential. Conductive substrates turn out to be charge-neutral, since regardless of the accelerating potential, the charges will quickly go to ground (Figure 28 (a)). For

insulating substrates, the situation is different: at low acceleration potentials the substrate will be positively charged (because of secondary electrons emission) while at high potentials it will be negatively charged (because electrons remain trapped far from the substrate surface) (Figure 28 (b)). Conductive substrates with an insulating coating will be positively charged in either case (Figure 28 (c)) (163). Thus, if CNTs are charged on an insulating substrate at low acceleration potential, M-CNTs will display a strong bright contrast while SC-CNTs will display a much lower contrast (Figure 28 (e)). In the case of high acceleration potential, contrast of SC CNTs is opposite to that of M ones (Figure 28 (d)).

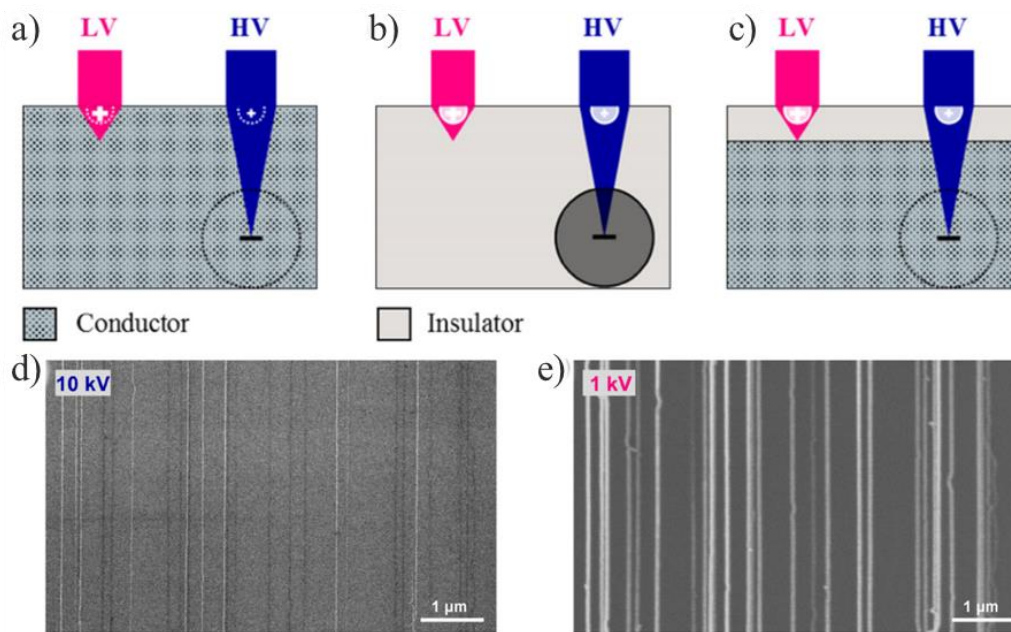


Figure 28 — Charge effects at high and low acceleration potentials for different types of substrates: a) conductor, b) insulator and c) insulator-coated conducting substrate. SEM images of the same area made with e) 10 kV and d) 1 kV of the acceleration voltage for the CNTs grown on SiO<sub>2</sub>/Si substrate. In image d) metallic CNTs appear as a bright vertical lines, while semiconducting are the dark ones. At low acceleration potential e) the contrast of semiconducting nanotubes is lower relative to that of metallic ones. Adapted from (163) for a-c) and from (165) for e,d).

# Chapter 3.

## Materials and methods

### 3.1 Substrates and catalysts

ST-cut quartz (ST = Stable Temperature) was used as substrate, due to its ability to promote the growth of CNTs horizontally aligned along the crystalline direction [100] (Figure 29). The ST-cut does not correspond to any low-index crystallographic surface of quartz but its cutting angle is nearly parallel to that of r-plane (01-11) (Figure 29) (166). To avoid the reduction of polarization purity caused by the back-side reflection of this birefringent substrate, a wedge with optical quality was made to deflect the back side reflection from the objective axis and, hence, reduce its influence on the image. To improve the top surface crystalline quality, all samples were annealed at 900 °C for 8 hours. To facilitate the localization of the imaging area, optical marks were made by optical lithography followed by plasma etching. The catalyst pattern (line segments with alphanumeric localization marks) was made by UV lithography using a Shipley Microposit S1818 photoresist doped with a FeCl<sub>3</sub> solution (10 mM) in methanol. Subsequent calcination in air at 700 °C for 5 minutes was made to remove the resist and oxidize the iron catalyst.

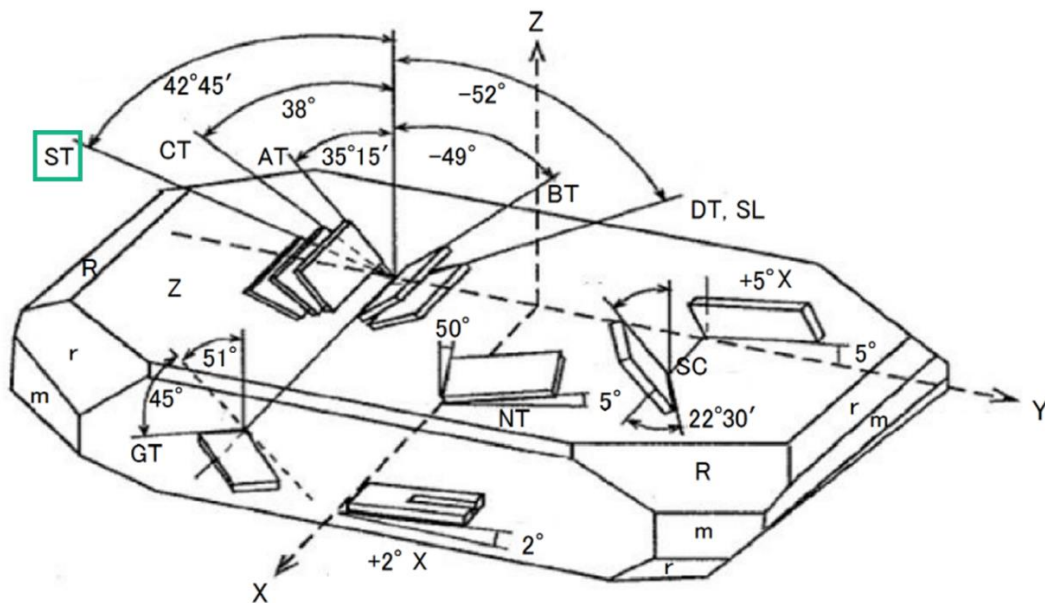


Figure 29 — Different cut orientations of quartz crystal. Adapted from (167).

### 3.2 CNT synthesis

For CNT growth, a homemade CVD setup consisting of a gas/vapor supply system with four mass-flow controllers and a miniaturized CVD cell with a top optical window (Linkam TS1500) was used. To ensure reproducibility, the cell was calcined at 700 °C for 10 minutes before each synthesis. The system was also connected to two gas/vapor lines: the first one passed through a flask with ethanol cooled at 0 °C and the second one supplied argon, which was used to adjust the partial pressure of ethanol in the CVD cell between 8 and 1600 Pa. All syntheses were performed at a total gas flow in the cell of 1422 sccm. The typical range of synthesis temperatures was from 700 to 950 °C. Gas detectors were installed at the outlet of the CVD cell to monitor the concentrations of H<sub>2</sub>O and O<sub>2</sub> in real time.

### 3.3 Optical imaging

A detailed schema of the optical setup is shown in Figure 30. This setup has two configurations: imaging and spectroscopy. Switching between them is primarily done by exchanging the Linkam cell and the piezo stage and by switching the laser beam from the camera to the spectrometer using mirror 5\_6.

A supercontinuum laser (Fianium SC-400-4, 2 ps pulses, 40 MHz, spectral range 400-2000 nm) was used as a white light source. To remove IR radiations, we used reflective filter made of a dichroic mirror and two beam traps (elements 4 and 12\_x). The alignment system (blue and yellow parts in the schema) was used to ensure high polarization purity, critical for high image contrast. It includes a system of lenses (elements 9\_1 to 9\_3) to reduce the beam diameter, and a spatial filter (50- $\mu$ m pinhole labeled 8\_5) to improve beam uniformity.

Two Glan-laser polarizers (labeled as 7\_2 and 7\_3) were used as polarizer and analyzer. A 80/20 (Transmission/Reflection) beam splitter (element 10) allowed to both illuminate the sample and collect the signal. Depending on the mode we used either of two objectives: a long-distance one (Nikon Plan Fluor ELWD 20x 0.45 C L) for *in situ* imaging or a short-distance one (Nikon TU Plan Fluor 50x 0.80 WD1.0) for spectroscopy measurements and *ex situ* imaging.

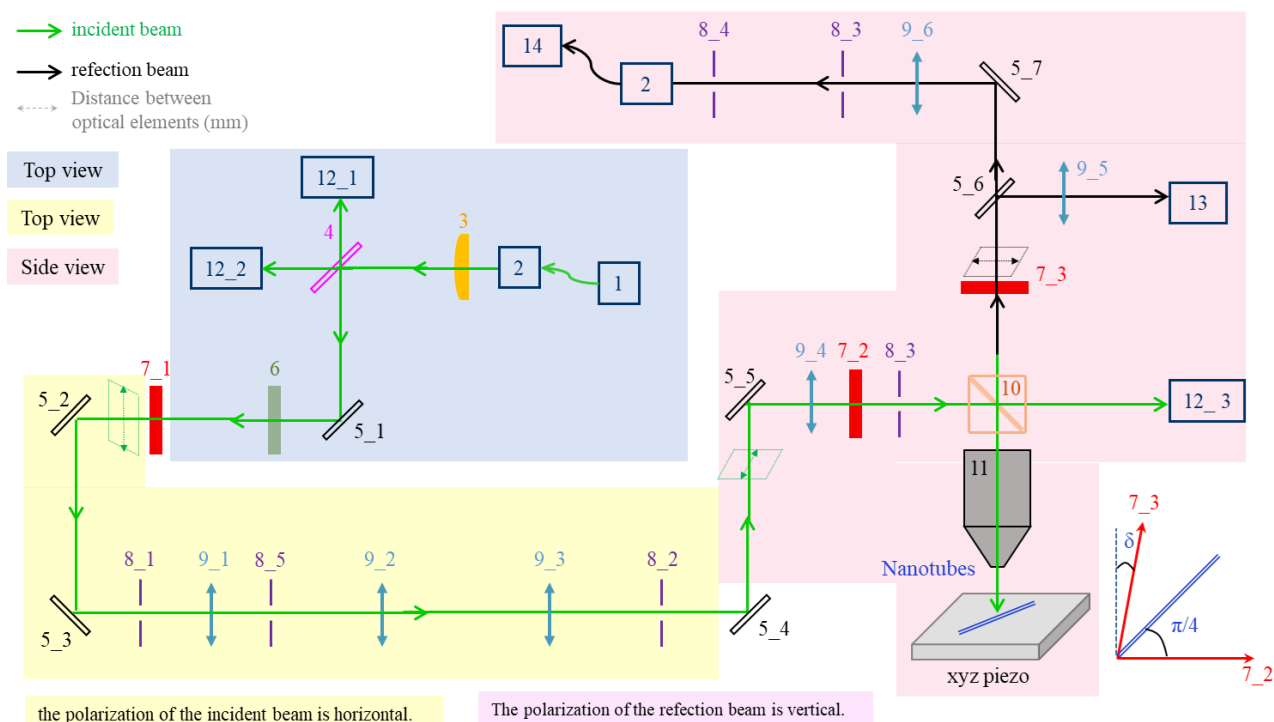


Figure 30 — Detailed schema of the optical setup. 1) supercontinuum laser, 2) XY translator, 3) collimator, 4) longpass dichroic mirror (950 nm Cutoff Wavelength), 5\_x) silver mirror, 6) polarizer to control the laser power, 7\_x) polarizer to control the orientation of the laser beam, 8\_x) aperture, 9\_x) lens, 10) non-polarizing 80/20 beamsplitter cube, 11) objective, 12\_x) beam trap, 13) camera (Hamamatsu digital camera c11440 ORCA-Flash4.0 LT), 14) mini-spectrometer (Hamamatsu TM-series C11697MB, spectral range 320-1000 nm, spectral resolution 6 nm).

Before each experiment, the beam was first aligned to minimize back reflection from the crucible. After that, a sample was placed in the cell and a region of interest (ROI) for further imaging was chosen. The main criteria for ROI selection are the presence of catalyst lines and optical marks (necessary for further SEM and Raman characterization), and a high polarization extinction ratio of  $\sim 10^5$ . The angle  $\delta$  between polarizers was then tuned to maximize the contrast. A short-pass filter with cutoff at 700 nm positioned after the beam-splitter was used to suppress the blackbody radiation emitted by the crucible. Finally, the exposure time of the camera was set (typically between 25 and 42 ms) to maximize the signal-to-noise ratio while avoiding detector saturation.

### 3.4 Raman measurements

Micro-Raman measurements were performed *ex situ* at five different laser wavelengths (488, 532, 633, 660, 785 nm) with linear polarization coinciding with the CNT axis, using two different spectrometers. Raman measurements at 532, 633 and 785 nm were performed using a Renishaw InVia

spectrometer equipped with a 2400 lines/mm grating (for 532 and 633 nm measurements) or a 1200 lines/mm grating (for 785 nm measurements); laser powers on the sample were between 0.2 and 0.5 mW and exposure times between 90 and 140 seconds. Raman measurements at 660 and 488 nm were performed using a home-made Raman setup based on a T64000 Jobin-Yvon spectrometer and equipped with an 1800 lines/mm grating; laser powers on the sample were between 0.8 and 1.2 mW and exposure times were between 100 and 150 seconds. Spectrometer calibration was performed using the Raman peak of Si at  $520.4\text{ cm}^{-1}$ . To correct the small variations of calibration during the day ( $< 1\text{ cm}^{-1}$ ), the quartz peak at  $128\text{ cm}^{-1}$  was used for a post-measurement internal recalibration of each RBM spectrum on ST-cut quartz.

### **3.5 Sample treatment with photoresist**

For the tests of release of strain of CNTs grown on quartz, a photoresist (S1818) was spin-coated on the samples during 30 s at 5000 rpm. The samples were then baked at  $110^{\circ}\text{C}$  during 1 minute and finally washed in acetone and rinsed by isopropanol and water.

### **3.6 Scanning electron microscopy**

SEM characterization was performed with a FEI Inspect S50 without sample metallization. Note that all CNTs grown from the same catalyst segment are electrically connected due to the percolation of the nanotube network in the catalyst pad, which enhances electrical charge dissipation, thus the charge contrast of CNTs. The catalyst pads were not electrically wired to any external ground during SEM observations. Metallic CNTs were observed by using a dwell time of  $3\text{ }\mu\text{s}$ : in these conditions, SC-CNTs (which have a low charge contrast because of their low conductivity) are nearly invisible. To observe all CNTs, we used the automatized integration mode to increase the charge contrast and the signal/noise ratio of SC-CNTs: we did this by averaging 32 consecutive frames measured at a dwell time of 600 ns.

# Chapter 4.

## Raman spectroscopy of CNTs grown on monocrystalline quartz

### 4.1 Raman features of horizontally aligned CNTs grown on quartz

After growth and SEM imaging using optical marks, the nanotubes were localized and analyzed by micro-Raman spectroscopy. As for suspended CNTs, we can distinguish three regions of interest in the spectrum of CNTs grown on quartz: RBM, G-D, and 2D (Figure 31 (a, b)). Due to the substrate, the spectra also contain the Raman peaks of quartz, which has advantages and drawbacks. On the minus side, these additional peaks can make it more difficult to identify a weak RBM because most quartz peaks are in the RBM area. On the plus side, quartz peaks can be used for internal calibration of the spectra thus increasing the measurement accuracy of the RBM frequency (Figure 31).

In our experiments the quartz peak at about  $130\text{ cm}^{-1}$  (between  $128$  and  $132\text{ cm}^{-1}$  depending on the spectrometer configuration) was used for inner calibration due to its high sharpness (full width at half maximum of  $\sim 2\text{ cm}^{-1}$ ) and intensity. Therefore, this peak can be easily resolved from the other peaks, which can correspond to RBMs and is the best candidate for the role of the inner calibration parameter. The value of  $128\text{ cm}^{-1}$  was used as a reference for all wavelengths (168).

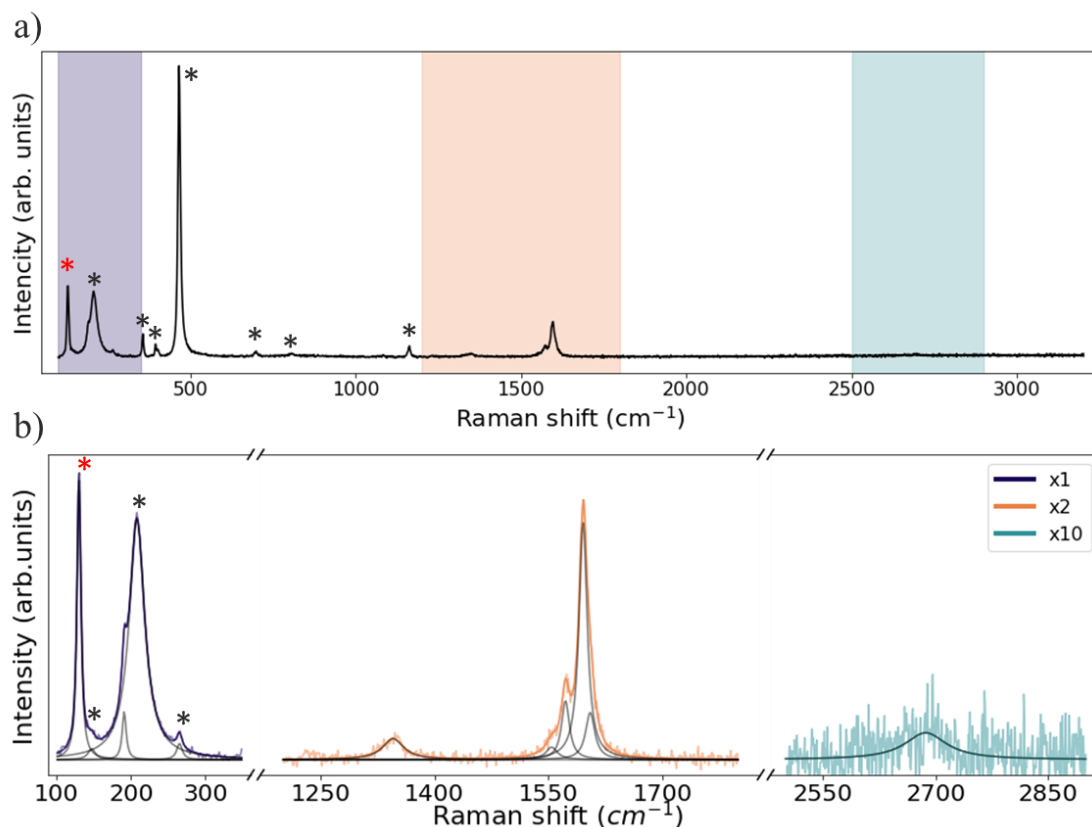


Figure 31 — a) Full spectrum of a SWCNT grown on quartz in the range from 100 to 3200  $\text{cm}^{-1}$  with highlighted regions of interest: RBM (purple, 100-350  $\text{cm}^{-1}$ ), G-D (orange, 1200-1800  $\text{cm}^{-1}$ ) and 2D (light green, 2500-2900  $\text{cm}^{-1}$ ). b) Spectrum of only these zones with fitting lines (in gray).

The asterisks corresponds to the quartz peaks (the red one marks the peak used for internal calibration). Spectra were obtained using laser wavelength of 532 nm.

One of the most noticeable differences in the spectra of horizontally aligned CNTs grown on quartz is the complex G-band structure. In the case of Raman measurements of free-standing nanotubes with laser polarization parallel to the nanotube axis, one or two peaks of G-band should be observed for achiral and chiral nanotubes, respectively (169). However, the number of G-band peaks of CNTs grown on quartz varies from 3 to 6, and we also observe the upshifts of the G-band peaks (Figure 32, Figure 33 and Figure 34 (b, c)). We named these components of G-band as  $G^-$  and  $G^+$ , and give them numbers from 1 to 3 each. This number was chosen based on the assumption that symmetry breaking may cause appearance of all theoretically expected modes in the spectra. Hence, in the case of chiral CNTs it would be 6 modes of 3 symmetry types ( $2A_1$ ,  $2E_1$ ,  $2E_2$ ) corresponding each to iTO and iLO (156).

To fit the G-bands we used between 3 and 4 peaks (only Lorentzian peaks for SC-SWCNTs, and 1 Breit-Wigner-Fano with 2-3 Lorentzian peaks for M-SWCNTs) (170). The choice of the number of peaks was based on two criteria: the fit results should be as close to the experimental data

as possible (Figure 32 (upper panels)), and the addition of new peaks should keep reducing the difference between the fit and experimental data (residuals) (Figure 32 (bottom panels)). In other words, new peaks were added until they kept noticeably reducing the root squared mean difference (RSMD) and standard deviation of the residuals and improving its shape. However, these metrics are not universal and some specific cases had to be resolved one by one. In Figure 32 are shown two examples. It is shown that, for the SC-SWCNT in panel (a), addition of new Lorentzian peaks reduces both RSMD and standard deviation of the residuals until 3 peaks are used. After adding more peaks, the residuals plot becomes flatter than before (STD starts increasing after adding more peaks while RSMD keeps decreasing slightly). For the M-SWCNT in panel (b), we can observe a decrease of both mean square difference and standard deviation until 3 peaks are added to fit. However, the shapes of residuals and fit does not show a perfect match. Moreover, the residuals plot for fit with less than 4 peaks contain some local deviation spikes. Therefore, the most appropriate number of peaks is 3 and 4 for G-band fit on the Figure 32 (a) and (b), respectively.

The reason for the appearance of additional peaks in the G-band is not clear yet, but different explanations can be proposed. Shim *et al.* studied the Raman spectra of M-SWCNTs grown on Si/SiO<sub>2</sub> substrates (171). They reported observation of additional G-band peaks which they assigned to a doping effect caused by oxygen and mediated by the substrate. However, although they provided clear evidence that oxygen doping causes a change in the positions and relative intensity of the G-band components (as expected from the literature), the evidence that doping is also at the origin of the additional G-band peaks is thinner: at the opposite they provided clear evidence that additional G-band peaks appear once the nanotube is on the Si/SiO<sub>2</sub> substrate whatever the CNT is doped or not.

A possible explanation for the shift of the G-band along nanotubes could be the stress caused by the strong van der Waals interaction of the CNTs with the quartz surface (96, 172). In the case of CNTs grown on quartz, axial compressive strain due to the difference in thermal expansion coefficients between the nanotubes and the substrate is the most likely explanation (96). Axial strain leads to upshifts of high-frequency modes (D, G) caused by changes in the C-C bond length without noticeably affecting the RBM position (173, 174). However, axial strain cannot lead to appearance of the additional peaks in the G-mode spectrum (175).

In contrast to the axial stress, the torsional stress can lead both to a G-band shift (mainly downshift) and to the appearance of new peaks in it due to the deformation of the C-C bond lengths (204). Moreover, in the case of achiral CNTs, such deformation leads to symmetry breaking, as a result of which the number of their Raman-active modes becomes similar to that of chiral CNTs (204). Moreover, the polarizability of vibrational modes can be disturbed, with the result that some G-band modes that are normally not active at a given polarization configuration become observable (206). Nevertheless, it is complicated to propose a mechanism inducing a variable torsional strain along the

nanotube in the absence of any manipulation of the CNTs (*i.e.* displaced using an AFM tip) (206, 207).

CNTs grown on a substrate can also undergo radial deformation due to the strong van der Waals interaction (176, 177). However, the result of such deformation is a shift of the entire spectrum (RBM, D, G, 2D modes) (175–177).

The bending deformation of nanotubes can also have a strong influence on the entire nanotube spectrum, shifting it. Moreover, new peaks in the G-band spectrum appear due to symmetry breaking (173). However, in our study we focused only on the CNTs perfectly aligned along the crystal axes of quartz, which allowed us to exclude the influence of this type of local deformation (Figure 34 (a)).

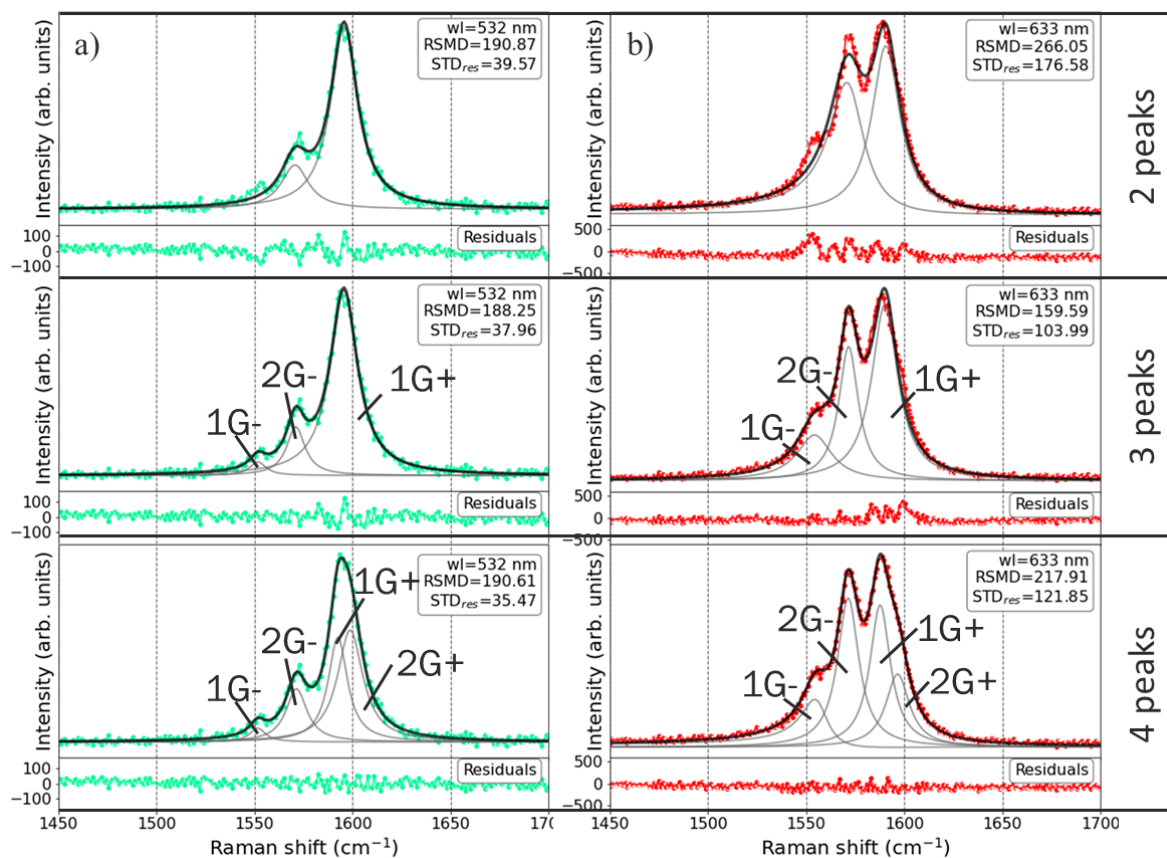


Figure 32 — G-band region of Raman spectra of the same a) SC-SWCNT (14,4) and b) M-SWCNT (11,8) on quartz fitted with different number of Lorentzian peaks in the upper panels and absolute difference of fit from experimental data (residuals) in the bottom panels.

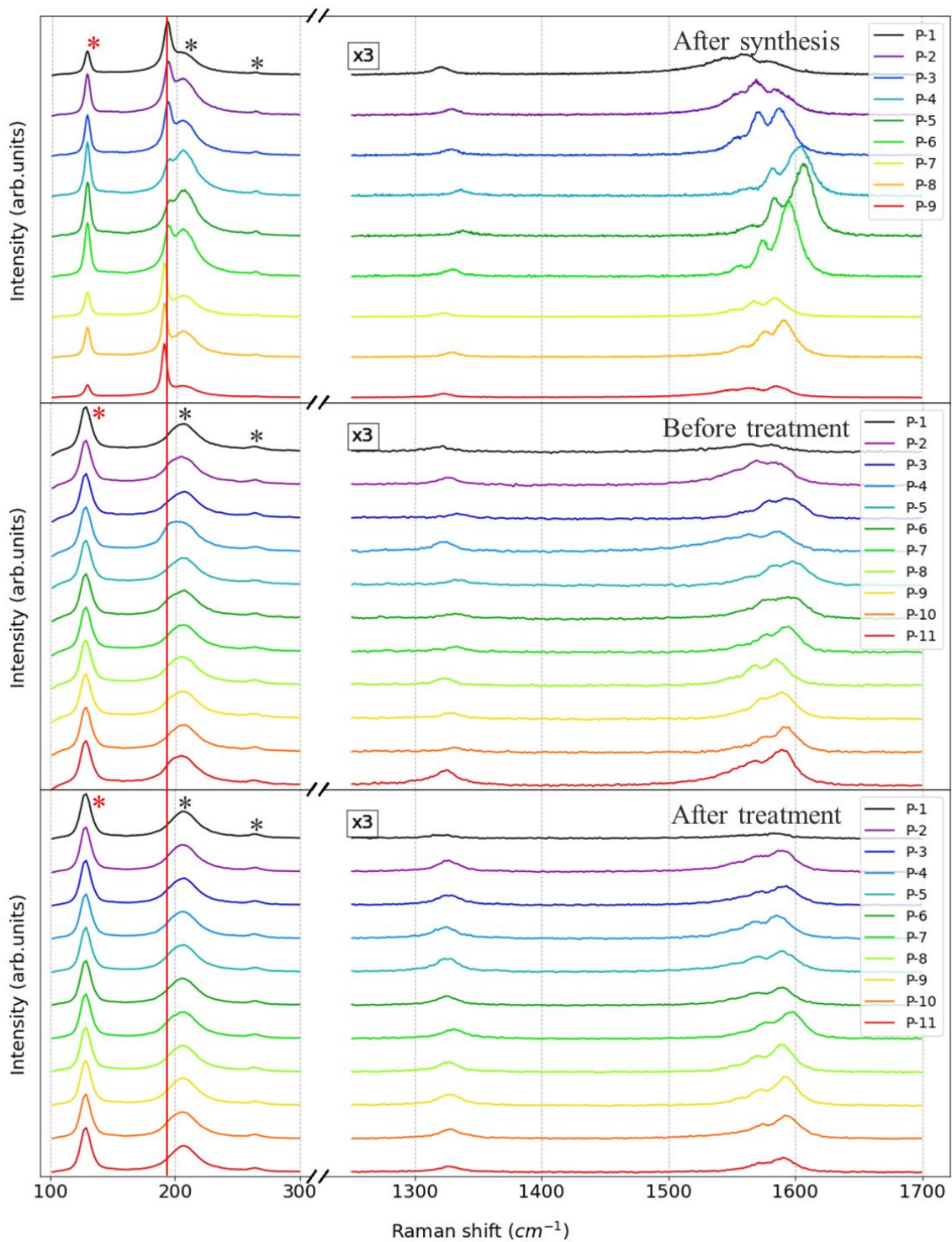


Figure 33 — Raman spectra along a nanotube (12,6) taken after synthesis (1 week later), before photoresist treatment (approximately 24 months after synthesis) and after photoresist treatment.

Asterisks correspond to the quartz peaks, the red one indicating the peak used for internal calibration. The vertical red line corresponds to the RBM For G-band fit, 6 peaks were used. All spectra were measured at a laser wavelength of 633 nm.

As mentioned above, we observed the presence of additional peaks in the G-band (Figure 32) and the coordinated shift of all peaks along the CNT (Figure 33). These shifts usually reach their

maximum values in the middle of the CNT, and decrease at its edges. It is possible that this is caused by lower strain accumulation, or even some tensile strain, at the extremities of the CNT.

The magnitude of the shift of the G and D-band peaks decreases after 24 months, and almost completely disappears after treatment with photoresist (Figure 33 and Figure 34 (b-e)). The use of this method for relaxation of CNT stress on the substrate was mentioned in the literature (96). However, the complex shape of the G-band does not change with time and after treatment (Figure 33), which indicates a separate origin.

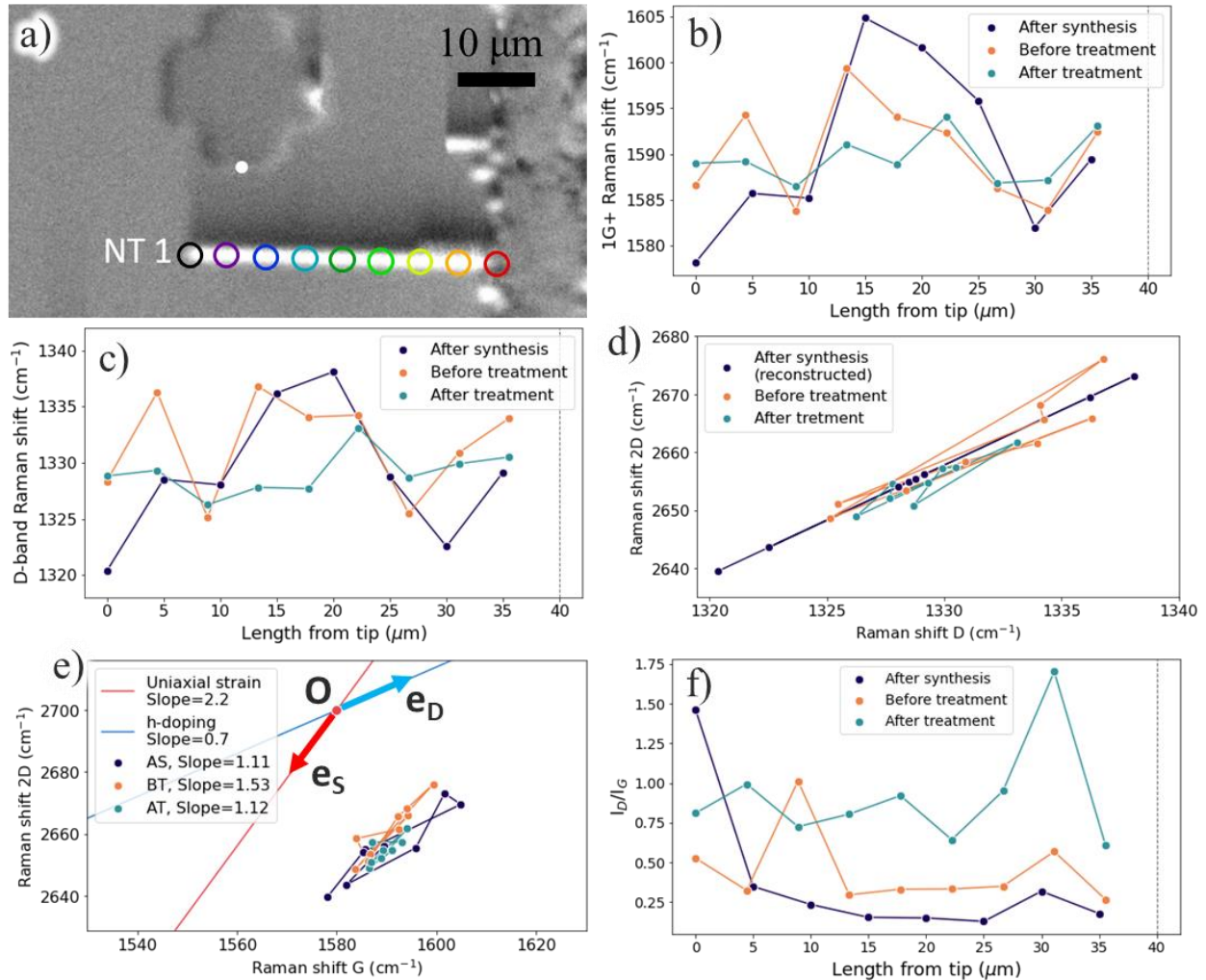


Figure 34 — a) SEM image of the CNT with marked positions where Raman spectra were measured on the Figure 33 (top panel). Evolution of b) 1G+ and c) D-mode frequency along the nanotube. d) Dependence of 2D-band peak position on D-band for CNT at the different stages of treatment. e) Evolution of the 2D mode Raman shift as a function of the 1G<sup>+</sup> mode frequency along the nanotube, before and after photoresist treatment. The vectors  $\mathbf{e}_S$  and  $\mathbf{e}_D$  show the theoretical directions of displacement in the case of graphene for axial strain and h-doping, respectively (159). The purple point **O** corresponds to theoretical position of G and 2D peaks of graphene (178). f)

Intensity ratio of D and 1G+ peaks along the nanotube measured after synthesis, before and after treatment. Vertical dashed line on plots b, c and f marks the beginning of the catalyst line.

In analogy with graphene, a 2D-band plot as a function of G band may be used to determine if G and 2D shifts originate from axial strain or from doping. According to the study of Lee et al. in the case of graphene, if the high-frequency modes are caused by axial strain, the points in the 2D vs G-band plot are shifted along a line with a slope of 2.2 with respect to the unstressed state, and in the case of doping along a line with a slope of 0.7 (Figure 34 (e)) (159, 179). Note that in our case, the 2D band spectra were not measured just after synthesis but only for CNTs before and after photoresist treatment, so, to give an estimation, the 2D peak positions for the spectra after synthesis were extrapolated from the linear fit of the 2D band vs D band plot for CNTs before photoresist treatment (Figure 34 (d)).

Figure 34 (e) shows that, after synthesis, the reconstructed distribution of the dots is rather widely scattered, and that their slope is between 2.2 and 0.7 (which may indicate the influence of both strain and doping on the shape and behavior of the G-band) although the uncertainty on the estimation of the 2D position is currently too high to make a solid conclusion. After about 24 months, the spectra were taken again before photoresist treatment. It is noteworthy that the scatter of points along the  $e_D$  is small (as evidenced by the slope being closer to 2.2), but the scatter along the  $e_S$  direction is rather large. After treatment with photoresist, the displacement along both directions decreased. Even though the slope of the distribution of these points has reduced and became closer to 0.7, the reduced scattering of these points confirms the reduction of strain without change of possible doping. Note that the photoresist treatment led to defects (structure modification or contaminant adsorption) as evidenced by the overall increase of the D/G ratio (Figure 34 (f)).

## 4.2 Wall number, chirality and diameter assignment

In order to assign the nanotube structure (diameter, wall number, chirality), a total of about 230 In order to assign the nanotube structure (diameter, wall number, chirality), a total of about 230 CNTs (corresponding to about 350 segments with different growth rates) were studied by Raman spectroscopy. Five different and complementary laser wavelengths (488, 532, 633, 660, and 785 nm) were chosen based on the Kataura plot to probe a large number of different nanotubes as summarized in Table 5. Note that *in situ* movies of their growth were also used to make sure that at the studied positions, no other nanotube had grown and that the studied nanotubes were truly individual (see

Chapter 5). Nanotubes possibly bundled or simply too close to be optically resolved were therefore not used in this study.

Table 2 — Number of nanotubes studied by Raman and type of response at each wavelength.

Wavelength (nm)	RBM and G peaks	Only G band	Not resonant	Total studied
488	1	4	29	34
532	21	69	80	170
633	65	21	100	186
660	15	14	59	88
785	3	14	138	155

#### 4.2.1 Identifying cases incompatible with individual SWCNTs

Based on the most extreme frequencies of radial modes we measured at all wavelengths, the nanotube diameters in the studied samples range between 1.0 and 2.0 nm. Considering an approximate difference of 0.7 nm in diameter between two concentric nanotubes in a MWCNT, this diameter range excludes the possibility of CNTs with three walls or more, even after taking into account the effect of inter-tube coupling on the frequency of the radial modes. However, DWCNTs remain possible.

A first criterion of definition of the SWCNTs is based on the analysis of the low-frequency region of the spectra. Unlike single-wall CNTs which have only one peak in the RBM region, double and multi-walled can display more than one radial mode, either in the same spectrum or separately at different resonance energies (Figure 37 (a) and Figure 35 (a)): in the case of DWCNTs, these modes are called radial breathing-like modes (RBLM), and correspond to the combination of in-phase and out-of-phase coupled vibrations of the two walls. In contrast to SWCNTs, there is no direct relationship between the frequency of these modes and the diameters of the constituent CNTs since it also depends on the inter-tube coupling (148). Thus, the observation of two RBMs (in the same spectrum or separately at different laser wavelengths) was a first criterion for assignment of a CNT as non-individual SWCNT. In addition, some CNTs displayed values of transition energy and RBM frequency corresponding to i) no expected resonance or to ii) two mutually incompatible resonances in the Kataura plot (Figure 35). Since inter-tube coupling in DWCNTs is known to cause significant modifications in transition energy and radial mode frequency compared to their constituent SWCNTs, such CNTs were assigned as probably double-wall in the absence of other explanation from SEM or video data (148).

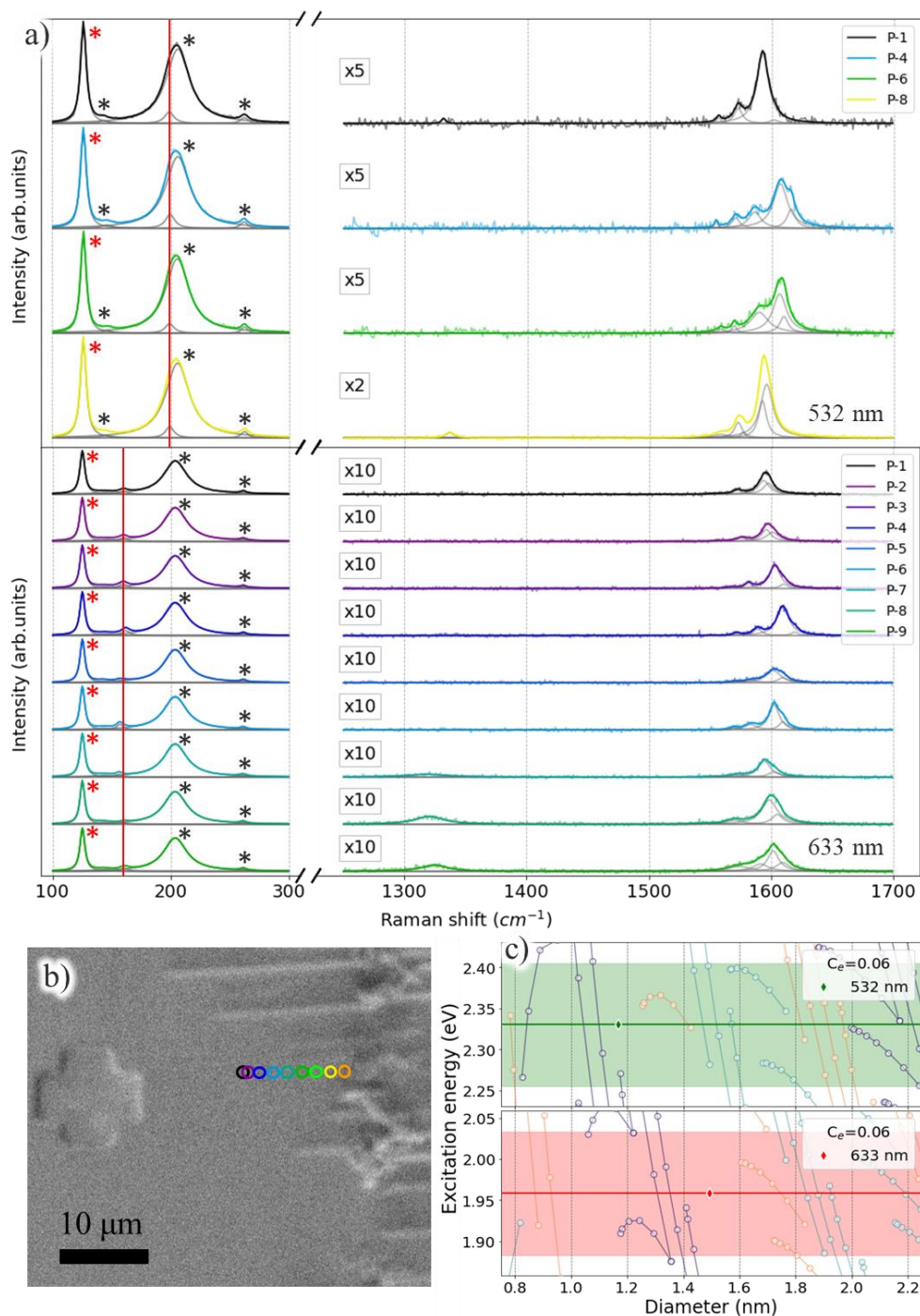


Figure 35 — a) Raman spectra for the same CNT measured at two wavelengths (532 nm (top) and 633 nm (bottom)) that are mutually incompatible with a single SWCNT. b) SEM image of the area where this CNT was located (SEM contrast does not allow to detect this nanotube, hence, it is supposed to be SC@SC DWCNT). c) Kataura plots for both RBM measured at different wavelength. Asterisks indicate characteristic quartz peaks, red indicates peaks used for internal calibration.

A second criterion for SWCNT discrimination was based on the G-band. The G mode of double-walled CNTs has a more complex structure than that of single-walled ones (148), although in

our case this criterion cannot be easily used because of the splitting already caused by the tube-substrate interaction. However, we observed a minority of CNTs grown on quartz displaying no evidence of axial strain, contrarily to the majority of CNTs which displayed a concerted shift of all their tangential modes. For this minority of CNTs, the D band (if visible) remained at a constant frequency along the CNT, all or some of the G-band components did not shift, the  $G^+$  frequency was typical of that encountered for unstrained CNTs (*i.e.* around  $1590\text{ cm}^{-1}$ ) (Figure 37 (b, c)). The most likely explanation for these observations is that the laser energy is in resonance with the inner CNT of a DWCNT which is protected by the outer CNT from the strain induced by the substrate (Figure 37 (b, c)). In such cases, the CNT was also assigned as probably double-wall. Note that the Raman peaks of G-band of CNTs assigned as probably DWCNT were significantly narrower than that of CNTs assigned as SWCNTs (Figure 36) for both G- and  $G^+$  peaks. However, since the G- peaks full width depends on the metallicity of the nanotube (148),  $G^+$  peaks are more suitable for such analysis (Figure 36 (b, c)). This provides an additional support to the assignment criteria since the inner tube of a DWCNT is expected to be less or not affected by homogeneous or heterogeneous broadening caused by the CNT environment (strain, doping...).

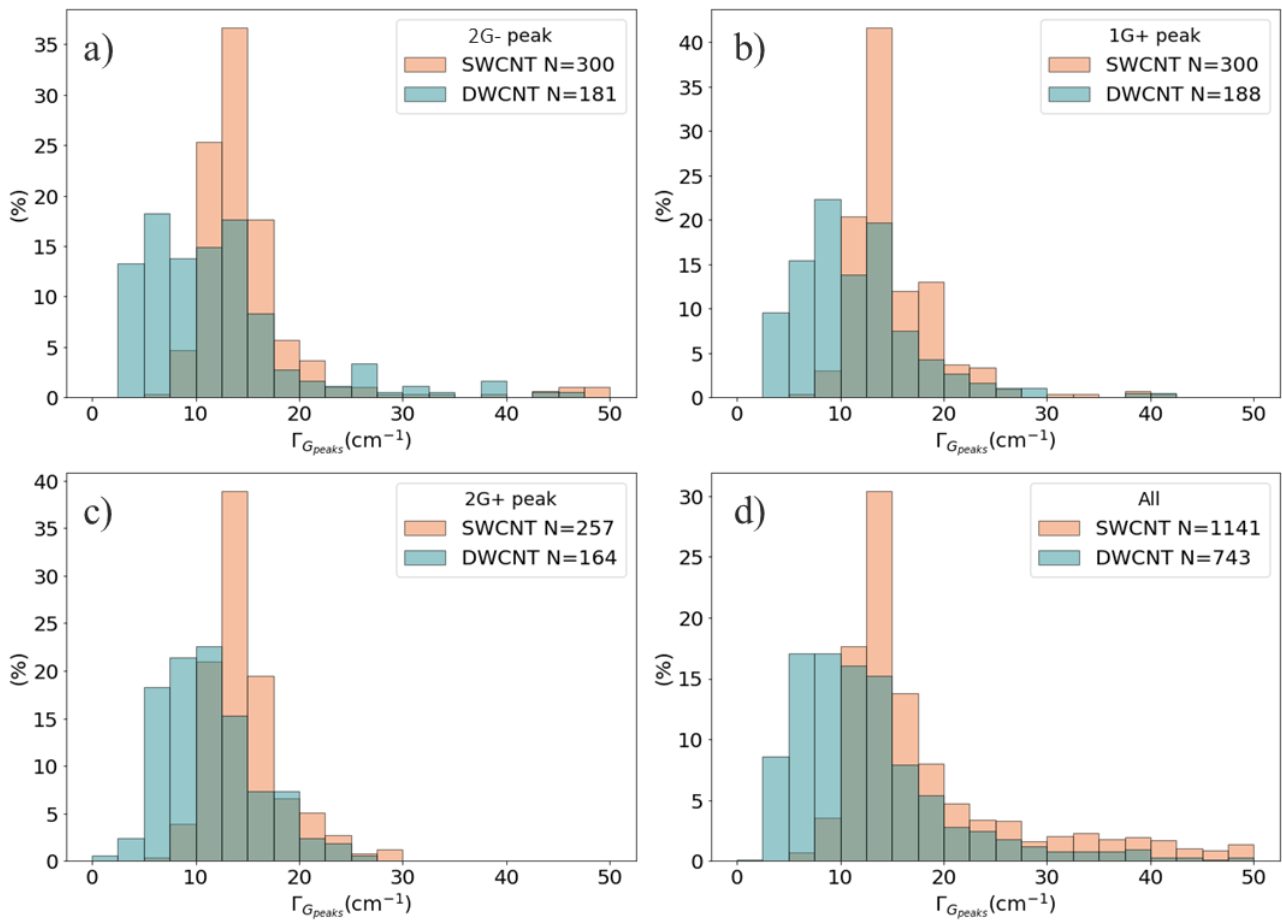


Figure 36 — Distributions of the full width at half maximum of different G peaks for CNTs assigned to SWCNTs or DWCNTs. Note that peak 1G- is not included in this comparison due to its dependence of its width on the CNT metallicity.

Among all CNTs with measured RBMs, about 30% were identified as probably not individual SWCNTs but double walled or close/bundled SWCNTs. The remaining CNTs (70 %) displayed all the expected features of individual SWCNTs grown on quartz at the different tested laser energies and were assigned as probably individual SWCNTs.

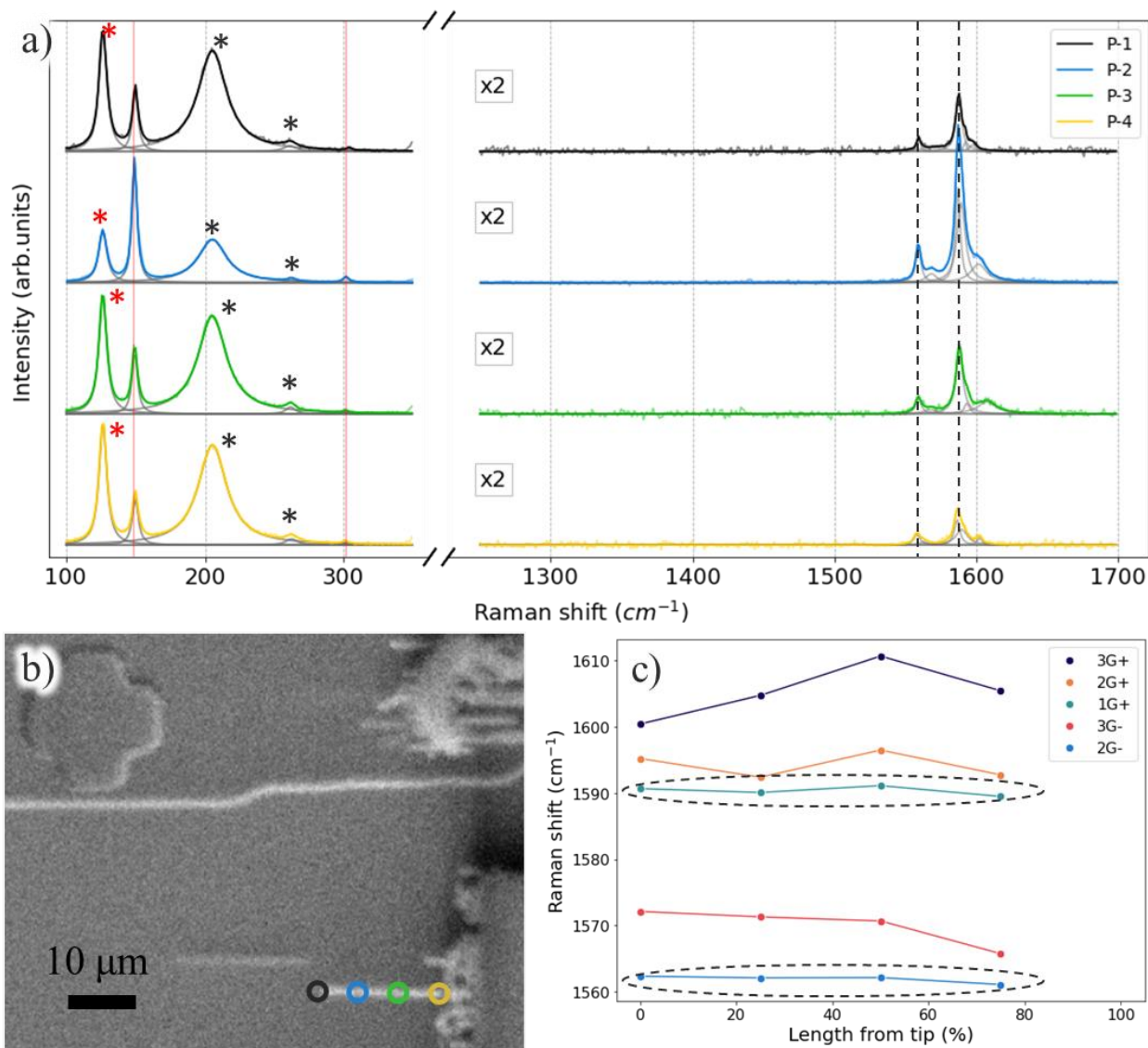


Figure 37 — a) Raman spectra of the DWCNT displaying two peaks in the RBM region (red vertical lines) and some G-band components not shifting along the nanotube (gray dashed lines). b)

SEM image of the CNT with spectrum positions indicated. c) Positions of the five G-band components along the nanotube. Asterisks indicate characteristic quartz peaks, red indicates peaks used for internal calibration. Horizontal ovals on panel (c) corresponds to the not shifting G-band peaks highlighted with vertical dashed lines on panel (a). All spectra were obtained at a laser wavelength of 532 nm.

### 4.2.2 Chirality assignment

The next step after identifying individual SWCNTs from other cases is their chirality assignment. It is possible to do it using an appropriate Kataura plot, which plots the transition energies of each (n, m) SWCNT as a function of its diameter. The former is within the excitation window defined by the excitation laser energy. The latter can be calculated from the RBM peak position using an adequate RBM law (Equation 10).

For correct assignment the first step is to determine the environmental constant  $C_e$  in the RBM law. To do this we first analyzed a large number of spectra measured inside the catalyst lines because of the high collection throughput (Figure 38). Then we attributed RBM peak positions corresponding to unambiguous cases and branch ends to particular chiralities (Figure 38 (e-f) colored points); in some cases one RBM peak was assigned to 2 or 3 possible chiralities with very close diameters (Figure 38 (e-f) gray points). This allowed us to make a plot of RBM positions as a function of diameter and extract the optimal environmental constant all wavelengths considered. In the case of the non-aligned SWCNTs in the catalyst lines,  $C_e$  was found equal to 0.061 (Figure 38 (a)). This value is close to the one reported for pristine free standing CNTs ( $C_e = 0.058$ ) (28, 180), rather than to the  $C_e$  value of  $0.082 \pm 0.008$  reported for SWCNT serpentines grown on quartz (41). This result can be understood since CNTs in the catalyst lines are randomly oriented (based on AFM and HRTEM images) and without strong interaction with the crystal lattice of quartz.

In addition, it was found that the diameter distribution of CNTs inside the catalyst lines ranges between 0.8 and 2.2 nm, which is similar to that found for the aligned CNTs having grown outside the catalyst lines which we studied individually. As previously, this diameter range is compatible with the presence of DWCNTs among SWCNTs.

After the analysis of the CNTs in the catalyst lines we moved to individual horizontally aligned CNTs, whose growth was video recorded. For certain SWCNTs, it was possible to assign their chirality due to their appropriate positions in the Kataura plot. These were predominantly nanotubes from branch 30 ((10,10), (11,8), (12,6), (13,4), (14,2)) (Figure 40 (a)) since their position in the Kataura plot allow their identification with a high degree of confidence and also because we could confirm the chirality assignment by measuring their spectra at the two neighboring wavelengths of 633 and 660 nm (Figure 39).

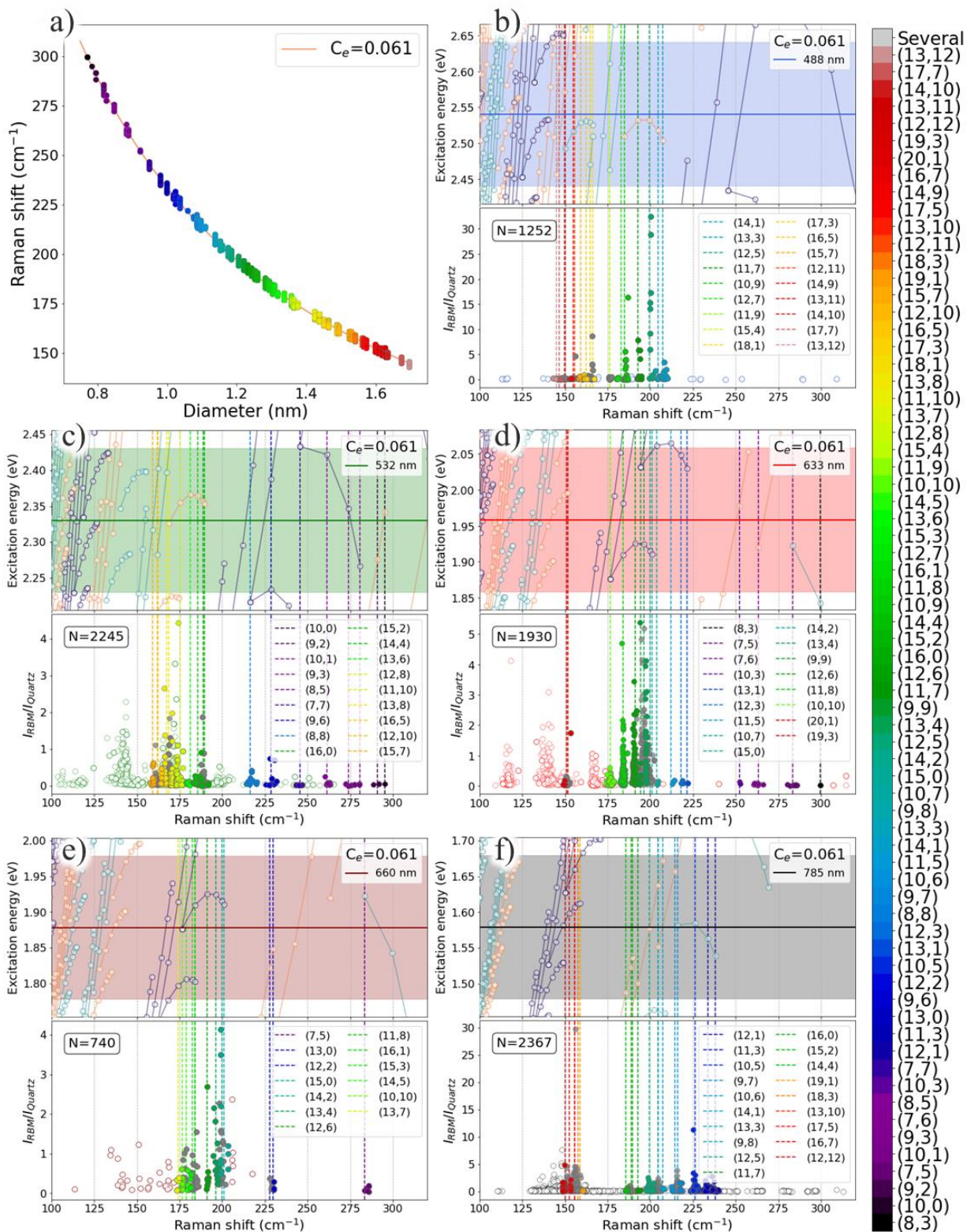


Figure 38 — a) RBM law for non-aligned SWCNTs in the catalyst line after chirality assignment .  
 Segments of Kataura plots for SWCNTs on quartz (top) and dependence of RBM peak intensity normalized on quartz peak intensity as a function of RBM position for CNTs, measured on quartz at the laser wavelengths of b) 488 nm, c) 532 nm, d) 633 nm, e) 660 nm, f) 785 nm. Colors on figure corresponds to CNTs which can be safely assigned to one single chirality, gray color corresponds to

multiple assignments (2 or 3 chiralities to one elongated cloud of points), empty dots corresponds to unassigned CNTs. The color bar on the right corresponds to colors of the circles on the insets (a-f).

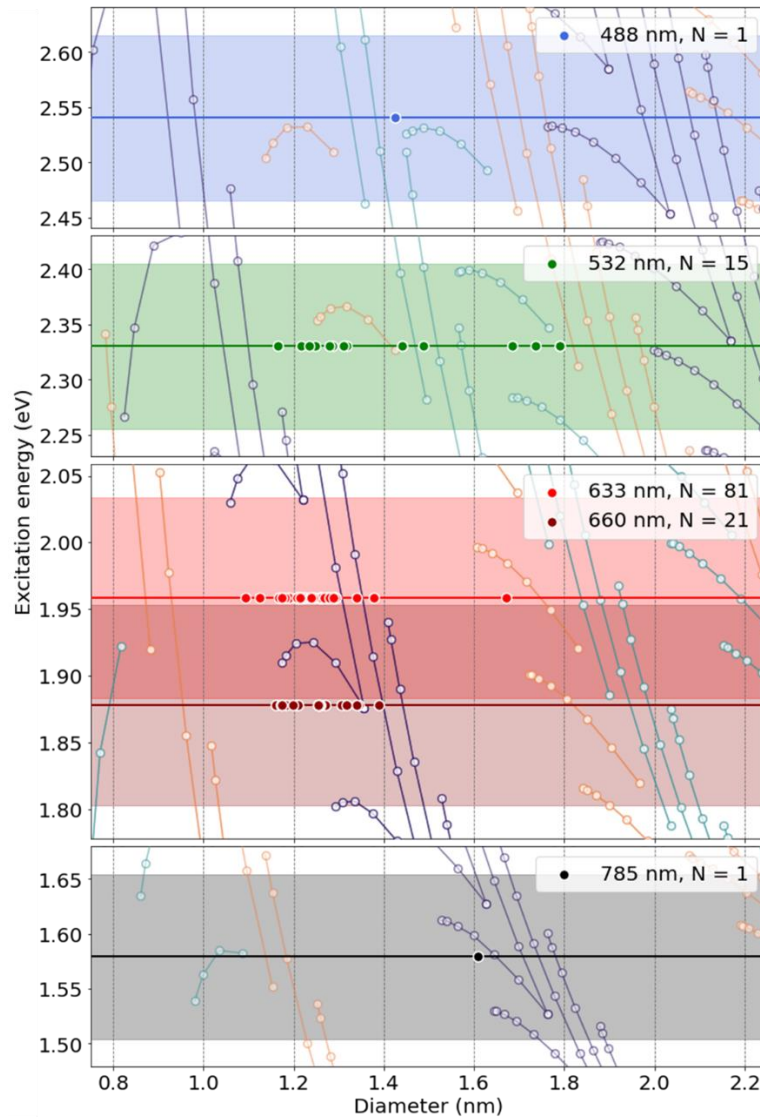


Figure 39 — Extracts of Kataura plot (36) at the five different laser wavelengths used together with RBM positions measured for individual carbon nanotubes grown on monocrystal quartz. Filled circles on the plots correspond to the RBMs we experimentally measured and attributed to SWCNTs using RBM law with  $C_e = 0.06$  (filled areas show the considered resonance window of  $\pm 0.075$  eV around each laser energy).

As shown in Figure 40 (a), the RBM can be locally upshifted along the CNT as commonly observed and attributed to local environment changes. However, a rather unexpected observation for CNTs on quartz is that the RBM upshift is not random: as most evident in the cases of (11,8) SWCNTs, the RBM frequency mainly switches between two stable values along the CNT despite its constant chirality (Figure 40 (a)). Analysis of the dependence of the position of the RBM peak on the diameter of these CNTs suggests the possibility of using RBM laws (equation 10) with two different

environment constants  $C_e$ . From our data fit one of them is equal to 0.06, which is close to the value of 0.056 generally observed for most SWCNT samples in literature (28, 181). Another constant is equal to 0.088, which is close to the value reported in the literature for SWCNTs grown on quartz (41) (Figure 40 (b)).

One of the possible reasons why our data could be fitted with RBM laws with different environmental constants can be a difference in interaction with the substrate.  $C_e$  value of 0.06 may correspond to a weak van der Waals coupling with quartz because the nanotube contact with the crystal surface is not optimal, giving the same  $C_e$  value as  $\text{SiO}_2$  because of the same chemical nature (145). The value of 0.088 may correspond to an optimum van der Waals coupling with the monocrystalline quartz surface (because of the perfect alignment with the crystal structure). Note that we observe no correlation between shift of 1G+ peak and RBM peak (Figure 40 (c)) which suggest that the RBM shift is not a secondary effect of strain. We also observe no correlation between the distance from the catalyst and the RBM shift which suggests that the RBM shift is also not due to a potential contamination caused by the proximity with the catalyst (Figure 40 (d)).

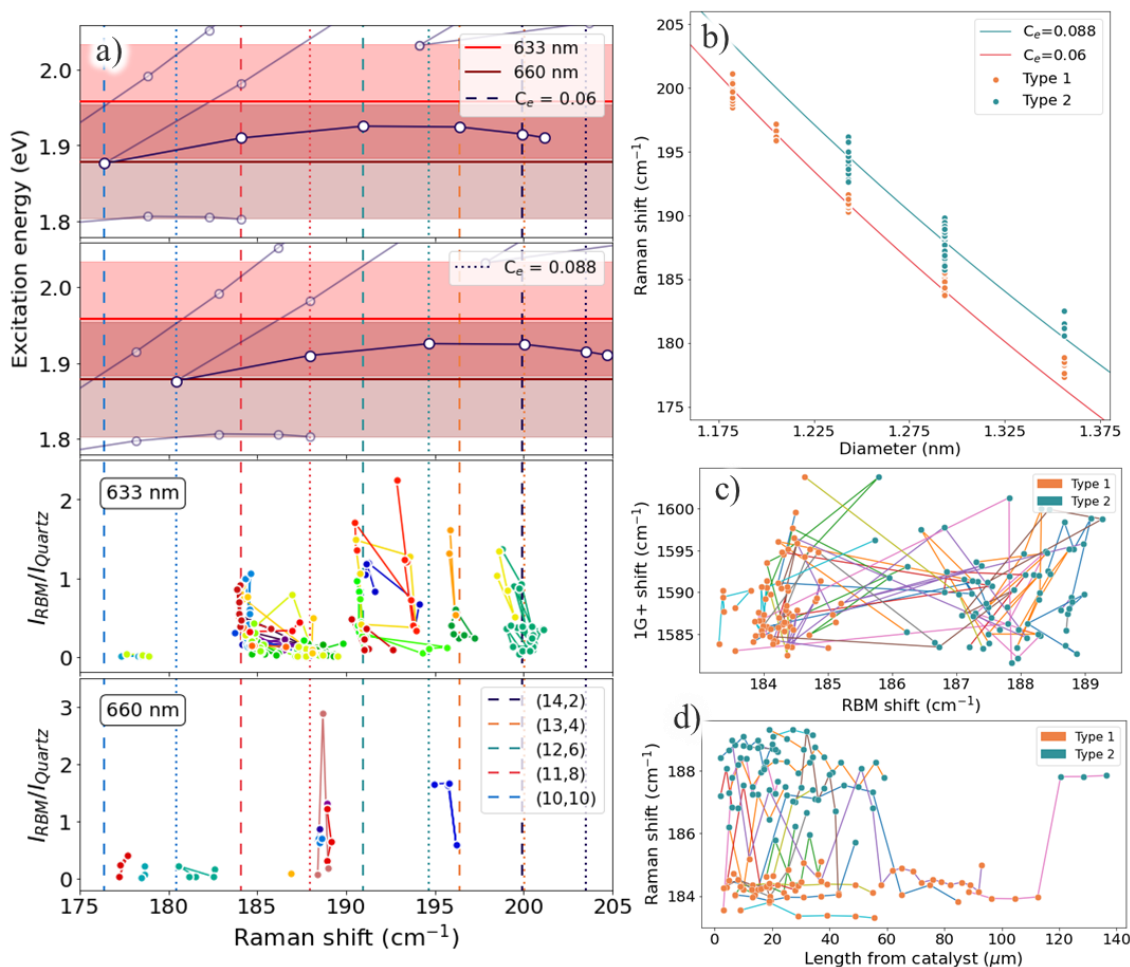


Figure 40 — a) Plot of the RBM peak intensity normalized to quartz peak intensity as a function of the RBM position for CNTs attributed to branch 30 (vertical lines corresponds to RBM positions calculated for the CNTs using RBM law with  $C_e = 0.06$ ). c) Plot of the RBM positions for the

CNTs with determined chirality versus its diameters with two fits of RBM laws showing two different environment constants. c) Position of 1G+ mode as a function of RBM shift. d) Correlation plot of RBM shift as a function of spectra position from catalyst.

### 4.3 Conclusion

Our study of Raman spectra of CNTs grown on ST-cut quartz evidenced the complex nature of the spectra caused by the strong and variable van der Waals interaction with the monocrystalline substrate. We notably reported the presence of 3-4 peaks in the spectra of G-band and that they displayed upshifts along the nanotubes correlated with D-band shifts. The shifts of the G and D-bands were most likely caused by uniaxial strain induced by the difference of CTEs of nanotubes and substrate. The additional peaks in the G-band can be the result of influence of the different mechanisms, such as radial deformation and/or doping caused or mediated by the substrate. Torsional strain is another possible explanation for both the additional peaks and shifts of the G-band but additional evidence for a mechanism inducing variable torsion along the CNT length would be needed: the nanotube rotations previously observed by Marchand *et al.* by *in situ* field emission may offer a track to explore (137). The analysis of a broader set of CNTs may help in understanding the origin. Moreover, we report the efficiency of a photoresist treatment to release the stress. However, it currently damages and/or contaminates the CNTs, so optimizing the cleaning would be needed if this method was further used.

Analysis of the CNT spectra also allowed us to define criteria to discriminate individual SWCNTs grown on quartz from other cases (e.g. DWCNTs, bundled or close SWCNTs). In addition to already known DWCNT features such as the presence of two RB(L)M peaks and the modification of resonance energies compared with those of the constituent SWCNTs, the absence of G-peak displacement along the nanotube appears as an additional signature in the case of monocrystalline substrates. Such a behavior can be the result of the shielding of the inner SWCNT from the substrate-induced strain by the outer SWCNT. Broader analysis combined with TEM observations of transferred CNTs may be used to confirm this hypothesis.

The presence of quartz peaks in the RBM area can hamper the detection of the weakest RBMs but can be used as internal standard for more accurate and reproducible measurements of the RBM positions. Nanotube chirality assignments in unambiguous cases allowed us to determine the environmental constant  $C_e$  relating the RBM position and the SWCNT diameter: this revealed two different environmental constants for SWCNTs grown on quartz. This was corroborated by many instances of individual CNTs whose RBM abruptly switches along their length from one given

frequency to another one differing by a few  $\text{cm}^{-1}$ . One  $C_e$  value, close to 0.06, can be attributed to CNTs having weak contact with quartz while a  $C_e$  value of 0.088 may correspond to CNTs with strong van der Waals interaction with the substrate. The analysis of unaligned CNTs grown in the catalyst area which revealed a  $C_e$  value of 0.061 is in favor of this hypothesis. Additional specific experiments, such as highly-resolved Raman measurements (RBM, D, G, 2D) along aligned CNTs freshly grown on quartz, would be required to confirm. Analysis of the evolution of strain for different CNTs and comparison of it with the CNT segments corresponding to different  $C_e$  values could provide additional evidences as well as the influence of photoresist treatment on such a behavior.



## Chapter 5.

# In situ optical imaging: video processing and analysis

The setup and the methods for *in situ* observations were previously developed by Léonard Monniello and Huy-Nam Tran during their postdoctoral works. They allowed to obtain *in situ* videos of nanotube growth but these raw videos were of insufficient quality to evidence the majority of individual nanotubes and to precisely measure their growth kinetics. I therefore developed a video processing system which I progressively improved and automated. As a result, the video processing was accelerated, revealing a new bottleneck on the way to high throughput: the rate of growth kinetics extraction. To solve this problem, I developed an AI-assisted system of video recognition, which also accelerated the process of video analysis and kinetic data extraction.

### 5.1 Video processing

The video obtained during *in situ* imaging is a stack of grayscale images whose number corresponds to the number of seconds of filming divided by the exposure time (for example, a 6-minute long video filmed at 40 ms exposure time will contain 7500 frames). Raw images are not suitable for the kinetic data extraction due to a low contrast (Figure 41).

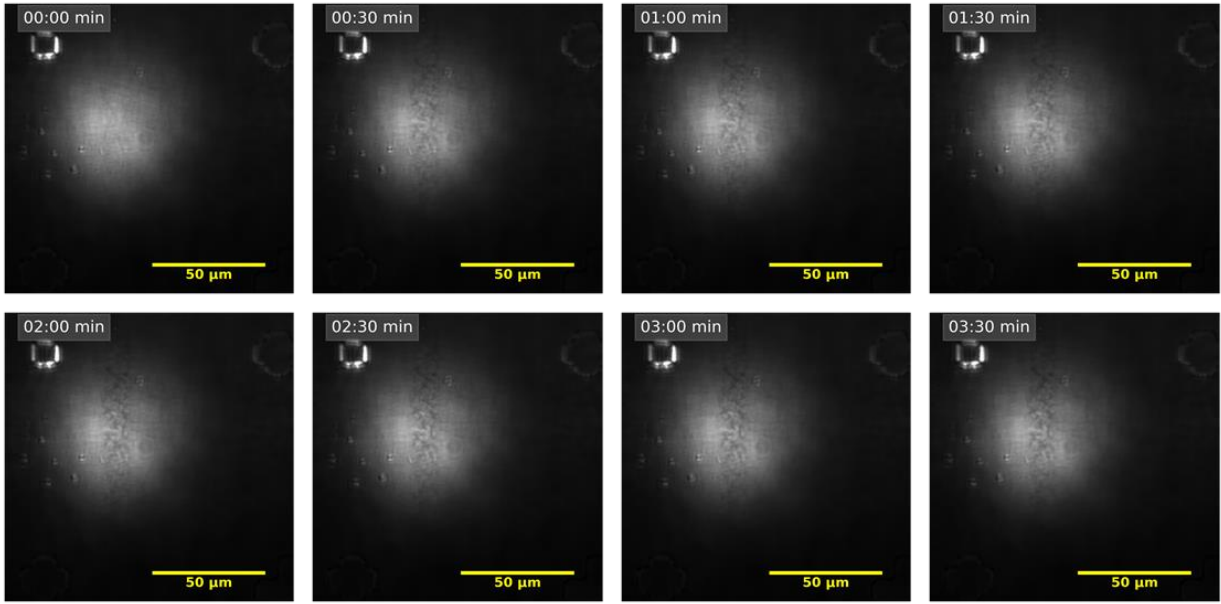


Figure 41 — Snapshots from a raw video.

### 5.1.1 Alignment

This first step is necessary to facilitate subsequent nanotube tracking and length measurement. I used the template matching algorithm from the Intel package OpenCV for python. This method uses a selected template and, by running through the frame for each pixel with coordinates  $(x, y)$  it calculates a correlation matrix using a chosen metric (Equation 11). As a metric I used the normalized correlation coefficient calculated by the following equation:

$$R(x, y) = \frac{\sum_{x', y'} (T'(x', y') \cdot I'(x+x', y+y'))}{\sqrt{\sum_{x', y'} T'(x', y')^2 \cdot \sum_{x', y'} I'(x+x', y+y')^2}} \quad (11)$$

where  $T'$  is a template of size  $(x', y')$ ,  $I'$  is a fragment of the image for alignment with sizes  $(x', y')$ , taken at the point  $(x, y)$  (182). When using this metric, after computing correlation matrix of size  $(x - x' + 1, y - y' + 1)$ , the coordinates of the maximum were found and compared with the coordinates of the template, after which the processed frame is aligned (Figure 42) (183).

The next step although optional allows to accelerate the subsequent processing speed. As already mentioned, our videos are filmed at 25 to 40 frames per second, allowing to access the kinetics of events occurring at timescales as small as 25 ms. In practice, such precision is not used, and the video size is reduced to one frame per second to facilitate file handling. However, to improve the signal-to-noise ratio, each frame of this reduced video is an average of the number of frames taken over one second.

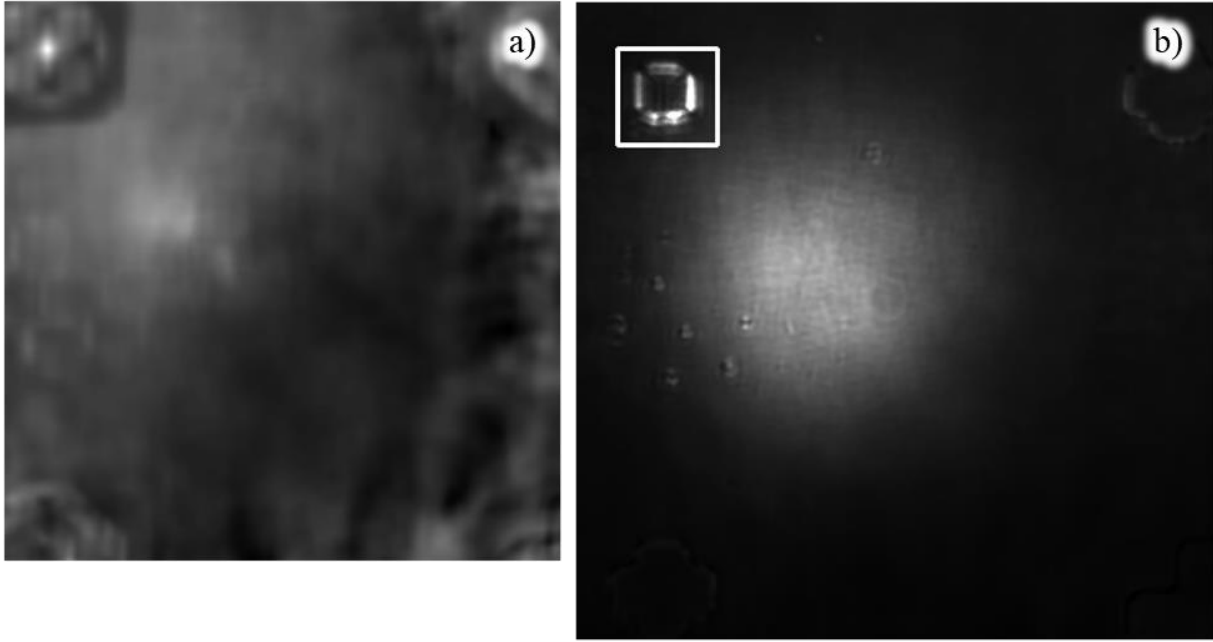


Figure 42 — a) Matrix of the template comparison results and b) the image for template matching alignment (the white square highlights the segment of image used as template).

### 5.1.2 Correction of illumination irregularities

The next step in the video treatment is shade correction, which is needed to compensate the uneven illumination in the frame which causes shading and vignetting (184).

During the filming, the nanotubes interact with the light, which, after passing through the entire system, is recorded by the camera. The resulting image can then be described by the following equation:

$$I(x, y) = I^{true}(x, y) \cdot S(x, y) + D(x, y) \quad (12)$$

where  $I^{true}$  is a real image of nanotubes,  $S$  is a multiplicative term describing unevenness of illumination on the image (as called flat field),  $D$  is an additive term describing image errors introduced by the camera, as well as environment (if the work is performed under external illumination) and existing even in absence of signal (as called dark field) (185). In our case, the latter term plays a negligible role since thermal noise of the camera on the image is  $\sim 1\%$ , and all experiments are carried out in the dark. The contribution of the multiplicative term  $S$  is much higher and it is composed of illumination unevenness caused by the alignment system (notably the beam reducer), as well as the high-aperture objective. (Figure 41).

To reconstruct the original image, we can use prospective (based on use of reference images, standard for the imaging system) and retrospective methods (based on use of the information from treated image only) (185). The first class of methods are not suitable for our work because each new

video is recorded after the alignment of the system and selection of the imaging area. Hence, it is impossible to obtain a single baseline reference image. The second class of approaches require individual processing of every frame to extract the background, which can slow down the processing. Therefore, in our work we used a combined approach: as a reference image we use part of the video (one or several frames).

Since the nanotubes in the video are much smaller in size than unevenness of illumination, and their contrast is always higher or lower than background the most appropriate method of image reconstruction is morphological multiplicative filtering (186). In this case the shading component can be described as follows (187):

$$S(x, y) = MPF(I(x, y)) \cdot C_M \quad (13)$$

where  $MPF(I(x, y))$  is the morphological filter or reference frame for a processed image,  $C_M = \frac{1}{\mu(MPF(I(x, y)))}$  is the normalization coefficient needed to restore the grayscale (for our videos it is inversely proportional to the mean of the reference). Thus, we used the following shade correction equation to restore the image:

$$I^{true}(x, y) = I(x, y) \cdot \left( \frac{\mu(MPF(I(x, y)))}{MPF(I(x, y))} \right) \quad (14)$$

An important aspect that affects the quality of the image is the choice of filter. Standard method of shade correction involves using a fixed frame from the video as a reference image (Figure 43 (a)), since it is usually taken before the carbon precursor release and contains information only about unevenness of illumination of the sample. However, as the processed frame is removed in time from the beginning of the video, the contrast of the image will decrease. This can be caused by signal interference from objects in the frame, which accumulates during the video.

To reduce the contribution of these interferences the differential method of video treatment was developed. In this case, a frame taken with a delay of several seconds (from 5 to 30) is used as a reference. This approach allowed a better background subtraction and to increase the contrast. Moreover, it allowed to evidence the evolutions during nanotube growth (Figure 43 (b)): dark contrast corresponds to an increase of absorption (*e.g.* caused by the CNT elongation), bright contrast corresponds to a decrease of absorption (*e.g.* caused by CNT shrinkage or change of chirality). Since this method of treatment preserve in each frame only information about changes that occurred during the delay time, it even allowed to resolve in time the CNTs that grew at the same location using the most appropriate delay time (Figure 44). Also the length of the segment is proportional to the instantaneous growth rate of the nanotube.

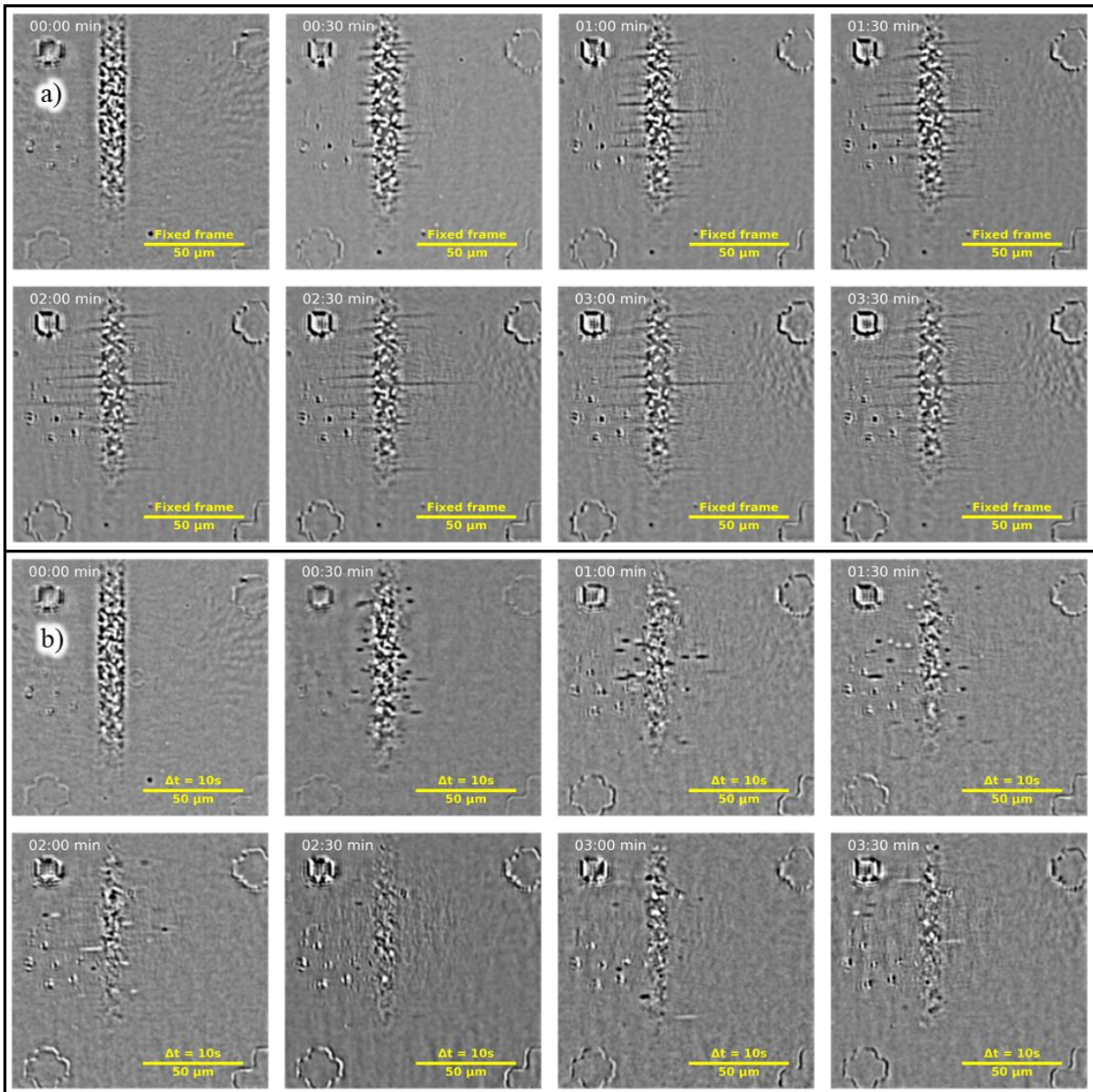


Figure 43 — Snapshots of the fully processed video treated with a) fixed frame and b) differential (delay time of 10s) shading correction. Snapshots are taken at the same time periods as on Figure 41 for convenience of comparison.

Figures 43 and 44 show the snapshots of fully processed videos. The objects in the video right after shade correction are hardly distinguishable (Figure 45 (a)). A parametric algorithm was developed to increase the contrast and adjust the brightness. This method builds a histogram of the image and finds the maximum number of pixels with the same intensity (distribution peak (Figure 45 (a, right))) and determines the cutoff limits by multiplying the number of pixels by a threshold value. Then the values of all pixels with intensities above and below the cutoff are adjusted to the nearest limit (the upper limit for the brighter ones, the lower limit for the dimmer ones). The frame itself is

then renormalized: the lower limit is equalized to 0, and the upper one to the image depth ( $2^{16}$  for our videos with depth of 16 bits) so that the intensity distribution becomes wider, which increases the contrast and brightness of the image (Figure 45 (histograms)).

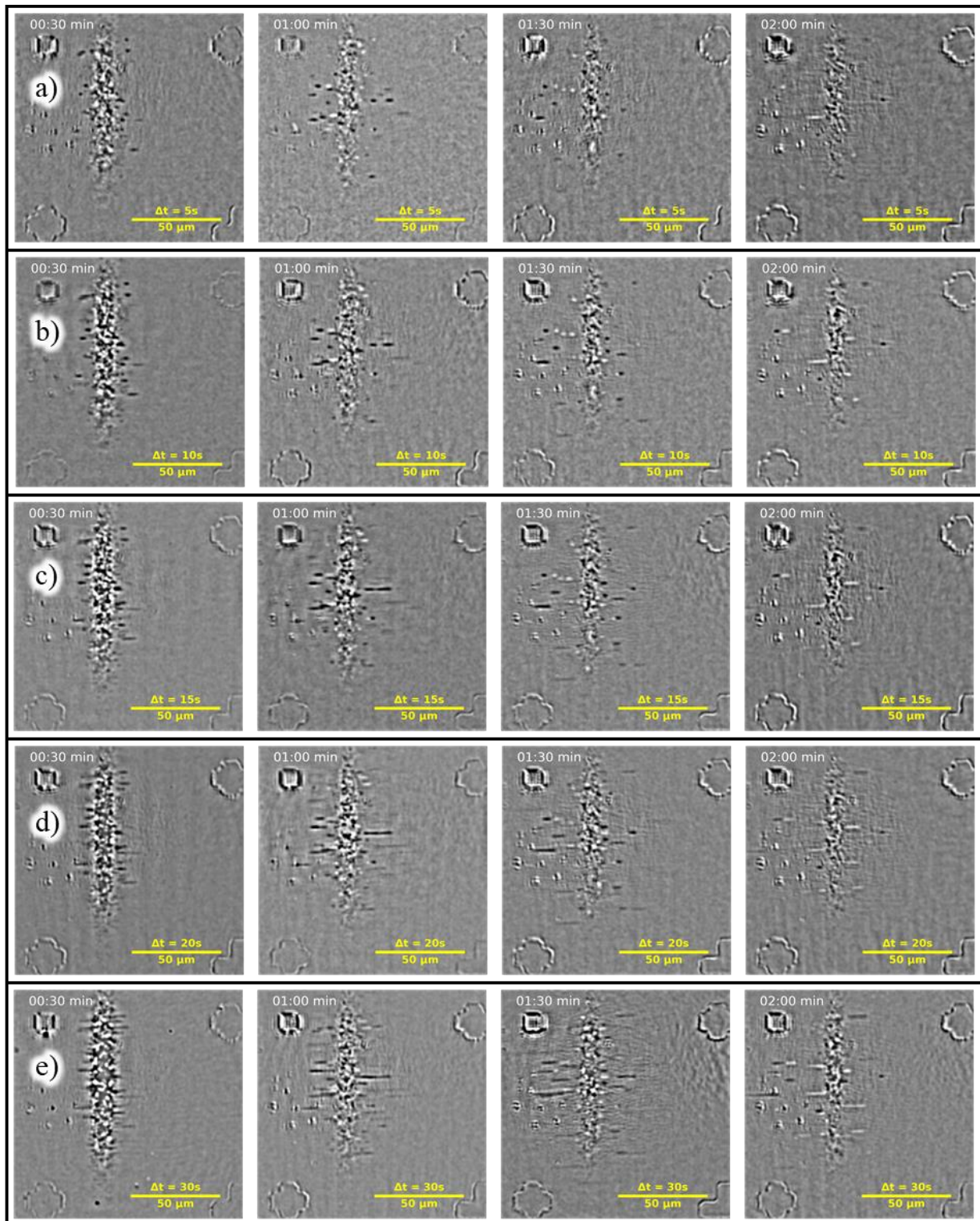


Figure 44 — Several snapshots of a fully processed video with differential shade corrections with delay times of a) 5 s, b) 10 s, c) 15 s, d) 20 s, and e) 30 s.

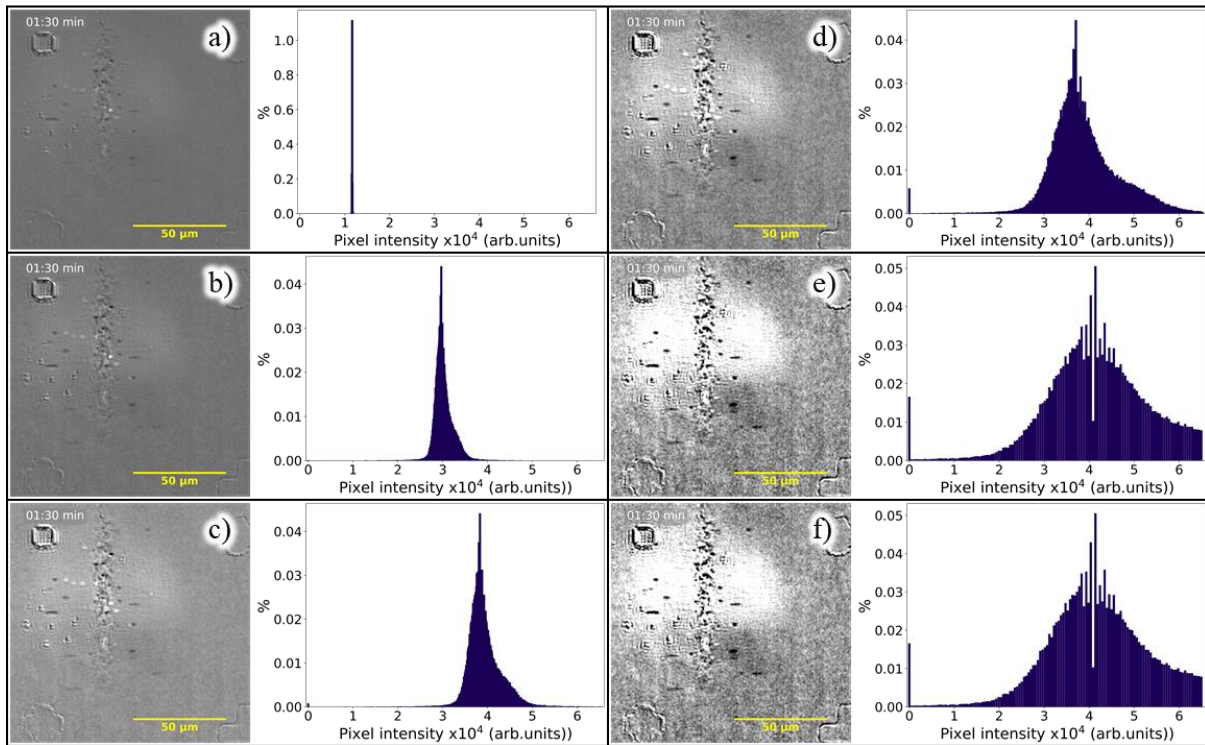


Figure 45 — Images (left inset) and intensity distribution histograms (right) a) after shade correction and after contrast and brightness adjustments with different thresholds: b) 0.00005, c) 0.0005, d) 0.005, e) 0.05, f) 0.1.

An important aspect of the work of this algorithm is the choice of the threshold value. If it is too low, the image sharpness will be insufficient (Figure 45 (b, c)); if it is too high the image may be oversaturated (Figure 45 (e, f)). In our case the optimal threshold value was that achieving the best balance of contrast and brightness for further video processing (Figure 45 (d)).

### 5.1.3 Noise filtration and edge enhancement

As mentioned above, the differential treatment allows to increase the contrast and compensate uneven illumination. However, the difference between the reference and processed frames can lead to background heterogeneity due to light fluctuations at a time scale shorter than the delay time (Figure 46 (a)).

To clean these residual unevenness of illumination, band-pass Fourier filtration was used (188, 189). For this purpose, FFT was performed on the whole image stack; after which all harmonics with sizes smaller than 3 and larger than 40 pixels were removed. Then the reverse FFT was performed and the filtered images were obtained. The use of the band-pass filter allowed to get rid of both the residual unevenness of illumination and fine noise (Figure 46 (b)).

As we can see from Figure 46 (b) the objects have low sharpness. To enhance the edges of the objects was used Gaussian band-pass filter (difference of Gaussians) (190). As the parameters for

these filters were used standard deviations:  $\sigma_{min} = 1,5$  and  $\sigma_{max} = 5$ . This approach allowed to increase the sharpness of the objects in the video (Figure 46 (c)).

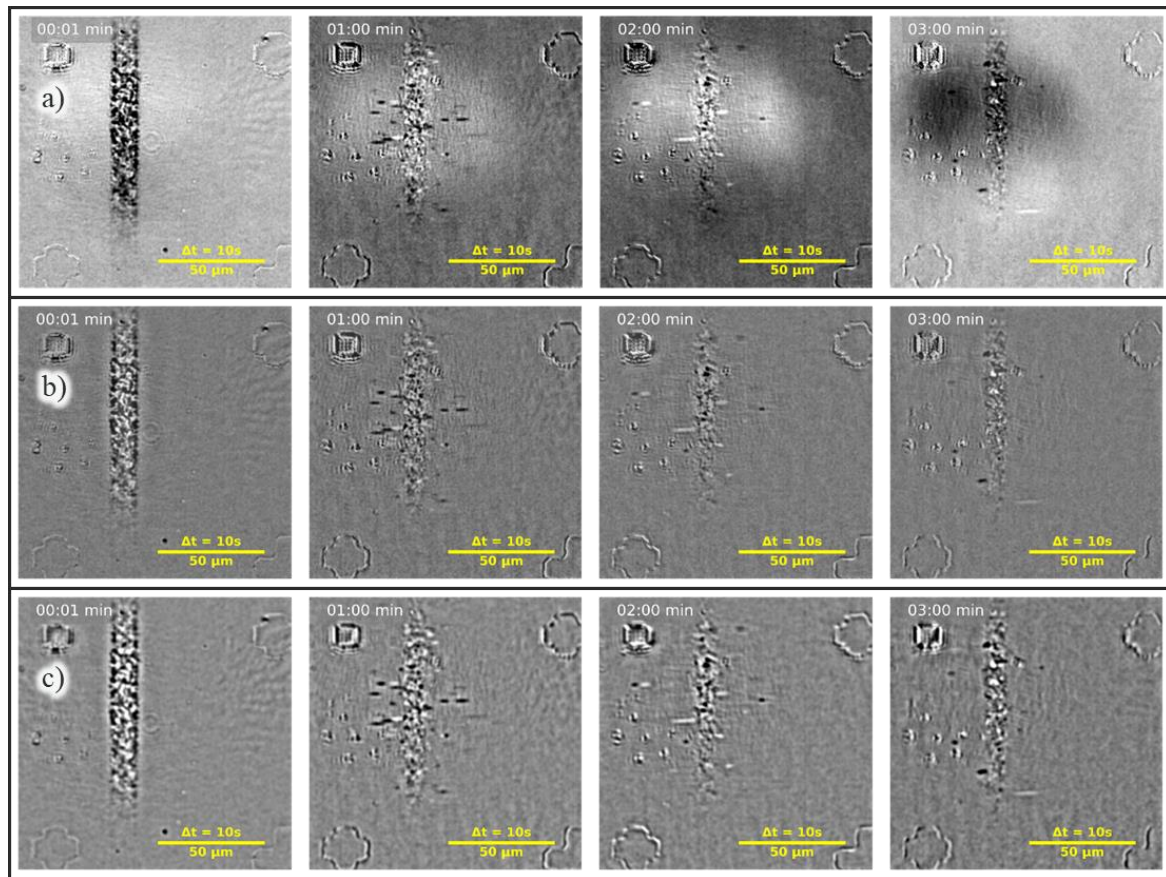


Figure 46 — Snapshots from the video after a) shade correction and contrast adjustment demonstrating the fluctuations of background, and after the band-pass filtering by a) Fast Fourier Transformation and b) Gaussian difference. Both lines of snapshots are taken after brightness and contrast adjustment.

## 5.2 AI recognition

The process of extracting the nanotube growth kinetics involves several steps. First, it is necessary to measure the length of the CNT at every moment, and then, using a linear fit, to determine the slope of the curve (Figure 47), which corresponds to the growth rate. Conducting such an analysis manually is a very time-consuming process. For example, it took about 10 days to extract the growth kinetics of 28 nanotubes from the video used as an example in the previous section. In addition, the length measurements were not made for each frame, but at small intervals, which means that the time resolution potential of our video data was not fully exploited (Figure 47 (a)). The ratio of number of length measurements to the total number of frames this CNT appears in video is called filling metric and for manual recognition its values is much smaller than for AI recognition.

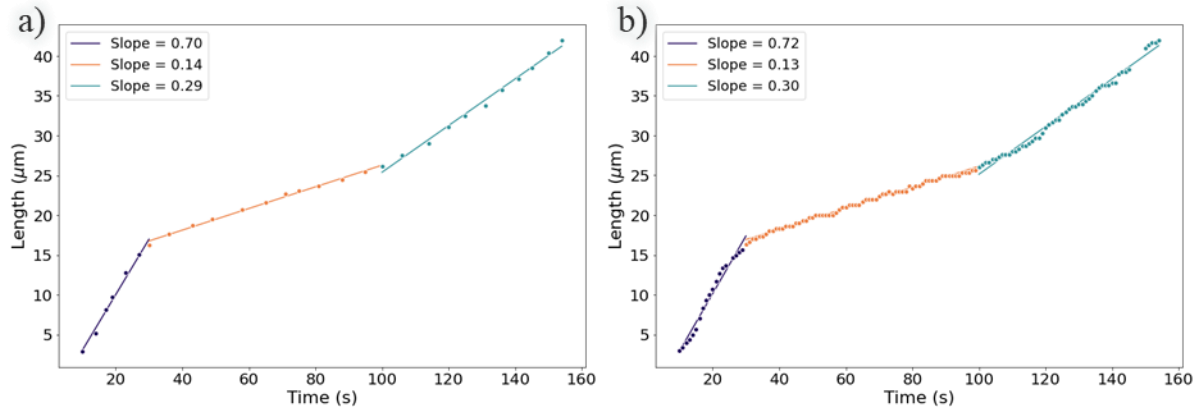


Figure 47 — Kinetic curves of the same nanotube a) measured manually and b) extracted using the automatic recognition system. The dots correspond to the measured nanotube length, the lines to the linear fits of these points.

To increase the processing speed, I developed an AI-assisted algorithm for extracting CNT kinetics (Figure 47 (b)). This kinetics measurement process proceeds in several steps:

1. Video recognition
2. Analysis of recognized segments fragmentation
3. Matching the recognized objects and tracking their movements
4. Kinetic curve measurements
5. Kinetic data extraction

The key element of the system is the segmentation model based on neural networks (NN). So before describing the method in more detail, a short description of the principles of neural networks will be given.

### 5.2.1 Principle of neural networks

Neural networks allow to solve a giant set of different problems (191). They are based on simple mathematical algorithms, such as least squares method (192) used to fit the plot shown in Figure 47. There it is used to determine the line segments, that would best describe the dependence of CNT length ( $l$ ) on growth time ( $t$ ):

$$l(t) = l_0 + v \cdot t \quad (15)$$

where  $l_0$  is the CNT length at time 0, or the intersection (of the line  $l(t)_{t=0}$ ),  $v$  is a growth rate, or the tangent of the slope of the curve  $l(t)$ . In general terms, equation 15 can be written in the form:

$$y(x) = y_0 + \omega \cdot x \quad (16)$$

where  $y_0$  is the intersection or bias,  $\omega$  is the slope or weight for parameter  $x$  (193). The goal of fitting is to find such biases and weights that the line will most accurately describe the location of the points (Figure 47). In the case of neural networks this problem is solved by the method of gradient descent in several steps (194). First, the weights and bias are randomly initiated. After that the average value of deviation of such curve from real data containing  $m$  points is calculated:

$$L = \frac{1}{m} \cdot \sqrt{\sum_m (\omega \cdot x_m + y_0 - y)^2} \quad (17)$$

The weights and biases are then updated by subtracting of its gradients of the loss function ( $L$ ) over them:

$$\omega = \omega - \eta \cdot \nabla_{\omega} L \quad (18)$$

$$y_0 = y_0 - \eta \cdot \nabla_{y_0} L \quad (19)$$

where  $\eta$  is the regularization coefficient needed to slow down the rate of gradient descent. After that, the mean square difference of the curve value from the real data is calculated again. And these operations are repeated until the gradient of the loss function either equals zero or is less than a certain threshold value (195).

The resulting linear model describes the behavior of the real data. While in case of fitting, as in Figure 47, the goal is to get the slopes of the curves, in the case of machine learning (ML), the main interest is the ability of the model to predict the value of  $y$  from the value of  $x$  that has not previously been encountered in the data.

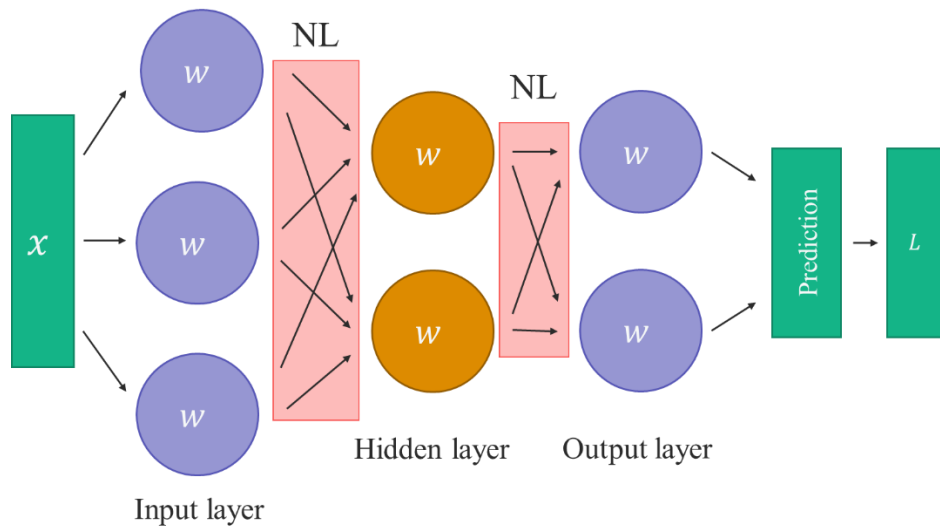


Figure 48 — Schematic of a fully connected neural network

When switching from machine learning to neural networks, one single model will represent one single neuron. The number of such neurons is limited only by the computational capabilities of the computer on which the AI will run (196). The neurons can be ordered in layers (Figure 48), which are formally divided into three groups: input, hidden and output. The input layers receive the

experimental data directly, *i.e.*, their size will be equal to the size of the input data. The output layers feed the results of its computation to the predictor and loss function, their size must correspond to the number of modeled parameters. Predictor is a part of NN which generate the final answer about the input parameters, while loss function verifies this answer. All other layers are called hidden, and their size and number depend only on the choice of network architecture. The important difference between NNs and ML algorithms is the presence of non-linear (NL) activation function between the neural network layers (Figure 48). In its absence the whole neural network could be replaced with a single layer that is a linear combination of all layers. Thus, introducing non-linear allows to complicate the neural network structure and, consequently, its data abstraction capability (196). Nowadays, the default activation function is the rectified linear unit (ReLU) (197, 198) (Figure 49), which can be defined as follows:

$$f(z) = \max\{0, z\} \quad (20)$$

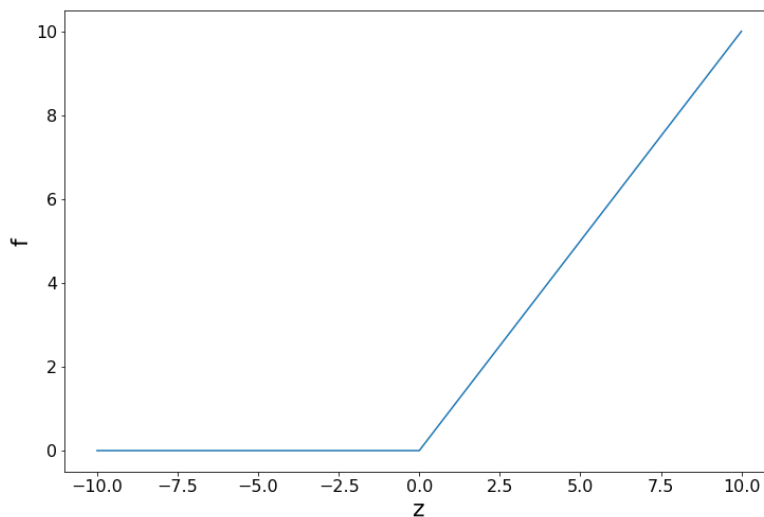


Figure 49 — Plot of ReLU activation function.

An important requirement for NN is that functions of each layer should be differentiable. This is necessary to train neural networks by gradient descent method. In this case error gradient is counted using partial derivatives on each neural network layer, and weights and biases are updated from the end to the beginning. This learning algorithm is called back propagation and allows to speed up the learning process and make it less computationally expensive due to step-by-step computations (199).

The NN shown in Figure 48 is called fully connected data since each of the outputs of the previous layer are fed to each input of the next layer. In case of small datasets, such an architecture works quite effectively. However, in case of larger amounts of data (*e.g.* image recognition as in our case where one single image contains around 160,000 pixels), it is more rational to use convolutional neural networks (CNN) (196, 200). In this case, weights and biases are arranged into 2D arrays, which convolve the image and extract useful features while passing through it with a step of several pixels

(defined by the developer of the particular AI). The output of the last layer is then transformed into 1D array or flattened, after which it is passed to the predictor through a fully connected layer.

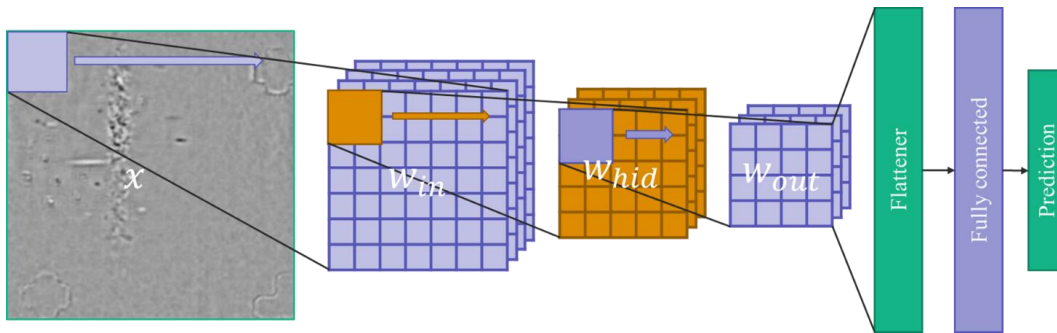


Figure 50 — Schematic of a convolutional neural network. Non-linearities between the layers are not shown for convenience.

NNs for segmentation combine several blocks training and working in the same flow. For example, the model I used combines three neural networks, which performs the following tasks: boundary box prediction, classification and offset mask prediction. The method on which this neural network is based is called mask region based convolutional network (Mask-RCNN) and is currently one of the most powerful methods of object recognition (201) (Figure 51).

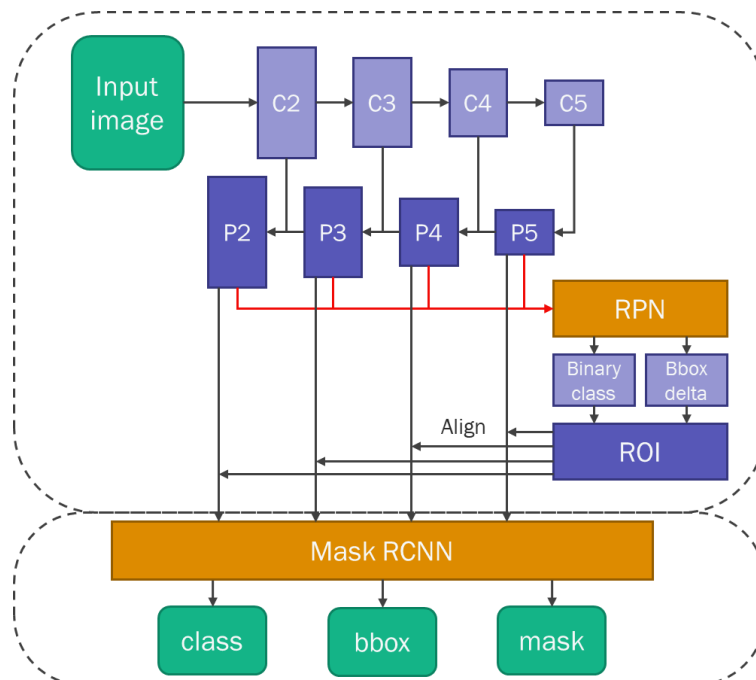


Figure 51 — Schematic of Mask-RCNN.

The architecture of this NN is shown in Figure 51. C2-C5 and P2-P5 are convolution and deconvolution neural networks or Feature Pyramid Network (FPN) (202). This part allows efficient detection of objects of different sizes. The results of its calculations come to the input of Region Proposal Network (RPN), which selects places on the image in which objects are most likely to be located. Then the selected ROIs, together with data from FPN, are fed to the Mask-RCNN input. As output, the model provides a mask of the object with the size of the original image, the boundary box, as well as the class of the object and the estimated reliability of the classification.

It is worth noting that not only the architecture is important for performing certain tasks, but also the loss functions which actually describe the problem to solve. The loss function from equation 17 is called Euclidean or L2 metric and is used for linear regression problems. For classification problems, the cross entropy loss function is most commonly used (196, 200):

$$L(y, k) = -\log\left(\frac{e^{y_k}}{\sum_i e^{y_i}}\right) \quad (21)$$

where  $k$  is the predicted class and  $i$  is the number of classes. This loss function allows to determine how accurately the object class was predicted, relative to the other ones.

For more complex tasks, other metrics can be used. Thus for segmentation NNs, whose task is to find the position of objects in the image, the metric intersection over union (IoU) or Jaccard distance is used:

$$J = \frac{C \cap P}{C \cup P} \quad (22)$$

where  $C$  is boundary box of the class, which NN is trained to find and  $P$  is predicted boundary box (Figure 52). In fact, IoU shows how accurately AI has located the objects. This metric is normalized in the range  $\{0,1\}$ , where 1 corresponds to a full match and 0 to not-intersecting boxes. This metric will be used not only by AI during training and recognition but also by the algorithms of nanotubes tracking.

Another important aspect is evaluation of the quality of the model. While in the case of linear fit the square of Pearson correlation coefficient or the standard deviation of the sample can be used to assess the quality, other metrics are also used to evaluate the quality of classification (203). They are based on a confusion matrix (contingency table), which determine all possible outcomes of the classification model work based on the relation of the real class of labeled data to the class predicted by the model.

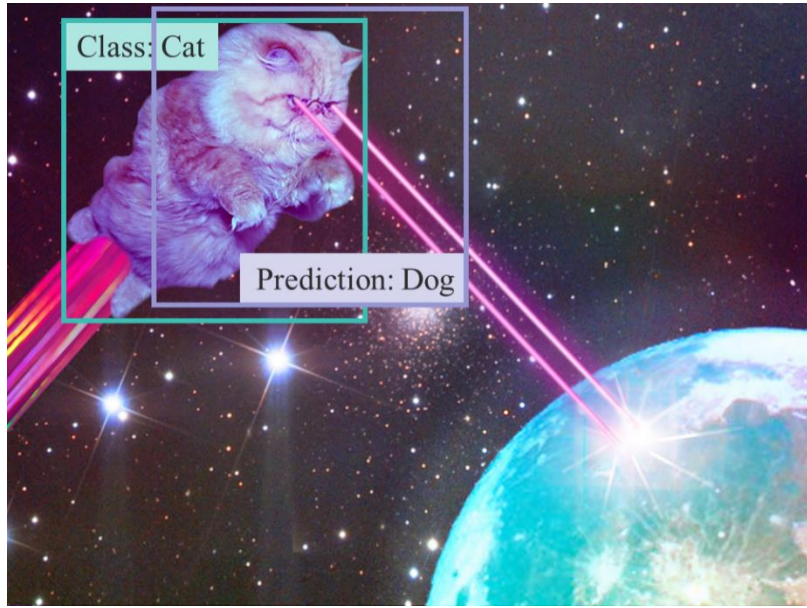


Figure 52 — Example of boundary box predicted by a segmentation neuron network.

Table 3 — Confusion matrix.

Total number = $N + P$		Predicted class	
		Negative (PN)	Positive (PP)
Actual class	Negative (N)	True negative (TN)	False negative (FN)
	Positive (P)	False positive (FP)	True positive (TP)

The evaluation metrics used for classification include precision (PR), recall (RC) and F1 metric:

$$PR = \frac{TP}{TP+FP} \quad (23)$$

$$RC = \frac{TP}{TP+FN} \quad (24)$$

$$F1 = \frac{2 \cdot PR \cdot RC}{PR+RC} = \frac{2 \cdot TP}{2 \cdot TP + FP + FN} \quad (25)$$

where TP, FP, FN are true positive, false positive and false negative, respectively (Table 3). Precision allows estimating the proportion of objects correctly assigned to a certain class, and Recall shows the proportion of correctly recognized objects. These two metrics are not sensitive to unbalanced datasets, where the number of objects of one class greatly exceeds the others (203). Therefore, in practice, a harmonic mean of precision and recall, called F1-metric, can be used.

To evaluate the classification quality of segmentation NNs, a metric called mean Average Precision (mAP) (204) was used, which can be defined as follows:

$$mAP = \frac{1}{N_C} \frac{\sum_{i=1}^l \frac{TP_i}{TP_i + FP_i}}{l} \quad (26)$$

where  $l$  is the number of the objects of one class,  $N_C$  is the number of classes. This metric is calculated for the subsets of each classes of sizes from 1 to  $l$ , with the different IoU (typically for 0.5, 0.75 and in the range from 0.5 to 0.99 with a step of 0.05), which allows to evaluate the classification quality for the fragmentarily objects recognized. This evaluation metric will be used to estimate the quality of the core model, used in the AI-assisted kinetic extraction system.

### 5.2.2 Core model

The Python programming language was used to write the system. AI solutions were implemented based on the PyTorch library from Facebook AI Research laboratory (205).

The core of the system responsible for CNT recognition is Mask-RCNN. As a backbone was used residual neuron network ResNET-50 (206) pre-trained on Microsoft COCO-2017 dataset (207). The use of neural networks already trained on any data, even if they are not relevant to the solution of a new task, allows to retrain them on new data in a shorter time interval (208).

The dataset consisted of 580 images, taken from different videos and manually labeled. In total, four classes of objects were identified for detection: objects with dark contrast, bright contrast, catalyst lines and optical marks (Figure 53).

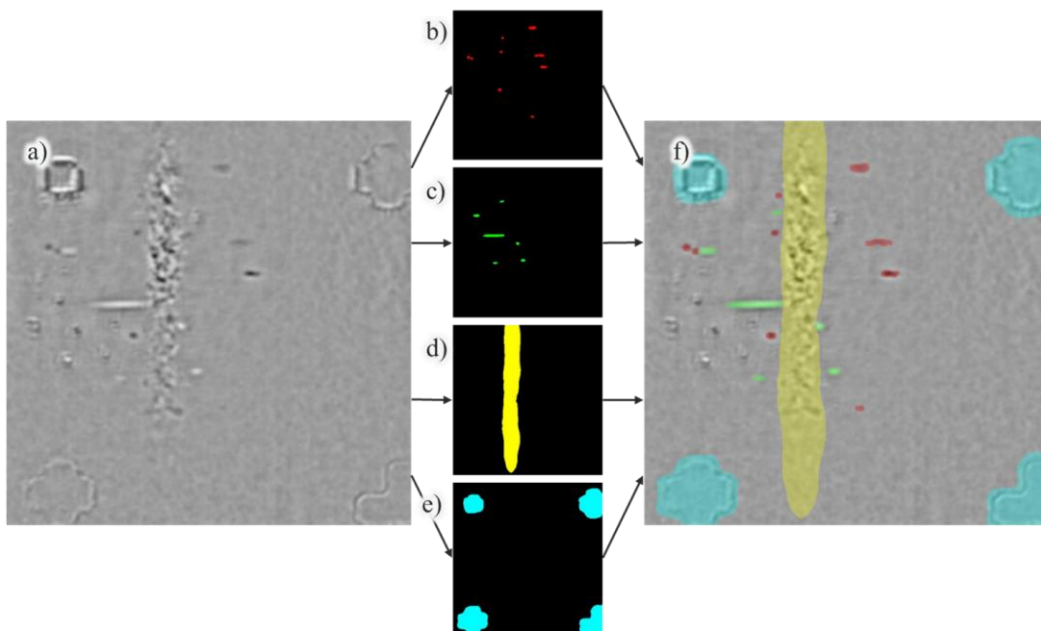


Figure 53 — a) A typical snapshot from the video used in the dataset for training the neural network with marked b) segments corresponding to an increase of absorption (dark contrast), c) segments

corresponding to a decrease of absorption (bright contrast), d) catalyst line and e) optical marks. f) Image with filters superimposed on it.

During training, the dataset was divided into training images (550 images) and validation images (30 images). To enhance the quality of training on such a small dataset, I used some augmentations (209) (Figure 54). Augmentations refer to any image transformations such as plastic transformations, its displacements, rotations, reflections, changes of brightness, contrast or saturation (210). Their use allows to train a neural network to recognize a larger number of different variations of the input data while maintaining the dataset size. For training the nanotube recognition neural network, I chose the following augmentations: horizontal and vertical flips, change of contrast and brightness (within defined limits). The probability of occurrence of each augmentation was equal to 0.5, and each image could be transformed by several augmentations. The presence of horizontal and vertical flips enhanced the ability of the model to localize the objects of interest, and brightness and contrast adjustments made the recognition process more robust with regards to the quality of raw data.

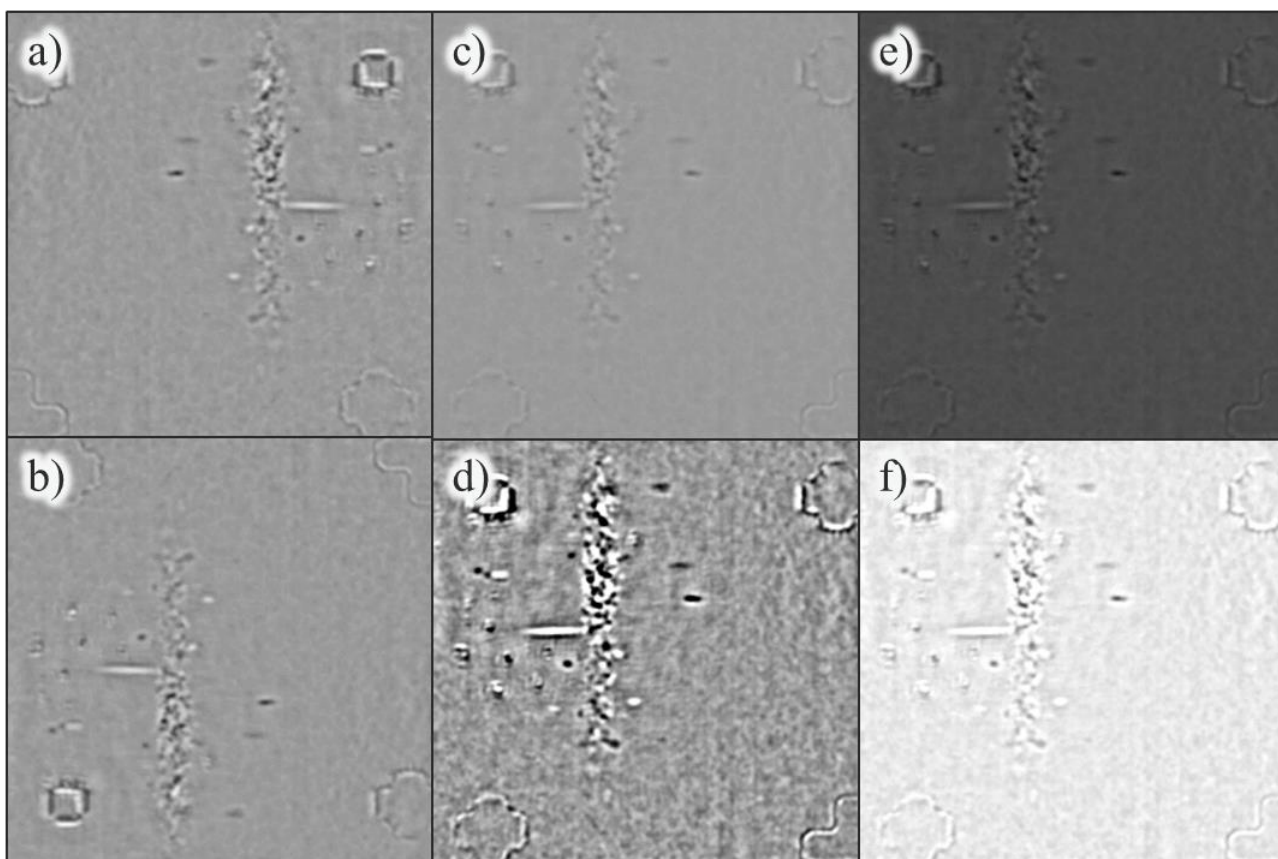


Figure 54 — The snapshot of Figure 53 (a) after various transformations. a) Horizontal and b) vertical flips, adjustment of the contrasts between c) minimum and d) maximum, brightness adjustment between e) minimum to f) maximum.

Training was performed on graphics processing units (GPU) provided by Google Colab (211) during 150 epochs (one epoch or iteration is a passage of the NN through the entire training dataset) with a learning rate of 0.005 which decreased by 10% each 5 epochs. Weight decay of 0.0005 with momentum of 0.9 was used.

Table 4 — Evaluation of the model after 150 epochs of training using mAP as a metric. The numeric subscripts beside the metrics correspond to the IoU values for recognized objects, and the alphabetic ones corresponds to the sizes of recognized objects in pixels: S for Small ( $area < 32^2$ ), M for Medium ( $32^2 < area < 96^2$ ) and L for Large ( $area > 96^2$ ).  $AP_{COCO}$  was calculated for IoU in the range from 0,5 to 0,99 with a step of 0,05.

Parameter \ Metric	$AP_{COCO}$	$AP_{50}$	$AP_{75}$	$AP_S$	$AP_M$	$AP_L$
Boundary Box	50.1	83.3	53.3	37.9	46.3	56.0
Mask	46.1	81.7	44.6	33.4	37.8	55.0

The speed of the model is about 3.5 frames per second while running on GPU (NVIDIA GeForce GTX 1050), which makes it unsuitable for video streaming recognition. However, for our purposes, the recognition quality was the main goal. It meets the modern standards of NN for object detection (201, 212) (Table 4).

### 5.2.3 Segment assignment and tracking

Model predictions are extremely important, but video recognition is only the first step to extracting growth kinetics data. The next step is to prefilter the recognized masks. Since the model is trained to recognize the objects with different IoU for a single CNT, it may predict several segments (Figure 55 (a-c)), or several segments corresponding to different CNTs may overlap (Figure 55 (d, e)).

To distinguish between these two types of collisions, I used an algorithm computing the intersection matrix of IoU for masks of the same class with themselves. Next, an alignment evaluation was performed for the intersecting masks. If the width of the mask made by merging the intersecting masks was not more than 1.5 times the width of each of the included masks, the segments were considered aligned and their merged mask replaced the set of included segments (Figure 55 (c)). In the case where all segments were 1.5 times less wide than their merged mask, they were marked as separate CNTs (Figure 55 (d)). Cases where some of the masks were larger and some smaller than merged ones were recognized as a mixture of correct recognition (each segment in the video corresponds to a recognized one) with recognition artifacts (several separate segments are recognized

as one) (Figure 55 (e)). The latter ones are deleted, while the former ones are stored as independent segments.

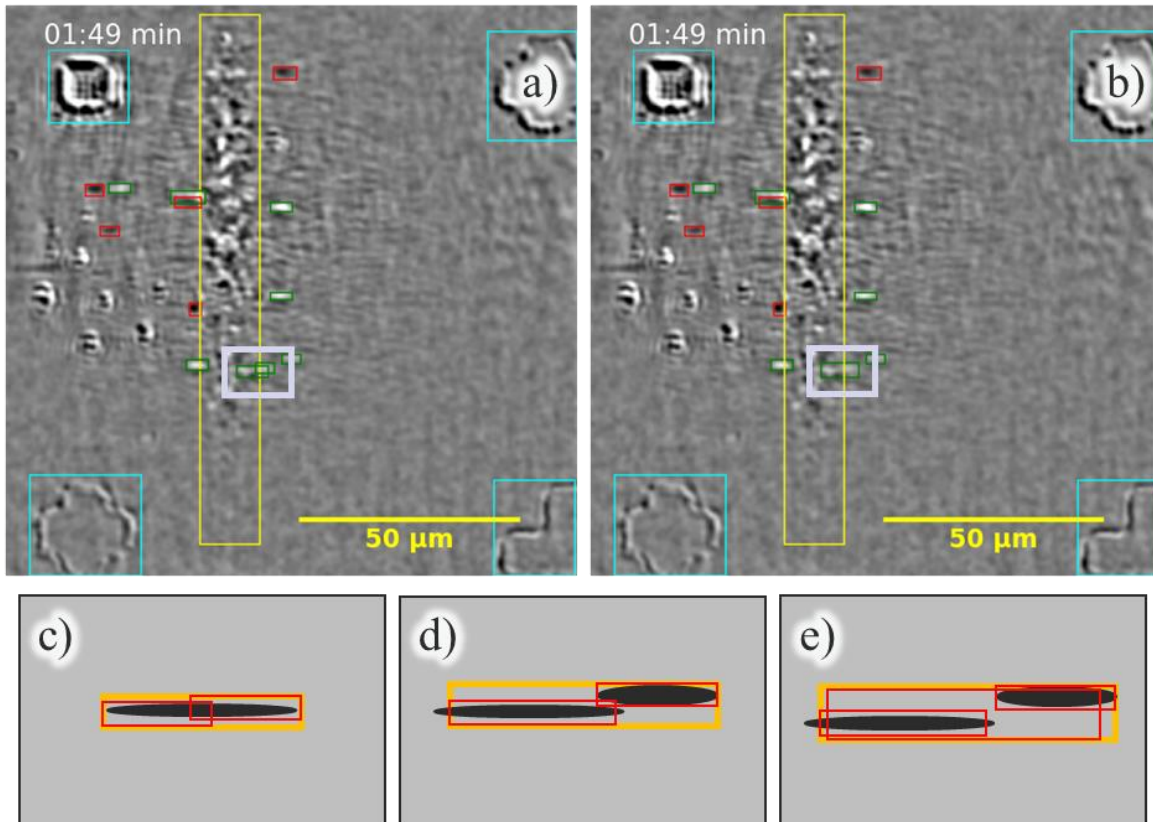


Figure 55 — Snapshots from the video with overlay from boundary boxes a) before prefiltering and b) after with merging of intersecting masks (light purple box). The schema of the different variants of intersecting masks: c) fragmentary recognition of a single segment, d) two different intersecting segments, and e) artifact of recognition with two separated segments. The black ovals corresponds to the grown segments, the red and orange rectangles to the boundary boxes of recognized and merged masks, respectively.

To extract the kinetics, it is also necessary to track the recognized segments through video, that is, to match the recognized masks from different frames with each other. For this purpose, were used Hungarian method (213) and Kalman filter (or Linear Quadratic Estimation) (214), which are widely used for image tracking (215).

The Hungarian method was used to track masks on consecutive frames. For this was calculated cost matrix of IoU for the objects on the next frame with the objects on the current frame (Table 5). Then all the cases were divided into several groups:

1. New segments, that is those that are present in the new frame but were not present in the previous frame. In the cost matrix their IoU everywhere is equal to zero (Table 5 (orange) and Figure 56 (a)).

2. Continued objects, that is those that can unambiguously be attributed to objects from the previous frame. In the cost matrix their IoU has only one non-zero element (Table 5 (blue) and Figure 56 (b)).

3. Collisions of different types (Table 5 (purple) and Figure 56 (c-e)). If several segments correspond to one from the previous frame (Table 5 (column 3)), if one segment corresponds to some previous frame (Table 5 (column 4,5)), or if some objects from the previous frame intersect with some objects (Table 5 (column 6,7)).

In the first two cases the segment was assigned to a new label and the mask label from the previous frame, respectively. The collisions, on the other hand, require more detailed consideration.

Table 5 — Typical IoU cost matrix for CNT tracking. The orange column corresponds to the case of new segment occurrence. The blue labels correspond to unambiguous assignment of the segment continuing growth. Purple marks denote different types of collisions.

Mask number		New frame (t+1)						
		1	2	3	4	5	6	7
Old frame (t)	1	0	0.8	0	0	0	0	0
	2	0	0	0.9	0	0	0	0
	3	0	0	0.3	0	0	0	0
	4	0	0	0	0.5	0.75	0	0
	5	0	0	0	0	0	0.8	0.1
	6	0	0	0	0	0	0.2	0.9

In case of collision of the first type (Table 5 (column 3)) the segment from new frame was attributed the label of the segment from the previous frame having the highest IoU with it (Figure 56 (c)).

For collisions of the second type (Table 5 (column 4, 5)) first the alignment of the two segments is checked by comparing their widths with the width of their merged mask. If they are aligned, both segments are attributed to the same CNT from the previous frame (Figure 56 (c)). Otherwise, only the segment with the highest IoU is attributed to the segment from the old frame, and the other one is defined as the new one.

Collisions of the third type are resolved by finding the max of IoUs in the cost matrix (Table 5 (column 6, 7)). If the IoU maximum of a segment from the new frame matches the maximum of a

segment from the previous frame, it inherits this segment label (Figure 56 (e)). If for the segment from the new frame all its intersections with the segments from the old frame are not maximal, it is assigned a new label.

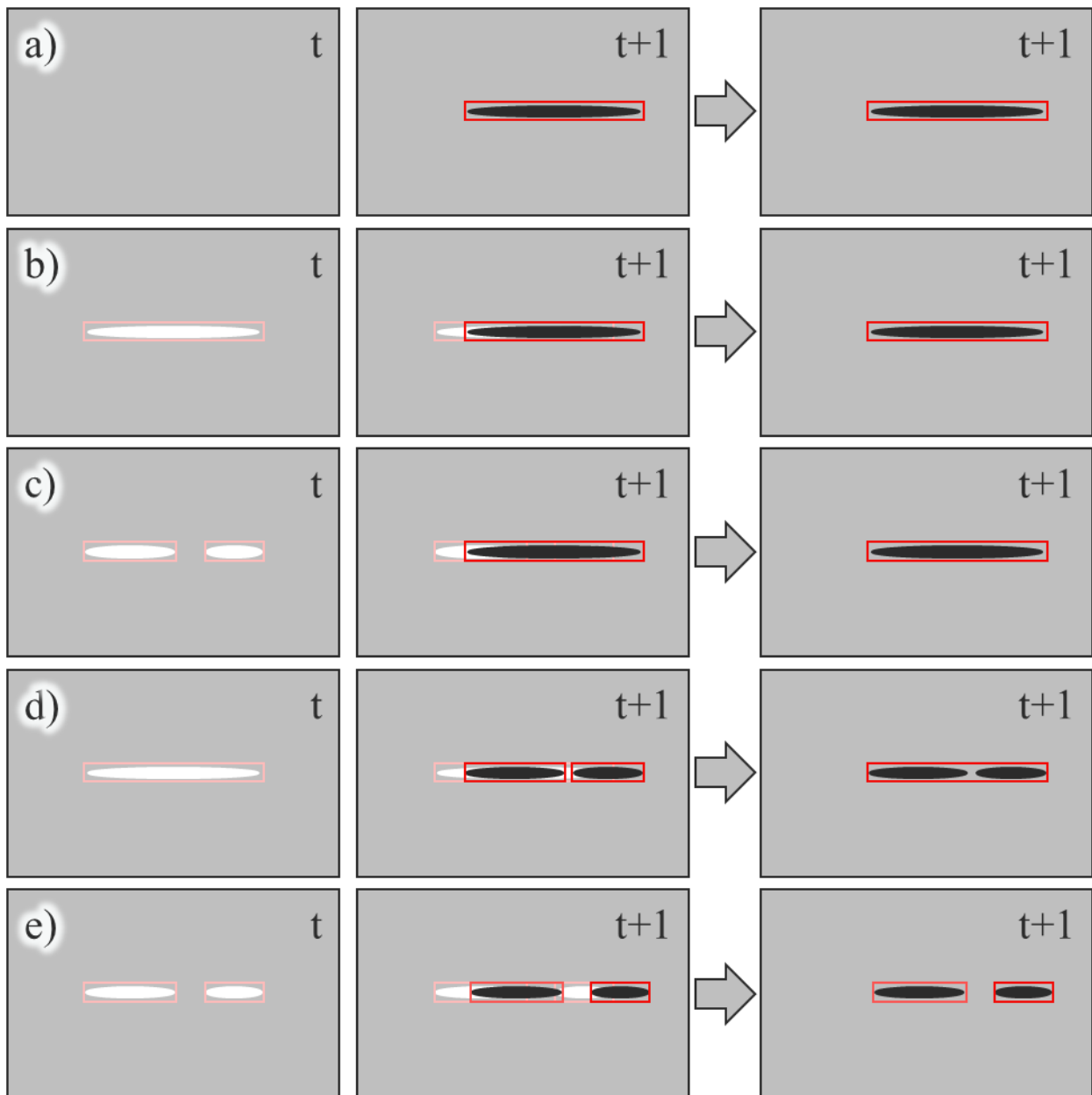


Figure 56 — Illustration of different variants of mask intersection on the old and new frames. a) New segment appearance, b) continuation of growth, c) intersection of several segments from the previous frame with one from the new frame, d) intersection of several segments with one from the previous frame, e) intersection of several segments from the previous frame with several ones from the new frame. White and pink marked segments and boundary boxes from the previous frame, black and red are from the new frame, respectively.

After completing the first stage of tracking, all segments were grouped into clusters of sizes ranging from one to several tens of masks corresponding to consecutive frames. The next step is to trace the matches between the clusters. This has to be done because some CNTs may either not be captured in all consecutive frames or may not be recognized due to low image contrast.

The Kalman filter is used to solve this problem (Figure 57). As input data, the previously tracked segments containing two or more masks were used. For each group, a modeling window was formed based on the average length of all masks ( $l_i$ ), the location of the first (for tracking back in time) and the last (for tracking forward in time) mask ( $X(t_i)$ ), and the growth rate and direction ( $v(t_i)$ ). The growth rate was calculated as a ratio of the average length of all masks to the delay time of the current video, and the growth directions was determined by the sign of the coordinate differences of the beginning and the end of the segment of the first and the last mask in the group. In this case, if the signs were opposite, such a group was excluded from consideration as a recognition artifact, because every segment should move in the same direction. The width of the window was defined as the maximum width of merged masks of the whole group.

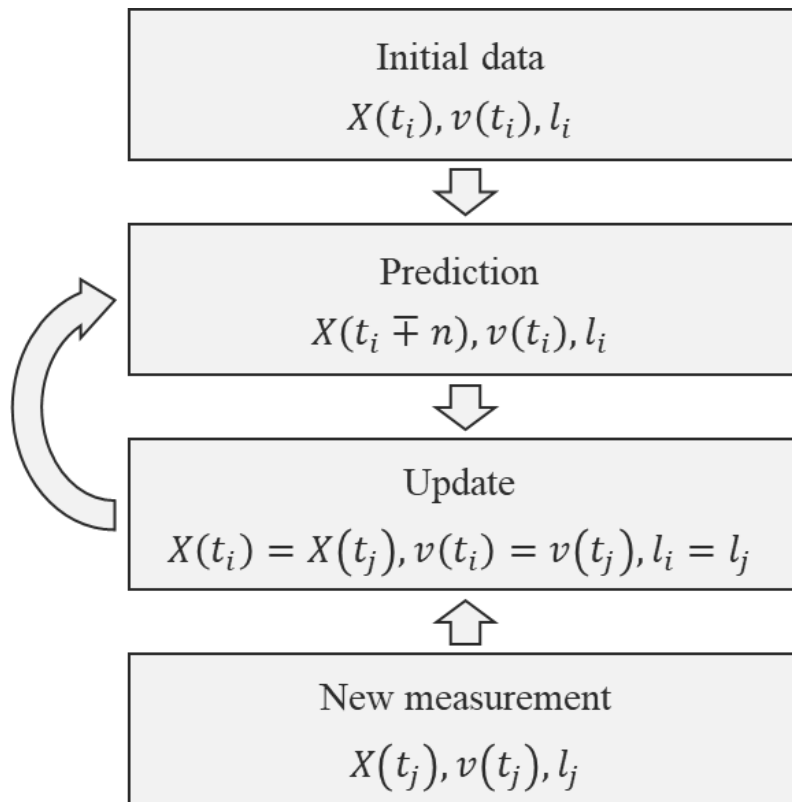


Figure 57 — Schematic of Kalman filter.

In the process of tracking the window movement was modeled based on the equation:

$$X_{tip,end}(t \mp n) = X_{tip,end}(t) \mp v(t) \cdot n \quad (27)$$

where  $n$  is greater than 1 ( $n = 1$  is the case of tracking masks on consecutive frames), plus corresponds to moving the mask forward in time calculated from the positions  $X_{tip,end}$  of the last

mask in the group, and minus models moving the window backward in time for  $X_{tip,end}$  of the first mask. In the case of forward tracking, intersections with groups of all sizes are searched. If a model window matched a single mask, it was added to the list of groups correlated with this one, and the search by model parameters continues till the end of the time limit of the video. If a group containing several masks coincides with a model window, it is also added to the list, and its model parameters replace the model parameters of the tracked group. Thus, if the growth rate, and consequently the segment size, changed, the model could correctly detect a new group of recognized segments belonging to the tracked one (Figure 58 (a)). In the case of backward segment tracking, the matches are searched only among the single masks, as they do not participate in the simulation and cannot be used to find their corresponding groups forward in time (Figure 58 (b)).

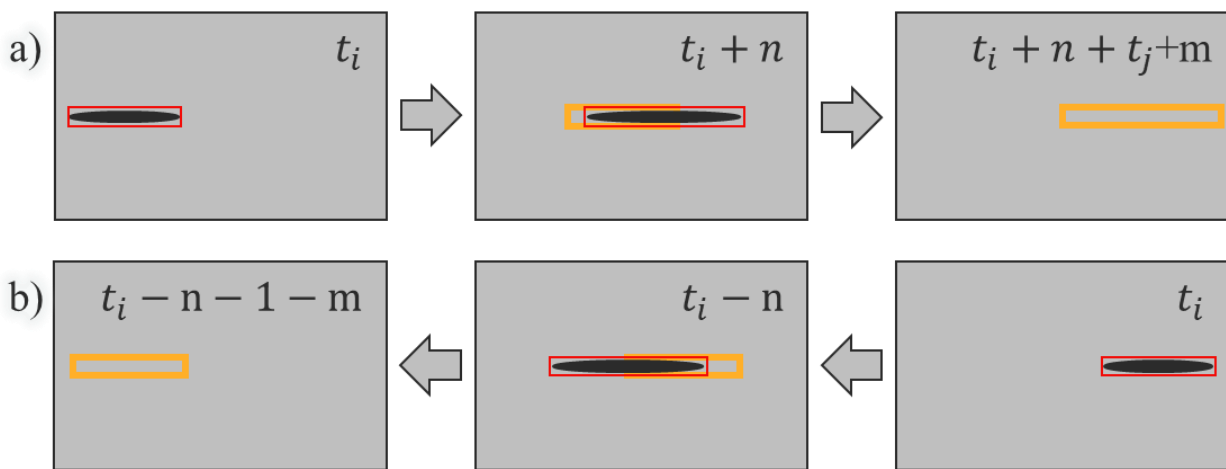


Figure 58 — The schematic of the CNT tracking a) forward and b) backward in time. Black ovals corresponds to recognized segments, red and orange rectangles corresponds to boundary boxes and modelling window, respectively.

#### 5.2.4 Human-supervised kinetic extraction

As a result of all tracking, a database is created in which numbers of all tracked groups are entered, distributed according to what initial group they belong to, as well as a video on which all numbers of these groups are displayed (Figure 59). Further work on extracting growth kinetics consists in analyzing this database and correcting it, as well as dividing kinetic curves into linear segments. Since we need high accuracy in the data analysis both of these steps are human-supervised.

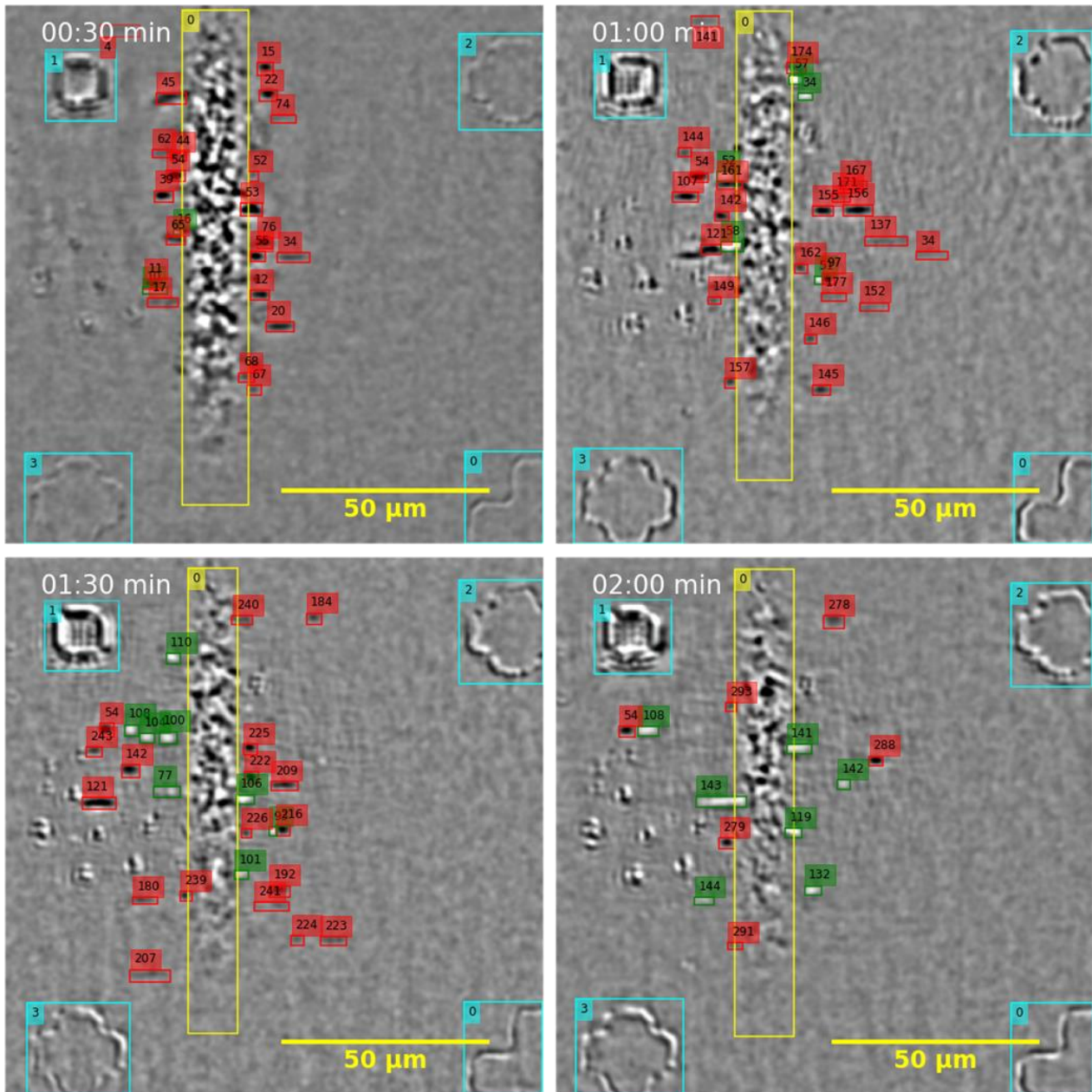


Figure 59 — Snapshots with numbered segments.

At the first step, we check the correctness of tracking groups of segments and make changes if necessary. This step is necessary because the Kalman filter does not always allow to track correctly the CNTs on the video due to changes in their growth rates, pauses, or shrinkages. Moreover, segments with different contrasts (Figure 59 (red, green)), corresponding to the grown CNTs (dark contrast), and to the changes in the structure (bright contrast) are matched to each other.

At the next stage, the kinetic curves are divided into fragments corresponding to the linear growth (Figure 60). After this database with this data is fitted and kinetic data are extracted from it.

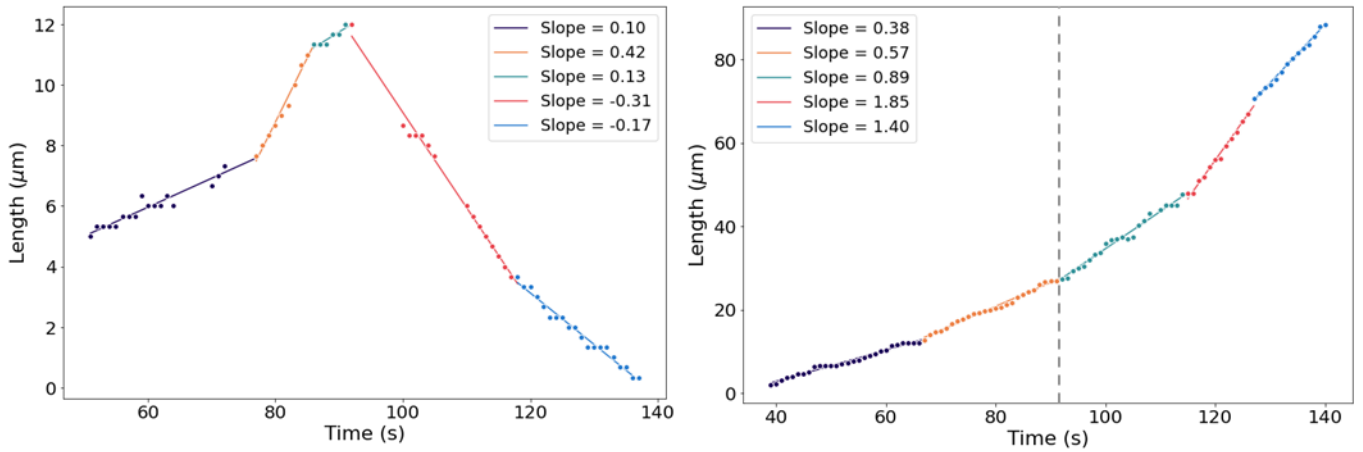


Figure 60 — Kinetic curves extracted with the AI-assisted system with linear fits of the data, as well as information about the growth rates (slopes). Linear segments highlighted with different colors. The vertical dashed line on the right panel corresponds to an observed change of structure (*i.e.* change of optical contrast).

### 5.3 Conclusion

Improvement of the process of video treatment qualitatively changed our possibilities of measurements of the kinetic data. Moreover, it allowed to clearly evidence the changes in CNT growth kinetics. It also allowed to distinguish individual CNTs having grown successively at very close positions.

Despite that, the algorithm of the treatment can still be improved. Such processes as brightness and contrast adjustment depends on empiric hyper parameters (threshold values). Development of self-tuning or nonparametric algorithm can be the next step towards improvement of this algorithm. The same can be said about the parameters of FFT and Gauss filtering. At the moment, they are fixed: one possible improvement might be the development of an algorithm of adjustment of filtered pixels' sizes for Fourier filtering and the range of standard deviations for difference of Gaussians.

The developed algorithm of kinetic extraction allowed to facilitate the process of growth rate measurements and speed it up drastically. This is based on state-of-the-art AI model whose recognition quality is comparable to currently existing models. However, an obvious drawback of the model is that it was trained on a very small dataset. One possible improvement is to train the model on a larger set of data. It is possible to use correctly recognized videos for these aims. It is also possible to change the model itself in future, if better ones become available. For such changes it will just be necessary to preserve the output formats of data generated by the current model.

The rest of the algorithm might be improved by development of different approaches for resolution of mask collisions. Moreover, entire recognition system can be optimized for weak computers by transition from treatment of entire video to frame by frame treatment of the video at the stages of video recognition and segment alignment. This would allow to improve memory usage. It is worth noting that human-controlled steps of kinetics extraction should be preserved without changes since they allow to verify the adequacy of recognition and tracking process.



# Chapter 6.

## Growth kinetics of individual carbon nanotubes

As shown hereafter, analysis of the obtained videos and extraction of CNT kinetics revealed that CNT growth at the individual level is more complex than previously thought and predicted by existing models.

A first dataset (dataset 1) included about 700 nanotubes grown in the same conditions: at 850°C and with an ethanol partial pressure of 1600 Pa. Note that, at the time of data analysis, growth kinetics were still measured manually. Only CNTs longer than 3  $\mu\text{m}$  were included in the analysis because kinetic measurements of shorter CNTs are not reliable given the localization accuracy of our system (0.3  $\mu\text{m}$ ). It is worth noting that the imaging area, which corresponds to the area directly illuminated by the incident beam, has a diameter of about 80  $\mu\text{m}$ , which imposes an upper limit to the measured nanotube lengths.

A second dataset (dataset 2) was obtained by the AI-assisted kinetics extraction of the videos recorded during the postdoctoral work of my former colleague Huy-Nam Tran. Thus, the statistics was supplemented with more than 2400 nanotubes, grown at temperatures ranging from 800°C to 900°C and at ethanol pressures ranging from 59 to 4000 Pa. Only nanotubes longer than 3  $\mu\text{m}$ , with a total Pearson's  $R^2$  higher than 0.8, with more than 7 points measured and nanotubes for which the total filling metric was more than 0.25 (that is, with measurements made during less than quarter of growth time) were considered (Table 6). The latter criterion was defined to estimate the density of recognition, and is used to filter the data which were measured with less regularity than manually recognized ones.

In the following, the dataset 1 is called MR (for Manually Recognized) and will be used to describe the general features of growth kinetics in given growth conditions while the dataset 2 or AI (for Artificial Intelligence) will be used to generalize the observations, and study the effects of temperature and ethanol pressure.

Table 6 —Dataset 2. Number of CNTs whose growth kinetics were extracted at different growth temperatures and partial pressures of ethanol and number of CNTs selected for further analysis (in brackets).

Pressure (Pa)	59	177	533	1600	4000
Temperature °C					
800			306 (214)		
825			273 (200)		
850	238 (181)	175 (117)	233 (189)	417 (315)	122 (93)
875			503 (404)		
900			143 (105)		

## 6.1 Types of kinetic behavior

All data mentioned in this section correspond to data set 1 and were therefore manually extracted. All CNTs were synthesized at 1600 Pa of ethanol partial pressure and temperature of 850°C using iron as a catalyst.

### 6.1.1 Linear growth

About half of the CNTs (309 CNTs) in MR dataset showed a linear growth, manifested on rolling-frame corrected videos by a steady translation of a segment with constant length and contrast from the emergence from the catalyst and until the end of growth. The SEM contrast and Raman resonance of such CNTs also remained unchanged throughout their length (Figure 61 (a)). The kinetic curve of such CNTs therefore corresponded to a straight line with an abrupt transition to a plateau corresponding to the growth termination (Figure 61 (b)).

We found an inverse relationship between the growth rate and the lifetime (Figure 61 (c)). A similar behavior was already reported for kinetics measured on nanotube ensembles (134, 216). Our study confirms a similar behavior at the individual level, which supports that the main cause of deactivation in the studied conditions is an excessive carbon supply (*e.g.*, integration of unhealed topological defects, coating of the catalyst with carbon) (216).

For 189 such CNTs, it was possible to determine their metallicity based on their SEM contrast (high contrast for metallic CNTs, low contrast or even undistinguishable from background for semiconducting CNTs). The other CNTs were too close to each other to reliably distinguish them by SEM or Raman, or were etched after growth. We further validated this method by checking the G-band shape of the CNTs giving resonant Raman spectra. It is worth reminding that CNTs with a

metallic SEM contrast can also include DWCNTs containing at least one metallic nanotube (i.e. M@SC, SC@M, M@M), while those with a semiconducting SEM contrast can include SC@SC DWCNTs: this was already reported by Zhu *et al.* and confirmed by our own Raman measurements (217). Importantly, analysis of the data showed no statistical difference in growth rates or lifetimes between metallic and semiconducting nanotubes (Figure 61 (c-e)). This is in contrast with a previous report by Zhu *et al.* that SC-CNTs would grow an order of magnitude faster than M-CNTs (217). However, this may be due to the use of different conditions: Zhu *et al.* also used Fe as catalyst but their substrates were SiO<sub>2</sub>/Si instead of ST-cut quartz, their precursor was methane with H<sub>2</sub>/Ar mixture as carrier gas with 0.5% of water instead of ethanol/argon, and they used kite growth instead of lattice-oriented growth (217).

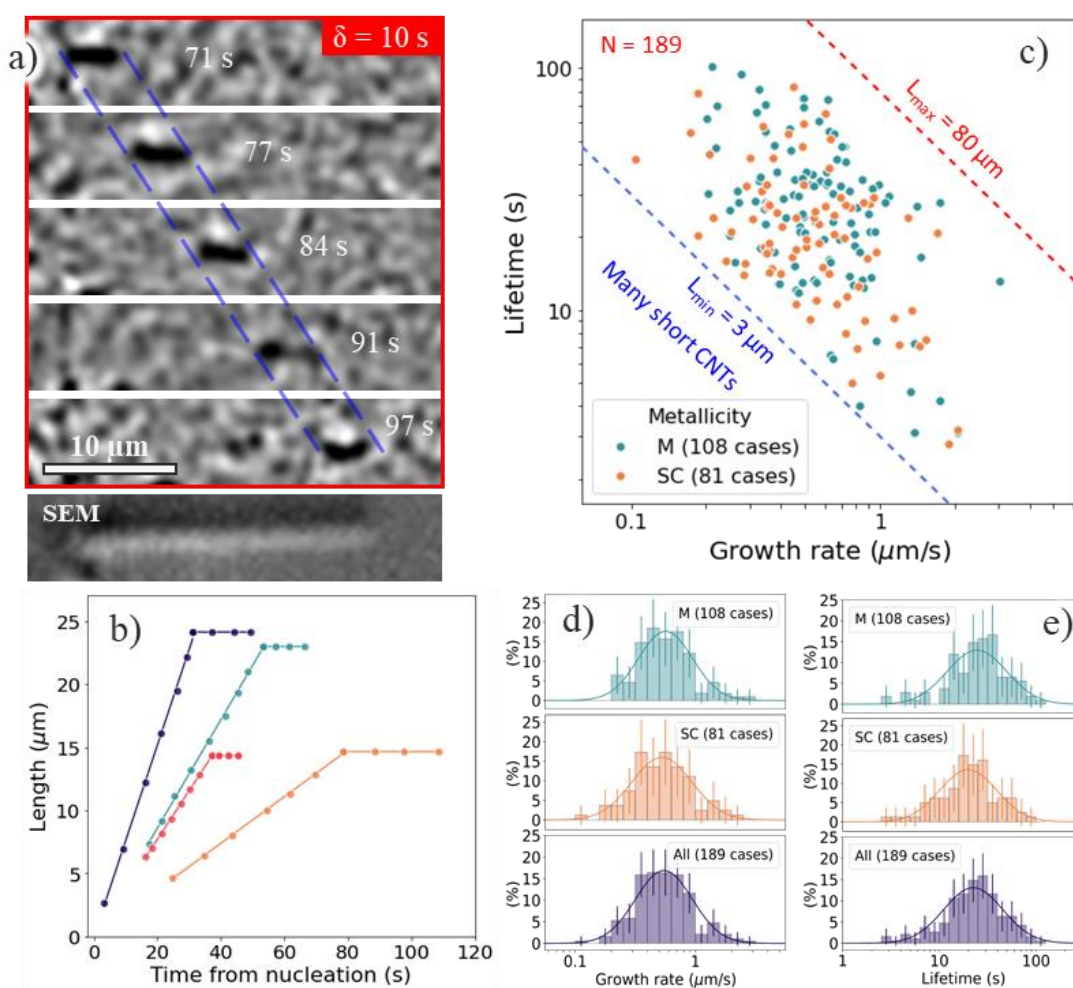


Figure 61 — a) Video snapshots (rolling-frame correction with  $\delta = 10$  s) showing a linear growth (top) and the corresponding SEM image taken after growth (bottom). b) Examples of kinetic curves of linear growth. c) Dependence of lifetime on growth rate for metallic and semiconducting nanotubes. d,e) Distributions of d) growth rates and e) lifetimes of metallic, semiconducting and all CNTs together. All nanotubes were grown at 1600 Pa of ethanol and 850 °C.

### 6.1.2 Broken-line kinetics

Unexpectedly, the rest of the nanotubes (368 CNTs) in the MR dataset displayed broken-line kinetics. I recall that all these CNTs were synthesized at 850°C and with a partial pressure of ethanol of 1600 Pa.

In about 84 % of these cases, the change of growth rate was not accompanied by a change of nanotube structure: such cases just manifested on differential videos as an abrupt change in length and speed of the translating segment (Figure 62 (a)). There was therefore no apparent change in optical absorption between the initially and newly grown CNT sections. For such cases, the absence of structure change was confirmed by Raman in the vast majority of cases (36 out of 43 CNTs with resonant Raman spectra, i.e. 87 %) (Figure 62 (b)).

However, in some cases (about 16%), the growth rate change was accompanied by the appearance of a second segment of the same length and speed behind the first one (Figure 62c). This second segment was either bright (most cases) which corresponds to a newly grown CNT section with a lower optical absorption than the first one, or dark (minority of cases) which corresponds to an increase in optical absorption. In this case, the change of optical contrast was always associated with a change in the resonant Raman features and very often with a change in SEM contrast (*i.e.* between M and SC) (Figure 62 (d)). Hence such changes correspond to changes of chirality. A few examples of multiple sequential changes of chirality were even observed.

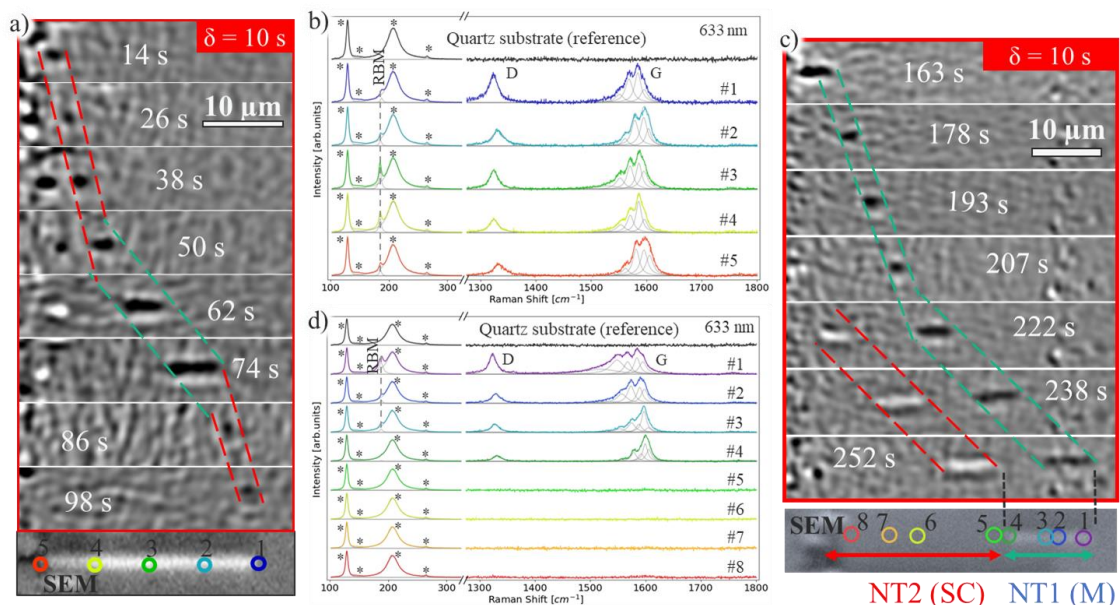


Figure 62 — a) Differential video snapshots showing non-linear CNT growth (top) without change of structure and with preserved SEM contrast (bottom) and b) Raman resonant features along the CNT (positions and color of the spectra corresponds to positions and color of the points in the bottom panel (a)). c) Differential video snapshots of a CNT growth with change of structure and

contrast on the video and SEM, as well as d) change of Raman resonance along the CNT (positions and color of the spectra corresponds to ones from the bottom panel (c)). Asterisks on (b, d) correspond to quartz peaks. All CNTs were grown at 1600 Pa of ethanol and 850 °C.

In both cases (with and without structure change), the CNT growth rates can change several times (Figure 63 (a, b)). These are always abrupt changes from one constant growth rate to another. The correlation plot of the growth rates after and before change shows two elongated clouds of points, one corresponding to acceleration events and one to deceleration events (Figure 63 (c) upper and lower clouds, respectively). Surprisingly, there is no significant difference in growth rate ratio between the CNTs grown with or without a change of structure (Figure 63 (c-e)). In both cases, an increase of growth rate is more often observed (209 cases out of 266, 76%) which supports a similar mechanism whatever the rate change is accompanied by structure change or not.

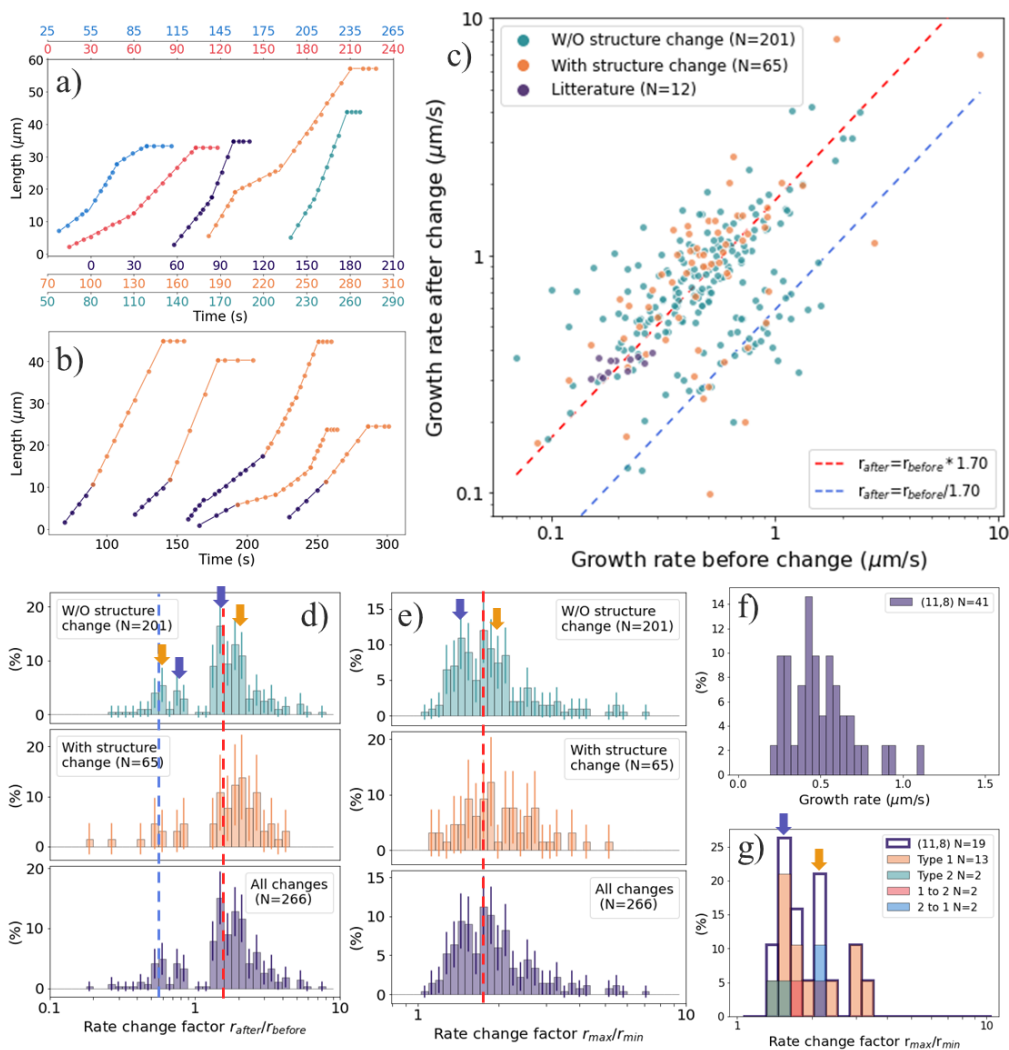


Figure 63 — Kinetic curves for nanotubes grown with changes of growth rate and a) without and b) with change of structure. c) Correlation plot of growth rates after and before the change (data from Koyano et al. were added for comparison (140)). d) Distribution of the rate change factor  $r_{after}/r_{before}$

and e) ratio of high to low growth rate  $r_{\max}/r_{\min}$ . f) Distribution of the growth rates for (11,8) nanotubes and g) distribution of growth rate ratio of these CNTs. In panels c-e, the dashed red and blue lines correspond to straight lines with a proportionality factor of 1.7 and 0.6, respectively. In panels d, e, and g, the purple and orange lines highlight a possible substructure.

The growth rate ratio values shown in Figure 63 (c) follow straight lines with the same proportionality factor of, on average, about 1.7 for rate increases and  $1/1.7=0.6$  for rate decreases. The same proportionality factor of 1.7 was previously reported by Koyano *et al.* for CNTs synthesized with a carbon feedstock interruption with water vapor (140) (Figure 63 (c), purple dots). It is also possible that there is a substructure in the rate change factor distribution (Figure 63 (d, e)), which may be a consequence of the presence of several stable states between whom the transitions occur.

A Raman characterization at several wavelengths allowed me to assign 41 nanotube segments to (11,8) SWCNTs grown in the same conditions (1600 Pa, 850 °C). The distribution of their growth rates is not monomodal, which contradicts existing theories (Figure 63 (f)). The growth rate ratios of these CNTs possibly shows the presence of a substructure although more statistics would be needed to confirm (Figure 63 (g)).

## 6.2 Ethanol pressure dependence

As mentioned above, improved video processing and analysis methods made it possible to extract the kinetic data from videos made earlier by my colleague Huy-Nam Tran during growths at different pressures and temperatures. Comparison of manually-measured kinetics with those extracted by AI for similar synthesis conditions shows that the data have similar centers and distributions (Figure 65 (a) and Figure 67 (a) gray and green dots for CNTs measured manually (MR) and automatically (AI), respectively), which demonstrates the accuracy and reliability of the AI method. Hence in the following chapters, I used all data available from both AI and MR datasets.

### 6.2.1 Types of growth kinetics

All the syntheses discussed in this part were made at a temperature of 850°C. The ratio of the number of linearly grown CNTs to those with broken-line kinetics varies widely with changes in pressure, but always remains larger than 1 (Table 7) and the dependence of the percentage of linearly and non-linearly grown CNTs from pressure shows complex behavior (Figure 64).

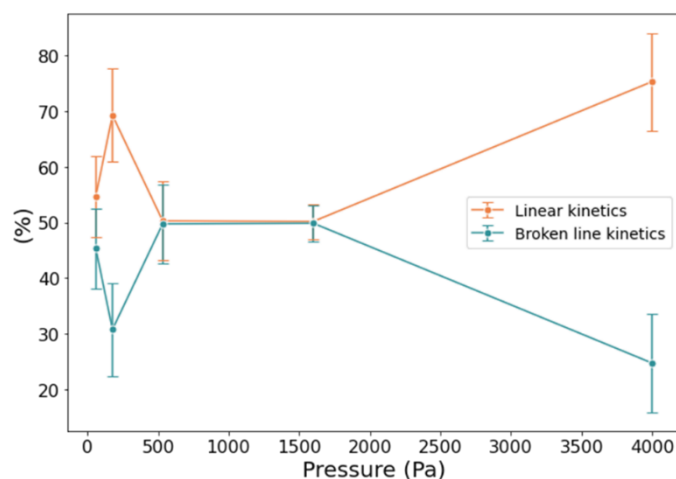


Figure 64 — Percentages of CNTs having linear and broken-line kinetics at each ethanol partial pressure. The statistical confidence interval at 95 % confidence (which depends on the number of measured CNTs) is shown for each value.

Table 7 — Number of CNTs with linear and broken-line kinetics grown at different partial pressures of ethanol.

Pressure (Pa)	Linear kinetics ( $N_{\text{tubes}}$ )	Broken-line kinetics ( $N_{\text{tubes}}$ )	Linear to broken-line ratio	Linear kinetics percentage (%)	Broken-line kinetics percentage (%)
4000	70	23	3.04	75.3	24.7
1600	473	470	1.01	50.2	49.8
533	95	94	1.01	50.3	49.7
177	81	36	2.25	69.2	30.8
59	99	82	1.21	54.7	45.3

The plot of the lifetime as a function of growth rate for the CNTs with linear growth at different partial pressures is shown in Figure 65 (a). Whatever the ethanol pressure, the inverse relation between the growth rate and lifetime is preserved. Except for the highest pressure (4000 Pa), the growth rate shows a decreasing trend with decreasing pressure, while the lifetime, on the contrary, increases with decreasing ethanol partial pressure (Figure 65 (b, c) black dashed curves). It supports again that growth and deactivation share a common step, e.g. high carbon supply causes faster growth but may also lead to a higher probability of integrating an unhealed topological defect causing abrupt CNT closure.

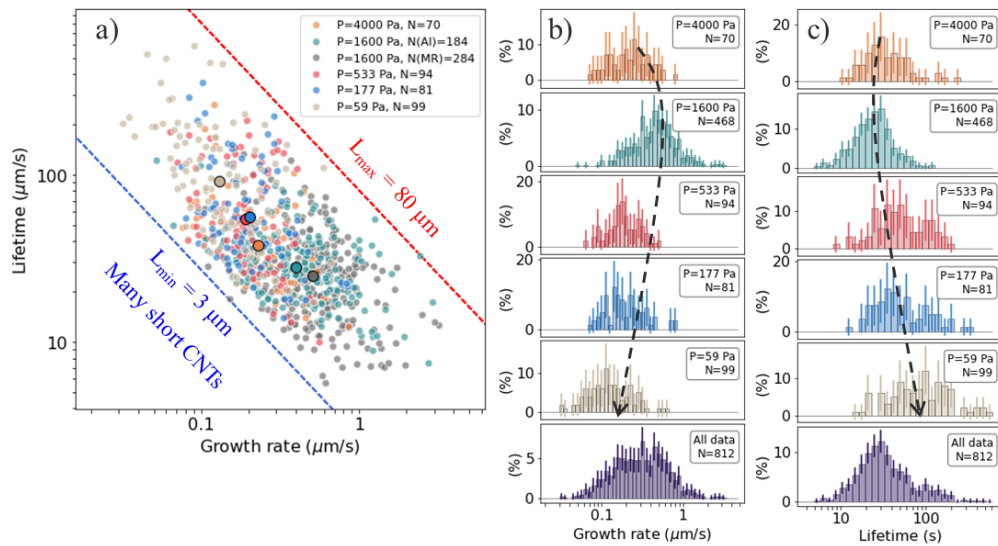


Figure 65 — CNTs grown with linear kinetics at different partial pressures of ethanol ( $T = 850 \text{ }^\circ\text{C}$ ).  
 a) Dependence of the lifetime on the growth rate . The big dots with black edges show the centers of distribution for each partial pressure. b,c) Distributions of growth rates (b) and lifetimes (c) at different ethanol pressures and their sum.

In the case of broken-line kinetics, we keep observing two elongated clouds of points corresponding to an average proportionality factor of about 1.7 and 1/1.7 for increase and decrease of growth rates, respectively (Figure 67 (a)). We note however that, except for the highest pressure (4000 Pa), the proportionality factor tends to increase with increasing pressure, (Figure 67 (b, c)). The percentage of growth rate increases is about 80 % and remains constant (i.e. in the same 95 % confidence interval) whatever the ethanol pressure (Table 8) and (Figure 66).

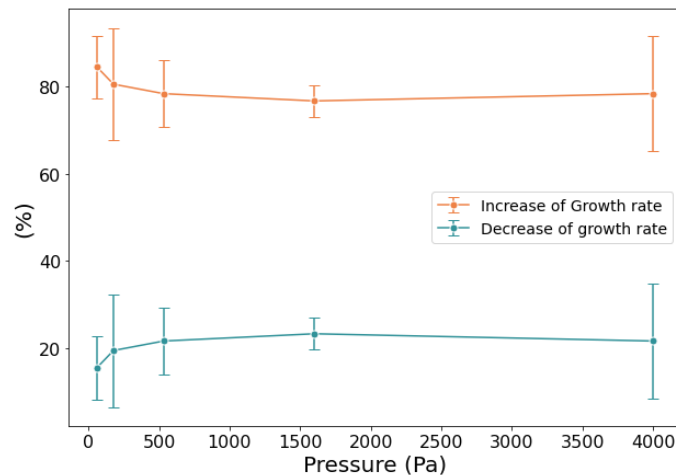


Figure 66 — Percentage of growth rate increase and decrease events at each ethanol partial pressure. The statistical confidence interval at 95 % confidence (which depends on the number of measured CNTs) is shown for each value.

Table 8 — Number of transitions towards increase or decrease of growth rates at different ethanol partial pressures.

Pressure (Pa)	Increases of growth rate ( $N_{\text{transitions}}$ )	Decreases of growth rate ( $N_{\text{transitions}}$ )	Ratio of number of growth rate increases to decreases	Increases percentage (%)	Decreases percentage (%)
4000	29	8	3.62	78.4	21.6
1600	392	119	3.29	76.7	23.3
533	87	24	3.62	78.4	21.6
177	29	7	4.14	80.6	19.4
59	82	15	5.47	84.5	15.5

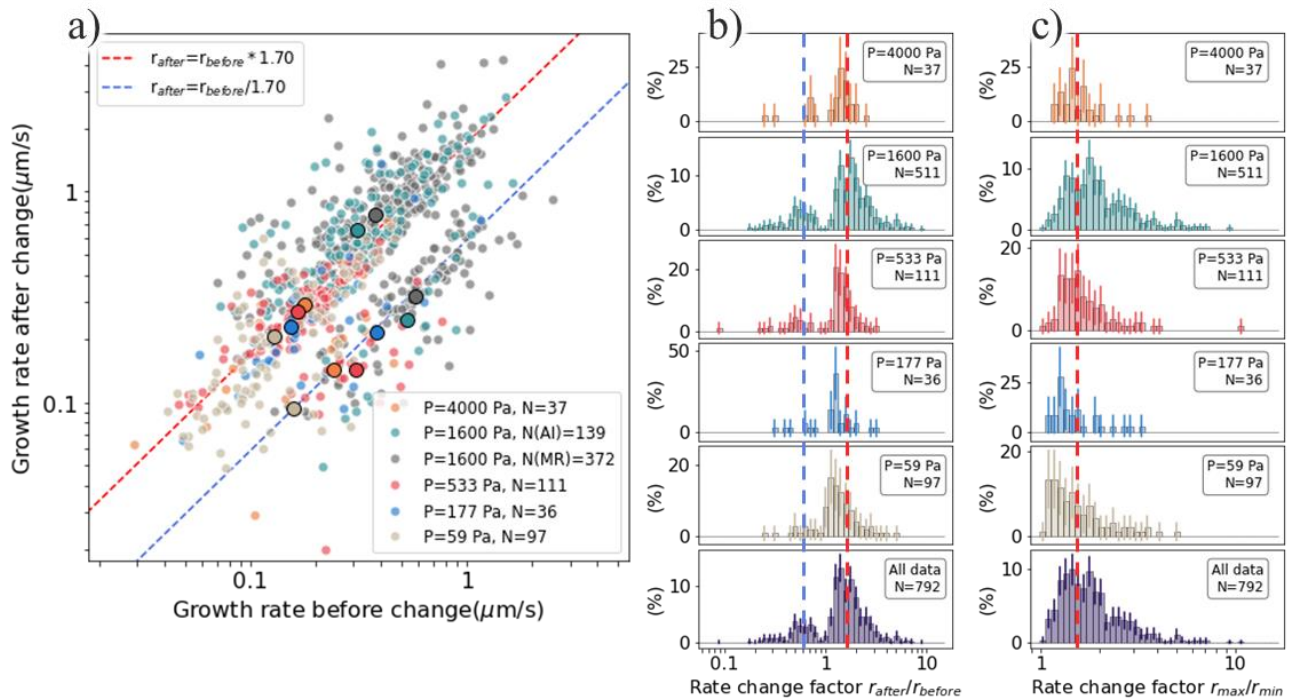


Figure 67 — a) Correlation plot of growth rates after and before change for different ethanol pressures ( $T= 850\text{ }^{\circ}\text{C}$ ). The big dots with black borders corresponds to the centers of distribution for each ethanol partial pressure for increase (top) and decrease (bottom) events. b) Distributions of the rate change factor and c) of the ratio of high to low growth rates. Red and blue dashed lines corresponding to proportionality factors of 1.7 and 1/1.7, respectively.

## 6.2.2 Reaction order

The availability of growth rate data at different pressures makes it possible to determine an apparent reaction order to characterize the dependence of growth kinetics on ethanol concentration. For this will be used the following kinetic equation:

$$\ln v = \ln A - \frac{E_a}{kT} + n \ln \frac{P}{P_0} \quad (28)$$

where  $A$  is the pre-exponential factor of Arrhenius law,  $E_a$  is the activation energy,  $k$  is the Boltzmann constant,  $n$  is the reaction order and  $P/P_0$  is the ethanol partial pressure normalized to 1 bar. From equation 28, one expects that the kinetics exhibits a power law with pressure and an Arrhenius behavior with temperature.

It can be seen that the calculated reaction orders are nearly the same whatever the type of kinetics (linear, broken line (fast, slow)), and approximately equal to 0.31. As a consequence, kinetic data will be used without distinction in the following (Figure 68 (a)).

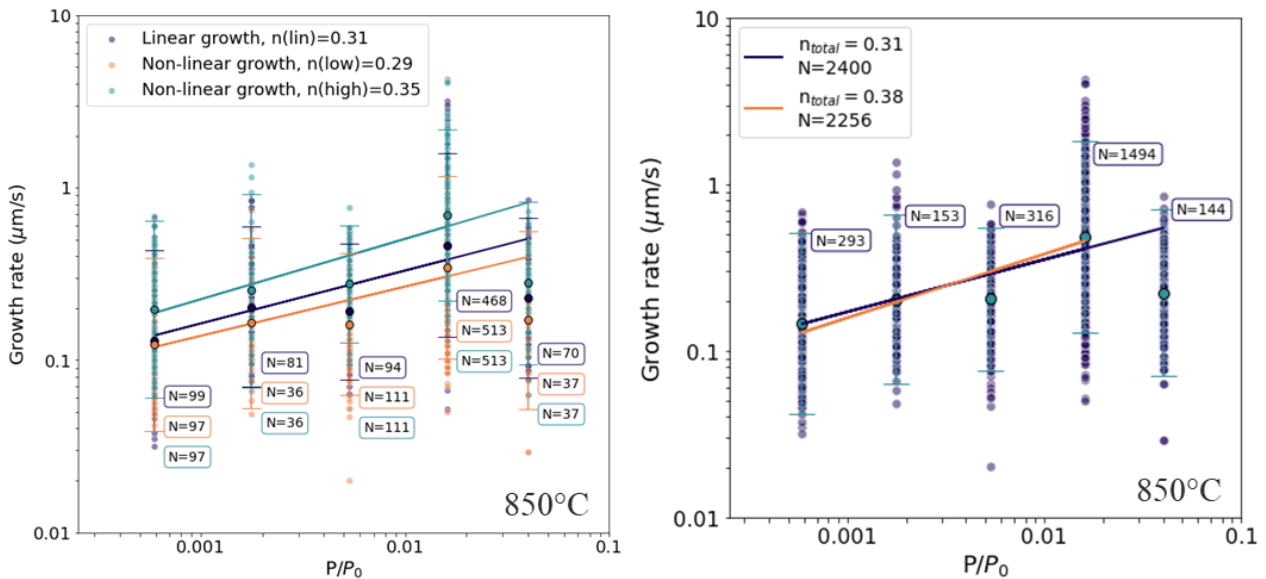


Figure 68 — Dependence of the growth rate on the normalized partial pressure a) with division into groups depending on their growth kinetics and b) for all CNTs without distinction. On the panel (a) are shown the growth rates corresponding to the linearly grown nanotubes and for broken-line growth, split in two subsets highest and lowest rates in the transitions. The big dots with black edges corresponds to mean values of the clouds and the whiskers correspond to 95% confidence intervals. Lines corresponds to the linear fits of the data and text in the boxes on the right from the scatters corresponds to the number of dots in the population.

The highest pressure (4000 Pa) displays an apparent decrease of the growth rate, which is a rather unexpected result. This may be the sign that the system changes at too high pressure (*e.g.*

change of nanotube structure or of catalyst phase). If this pressure is omitted, the reaction order is 0.38, compared to 0.31 for the entire dataset (Figure 68 (b)).

Non-integer reaction orders are characteristic of complex chemical reactions proceeding in several steps. A reaction order of  $0.6 \pm 0.03$  was previously reported by Wirth *et al.* for CNT synthesis using the Fe-acetylene system (218). They modeled nanotube growth as two consecutive steps: dissociative adsorption of acetylene at the catalyst surface and diffusion of free carbon atoms through or over the nanoparticle surface. They showed that a fractional reaction order of 0.5 could theoretically arise from a pre-equilibrium during the first step, while the second step was reported to be the limiting one for the CNT growth rate (218).

A similar mechanism may be invoked to account for the non-integer reaction order we measured. However, the process is probably more complex than in the case of acetylene since the catalytic decomposition of ethanol can proceed in many different pathways with the formation of different intermediates including etchants such as H<sub>2</sub>O (219, 220). Thus, a direct description of the reaction process is difficult. However, the fact that the reaction order remains similar for the different types of kinetics (linear, highest rate, lowest rate) allows to conclude that the chemical process of catalytic decomposition of ethanol is probably similar whatever the type of kinetics.

### **6.3 Temperature dependence**

In this section, all syntheses were performed at an ethanol partial pressure of 533 Pa but at different temperatures ranging from 800 to 900 °C.

#### **6.3.1 Growth kinetics**

Based on a reasonable interval of statistical confidence (95 %), the ratio of linear versus broken-line kinetics tends to slightly increase (from about 1.37 to about 2.6) with increasing temperature (Table 9) and (Figure 69).

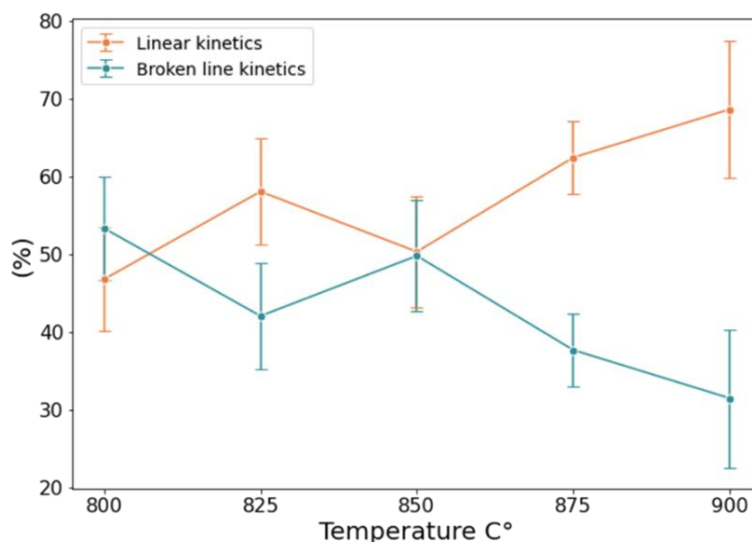


Figure 69 — Percentages of CNTs having linear and broken-line kinetics at each temperature. The statistical confidence interval at 95 % confidence (which depends on the number of measured CNTs) is shown for each value.

Table 9 — Number of CNTs with linear and non-linear kinetics at different temperatures.

Temperature (°C)	Linear kinetics (N <sub>tubes</sub> )	Broken-line kinetics (N <sub>tubes</sub> )	Linear to broken-line ratio	Linear kinetics percentage (%)	Broken-line kinetics percentage (%)
800	100	114	0.88	46.7	53.3
825	116	84	1.38	58.0	42.0
850	95	94	1.01	50.3	49.7
875	252	152	1.66	62.4	37.6
900	72	33	2.18	68.6	31.4

As previously observed as a function of ethanol pressure, the CNTs with linear kinetics, preserve and extend the anticorrelation between lifetime on growth rate (Figure 70 (a)). At the same time, with increasing temperature, the growth rates tend to increase and the lifetimes to decrease (Figure 70 (b, c)). The trend is stronger than that observed as a function of the ethanol partial pressure (Figure 65).

In the case of broken-line growths, the average proportionality factor of 1.7 is still observed for the increase and 1/1.7 for decrease of growth rate regardless of the synthesis temperature (Figure 72 (a, b)). A slight tendency of the growth rate ratio to increase with increasing temperature may be observed (Figure 72 (b, c)). Note that, contrary to the data at (850 °C, 1600 Pa), the statistics at each

temperature are too low to discuss the possibility of a substructure. The percentage of increase events diminishes drastically from about 83% to about 44% with increasing temperature (Table 10) and (Figure 71).

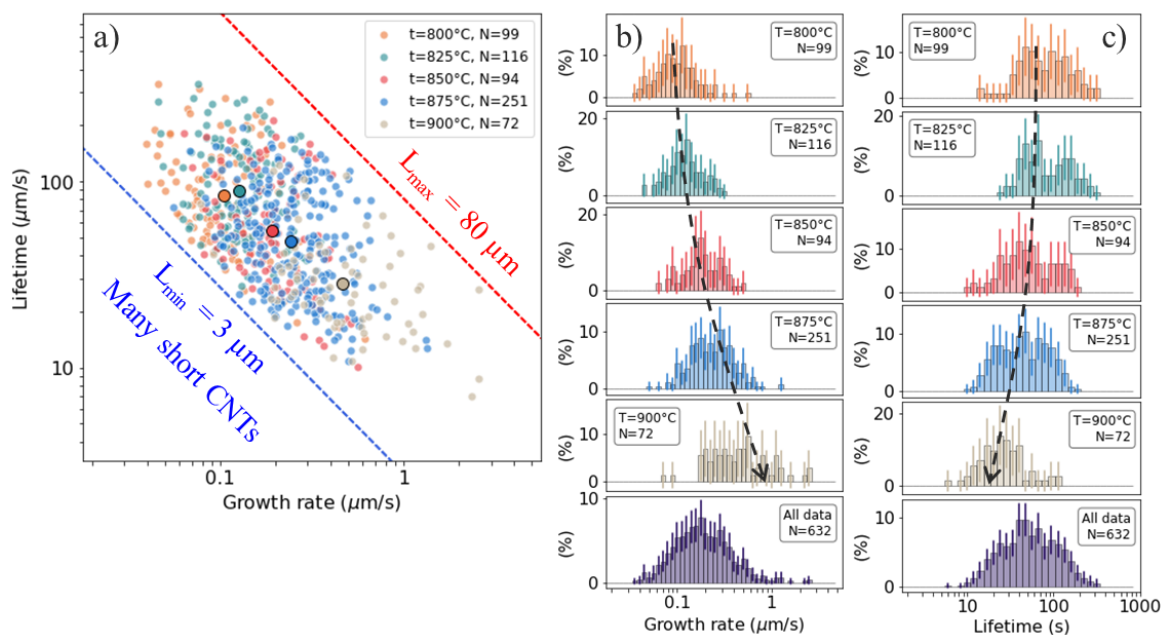


Figure 70 — CNTs with linear kinetics. a) Dependence of lifetime on growth rate for CNTs synthesized at different temperatures ( $P_{\text{ethanol}} = 533 \text{ Pa}$ ). The big dots with black edges corresponds to the centers of distribution of subsets of data. The distributions of b) growth rates and c) lifetimes for CNTs grown at different temperatures, as well as their sum.

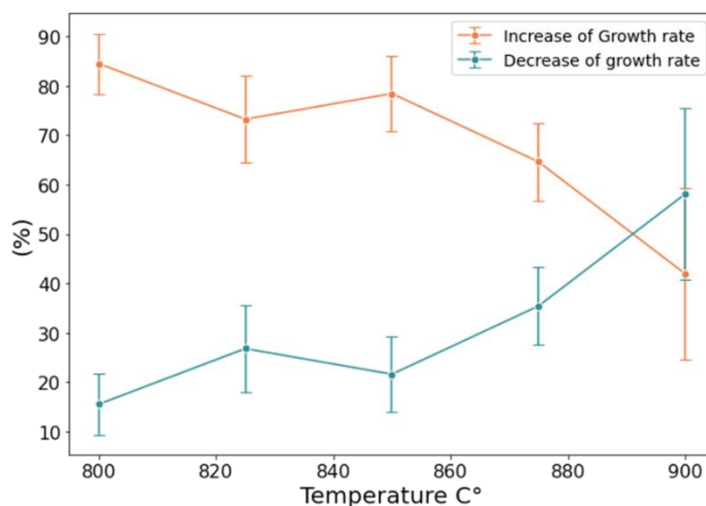


Figure 71 — Percentages of growth rate increase and decrease events at each temperature. The statistical confidence interval at 95 % confidence (which depends on the number of measured CNTs) is shown for each value.

Table 10 — The number of transitions towards the increase and decrease of growth rate at different temperatures.

Temperature (°C)	Increase of growth rate (N <sub>transitions</sub> )	Decrease of growth rate (N <sub>transitions</sub> )	Ratio of number of growth rate increases to decreases	Increases percentage (%)	Decreases percentage (%)
800	114	21	5.43	84.4	15.6
825	71	26	2.73	73.2	26.8
850	87	24	3.62	78.4	21.6
875	93	51	1.82	64.6	35.4
900	13	18	0.72	41.9	58.1

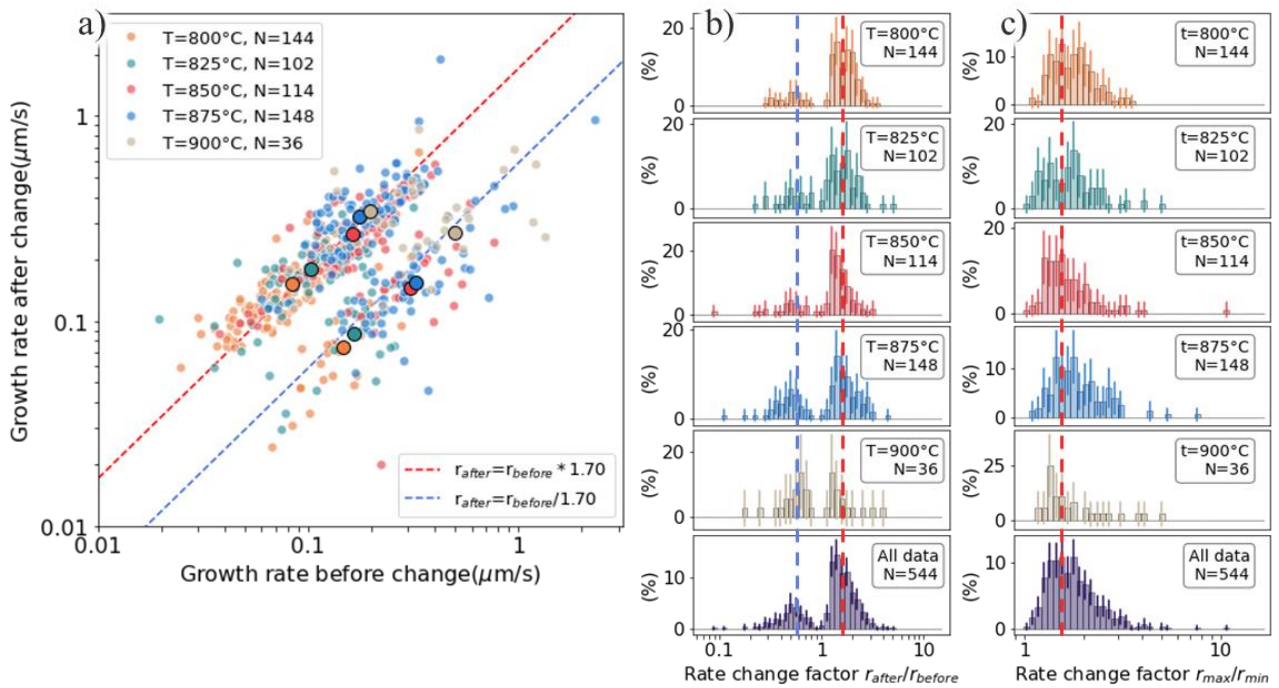


Figure 72 — a) Correlation plot of growth rates after and before change for CNTs synthesised at different temperatures ( $P_{ethanol} = 533$  Pa). Big dots with black edges corresponds to the centers of distributions for increase (upper) and decrease (lower) of growth rates. b) Distributions of rate change factors and c) ratio of high to low growth rates. Red and blue dashed lines shows the proportionality factors of 1.7 and 1/1.7, respectively.

### 6.3.2 Activation energies

Using the temperature dependence of the growth rates it is possible to extract the activation energy assuming an Arrhenius law (Figure 73).

Activation energies appears to be the same for high and low growth rate regimes (1.11 eV). The activation energy for linear growth seems slightly higher (1.47 eV) but their growth rates are intermediate between low and high ones: this suggest that more linear growth CNTs tend to start and remain in the “high rate” regime with increasing temperature and, as a consequence, less transitions toward increase of growth rate are observed. This shift would cause an apparently higher activation energy (Figure 73).

The value of the activation energy can provide insights about the reaction mechanism, the limiting step and the catalyst state during the growth. The value measured, in the order of 1.1 eV, is lower than the values of bulk diffusion of carbon through fcc-Fe (1.53-1.57 eV and iron carbide (1.60-1.92 eV in Fe<sub>3</sub>C) but in the order of that in bcc Fe (0.83 eV) (221). This suggests that during synthesis catalyst contains a mixture of different states of Fe nanoparticles. Moreover, it is currently not possible to exclude surface diffusion (which usually displays lower activation energies that in bulk solid). Bartsch *et al.* reported activation energies of 0.3-0.6 eV for MWCNTs grown at temperatures of 900-1100°C, which they assigned to diffusion through liquid iron (222) but the value we measured is significantly higher. Ethanol decomposition and carbon integration at the nanotube edge are other possibilities. The fact that the activation energy is the same in the slow and fast regimes is in favor of the latter since carbon integration is the only step where a change of pre-factor with no change in the activation energy (due to a change in the edge configuration) may be envisioned. Detailed kinetic modeling also including the reaction order (see below) would be needed to discriminate between the different options.

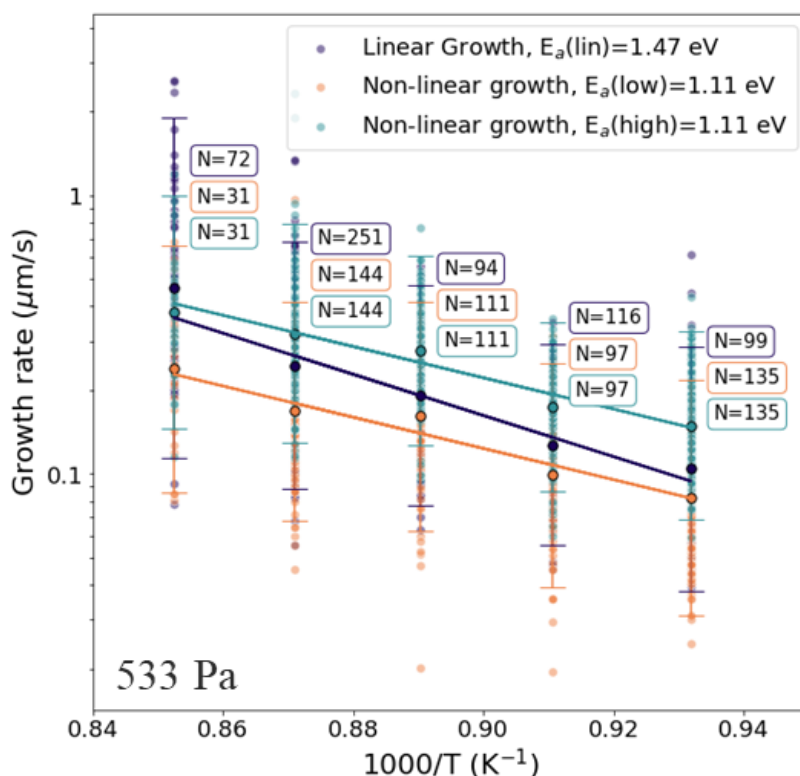


Figure 73 — Arrhenius plots for CNTs synthesised at partial pressure of ethanol of 533 Pa. Growth rates correspond to linearly grown CNTs, and to lowest and highest growth rate in the transition. Big points with black edge corresponds to the means of distributions and whiskers shows the 95 % confidence intervals. The lines corresponds to linear fits, used to extract activation energy. Numbers in the boxes on the right from the clouds corresponds to the number of points in each distribution.

Arrhenius law also contains a pre-exponential term proportional to the number of the collisions of molecules with configuration suitable for the reaction, which is also called the frequency factor. For nanotubes this term could also describe the number of configurations suitable for the growth of a given  $(n, m)$  nanotube (configuration degeneracy) in the configuration entropy models developed by Bichara *et. al.* (126, 130). In our case, it can be derived from equation 28 and the intersections of the Arrhenius plots (Figure 73) using the following expression:

$$A = \exp\left(\text{intercept} - n \ln \frac{P}{P_0}\right) \quad (29)$$

Since two values of reaction orders were found (Figure 73), two different sets of frequency factors were calculated (Table 11). The pre-exponential factor of linearly grown CNTs is significantly higher than that of broken-line growths (high or low rates). However the data in Figure 73 suggests that linear growth it is not a particular growth mode, but one of these two modes (high or low) with a percentage varying with temperature. Therefore, the pre-exponential factor and activation energy for linear growths can probably not be directly interpreted. In contrast, the values for broken-line growths are of interest and may be directly compared with those expected from theoretical models.

Table 11 — Pre-exponential factors for the different types of CNT growth kinetics (Figure 73).

Activation energy	Value (eV)	Intercept	Pre exponential factor (n=0.31)	Pre exponential factor (n=0.38)
$E_{a(tin)}$	1.47	13.49	$3.66 \cdot 10^6$	$5.27 \cdot 10^6$
$E_{a(high)}$	1.11	10.11	$1.25 \cdot 10^5$	$1.80 \cdot 10^5$
$E_{a(low)}$	1.11	9.52	$6.88 \cdot 10^4$	$9.92 \cdot 10^4$

#### 6.4 Other catalysts

Although my project focused on work only with a system of Fe-ethanol, several other catalysts were also tested by our group. The syntheses were part of Eira Zamudio Medina's master internship and its main goal was to find optimal conditions for CNT growth. During that work were screened a wide range of different catalysts (Pt, W, Mo, Co, FeRu, Ni), and wide variety of temperatures and pressures (750-950°C and 1600-19.7 Pa). For Ni, FeRu and Co we were able to find conditions suitable for the syntheses, as well as to make a video and analyze them (Table 12). In total kinetics were collected from 7 samples (3 for Ni, 2 for FeRu and 2 for Co).

Table 12 — The list of catalysts, synthesis conditions and number of CNTs with linear and broken-line growths.

Catalyst	Temperature °C	Ethanol Pressure (Pa)	Linear kinetics	Broken-line kinetics
Co	800	1600	3	3
Co	825	1600	-	1
FeRu	850	533	1	-
FeRu	900	177	2	2
Ni	850	266	19	7

In the case of linear growths, for all three catalysts the anticorrelation dependence between growth rate and lifetimes is preserved. In the case of Ni, we can observe a large scatter of growth rates and lifetimes, almost comparable to the data for Fe. Co and FeRu show smaller distribution in the data and quite similar behavior (Figure 74). However, the number of CNTs with measured kinetics for these two catalysts does not allows us to make any solid conclusion yet.

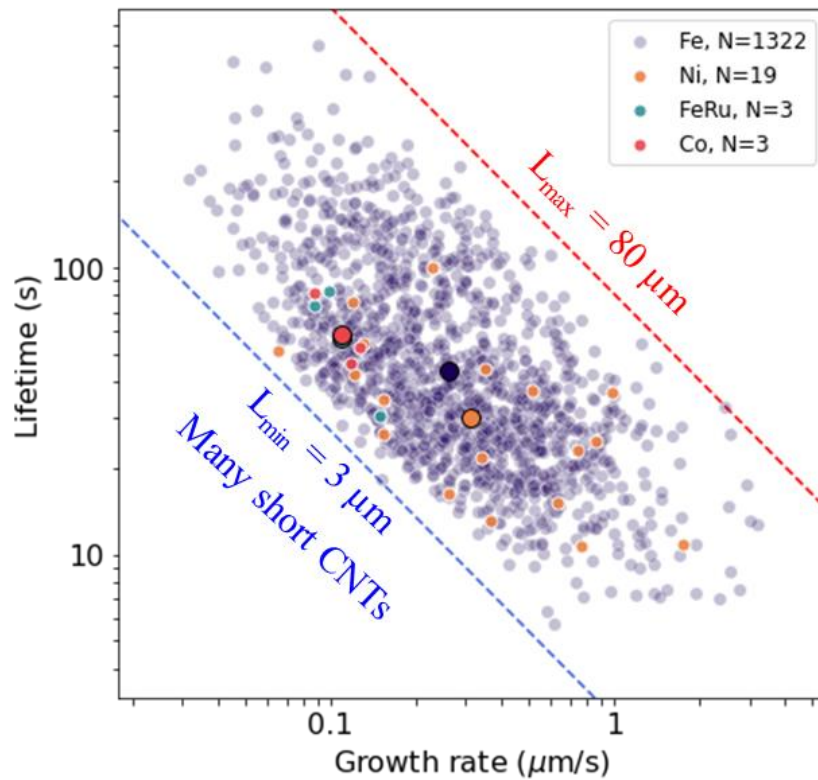


Figure 74 — Dependence of the lifetime on the growth rate for CNTs synthesized with different catalysts. The big dots with black edges corresponds to centers of the distributions. Blue and red dashed lines corresponds to the CNT lengths of 3 and 80  $\mu\text{m}$ , respectively.

As with iron, growth rate changes were also observed in the case of Ni, Co and FeRu: this demonstrates that dynamic instability is not restricted to a specific catalyst but appears to be a general behavior. For broken-line growths, average rate proportionality factors of 1.7 and 1/1.7 are observed, as for Fe, although more statistics are needed to validate this conclusion. In contrast to Fe a higher percentage of rate decrease events seems to be observed in the case of Ni and FeRu (8 decreases against 2 increases for Ni and 2 decreases versus 0 increases for FeRu). In all cases, more statistical data are required for drawing definitive conclusions.

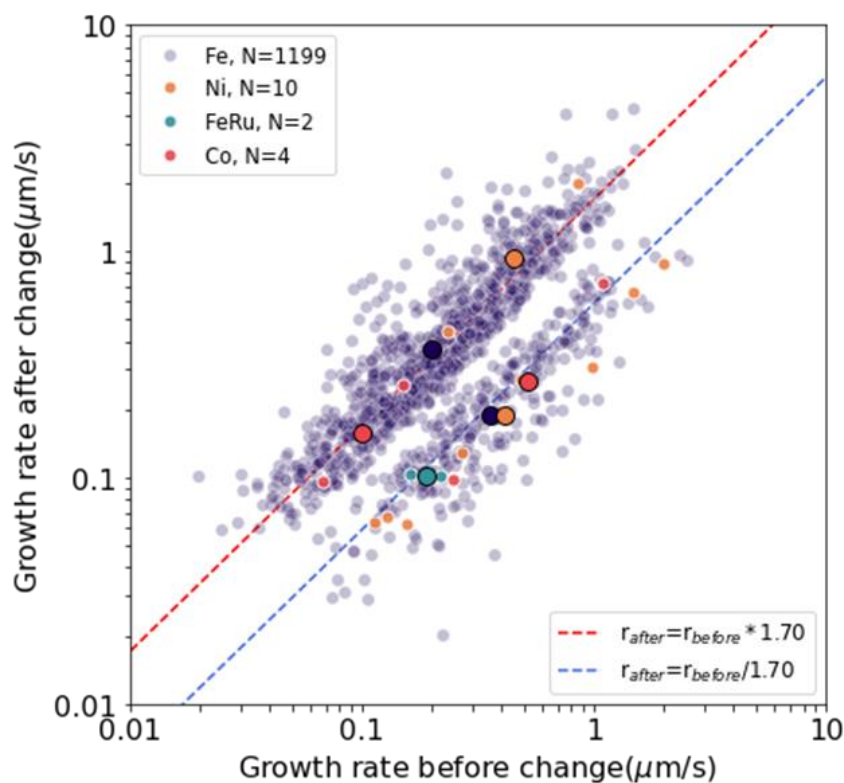


Figure 75 — Correlation plot of growth rates before and after change for different catalysts. The big dots with black edges corresponds to the centers of distributions for increases (top) and decreases (bottom) of growth rates.

## 6.5 Conclusion

Analyzed videos of horizontally aligned CNTs grown on quartz revealed a complex kinetic behavior even for nanotubes synthesized in stable conditions of temperature and precursor supply. About half of CNTs displayed a constant growth rate all along their growth lifetime. Almost half of the CNTs demonstrated stochastic switches of growth rates which in some cases can be accompanied by a change of structure. The existence of different growth rates even for nanotubes of the same chirality was also evidenced.

Moreover, the general nature of the growth dynamic instability was confirmed by the kinetic data collected at different temperatures, partial pressures and with different catalysts. An unexpected result in the case of broken-line growths was that the rate change ratio tends towards a similar average factor of 1.7 whatever with or without chirality change. This average factor also displays no or little dependence with the temperature, precursor pressure or type of catalyst. Interestingly, a similar value was reported by another group for CNTs grown after a pause under water exposure, which suggests a similar mechanism despite different conditions (140). The independence from growth conditions

and catalyst type suggests that the growth rate ratio may be an intrinsic feature of the nanotubes themselves such as, for instance, the total number of possible edge configurations for each (n, m) nanotube.

The analysis of the growth kinetics (reaction order, activation energy) suggests the same reaction mechanism whatever the type of kinetic behavior. However, the Arrhenius plots suggest that linear growth cases are actually a mixture of CNTs having grown only in either the slow or fast growth regime and with proportions varying with temperature.: this interpretation is favored by the changes of the linear rates from near-low to near-high with the increase of temperature (Figure 73). The pre-exponential factors for slow and fast regimes have a ratio of around 1.7 which might of interest for comparison with theoretical models such as that of Bichara et al. based on edge configuration degeneration (130).

# Chapter 7.

## Etching and pauses

In addition to linear and broken-line growths, we also observed switches between growth and shrinkage (Figure 76 (a)). Such switches can occur after either linear or broken-line growths (Table 13). Moreover, pauses (with durations from about 1 to 100 seconds) may occur between two growth stages, between growth and shrinkage or between two shrinkage stages (Table 13) (Figure 76 (b, c)). In rare cases (about 2 % of the total number of cases with broken-line kinetics), multiple stochastic switches between growth, shrinkage, and regrowth were even observed (Figure 76 (c)).

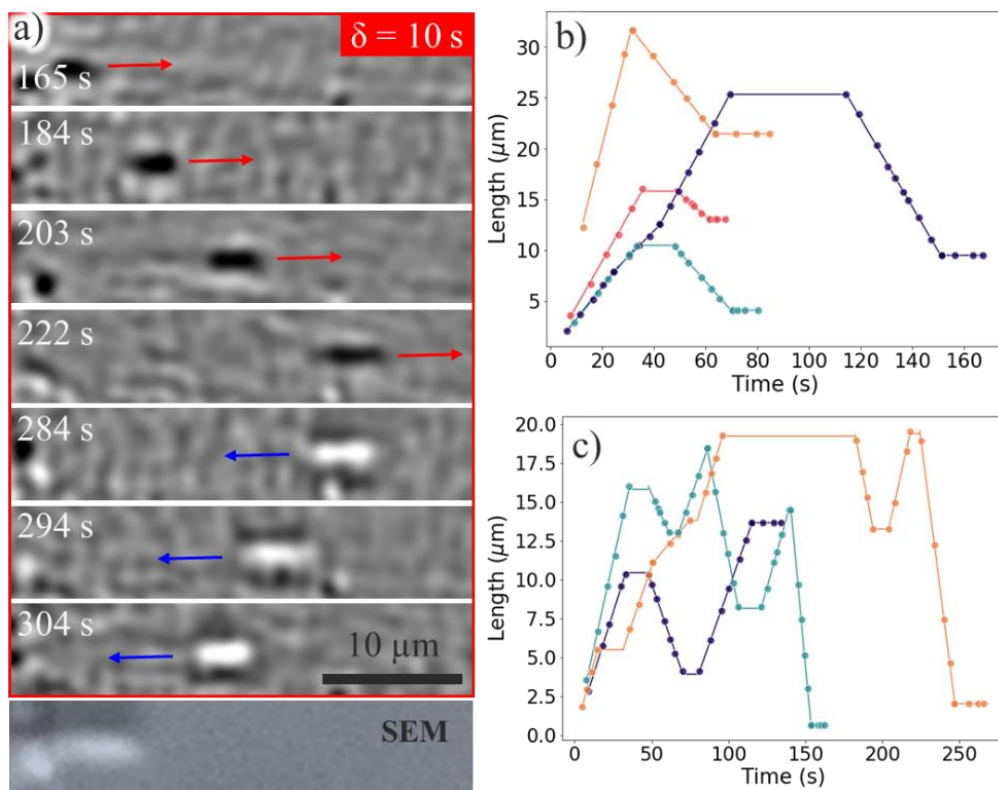


Figure 76 — a) Snapshots from a video showing a switch from growth to shrinkage (top), as well as the SEM picture of the remaining segment. b) Kinetic curves of similar cases. c) Examples of multiple switches between growth, pause and shrinkage.. In panels (b, c) the time scales correspond to the time from the beginning of growth (i.e. the nucleation time of each nanotube was subtracted for easier viewing).

Nanotube shrinkage is manifested on differential videos as a change in direction of the translating segment along with an inversion of its contrast (Figure 76 (a)). In the case of CNTs having previously had a change in structure, the contrast of all segments is inverted. Observations of such examples confirm that the shrinkage does not occur from the tip of the CNT, but proceeds from the open edge at the interface with the catalyst particle. I recall that in the conditions we used, we have a base-growth mechanism (i.e. the catalyst remains fixed while the CNT slides on the substrate) as evidenced by the chirality change cases (see Figure 62 (c)). To differentiate this etching from the catalyst tip from homogeneous etching (all along the CNT), we will refer to it as catalytic etching in agreement with the term previously used by Koyano et al (140).

Table 13 — Number and percentage from overall number of CNTs of linearly and broken-line growth cases with shrinkage and pauses.

	Number of cases with shrinkage	Number of cases with pause	Total number of cases
Linear kinetics	108 (7.9%)	62 (4.5 %)	1358
Broken-line kinetics	123 (11.3%)	245 (22.5 %)	1088

Since shrunk CNTs are often completely etched, *ex situ* analyses of their structure are often not possible. Nevertheless, we can analyze the kinetics of CNTs that have been etched or grown with pauses. In the following, five types of transitions will be taken into consideration:

1. Transition from growth to shrinkage (Shrinkage)
2. Transition from shrinkage to growth (Regrowth)
3. Transitions between etching rates (ER changes)
4. Change of structure with a pause in between (Change of structure with pause)
5. Growth rate changes with a pause but no structure change (GR changes with pause)

## 7.1 Pressure dependence

The percentages of cases displaying shrinkage tend to increase with increasing the partial pressure of ethanol from 2% to about 10% at pressure of 1600 Pa with further decrease at higher pressure (Figure 77 (a)). In addition, the number of transitions accompanied by pauses also increases from about 5% to about 18% at the pressure of 1600 Pa (Figure 77 (b)).

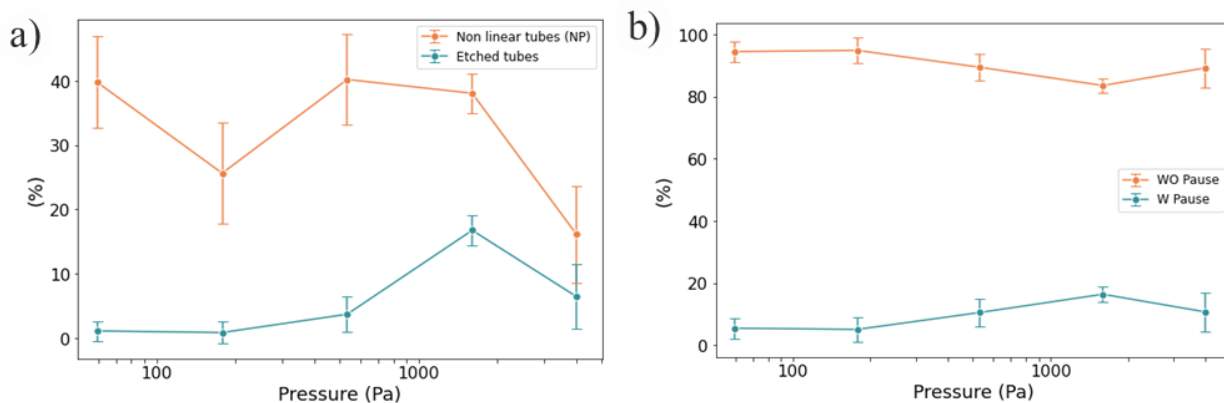


Figure 77 — Percentages of a) etchings and non linearly grown CNTs without pauses and b) and CNTs grown with and without pauses relative to the total number of CNTs. All syntheses were performed at 850°C.

### 7.1.1 Growth kinetics

In the case of switches between growth and shrinkage, we can observe a weak linear trend with a ratio of 1 between the subsequent etching rate and the preceding growth rate, with or without pause in between (Figure 78 (a)).

As a consequence, the distribution of the ratio of rate change between growth and etching displays a peak at a value close to 1, (Figure 78 (b)). There is currently not enough data to determine how this dependence may evolve with the partial pressure of ethanol.

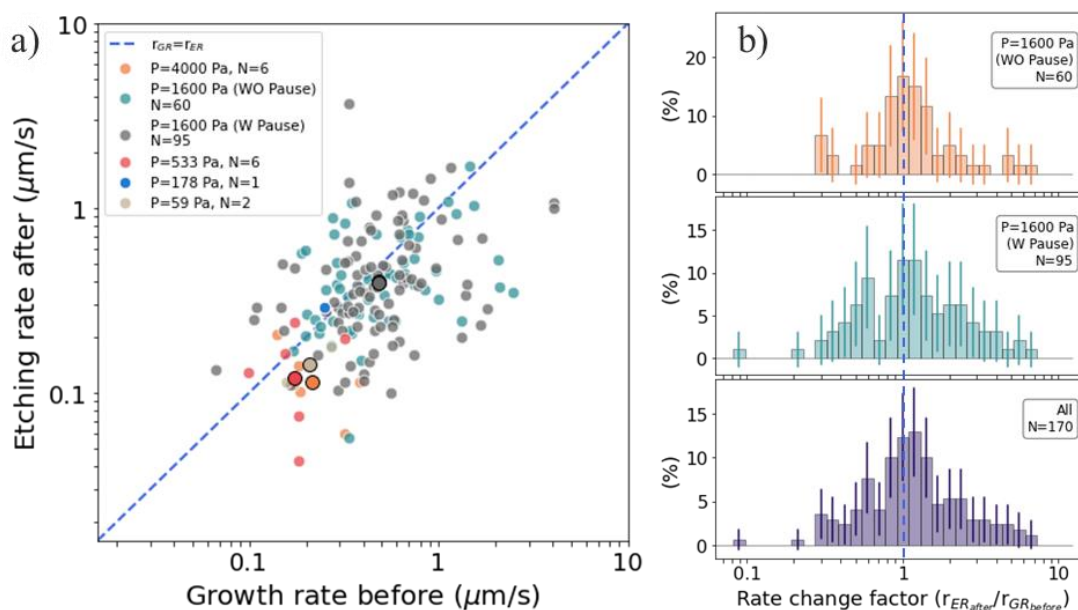


Figure 78 — a) The plot of the ratio of the rate increase to the rate decrease in the transition to shrinkage at different partial pressures of ethanol, as well as with and without pauses. The large points with black borders correspond to the centers of distributions. b) Distributions of ratios of

growth and etching rates at the transition to shrinkage for CNTs grown with and without pauses as well as for all CNTs. The blue dashed lines correspond to the ratio of growth and decay rates equal to 1. The purple and orange arrows indicate possible peaks of the substructure. All syntheses were performed at 850°C.

The number of transitions from etching to growth in our statistics is small but is shown for the sake of completeness (Figure 79 (a)). The trend is the same as before for the inverse transition with a distribution of rate ratios displaying a prominent peak at a value close to one (Figure 79 (b)).

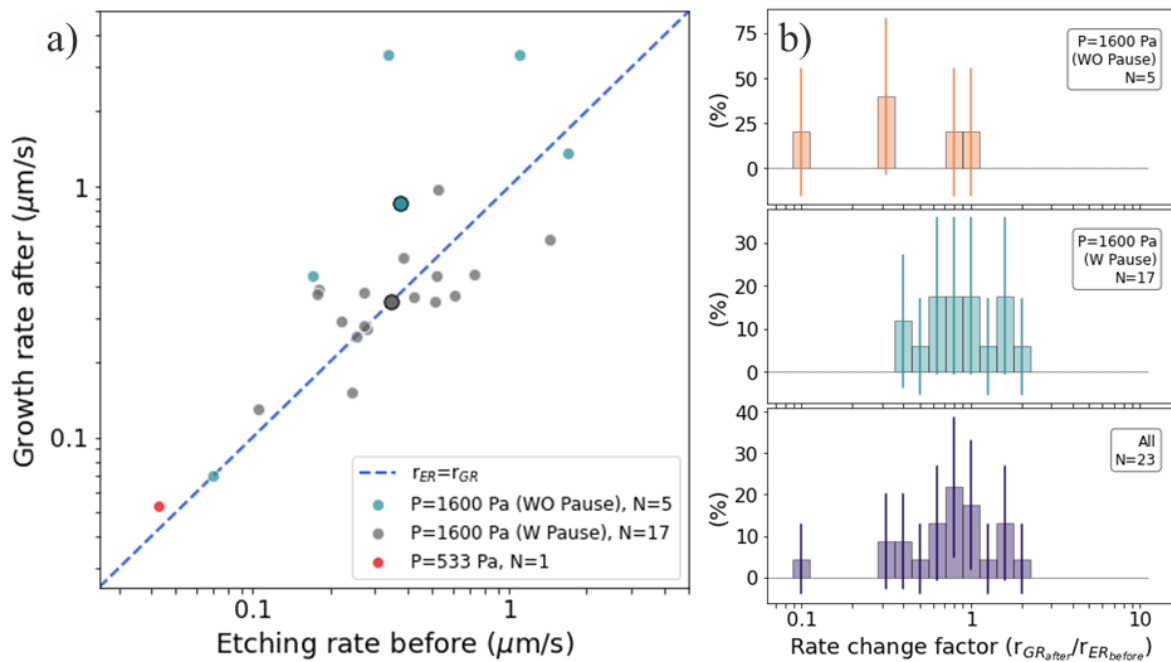


Figure 79 — a) Ratios of the growth to etching rates in the transitions from shrinkage to growth as well as b) distributions for transitions with and without pauses. All syntheses were performed at 850°C.

Besides changes in growth rates, changes in etching rates are also possible (Figure 80 (a)). In this case, the rate change factor also has peaks in the distribution around values equal to 1.7 for the rate increase and 0.6 for the rate decrease (Figure 80 (b)). This suggests that changes in etching rates have the same origin as those in growth rates. However, more data are needed to analyze the rate dependences of these transitions with and without pauses on the partial pressure of ethanol.

Another case requiring separate consideration is growth rate changes occurring with pauses (Figure 81 (a)). In contrast to growth rate changes without pauses, growth rate changes with pauses demonstrate a proportionality factor of  $\sim 1$ , instead of 1.7 and 1/1.7 (Figure 81 (b)): that is, in most cases, growth restarts at the same rate as before the pause. This suggests that pauses are not associated

with a change in the nanotube-catalyst configuration or that pauses correspond to extremely slow rates below the resolution of our experiments.

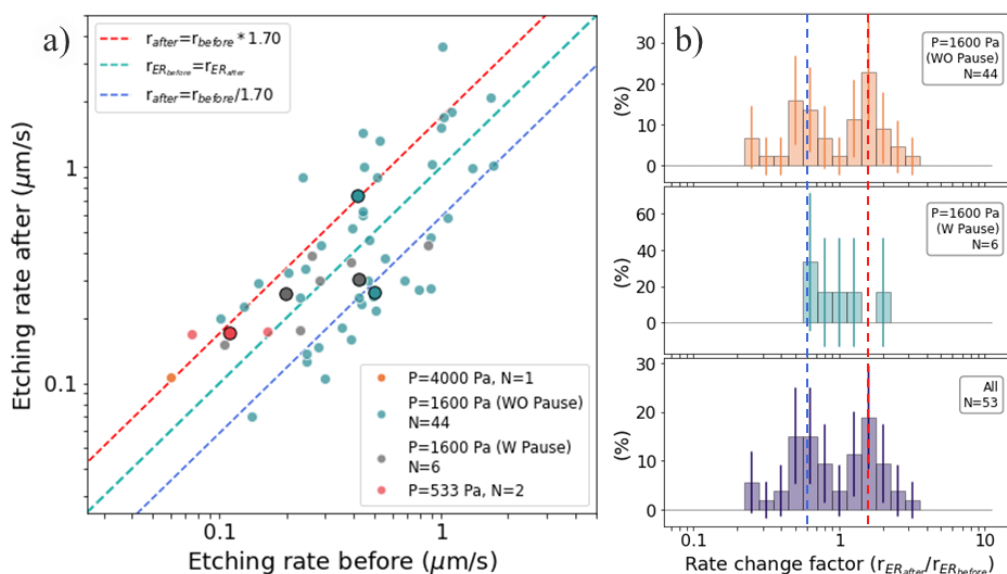


Figure 80 — a) Dependence of the shrinkage rate before and after the change for different partial pressures of ethanol, as well as b) distribution of the rate change factor for the transitions with and without pauses, and for all data. All syntheses were performed at 850°C.

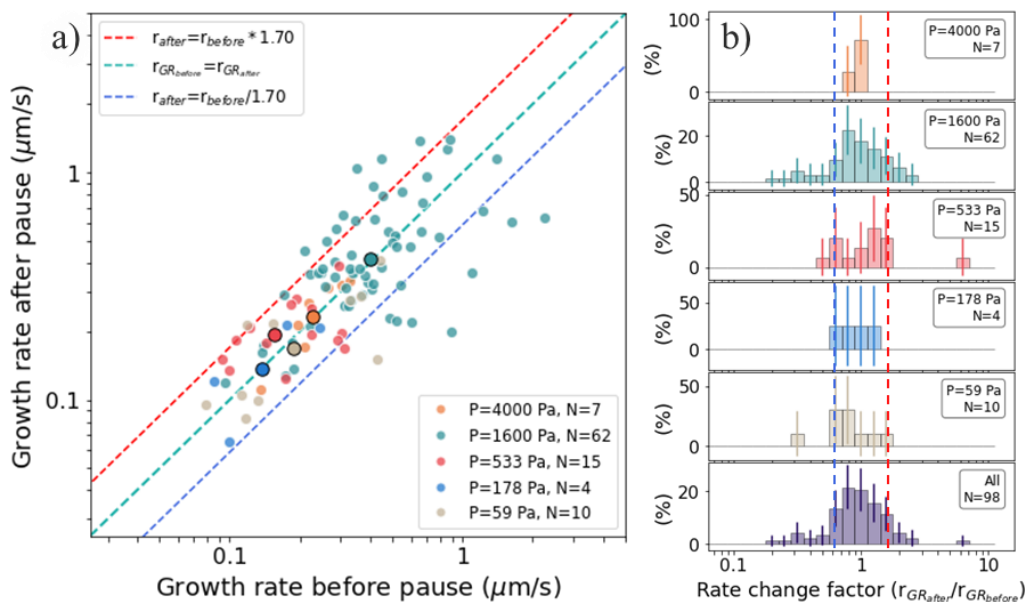


Figure 81 — a) The changes of growth rates of the CNTs growing with pauses at different partial pressures of ethanol, as well as b) the distributions of the ratio of growth rates before and after the transition. All syntheses were performed at 850°C.

### 7.1.1 Reaction kinetics

Analysis of changes in growth rates depending on the partial pressure of ethanol, as mentioned above, allows us to extract information about the orders of reactions using Equation 28. In the case of the transitions involving nanotube shrinkage, there is insufficient data to conclude on the influence of the precursor pressure on the rates (Figure 82).

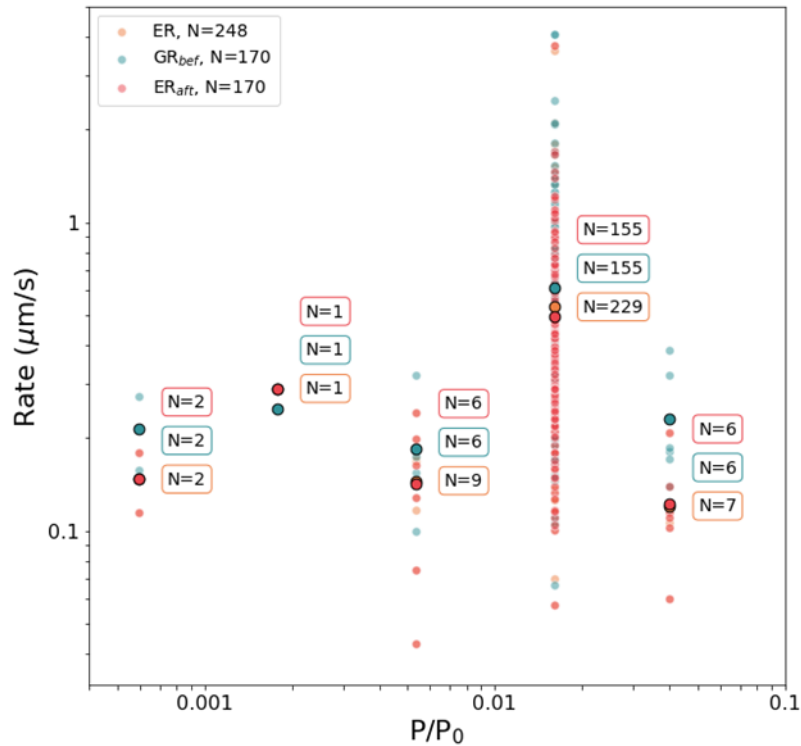


Figure 82 — The plot of the rates of nanotube shrinkage, as well as the growth and etching rates for the transition to shrinkage as a function of ethanol partial pressure. The large black-bordered dots show the mean values of the distributions, the color-bordered boxes to the right of the scatter clouds show the number of dots. The whiskers correspond to 95 % confidence intervals of mean values.

All syntheses were performed at 850°C.

### 7.2 Temperature dependence

All measurements in this chapter were performed at a partial pressure of ethanol of 533 Pa. The number of transitions depends nonlinearly on the temperature. The minimum number of almost all transitions is observed at 850° (Figure 83 (a)). Moreover, at the same temperature the percentage of transitions with pauses is minimal (Figure 83 (b)).

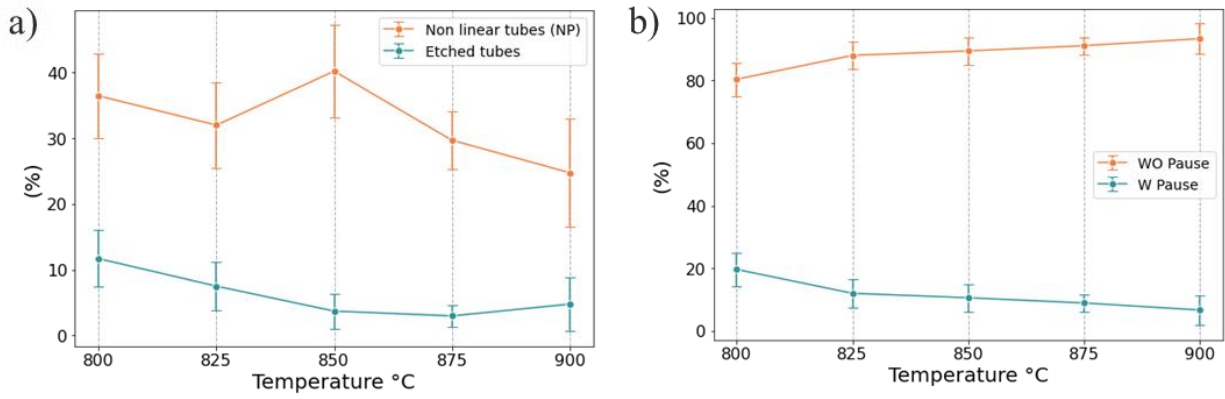


Figure 83 — Percentages of a) etchings and non linearly grown CNTs without pauses and b) and CNTs grown with and without pauses relative to the total number of nanotubes.

### 7.2.1 Growth kinetics

Since rates in the transition from growth to shrinkage behaves very similar with or without pause (Figure 84 (a)), they are considered together in the following. The data as a function of temperature are shown for the sake of completeness but conclusions cannot be drawn due to the insufficient amount of data (Figure 84 (b)). Also, concerning the transitions from shrinkage to growth, there are only three cases which prevents any statistical discussion.

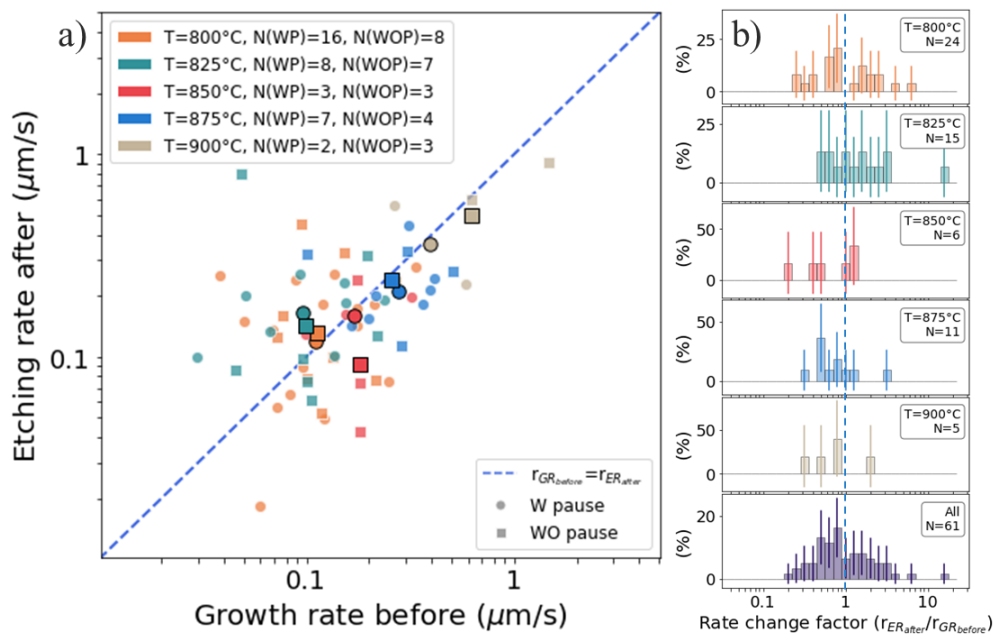


Figure 84 — a) Growth and shrinkage rates before and after transitions with and without pauses at different temperatures, as well as b) their ratios.

Growth rates before and after pauses show a clear tendency to increase with increasing temperature, in agreement with the observations for growths without pauses (Figure 85 (a)). The distribution of rate change factors displays several peaks, the largest being close to 1 although more data would be required to clearly resolve them (Figure 85 (b)).

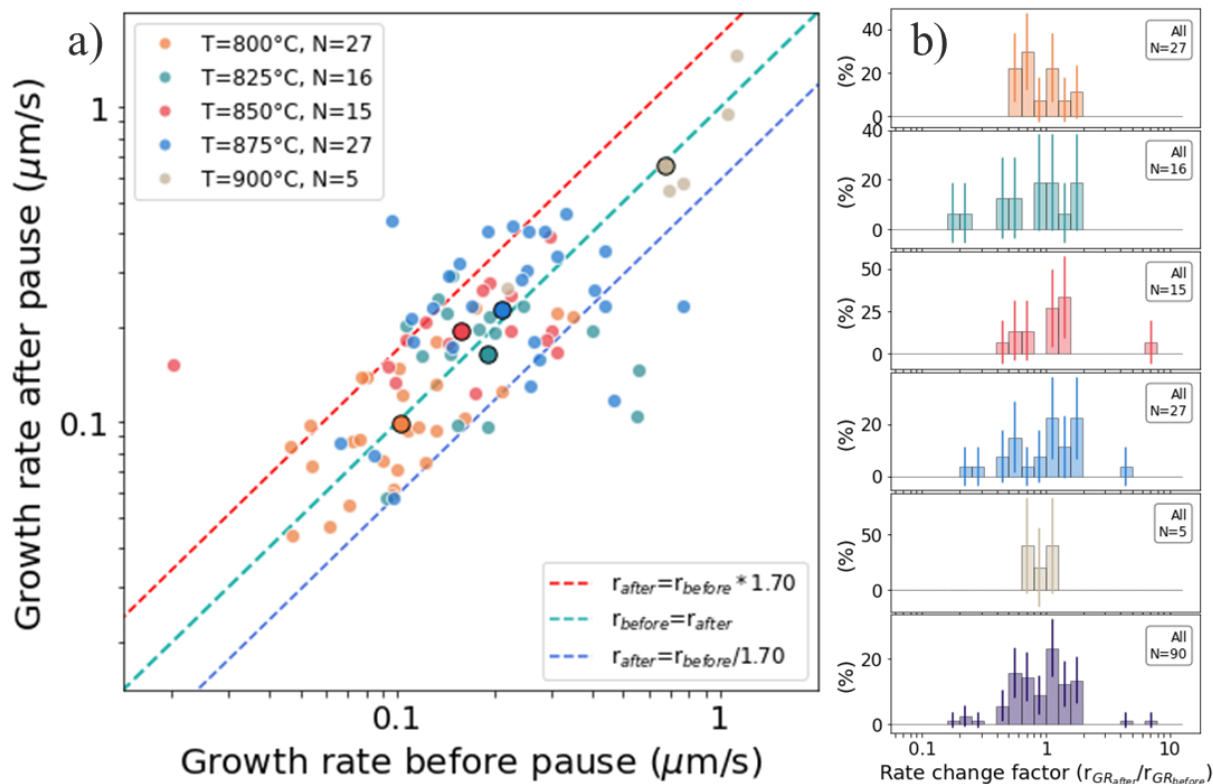


Figure 85 — a) Changes of growth rates of paused CNTs at different temperatures, as well as b) distributions of the ratio of growth rates before and after the transition.

### 7.2.1 Reaction kinetics

Concerning the influence of temperature on the etching rates, the data are limited but supports an increase of the etching rates with increasing temperature (Figure 86). This behavior may imply that at lower temperatures the shrinkage of the CNTs proceeds in a diffuse mode.

The changes in growth rates with pauses at different temperatures show similar behavior before and after transition, which allows us to consider them together (Figure 87 (a)). In agreement with previous observations, the growth rates tend to increase with increasing temperature. (Figure 87 (b)).

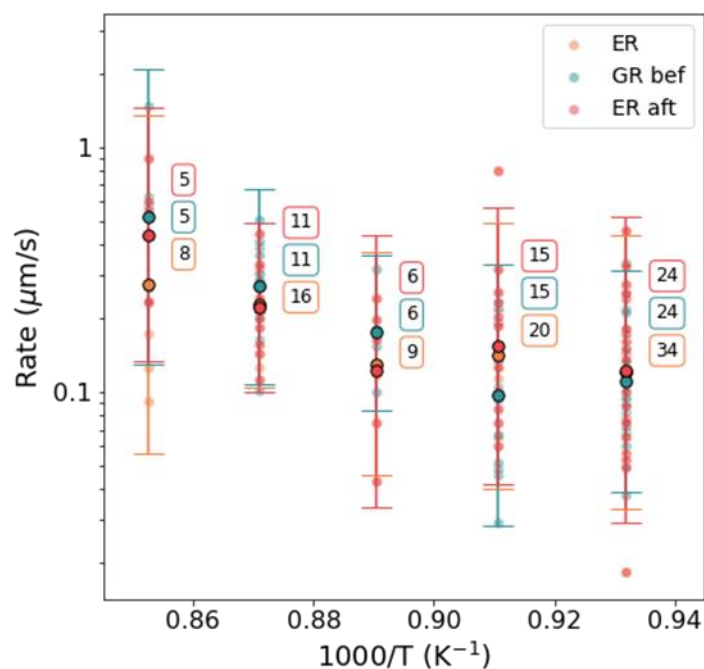


Figure 86 — Shrinkage rates, as well as the growth and etching rates for the transition to shrinkage, as a function of the inverse temperature. The big dots with black edges show the average value for the distribution, the boxes with colored borders on the right of the scatter clouds show the number of dots. The whiskers correspond to 95 % confidence intervals for mean values. All syntheses were performed at an ethanol partial pressure of 533 Pa.

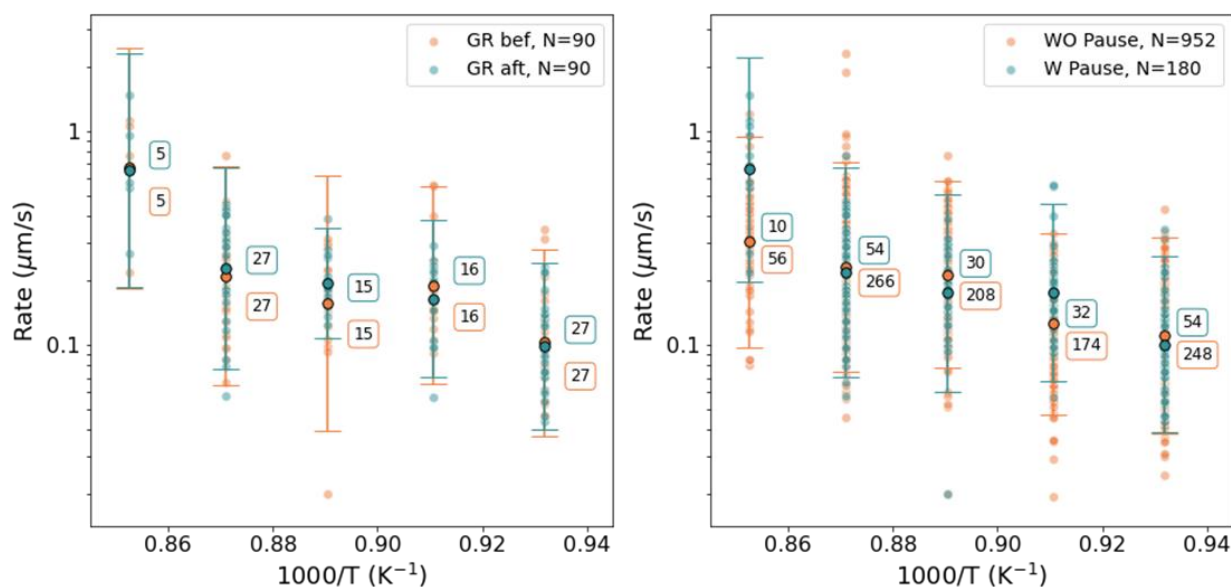


Figure 87 — The plots of the rate dependences (a) before and after the change, as well as (b) for rate changes with and without pauses on the partial pressures of ethanol. The whiskers correspond to 95 % confidence intervals of mean values. All syntheses were performed at an ethanol partial pressure of 533 Pa.

## 7.2.2 Pause behavior

Concerning pauses, their duration tends to decrease with increasing temperature (Figure 88 (a)) whatever the type of transition (Figure 88 (b)).

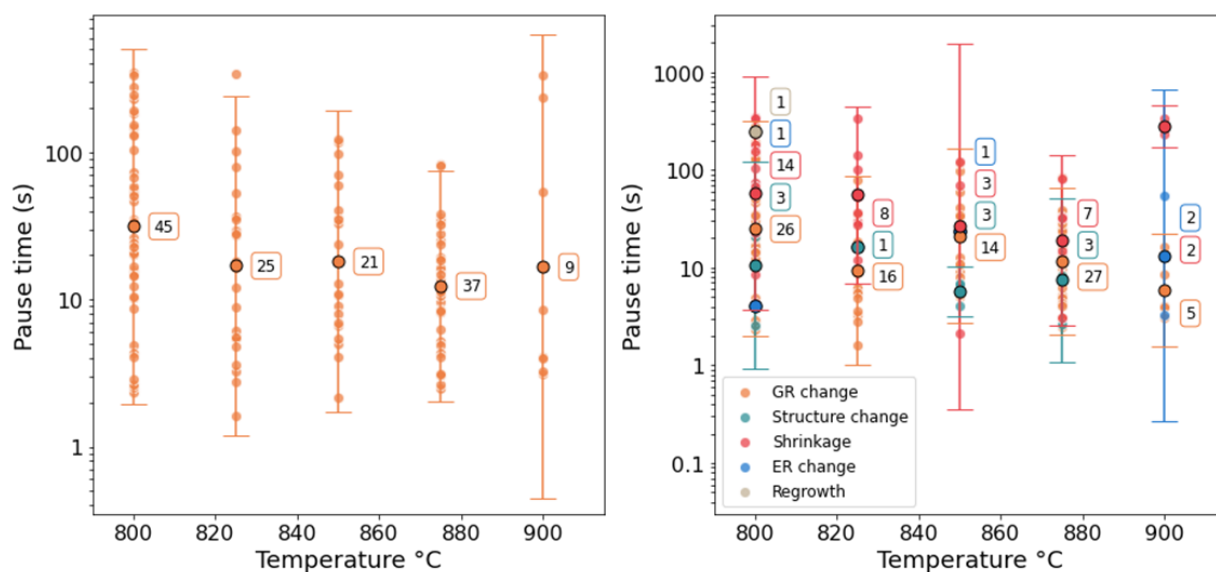


Figure 88 — Pause times as a function of the partial pressure of ethanol for a) all transitions and b) the different types of transition . The whiskers correspond to 95 % confidence intervals of mean values. All syntheses were performed at ethanol partial pressure of 533 Pa.

## 7.3 Conclusion

Etchings and pauses are part of the complex growth behavior of nanotubes. Their occurrence apparently has a stochastic nature like the growth rate changes which we previously described. The analysis of the dependence of etching on the structure is complicated by the vanishing of CNTs of interest. Statistical analysis is also complicated because etching and pause events are rarer than transitions in growth rates. A few qualitative trends can still be drawn: i) the growth and etching rates of the same CNT tends to be positively correlated, ii) the number of etched CNTs tend to decrease with increasing temperature, iii) etching rates tend to increase with increasing temperature, iv) pause durations tend to decrease with increasing temperature.

It is important to highlight the absence of shrinkage events with catalysts different from iron: this supports that shrinkage events are less general than growth rate transitions and may be specific to catalysts displaying several possible phases during growth like iron (*e.g.* Fe and Fe<sub>3</sub>C).

In the future, it would be interesting to collect more experimental data at different pressures and temperatures in order to access the activation energy and apparent reaction order (with regards to ethanol) of the etching process and compare with growth.

# Chapter 8.

## Discussion

A key result of this work was to reveal the complexity of CNT growth kinetics at the individual nanotube level, a complexity that is not taken into account by current growth models. For instance, the model of self-exhausting kinetics caused by a progressive carbon coating of the catalyst particle of Poretzky *et al.* (223) is invalidated by our observations: exponential decay is never observed at the level of individual CNTs. As shown in Figure 89, exponential decay arises from the sum of a large number of individual growth kinetics. This is the consequence of the large distribution of lifetimes in mathematical analogy with radioactive decay theory which assumes a constant probability of deactivation at all times. At the individual CNT level, growth termination is a sudden event, which supports that it is related to a catastrophic event such as the detachment of the catalyst particle or the incorporation of a defect preventing any further growth. The stochastic nature of the deactivation raises the questions of whether it is possible to control this process and whether it depends on the nanotube structure.

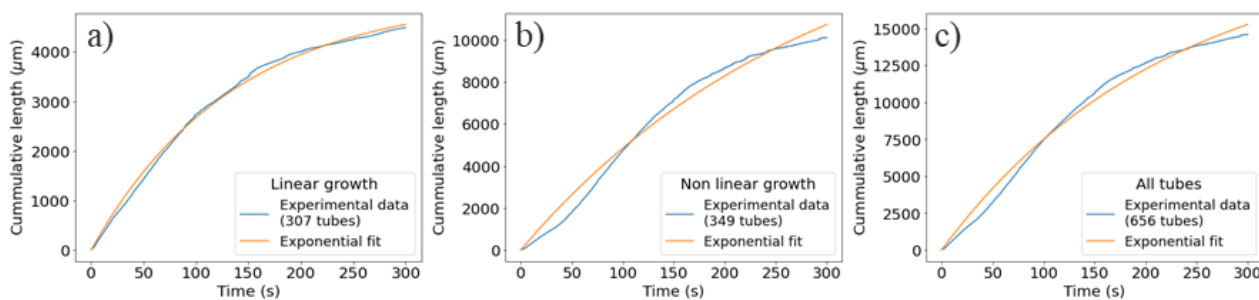


Figure 89 — Cummulative length of the nanotubes over time for the cases of a) linear growth, b) non linear growth and c) them together. Data of CNTs synthesised at 850°C and 1600 Pa of ethanol partial pressure.

Our analysis of a large data set of individual CNTs gave no statistical correlation between the growth rate and the metallicity of nanotubes. This indicates that the previously reported difference in growth rate between M and SC CNTs (217) is not an intrinsic property of nanotubes but probably depends on the growth conditions. I notably suggest that the concentration of water vapor (as background traces or as by-product of the precursor decomposition) may be a key parameter likely to drive this type of kinetic selectivity.

Importantly, we found that the growth rate of a nanotube can change suddenly and stochastically. Analysis of the growth kinetics at the level of the single chirality (11,8) showed that the growth rate can vary over a wide range even for a single chirality. This contradicts the current models, which predict a single growth rate for a given chirality. By many aspects, this kinetic behavior resembles the dynamic instability of microtubule growth (224, 225), although in a very different context. One can still note that similar behaviors have been previously reported for the catalytic growth of nanowires, which can be accompanied by fluctuations in growth rates (226), catalyst movements between different facets (227), and oscillations of the growth interface (228). The absence of spatial or temporal correlation between the kinetic behaviors of the nanotubes excludes the possibility of the influence of local fluctuations in the growth conditions. Moreover, the fact that the reaction orders for linear and broken-line growths are similar indicates that the decomposition of ethanol proceeds in a similar way in both cases, that is in particular with the same phase for the catalyst particle. Changes in the size of the catalyst by ripening during CNT growth cannot explain the reversible changes between discrete states that we observed, since ripening is an irreversible thermodynamic process. Moreover, the analysis of the growth rates of CNTs grown using catalysts other than iron (*i.e.* Co, Ni, and FeRu) showed a similar proportionality factor of  $\sim 1.7$ . Having excluded other hypotheses, this suggests that the observed dynamic instability originates from stochastic switches of the nanotube edge configurations and/or the catalyst particle phase. Although the atomic structure of the nanotube edge during growth is not in the reach of any current experiment, an attractive hypothesis is that switches between different edge configurations (e.g., with a large number of armchair or zigzag sites) drive CNT growth rate switches. In this bi-stable edge hypothesis, the rate change factor as well as the switching rate should strongly depend on the chirality of the nanotube (Figure 90). To explain this phenomenon, the development of new models that take into account the instability of CNT growth rates is necessary. For this purpose, the data on the growth kinetics, in particular the activation energies of the different growth modes and the corresponding pre-exponential factors, may be useful inputs.

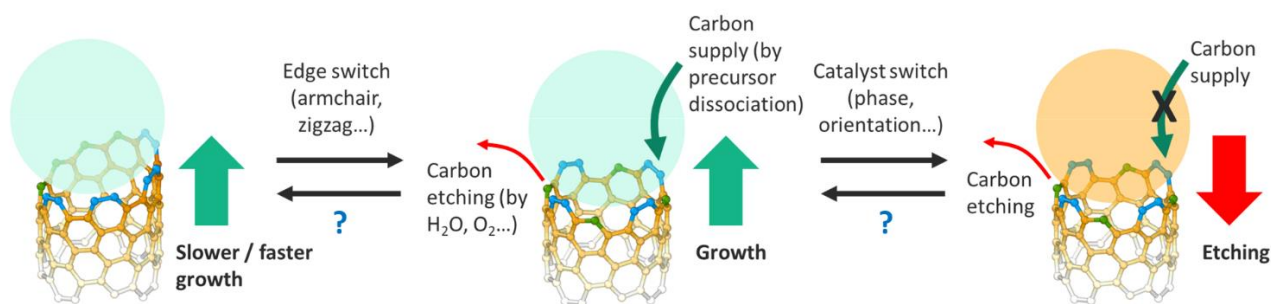


Figure 90 — Schematic of possible mechanisms governing rate changes and etching.

However, within the above-described hypothesis, it is impossible to explain the switches between growth and shrinkage. This behavior requires a change in the chemical potential of carbon at the catalyst-tube interface. One possible mechanism could be switches between two catalyst phases with different catalytic activities (*e.g.*, metallic and carbide). In the case of iron, *in-situ* TEM (229) and *in-situ* XPS (230) during CNT growth demonstrated the possibility of different phases with different catalytic activities, such as  $\alpha$ -Fe,  $\gamma$ -Fe, Fe<sub>3</sub>C, and Fe<sub>5</sub>C<sub>2</sub>. Moreover, CNT growth deactivation accompanied by transition from Fe<sub>3</sub>C to Fe<sub>5</sub>C<sub>2</sub> (229) or from Co<sub>2</sub>C to Co<sub>3</sub>C (231) was also reported. The stability of these phases depends on the carbon concentration, so the transitions may be caused by an imbalance between carbon consumption and carbon supply. This explanation is also supported by the observed increase in the number of growth-to-shrinkage transitions with increasing ethanol partial pressure (Figure 77 (a)). Moreover, when using Ni as a catalyst, we did observe growth rate changes but we did not observe any shrinkage, which also supports the hypothesis of a phase change for shrinkage switches since there is no stable carbide for nickel contrary to iron. Further experimental and theoretical studies such as *in situ* HRTEM and advanced computer simulations are now needed to determine the origin of this behavior.

Further understanding of the tube growth processes, as well as the determination of the driving mechanisms of the various kinetic modes evidenced in this work may form the basis for the development of new selective growth methods.



# Conclusion

This work was aimed at investigating the growth kinetics of individual carbon nanotubes using an *in-situ* optical setup based on homodyne polarization microscopy.

Beside this main objective, the Raman study of horizontally aligned CNTs grown on monocrystalline quartz made it possible to develop criteria for discriminating individual SWCNTs from other cases. Also, the study evidenced two different environment constant  $C_e$  for horizontally aligned suggesting two different types of interaction or configuration for CNTs aligned on quartz substrates. This unexpected result requires further experimental studies such as highly-resolved Raman measurements (RBM, D, G, 2D) along aligned CNTs freshly grown on quartz.

To extract the growth kinetics of individual CNTs from *in situ* optical microscopy data, tools were developed to speed up and automatize video data collection, processing and analysis. Although the application of these methods was focused on solving problems related to the processing of video of CNT growth, the concepts developed can be applied to other tasks of video processing and recognition.

These *in situ* data allowed us to evidence the complexity of the growth kinetics at the level of individual CNTs and to address some of the important questions highlighted in section 1.4. It was notably observed that the growth rate does not follow an exponential decay at the level of individual CNTs. At the opposite, the growth rate is either constant or switches between different stable values. The ratio of rates before and after the change displays an average proportionality factor of  $\sim 1.7$  for both acceleration and deceleration events, regardless of the synthesis temperature, the partial pressure of ethanol, and the catalyst used. Among the possible kinetic modes of the CNTs, switches to shrinkage were also evidenced. As in the case of growth, this process proceeds at the interface between the CNT and the catalyst. Moreover, all type of transitions can proceed with pauses. Also, in some cases, multiple transitions between growth, shrinkage, and pauses have been observed.

Kinetically, the transitions investigated in this paper were stochastic in nature with no temporal or spatial correlation between them. It can be assumed that growth rate changes and transitions to shrinkage are the results of different processes: growth rate changes may be related to fluctuations of the structure of the CNT edge, while transitions from growth to shrinkage may be related to fluctuations of the catalyst phase. An appealing prospect is the development of selective synthesis techniques based on the controlled and iterative interaction of these processes. For this

purpose, it is necessary to establish the causes of each of the phenomena and their dependence on the nanotube metallicity and /or chirality during future experimental studies using reliable chirality assignment protocols based on optical spectroscopies and/or aberration-corrected TEM. No less interesting is the comparison of the structure and kinetics of the CNTs, which showed that, contrary to existing theories, CNTs can grow at different rates even at constant chirality. This confirms the need to develop new theories able to model these stochastic transitions.

Finally, the conducted study allowed us to establish a possible relationship between the structure of the CNT edge and its growth rate. More structural assignments for CNTs with known kinetics are still needed to establish the influence of the nanotube structure itself on its kinetics. In the future, it would also be interesting to study the influence of controlled concentrations of gaseous etchants, such as water and oxygen, on the stochastic fluctuations evidenced during this work.

# Résumé étendu en français

Les connaissances scientifiques progressent constamment et la technologie est toujours à la recherche de performances supérieures, d'un coût moindre et d'une plus grande miniaturisation. Alors que l'utilisation du silicium comme matériau de base des dispositifs microélectroniques atteint aujourd'hui ses limites en raison de contraintes physiques, de nouveaux matériaux aux propriétés comparables voire supérieures entrent en scène. Les nanomatériaux présentent un intérêt particulier en raison de leur taille intrinsèquement petite et parce que leurs propriétés peuvent être adaptées par de légères modifications de leur taille, de leur forme ou de leur structure cristalline.

Parmi eux, les nanotubes de carbone (NTC) sont un substitut prometteur aux matériaux modernes dans les dispositifs électroniques et optiques en raison de leurs propriétés exceptionnelles qui ont déjà été démontrées en théorie et en pratique. Toutefois, pour passer à une utilisation massive des NTC, il faut d'abord fabriquer sur mesure des nanotubes présentant des structures et des propriétés contrôlées en termes de diamètre, d'angle hélicoïdal ou de type de conductivité. Il existe deux façons d'accomplir cette tâche : le tri post-synthèse et la synthèse sélective. La seconde approche est préférable du point de vue pratique et industriel car elle ne nécessite pas d'étapes supplémentaires dans le processus de fabrication du dispositif. Cependant, elle nécessite la compréhension des processus qui régissent la sélectivité chirale durant la croissance.

Pour des cristaux 3D et 2D, la vitesse de croissance dépend de la face cristalline ou du bord du cristal. Ainsi, en première approche, la croissance des nanotubes n'est qu'un cas particulier de croissance cristalline pour un cristal 1D ayant un bord circulaire. Cela soulève plusieurs questions : quelle est la structure du bord du nanotube pendant la croissance ? Ou quelles sont les différentes structures stables possibles ? Quelle est l'influence à la chiralité du nanotube et de la nature du catalyseur sur la structure du bord ? Enfin, quelle est l'influence de la structure du bord du nanotube sur la cinétique de croissance ?

Plusieurs méthodes ont été utilisées pour répondre à ces questions. Plusieurs de ces méthodes ont permis d'accéder à la chiralité et à la cinétique de croissance des nanotubes, mais aucune d'entre elles n'a permis d'observer directement la croissance de NTC individuels en temps réel avec une haute résolution temporelle et en condition réelle de croissance.

Pour pallier à ces difficultés, nous avons utilisé une nouvelle technique de microscopie optique appelée microscopie à polarisation homodyne, mise au point par Lefebvre et Finnie à Ottawa, d'une

part, et Kaihui Liu *et al.* à Berkeley, d'autre part. Cette méthode exploite la forte anisotropie optique des nanotubes de carbone pour extraire leur faible signal optique du fond induit par le substrat et l'environnement en général. Pour cela, nous avons utilisé une source blanche, intense et directionnelle de type supercontinuum pour exciter les nanotubes dans tout le spectre visible. Pour réduire la réflexion par le substrat, nous avons utilisé deux polariseurs en configuration croisée et des nanotubes alignés à un angle de  $45^\circ$  par rapport aux axes des polariseurs. Le faible signal des nanotubes a été encore amplifié par homodynage, c'est-à-dire par couplage interférentiel avec le champ réfléchi par le substrat.

Cette technique permet de mesurer le spectre optique de NTC individuels sur substrat mais aussi de les imager. Nous avons appliqué cette technique à l'imagerie *in situ* de nanotubes individuels dans des conditions réelles de croissance, c'est-à-dire à pression atmosphérique et sur un substrat. Pour ce faire, nous avons utilisé un substrat monocristallin, le quartz avec coupe de type ST, qui a l'avantage de favoriser la croissance de nanotubes de carbone monofeuillets longs et parfaitement alignés le long d'une direction cristalline spécifique du quartz. Enfin, nous avons orienté le substrat de manière à ce que les nanotubes croissent à  $45^\circ$  par rapport aux axes des polariseurs.

Cette méthode nous a permis d'observer la croissance des nanotubes de carbone en temps réel. Cependant, les vidéos brutes étant difficilement utilisables pour l'extraction de la cinétique de croissance, elles ont été traitées afin d'augmenter le contraste des objets enregistrés et de réduire le bruit de l'image. Une partie importante de mon travail a été l'automatisation et l'amélioration de l'algorithme de traitement vidéo. En conséquence, nous avons développé et appliqué une technique de traitement différentiel, qui permet non seulement d'augmenter la qualité des vidéos, mais aussi de mettre en évidence la vitesse de croissance instantanée ainsi que les changements de structurelle d'un nanotube pendant sa croissance.

Pour vérifier l'applicabilité de notre système d'imagerie, nous avons fait la comparaison des vidéos avec des images de Microscopie à Force Atomique (AFM), ce qui a montré que la méthode permet de détecter jusqu'à 95% des nanotubes pendant leur croissance. Nous avons également utilisé l'imagerie MEB en mode de faible contraste des NTC semiconducteurs, ce qui nous a permis de déterminer la métallicité des NTC en comparant ces images avec les vidéos *in situ*.

Notre système d'imagerie a fourni une très grande quantité de données sur la croissance des nanotubes, donc après le développement de l'algorithme de traitement vidéo, l'extraction des données cinétiques est devenue une étape limitante dans mon projet.

Pour accélérer ce processus, j'ai développé un système de reconnaissance vidéo basé sur l'intelligence artificielle (IA). Mask-RCNN a été utilisé comme modèle de base, une IA initialement développée pour reconnaître les objets enregistrés par des caméras vidéo dans la rue. Le processus de reconnaissance dans ce système se déroule en trois étapes : changement d'échelle des images,

génération de propositions de localisation des objets, et la prédiction de leurs classes (par exemple, humain, arbre, feu de circulation, avion, etc.). Comme le réseau de neurones de base, nous avons utilisé un ResNet-50 pré-entraîné sur le jeu de données COCO-2017, ce qui nous a permis d'accélérer le processus d'entraînement. Notre ensemble de données pour la formation contenait 575 images marquées manuellement, avec quatre classes d'objets : les NTC en cours de croissance, les NTC avec un changement de structure ou un rétrécissement, ainsi qu'une reconnaissance de la ligne de catalyseur et des marques optiques.

Pour compenser la taille de l'ensemble des données initiales, j'ai utilisé certaines transformations d'images qui ont permis d'améliorer la capacité du modèle à reconnaître des objets sans augmenter la quantité de données utilisées pour l'entraînement. Ces transformations sont appelées augmentations et peuvent apparaître pendant l'entraînement avec une probabilité de 0,5. Des retournements horizontaux et verticaux ont été utilisés afin d'augmenter la capacité du modèle à localiser les objets, tandis que des ajustements du contraste et de la luminosité ont augmenté la capacité du modèle à travailler avec des vidéos de qualités différentes.

Le modèle prédit les classes des objets avec des boîtes de délimitation et des masques prédisant leurs emplacements. Ensuite, j'ai utilisé l'algorithme de hongrois et le filtre Kalman pour suivre les NTC individuellement et extraire leur cinétique, cinétique qui s'est avérée beaucoup plus complexe qu'initialement imaginée et constituée de plusieurs cas.

Le premier cas qui a représenté environ la moitié des NTC dans les conditions que nous avons étudiées (catalyseur fer et précurseur éthanol) est une vitesse de croissance constante jusqu'à un arrêt brusque. Pour ces cas, nous avons pu identifier la nature métallique ou semi-conductrice de chaque nanotube à partir de leur contraste en Microscopie Électronique à Balayage (MEB) et de leur signature Raman et nous n'avons observé aucune différence en termes de vitesse de croissance ou de durée de vie entre nanotubes métalliques et semi-conducteurs. Ceci est en contradiction avec un rapport récent que les nanotubes semiconducteurs dépasseraient en vitesse de croissance les métalliques par environ un ordre de grandeur. Cependant, cette différence de résultats pourrait s'expliquer l'utilisation de conditions de croissance différentes, et d'un précurseur de carbone différent (méthane au lieu d'éthanol), en particulier.

Une autre observation importante est que la vitesse de croissance et le temps de vie tendent à être inversement corrélés comme illustré par deux nuages de points allongés dans les graphes de corrélation, Cette corrélation inverse est également observée lorsque l'on fait varier la température : les vitesses de croissance ont tendance à augmenter avec l'augmentation de la température alors que la durée de vie a tendance à diminuer. J'ai également observé cette même corrélation inverse lors des études en fonction de la pression partielle d'éthanol.

Cela confirme que le principal processus de désactivation est lié à l'ajout d'atomes de carbone, par exemple par la création de défauts permanents, non cicatrisés, à la périphérie du nanotube ou par couverture de nanoparticule de catalyseur avec le

Le deuxième cas observé est constitué par des changements stochastiques de la vitesse de croissance. Dans une minorité de cas, ce changement de vitesse s'accompagne d'un changement de la structure du NTC qui s'illustre par un changement du contraste optique (et du contraste en MEB dans le cas d'un changement entre nanotube métallique et semiconducteur), ainsi que par le changement des caractéristiques Raman résonantes du nanotube. Dans les deux cas, les courbes cinétiques sont caractérisés par des changements abrupts d'une vitesse constante à une autre vitesse constante.

Nous avons cherché une corrélation entre les vitesses avant et après changement et nous avons trouvé une corrélation forte entre les deux, à la fois pour les événements d'augmentation et de diminution de vitesse. Dans les deux cas, la distribution des rapports de vitesses peut être ajustée par une loi linéaire de pente 1,7 (pour les cas d'augmentation) ou de son inverse 1/1,7 (pour les cas de diminution). De manière intéressante, un facteur similaire de 1,7 a été rapporté par Koyano *et al.* (140) après avoir exposé des nanotubes à de la vapeur d'eau, causant probablement ainsi une modification de l'interface nanotube-catalyseur. Une observation importante est que le même facteur de proportionnalité est observé quelle que soit la température et la pression partielle de précurseur éthanol et qu'il y ait ou non un changement de chiralité. De plus, les expériences avec différents catalyseurs (FeRu, Co, Ni) ont également donné le même facteur de proportionnalité. Cela confirme que le changement de vitesse est davantage relié à un changement de la configuration géométrique à l'interface nanotube-catalyseur (c'est-à-dire au facteur pré-exponentiel de la loi d'Arrhenius), qu'aux énergies d'activation impliquées dans chaque état, lent ou rapide.

Le troisième cas que nous avons mis en évidence est celui de changements stochastiques entre croissance et rétrécissement. Nous avons observé que le rétrécissement ne se fait pas à partir de l'extrémité du nanotube mais à partir de l'interface avec la particule de catalyseur par gravure catalytique. Il est également intéressant de noter que des pauses peuvent être observées entre la croissance et le rétrécissement ou entre deux périodes de croissance ou deux périodes de rétrécissement. Par de nombreux aspects, cela est analogue à la croissance des microtubules dans les cellules biologiques même si le système est bien sûr de nature très différente. Enfin, certains nanotubes peuvent même présenter de multiples basculements de vitesses de croissance ou entre croissance et rétrécissement, au cours de leur vie.

Au cours de mon travail de thèse, j'ai également réalisé une étude par spectroscopie Raman dont le but était de déterminer la structure de nanotubes individuels afin de la corrélérer avec leur cinétique de croissance. Ce travail d'identification a été compliqué par à la fois par le signal Raman

du substrat en quartz dont les pics caractéristiques coïncident avec la zone RBM des nanotubes, ainsi que par la forte interaction avec le substrat qui affecte les spectres des nanotubes. Cependant, nous avons développé des outils pour transformer certains de ces inconvénients en avantages pour nos besoins.

Une étude approfondie de l'échantillon de quartz seul avec un spectromètre Raman calibré à l'aide d'une lampe spectrale a permis de déterminer le pic que nous pouvons utiliser pour la calibration interne des spectres avec nanotubes. Ceci a permis de localiser précisément les positions des RBMs. L'étude des décalages des bandes G et D induits par une forte interaction entre le nanotube et le substrat nous a permis de développer une méthode de discrimination entre NTC monofeuillets individuels et les autres cas (nanotube bifeuillets, fagot de deux nanotubes, etc...).

L'analyse approfondie des NTC individuels et des NTC non-orientés produits dans les lignes de catalyseur nous a permis de déterminer la loi reliant fréquence RBM et diamètre du nanotube, loi nécessaire à la détermination de la chiralité de NTC par Raman. Nous avons découvert que les NTCs produits dans les lignes de catalyseur présentent une interaction plus faible avec le substrat, ce qui se manifeste par une constante environnementale proche de celle des nanotubes libres. Les NTCs, produits alignés sur la surface de quartz montrent un comportement plus complexe. Nous avons montré que la fréquence du RBM peut brusquement changer le long d'un nanotube, ce qui peut être décrit par deux constantes environnementales différentes, une similaire à celle des nanotubes libres, et une autre plus proche de celle rapportée dans la littérature pour les NTCs synthétisés sur quartz. Ceci suggère que les NTCs peuvent avoir deux types d'interaction, une forte et une faible, avec le substrat en quartz.

Suite à ces études Raman, 41 nanotubes ont pu être attribués à la chiralité (11,8). Nous avons trouvé que la distribution des vitesses de croissance pour cette chiralité unique n'est pas monomodale, en désaccord avec les modèles cinétiques actuels. Au contraire, la distribution présente deux (voire trois) pics principaux.

Une explication possible aux comportements cinétiques observés (changement de vitesse de croissance) pourrait être que le bord du nanotube passe stochastiquement d'une configuration stable à une autre configuration stable, par exemple plus en fauteuil ou plus en zigzag. Des simulations de type Monte Carlo cinétique pourraient aider à déterminer la probabilité de cette hypothèse et son mécanisme exact.

En revanche, le basculement entre croissance et gravure ne peut pas être expliqué par un changement de structure du bord. Il doit être lié au potentiel chimique en carbone réellement vu par le bord du nanotube. Dans ce cas, une hypothèse probable est un basculement du catalyseur entre deux phases : une phase hautement active pour la décomposition catalytique du précurseur carboné (par exemple une phase métallique) et une phase avec une activité catalytique plus faible (par exemple

une phase carbure). Nous suggérons que des observations TEM in situ dans des conditions plus réalistes pourraient aider à évaluer cette hypothèse. Dans tous les cas, les modèles de croissance des nanotubes devraient être révisés pour prendre en compte la complexité révélée par nos observations.

# References

1. J. Bernholc, D. Brenner, M. Buongiorno Nardelli, V. Meunier, C. Roland, Mechanical and Electrical Properties of Nanotubes. *Annu. Rev. Mater. Res.* **32**, 347–375 (2002), doi:10.1146/annurev.matsci.32.112601.134925.
2. A. D. Franklin *et al.*, Sub-10 nm carbon nanotube transistor. *Nano letters.* **12**, 758–762 (2012), doi:10.1021/nl203701g.
3. G. Hong *et al.*, Separation of metallic and semiconducting single-walled carbon nanotube arrays by "scotch tape". *Angewandte Chemie (International ed. in English).* **50**, 6819–6823 (2011), doi:10.1002/anie.201101700.
4. H. Liu, D. Nishide, T. Tanaka, H. Kataura, Large-scale single-chirality separation of single-wall carbon nanotubes by simple gel chromatography. *Nature communications.* **2**, 309 (2011), doi:10.1038/ncomms1313.
5. X. Tu, S. Manohar, A. Jagota, M. Zheng, DNA sequence motifs for structure-specific recognition and separation of carbon nanotubes. *Nature.* **460**, 250–253 (2009), doi:10.1038/nature08116.
6. C. Ducati, I. Alexandrou, M. Chhowalla, G. A. J. Amaratunga, J. Robertson, Temperature selective growth of carbon nanotubes by chemical vapor deposition. *Journal of Applied Physics.* **92**, 3299–3303 (2002), doi:10.1063/1.1499746.
7. Y. J. Jung *et al.*, Mechanism of Selective Growth of Carbon Nanotubes on SiO<sub>2</sub>/Si Patterns. *Nano Lett.* **3**, 561–564 (2003), doi:10.1021/nl034075n.
8. A. Galano, Carbon nanotubes: promising agents against free radicals. *Nanoscale.* **2**, 373–380 (2010), doi:10.1039/b9nr00364a.
9. Hamada, Sawada, Oshiyama, New one-dimensional conductors: Graphitic microtubules. *Physical review letters.* **68**, 1579–1581 (1992), doi:10.1103/PhysRevLett.68.1579.
10. M. S. Strano, Carbon nanotubes: sorting out left from right. *Nature nanotechnology.* **2**, 340–341 (2007), doi:10.1038/nnano.2007.157.
11. X. Peng *et al.*, Optically active single-walled carbon nanotubes. *Nature nanotechnology.* **2**, 361–365 (2007), doi:10.1038/nnano.2007.142.

12. A. A. Green, M. C. Duch, M. C. Hersam, Isolation of single-walled carbon nanotube enantiomers by density differentiation. *Nano Res.* **2**, 69–77 (2009), doi:10.1007/s12274-009-9006-y.
13. G. G. Samsonidze *et al.*, The concept of cutting lines in carbon nanotube science. *Journal of nanoscience and nanotechnology.* **3**, 431–458 (2003), doi:10.1166/jnn.2003.231.
14. S. Iijima, Helical microtubules of graphitic carbon. *Nature.* **354**, 56–58 (1991), doi:10.1038/354056a0.
15. K. K. K. Koziol, C. Ducati, A. H. Windle, Carbon Nanotubes with Catalyst Controlled Chiral Angle. *Chem. Mater.* **22**, 4904–4911 (2010), doi:10.1021/cm100916m.
16. A. Ghedjatti *et al.*, Structural Properties of Double-Walled Carbon Nanotubes Driven by Mechanical Interlayer Coupling. *ACS nano.* **11**, 4840–4847 (2017), doi:10.1021/acsnano.7b01328.
17. Mingqi Liu, John M. Cowley, Growth behavior and growth defects of carbon nanotubes. *Materials Science and Engineering* (1994).
18. T. Haugan, P. N. Barnes, R. Wheeler, F. Meisenkothen, M. Sumption, Addition of nanoparticle dispersions to enhance flux pinning of the YBa<sub>2</sub>Cu<sub>3</sub>O<sub>7-x</sub> superconductor. *Nature.* **430**, 867–870 (2004), doi:10.1038/nature02792.
19. K. Suenaga *et al.*, Imaging active topological defects in carbon nanotubes. *Nature nanotechnology.* **2**, 358–360 (2007), doi:10.1038/nnano.2007.141.
20. G. Brinkmann, P.W. Fowler, D.E. Manolopoulos, A.H.R. Palser, A census of nanotube caps. *Chemical Physics Letters.* **315**, 335–347 (1999), doi:10.1016/S0009-2614(99)01111-2.
21. D. A. Gómez-Gualdrón, P. B. Balbuena, The role of cap chirality in the mechanism of growth of single-wall carbon nanotubes. *Nanotechnology.* **19**, 485604 (2008), doi:10.1088/0957-4484/19/48/485604.
22. S. Iijima, T. Ichihashi, Y. Ando, Pentagons, heptagons and negative curvature in graphite microtubule growth. *Nature.* **356**, 776–778 (1992), doi:10.1038/356776a0.
23. S. Iijima, Growth of carbon nanotubes. *Materials Science and Engineering.* **B19** (1993).
24. D. L. Carroll, P. Redlich, P. M. Ajayan†, Electronic Structure and Localized States at Carbon Nanotube Tips. *Physical review letters.* **78** (1997).
25. A. J. Stone, D. J. Wales, Theoretical studies of icosahedral C<sub>60</sub> and some related species. *Chemical Physics Letters.* **128**, 501–503 (1986), doi:10.1016/0009-2614(86)80661-3.
26. N. W. Ashcroft, N. D. Mermin, *Solid state physics* (Holt, New York, London, 1977).
27. T. W. Odom, J.-L. Huang, P. Kim, C. M. Lieber, Structure and Electronic Properties of Carbon Nanotubes. *J. Phys. Chem. B.* **104**, 2794–2809 (2000), doi:10.1021/jp993592k.

28. P. T. Araujo *et al.*, Nature of the constant factor in the relation between radial breathing mode frequency and tube diameter for single-wall carbon nanotubes. *Phys. Rev. B.* **77** (2008), doi:10.1103/PhysRevB.77.241403.
29. G. G. Samsonidze *et al.*, Family behavior of the optical transition energies in single-wall carbon nanotubes of smaller diameters. *Appl. Phys. Lett.* **85**, 5703–5705 (2004), doi:10.1063/1.1829160.
30. W. Plank *et al.*, Electronic structure of carbon nanotubes with ultrahigh curvature. *ACS nano.* **4**, 4515–4522 (2010), doi:10.1021/nm100615d.
31. N. G. Bobenko *et al.*, Experimental and theoretical study of electronic structure of disordered MWCNTs. *Carbon.* **153**, 40–51 (2019), doi:10.1016/j.carbon.2019.06.104.
32. R. R. He, H. Z. Jin, J. Zhu, Y. J. Yan, X. H. Chen, Physical and electronic structure in carbon nanotubes. *Chemical Physics Letters.* **298**, 170–176 (1998), doi:10.1016/S0009-2614(98)01213-5.
33. S. Zhao *et al.*, Observation of Drastic Electronic-Structure Change in a One-Dimensional Moiré Superlattice. *Physical review letters.* **124**, 106101 (2020), doi:10.1103/PhysRevLett.124.106101.
34. H. Kataura *et al.*, Optical properties of single-wall carbon nanotubes. *Synthetic Metals.* **103**, 2555–2558 (1999), doi:10.1016/S0379-6779(98)00278-1.
35. V. N. Popov, L. Henrard, Comparative study of the optical properties of single-walled carbon nanotubes within orthogonal and nonorthogonal tight-binding models. *Phys. Rev. B.* **70**, 1949 (2004), doi:10.1103/PhysRevB.70.115407.
36. A. Jorio *et al.*, The Kataura plot over broad energy and diameter ranges. *phys. stat. sol. (b).* **243**, 3117–3121 (2006), doi:10.1002/pssb.200669192.
37. K. Liu *et al.*, An atlas of carbon nanotube optical transitions. *Nature nanotechnology.* **7**, 325–329 (2012), doi:10.1038/nnano.2012.52.
38. S. Berciaud, L. Cognet, P. Poulin, R. B. Weisman, B. Lounis, Absorption spectroscopy of individual single-walled carbon nanotubes. *Nano letters.* **7**, 1203–1207 (2007), doi:10.1021/nl062933k.
39. M. Paillet *et al.*, Probing the structure of single-walled carbon nanotubes by resonant Raman scattering. *phys. stat. sol. (b).* **247**, 2762–2767 (2010), doi:10.1002/pssb.201000147.
40. M. Jones *et al.*, Analysis of photoluminescence from solubilized single-walled carbon nanotubes. *Phys. Rev. B.* **71**, 380 (2005), doi:10.1103/PhysRevB.71.115426.
41. J. S. Soares, L. G. Cançado, E. B. Barros, A. Jorio, The Kataura plot for single wall carbon nanotubes on top of crystalline quartz. *phys. stat. sol. (b).* **247**, 2835–2837 (2010), doi:10.1002/pssb.201000239.

42. T. Michel *et al.*, E33 and E44 optical transitions in semiconducting single-walled carbon nanotubes: Electron diffraction and Raman experiments. *Phys. Rev. B.* **75** (2007), doi:10.1103/PhysRevB.75.155432.
43. Thess *et al.*, Crystalline Ropes of Metallic Carbon Nanotubes. *Science.* **273**, 483–487 (1996), doi:10.1126/science.273.5274.483.
44. D. S. Bethune *et al.*, Cobalt-catalysed growth of carbon nanotubes with single-atomic-layer walls. *Nature.* **363**, 605–607 (1993), doi:10.1038/363605a0.
45. T. W. Ebbesen, P. M. Ajayan, Large-scale synthesis of carbon nanotubes. *Nature.* **358**, 220–222 (1992), doi:10.1038/358220a0.
46. R. Saito, G. Dresselhaus, M. S. Dresselhaus, *Physical Properties of Carbon Nanotubes, Synthesis of Carbon Nanotubes* (PUBLISHED BY IMPERIAL COLLEGE PRESS AND DISTRIBUTED BY WORLD SCIENTIFIC PUBLISHING CO, 1998).
47. P. Nikolaev, A. Thess, A. G. Rinzler, D. T. Colbert, R. E. Smalley, Diameter doubling of single-wall nanotubes. *Chemical Physics Letters.* **266**, 422–426 (1997), doi:10.1016/S0009-2614(97)00053-5.
48. T. Guo, P. Nikolaev, A. Thess, D. T. Colbert, R. E. Smalley, Catalytic growth of single-walled nanotubes by laser vaporization. *Chemical Physics Letters.* **243**, 49–54 (1995), doi:10.1016/0009-2614(95)00825-O.
49. H. Dai *et al.*, Single-wall nanotubes produced by metal-catalyzed disproportionation of carbon monoxide. *Chemical Physics Letters.* **260**, 471–475 (1996), doi:10.1016/0009-2614(96)00862-7.
50. A. M. Cassell, J. A. Raymakers, J. Kong, H. Dai, Large Scale CVD Synthesis of Single-Walled Carbon Nanotubes. *J. Phys. Chem. B.* **103**, 6484–6492 (1999), doi:10.1021/jp990957s.
51. R. Rao *et al.*, Carbon Nanotubes and Related Nanomaterials: Critical Advances and Challenges for Synthesis toward Mainstream Commercial Applications. *ACS nano.* **12**, 11756–11784 (2018), doi:10.1021/acsnano.8b06511.
52. Y. Yan *et al.*, Carbon nanotube catalysts: recent advances in synthesis, characterization and applications. *Chemical Society reviews.* **44**, 3295–3346 (2015), doi:10.1039/c4cs00492b.
53. J.-F. Colomer *et al.*, Large-scale synthesis of single-wall carbon nanotubes by catalytic chemical vapor deposition (CCVD) method. *Chemical Physics Letters.* **317**, 83–89 (2000), doi:10.1016/S0009-2614(99)01338-X.
54. E. Couteau *et al.*, CVD synthesis of high-purity multiwalled carbon nanotubes using CaCO<sub>3</sub> catalyst support for large-scale production. *Chemical Physics Letters.* **378**, 9–17 (2003), doi:10.1016/S0009-2614(03)01218-1.

55. K. Dasgupta, J. B. Joshi, S. Banerjee, Fluidized bed synthesis of carbon nanotubes – A review. *Chemical Engineering Journal*. **171**, 841–869 (2011), doi:10.1016/j.cej.2011.05.038.
56. A. T. Harris, C. H. See, J. Liu, O. Dunens, K. MacKenzie, Towards the large-scale synthesis of carbon nanotubes in fluidised beds. *Journal of nanoscience and nanotechnology*. **8**, 2450–2457 (2008), doi:10.1166/jnn.2008.118.
57. G. S.B. McKee, C. P. Deck, K. S. Vecchio, Dimensional control of multi-walled carbon nanotubes in floating-catalyst CVD synthesis. *Carbon*. **47**, 2085–2094 (2009), doi:10.1016/j.carbon.2009.03.060.
58. R. N. Othman, I. A. Kinloch, A. N. Wilkinson, Synthesis and characterisation of silica–carbon nanotube hybrid microparticles and their effect on the electrical properties of poly(vinyl alcohol) composites. *Carbon*. **60**, 461–470 (2013), doi:10.1016/j.carbon.2013.04.062.
59. M. S. Mohlala, N. J. Coville, Floating catalyst CVD synthesis of carbon nanotubes from CpFe(CO)2X (X=Me, I): Poisoning effects of I. *Journal of Organometallic Chemistry*. **692**, 2965–2970 (2007), doi:10.1016/j.jorganchem.2007.03.013.
60. H. Byeon, S. Y. Kim, K. H. Koh, S. Lee, Growth of ultra long multiwall carbon nanotube arrays by aerosol-assisted chemical vapor deposition. *Journal of nanoscience and nanotechnology*. **10**, 6116–6119 (2010), doi:10.1166/jnn.2010.2574.
61. C. Castro, M. Pinault, D. Porterat, C. Reynaud, M. Mayne-L’Hermite, The role of hydrogen in the aerosol-assisted chemical vapor deposition process in producing thin and densely packed vertically aligned carbon nanotubes. *Carbon*. **61**, 585–594 (2013), doi:10.1016/j.carbon.2013.05.040.
62. H. Wang, J. J. Moore, Low temperature growth mechanisms of vertically aligned carbon nanofibers and nanotubes by radio frequency-plasma enhanced chemical vapor deposition. *Carbon*. **50**, 1235–1242 (2012), doi:10.1016/j.carbon.2011.10.041.
63. H. Wang *et al.*, Controlled synthesis of aligned carbon nanotube arrays on catalyst patterned silicon substrates by plasma-enhanced chemical vapor deposition. *Applied Surface Science*. **181**, 248–254 (2001), doi:10.1016/S0169-4332(01)00391-9.
64. M. Mao, A. Bogaerts, Investigating the plasma chemistry for the synthesis of carbon nanotubes/nanofibres in an inductively coupled plasma enhanced CVD system: the effect of different gas mixtures. *J. Phys. D: Appl. Phys.* **43**, 205201 (2010), doi:10.1088/0022-3727/43/20/205201.
65. Y. Fukuda *et al.*, Remote Plasma Chemical Vapor Deposition of Carbon Nanotubes and Analysis of Plasma Effect. *IEEE Trans. Plasma Sci.* **39**, 3133–3139 (2011), doi:10.1109/TPS.2011.2164945.

66. Y. Li, W. Ruan, Z. Wang, Localized Synthesis of Carbon Nanotube Films on Suspended Microstructures by Laser-Assisted Chemical Vapor Deposition. *IEEE Trans. Nanotechnology*. **12**, 352–360 (2013), doi:10.1109/TNANO.2013.2248091.
67. K. Akahane *et al.*, Synthesis of carbon nanotubes by laser-assisted alcohol chemical vapor deposition. *Physica E: Low-dimensional Systems and Nanostructures*. **56**, 452–455 (2014), doi:10.1016/j.physe.2013.08.018.
68. W. Ruan, Z. Wang, J. Li, K. Jiang, L. Liu, Synthesis of Carbon Nanotubes on Suspending Microstructures by Rapid Local Laser Heating. *IEEE Sensors J.* **11**, 3424–3425 (2011), doi:10.1109/JSEN.2011.2161280.
69. F. Yang *et al.*, Templated Synthesis of Single-Walled Carbon Nanotubes with Specific Structure. *Accounts of chemical research*. **49**, 606–615 (2016), doi:10.1021/acs.accounts.5b00485.
70. A. M. Cassell, J. A. Raymakers, J. Kong, H. Dai, Large Scale CVD Synthesis of Single-Walled Carbon Nanotubes. *J. Phys. Chem. B.* **103**, 6484–6492 (1999), doi:10.1021/jp990957s.
71. C. Liu, H.-M. Cheng, Controlled Growth of Semiconducting and Metallic Single-Wall Carbon Nanotubes. *Journal of the American Chemical Society*. **138**, 6690–6698 (2016), doi:10.1021/jacs.6b00838.
72. J. Wang *et al.*, Growing highly pure semiconducting carbon nanotubes by electrotwisting the helicity. *Nat Catal.* **1**, 326–331 (2018), doi:10.1038/s41929-018-0057-x.
73. F. Zhang *et al.*, Growth of semiconducting single-wall carbon nanotubes with a narrow band-gap distribution. *Nature communications*. **7**, 11160 (2016), doi:10.1038/ncomms11160.
74. M. He *et al.*, Predominant (6,5) single-walled carbon nanotube growth on a copper-promoted iron catalyst. *Journal of the American Chemical Society*. **132**, 13994–13996 (2010), doi:10.1021/ja106609y.
75. H. Wang, G. Gu, S. Zhu, L. Yang, Y. Chen, Synthesis of (9,8) single-walled carbon nanotubes on CoSO<sub>4</sub>/SiO<sub>2</sub> catalysts: The effect of Co mass loadings. *Carbon*. **169**, 288–296 (2020), doi:10.1016/j.carbon.2020.07.043.
76. D. Yuan *et al.*, Horizontally aligned single-walled carbon nanotube on quartz from a large variety of metal catalysts. *Nano letters*. **8**, 2576–2579 (2008), doi:10.1021/nl801007r.
77. S. M. Bachilo *et al.*, Narrow (n,m)-distribution of single-walled carbon nanotubes grown using a solid supported catalyst. *Journal of the American Chemical Society*. **125**, 11186–11187 (2003), doi:10.1021/ja036622c.
78. W.-H. Chiang, R. M. Sankaran, Linking catalyst composition to chirality distributions of as-grown single-walled carbon nanotubes by tuning Ni(x)Fe(1-x) nanoparticles. *Nature materials*. **8**, 882–886 (2009), doi:10.1038/nmat2531.

79. X. Li *et al.*, Selective synthesis combined with chemical separation of single-walled carbon nanotubes for chirality selection. *Journal of the American Chemical Society*. **129**, 15770–15771 (2007), doi:10.1021/ja077886s.
80. Y. Miyauchi, S. Chiashi, Y. Murakami, Y. Hayashida, S. Maruyama, Fluorescence spectroscopy of single-walled carbon nanotubes synthesized from alcohol. *Chemical Physics Letters*. **387**, 198–203 (2004), doi:10.1016/j.cplett.2004.01.116.
81. C. Zoican Loebick *et al.*, Selective synthesis of subnanometer diameter semiconducting single-walled carbon nanotubes. *Journal of the American Chemical Society*. **132**, 11125–11131 (2010), doi:10.1021/ja102011h.
82. S. Huang, Q. Cai, J. Chen, Y. Qian, L. Zhang, Metal-catalyst-free growth of single-walled carbon nanotubes on substrates. *Journal of the American Chemical Society*. **131**, 2094–2095 (2009), doi:10.1021/ja809635s.
83. F. Yang *et al.*, Chirality-specific growth of single-walled carbon nanotubes on solid alloy catalysts. *Nature*. **510**, 522–524 (2014), doi:10.1038/nature13434.
84. Y. Chen *et al.*, Effect of different carbon sources on the growth of single-walled carbon nanotube from MCM-41 containing nickel. *Carbon*. **45**, 2217–2228 (2007), doi:10.1016/j.carbon.2007.06.022.
85. Y. Yamamoto, S. Inoue, Y. Matsumura, Thermal decomposition products of various carbon sources in chemical vapor deposition synthesis of carbon nanotube. *Diamond and Related Materials*. **75**, 1–5 (2017), doi:10.1016/j.diamond.2016.11.017.
86. K. A. Shah, B. A. Tali, Synthesis of carbon nanotubes by catalytic chemical vapour deposition: A review on carbon sources, catalysts and substrates. *Materials Science in Semiconductor Processing*. **41**, 67–82 (2016), doi:10.1016/j.mssp.2015.08.013.
87. G. Lolli *et al.*, Tailoring (n,m) structure of single-walled carbon nanotubes by modifying reaction conditions and the nature of the support of CoMo catalysts. *The journal of physical chemistry. B*. **110**, 2108–2115 (2006), doi:10.1021/jp056095e.
88. B. Wang *et al.*, (n,m) Selectivity of single-walled carbon nanotubes by different carbon precursors on Co-Mo catalysts. *Journal of the American Chemical Society*. **129**, 9014–9019 (2007), doi:10.1021/ja070808k.
89. S.-P. Chai, S. H. S. Zein, A. R. Mohamed, Preparation of carbon nanotubes over cobalt-containing catalysts via catalytic decomposition of methane. *Chemical Physics Letters*. **426**, 345–350 (2006), doi:10.1016/j.cplett.2006.05.026.
90. S. J. Kang *et al.*, High-performance electronics using dense, perfectly aligned arrays of single-walled carbon nanotubes. *Nature nanotechnology*. **2**, 230–236 (2007), doi:10.1038/nnano.2007.77.

91. C. Kocabas *et al.*, Guided growth of large-scale, horizontally aligned arrays of single-walled carbon nanotubes and their use in thin-film transistors. *Small (Weinheim an der Bergstrasse, Germany)*. **1**, 1110–1116 (2005), doi:10.1002/sml.200500120.
92. C. Kocabas, M. Shim, J. A. Rogers, Spatially selective guided growth of high-coverage arrays and random networks of single-walled carbon nanotubes and their integration into electronic devices. *Journal of the American Chemical Society*. **128**, 4540–4541 (2006), doi:10.1021/ja0603150.
93. N. Ishigami *et al.*, Crystal plane dependent growth of aligned single-walled carbon nanotubes on sapphire. *Journal of the American Chemical Society*. **130**, 9918–9924 (2008), doi:10.1021/ja8024752.
94. S. Han, X. Liu, C. Zhou, Template-free directional growth of single-walled carbon nanotubes on a- and r-plane sapphire. *Journal of the American Chemical Society*. **127**, 5294–5295 (2005), doi:10.1021/ja042544x.
95. M. Maret *et al.*, Oriented growth of single-walled carbon nanotubes on a MgO(001) surface. *Carbon*. **45**, 180–187 (2007), doi:10.1016/j.carbon.2006.07.016.
96. T. Ozel, D. Abdula, E. Hwang, M. Shim, Nonuniform compressive strain in horizontally aligned single-walled carbon nanotubes grown on single crystal quartz. *ACS nano*. **3**, 2217–2224 (2009), doi:10.1021/nn900539t.
97. Y. Miyauchi, S. Chiashi, Y. Murakami, Y. Hayashida, S. Maruyama, Fluorescence spectroscopy of single-walled carbon nanotubes synthesized from alcohol. *Chemical Physics Letters*. **387**, 198–203 (2004), doi:10.1016/j.cplett.2004.01.116.
98. B. Wang *et al.*, Pressure-Induced Single-Walled Carbon Nanotube ( n,m ) Selectivity on Co–Mo Catalysts. *J. Phys. Chem. C*. **111**, 14612–14616 (2007), doi:10.1021/jp0762525.
99. E.F. Kukovitsky, S.G. L’vov, N.A. Sainov, VLS-growth of carbon nanotubes from the vapor. *Chemical Physics Letters*. **317** (2000).
100. Henning Kanzow, Adalbert Ding, Formation mechanism of single-wall carbon nanotubes on liquid-metal particles. *Physical review B*. **60** (1999).
101. Y. Chen, J. Zhang, Diameter controlled growth of single-walled carbon nanotubes from SiO<sub>2</sub> nanoparticles. *Carbon*. **49**, 3316–3324 (2011), doi:10.1016/j.carbon.2011.04.016.
102. J.-P. Tessonnier, D. S. Su, Recent progress on the growth mechanism of carbon nanotubes: a review. *ChemSusChem*. **4**, 824–847 (2011), doi:10.1002/cssc.201100175.
103. C. T. Wirth, S. Hofmann, J. Robertson, State of the catalyst during carbon nanotube growth. *Diamond and Related Materials*. **18**, 940–945 (2009), doi:10.1016/j.diamond.2009.01.030.
104. M. V. Kharlamova, Investigation of growth dynamics of carbon nanotubes. *Beilstein journal of nanotechnology*. **8**, 826–856 (2017), doi:10.3762/bjnano.8.85.

105. Mukul Kumar, *Carbon Nanotube Synthesis and Growth Mechanism* (2011).
106. G. D. Nessim, Properties, synthesis, and growth mechanisms of carbon nanotubes with special focus on thermal chemical vapor deposition. *Nanoscale*. **2**, 1306–1323 (2010), doi:10.1039/b9nr00427k.
107. F. Yang *et al.*, Chirality Pure Carbon Nanotubes: Growth, Sorting, and Characterization. *Chemical reviews*. **120**, 2693–2758 (2020), doi:10.1021/acs.chemrev.9b00835.
108. M. Li *et al.*, Metallic Catalysts for Structure-Controlled Growth of Single-Walled Carbon Nanotubes. *Topics in current chemistry (Cham)*. **375**, 29 (2017), doi:10.1007/s41061-017-0116-9.
109. M.-F. C. Fiawoo *et al.*, Evidence of correlation between catalyst particles and the single-wall carbon nanotube diameter: a first step towards chirality control. *Physical review letters*. **108**, 195503 (2012), doi:10.1103/PhysRevLett.108.195503.
110. M. He *et al.*, Linking growth mode to lengths of single-walled carbon nanotubes. *Carbon*. **113**, 231–236 (2017), doi:10.1016/j.carbon.2016.11.057.
111. F. Zhang *et al.*, Growth of semiconducting single-wall carbon nanotubes with a narrow band-gap distribution. *Nature communications*. **7**, 11160 (2016), doi:10.1038/ncomms11160.
112. P. Nikolaev, D. Hooper, N. Perea-López, M. Terrones, B. Maruyama, Discovery of wall-selective carbon nanotube growth conditions via automated experimentation. *ACS nano*. **8**, 10214–10222 (2014), doi:10.1021/nn503347a.
113. J. Chang *et al.*, Efficient Closed-loop Maximization of Carbon Nanotube Growth Rate using Bayesian Optimization. *Scientific reports*. **10**, 9040 (2020), doi:10.1038/s41598-020-64397-3.
114. S. Reich, L. Li, J. Robertson, Control the chirality of carbon nanotubes by epitaxial growth. *Chemical Physics Letters*. **421**, 469–472 (2006), doi:10.1016/j.cplett.2006.01.110.
115. S. Reich, L. Li, J. Robertson, Epitaxial growth of carbon caps on Ni for chiral selectivity. *phys. stat. sol. (b)*. **243**, 3494–3499 (2006), doi:10.1002/pssb.200669224.
116. D. A. Gómez-Gualdrón, J. Zhao, P. B. Balbuena, Nanocatalyst structure as a template to define chirality of nascent single-walled carbon nanotubes. *The Journal of chemical physics*. **134**, 14705 (2011), doi:10.1063/1.3509387.
117. D. Dutta, W.-H. Chiang, R.M. Sankaran, V. R. Bhethanabotla, Epitaxial nucleation model for chiral-selective growth of single-walled carbon nanotubes on bimetallic catalyst surfaces. *Carbon*. **50**, 3766–3773 (2012), doi:10.1016/j.carbon.2012.03.051.
118. F. Yang *et al.*, Growing Zigzag (16,0) Carbon Nanotubes with Structure-Defined Catalysts. *Journal of the American Chemical Society*. **137**, 8688–8691 (2015), doi:10.1021/jacs.5b04403.

119. E. S. Penev, V. I. Artyukhov, B. I. Yakobson, Extensive energy landscape sampling of nanotube end-caps reveals no chiral-angle bias for their nucleation. *ACS nano*. **8**, 1899–1906 (2014), doi:10.1021/nn406462e.
120. M. Luo, E. S. Penev, A. R. Harutyunyan, B. I. Yakobson, Effect of Cap–Catalyst Structural Correlation on the Nucleation of Carbon Nanotubes. *J. Phys. Chem. C*. **121**, 18789–18794 (2017), doi:10.1021/acs.jpcc.7b07451.
121. F. Ding, A. R. Harutyunyan, B. I. Yakobson, Dislocation theory of chirality-controlled nanotube growth. *Proceedings of the National Academy of Sciences of the United States of America*. **106**, 2506–2509 (2009), doi:10.1073/pnas.0811946106.
122. H. Dumlich, S. Reich, Chirality-dependent growth rate of carbon nanotubes: A theoretical study. *Phys. Rev. B*. **82** (2010), doi:10.1103/PhysRevB.82.085421.
123. V. I. Artyukhov, E. S. Penev, B. I. Yakobson, Why nanotubes grow chiral. *Nature communications*. **5**, 4892 (2014), doi:10.1038/ncomms5892.
124. V. I. Artyukhov, Y. Liu, B. I. Yakobson, Equilibrium at the edge and atomistic mechanisms of graphene growth. *Proceedings of the National Academy of Sciences of the United States of America*. **109**, 15136–15140 (2012), doi:10.1073/pnas.1207519109.
125. K. N. Kudin, G. E. Scuseria, B. I. Yakobson, C<sub>2</sub>F, BN, and C nanoshell elasticity from ab initio computations. *Phys. Rev. B*. **64**, 56 (2001), doi:10.1103/PhysRevB.64.235406.
126. Y. Magnin, H. Amara, F. Ducastelle, A. Loiseau, C. Bichara, Entropy-driven stability of chiral single-walled carbon nanotubes. *Science (New York, N.Y.)*. **362**, 212–215 (2018), doi:10.1126/science.aat6228.
127. O. Gülseren, T. Yildirim, S. Ciraci, Systematic ab initio study of curvature effects in carbon nanotubes. *Phys. Rev. B*. **65**, 1579 (2002), doi:10.1103/PhysRevB.65.153405.
128. K. V. Bets, E. S. Penev, B. I. Yakobson, Janus Segregation at the Carbon Nanotube-Catalyst Interface. *ACS nano*. **13**, 8836–8841 (2019), doi:10.1021/acsnano.9b02061.
129. E. S. Penev, K. V. Bets, N. Gupta, B. I. Yakobson, Transient Kinetic Selectivity in Nanotubes Growth on Solid Co-W Catalyst. *Nano letters*. **18**, 5288–5293 (2018), doi:10.1021/acs.nanolett.8b02283.
130. G. D. Förster, T. D. Swinburne, H. Jiang, E. Kauppinen, C. Bichara, A semi-grand canonical kinetic Monte Carlo study of single-walled carbon nanotube growth. *AIP Advances*. **11**, 45306 (2021), doi:10.1063/5.0030943.
131. D. N. Futaba *et al.*, Kinetics of water-assisted single-walled carbon nanotube synthesis revealed by a time-evolution analysis. *Physical review letters*. **95**, 56104 (2005), doi:10.1103/PhysRevLett.95.056104.

132. E. R. Meshot, A. J. Hart, Abrupt self-termination of vertically aligned carbon nanotube growth. *Appl. Phys. Lett.* **92**, 113107 (2008), doi:10.1063/1.2889497.
133. E. Einarsson, Y. Murakami, M. Kadowaki, S. Maruyama, Growth dynamics of vertically aligned single-walled carbon nanotubes from in situ measurements. *Carbon.* **46**, 923–930 (2008), doi:10.1016/j.carbon.2008.02.021.
134. M. Picher, E. Anglaret, R. Arenal, V. Jourdain, Self-deactivation of single-walled carbon nanotube growth studied by in situ Raman measurements. *Nano letters.* **9**, 542–547 (2009), doi:10.1021/nl802661z.
135. R. Rao, D. Liptak, T. Cherukuri, B. I. Yakobson, B. Maruyama, In situ evidence for chirality-dependent growth rates of individual carbon nanotubes. *Nature materials.* **11**, 213–216 (2012), doi:10.1038/nmat3231.
136. H. Yoshida, S. Takeda, T. Uchiyama, H. Kohno, Y. Homma, Atomic-scale in-situ observation of carbon nanotube growth from solid state iron carbide nanoparticles. *Nano letters.* **8**, 2082–2086 (2008), doi:10.1021/nl080452q.
137. M. Marchand *et al.*, Growing a carbon nanotube atom by atom: "and yet it does turn". *Nano letters.* **9**, 2961–2966 (2009), doi:10.1021/nl901380u.
138. K. Liu, K. Jiang, C. Feng, Z. Chen, S. Fan, A growth mark method for studying growth mechanism of carbon nanotube arrays. *Carbon.* **43**, 2850–2856 (2005), doi:10.1016/j.carbon.2005.06.002.
139. K. Otsuka *et al.*, Digital Isotope Coding to Trace the Growth Process of Individual Single-Walled Carbon Nanotubes. *ACS nano.* **12**, 3994–4001 (2018), doi:10.1021/acsnano.8b01630.
140. B. Koyano *et al.*, Regrowth and catalytic etching of individual single-walled carbon nanotubes studied by isotope labeling and growth interruption. *Carbon.* **155**, 635–642 (2019), doi:10.1016/j.carbon.2019.09.031.
141. J. Lefebvre, P. Finnie, Polarized light microscopy and spectroscopy of individual single-walled carbon nanotubes. *Nano Res.* **4**, 788–794 (2011), doi:10.1007/s12274-011-0135-8.
142. K. Liu *et al.*, High-throughput optical imaging and spectroscopy of individual carbon nanotubes in devices. *Nature nanotechnology.* **8**, 917–922 (2013), doi:10.1038/nnano.2013.227.
143. L. Monniello *et al.*, Comprehensive model of the optical spectra of carbon nanotubes on a substrate by polarized microscopy. *Phys. Rev. B.* **99**, 1251 (2019), doi:10.1103/PhysRevB.99.115431.
144. M. S. Dresselhaus, G. Dresselhaus, P. C. Eklund, *Science of fullerenes and carbon nanotubes* (Academic Press, San Diego, London, 1996).

145. R. Saito, M. Hofmann, G. Dresselhaus, A. Jorio, M. S. Dresselhaus, Raman spectroscopy of graphene and carbon nanotubes. *Advances in Physics*. **60**, 413–550 (2011), doi:10.1080/00018732.2011.582251.
146. L. G. Cançado *et al.*, Anisotropy of the Raman spectra of nanographite ribbons. *Physical review letters*. **93**, 47403 (2004), doi:10.1103/PhysRevLett.93.047403.
147. M. S. Dresselhaus, G. Dresselhaus, R. Saito, A. Jorio, Raman spectroscopy of carbon nanotubes. *Physics Reports*. **409**, 47–99 (2005), doi:10.1016/j.physrep.2004.10.006.
148. D. I. Levshov *et al.*, Accurate determination of the chiral indices of individual carbon nanotubes by combining electron diffraction and Resonant Raman spectroscopy. *Carbon*. **114**, 141–159 (2017), doi:10.1016/j.carbon.2016.11.076.
149. F. Hennrich *et al.*, Raman spectroscopy of individual single-walled carbon nanotubes from various sources. *The journal of physical chemistry. B*. **109**, 10567–10573 (2005), doi:10.1021/jp0441745.
150. M. Szybowicz, A. B. Nowicka, A. Dychalska, in *Characterization of Nanomaterials* (Elsevier, 2018), vol. **23**, pp. 1–36.
151. M. S. Dresselhaus *et al.*, Resonance Raman scattering on one-dimensional systems. *Indian Journal of Physics*. **77**, 75–99.
152. O. E. Alon, Number of Raman- and infrared-active vibrations in single-walled carbon nanotubes. *Phys. Rev. B*. **63**, 56 (2001), doi:10.1103/PhysRevB.63.201403.
153. M. S. Dresselhaus, P. C. Eklund, Phonons in carbon nanotubes. *Advances in Physics*. **49**, 705–814 (2000), doi:10.1080/000187300413184.
154. R. Saito *et al.*, Double resonance Raman spectroscopy of single-wall carbon nanotubes. *Physical review letters*. **5**, 157 (2003), doi:10.1088/1367-2630/5/1/157.
155. R. Graupner, Raman spectroscopy of covalently functionalized single-wall carbon nanotubes. *J. Raman Spectrosc.* **38**, 673–683 (2007), doi:10.1002/jrs.1694.
156. M. V. Avramenko, S. B. Rochal, Y. I. Yuzyuk, Symmetry of the carbon nanotube modes and their origin from the phonon branches of graphene. *Phys. Rev. B*. **87** (2013), doi:10.1103/PhysRevB.87.035407.
157. L. Alvarez *et al.*, Resonant Raman study of the structure and electronic properties of single-wall carbon nanotubes. *Chemical Physics Letters*. **316**, 186–190 (2000), doi:10.1016/S0009-2614(99)01291-9.
158. Thomsen, Reich, Double resonant raman scattering in graphite. *Physical review letters*. **85**, 5214–5217 (2000), doi:10.1103/PhysRevLett.85.5214.
159. J. E. Lee, G. Ahn, J. Shim, Y. S. Lee, S. Ryu, Optical separation of mechanical strain from charge doping in graphene. *Nature communications*. **3**, 1024 (2012), doi:10.1038/ncomms2022.

160. Louis-Victor de Broglie (1925).
161. M. Knoll, E. Ruska, Das elektronenmikroskop. *Zeitschrift für physik.* **78**, 318–339 (1932).
162. E. Ruska, Nobel lecture. The development of the electron microscope and of electron microscopy. *Bioscience reports.* **7**, 607–629 (1987), doi:10.1007/BF01127674.
163. D. Li *et al.*, Scanning electron microscopy imaging of single-walled carbon nanotubes on substrates. *Nano Res.* **10**, 1804–1818 (2017), doi:10.1007/s12274-017-1505-7.
164. J. Li *et al.*, Direct identification of metallic and semiconducting single-walled carbon nanotubes in scanning electron microscopy. *Nano letters.* **12**, 4095–4101 (2012), doi:10.1021/nl301561f.
165. D. Li *et al.*, Direct discrimination between semiconducting and metallic single-walled carbon nanotubes with high spatial resolution by SEM. *Nano Res.* **10**, 1896–1902 (2017), doi:10.1007/s12274-016-1372-7.
166. S. Chiashi *et al.*, Growth of Horizontally Aligned Single-Walled Carbon Nanotubes on the Singular R-Plane (10–11) of Quartz. *J. Phys. Chem. C.* **116**, 6805–6808 (2012), doi:10.1021/jp210121n.
167. Quartz Crystal Industry Association of Japan, *Quartz crystal device* (2021).
168. M. Cisneros, K. T. Ashley, R. J. Bodnar, Evaluation and application of the quartz-inclusions-in-epidote mineral barometer. *American Mineralogist.* **105**, 1140–1151 (2020), doi:10.2138/am-2020-7379.
169. A. Rahmani, J.-L. Sauvajol, S. Rols, C. Benoit, Nonresonant Raman spectrum in infinite and finite single-wall carbon nanotubes. *Phys. Rev. B.* **66**, 705 (2002), doi:10.1103/PhysRevB.66.125404.
170. S. D. M. Brown *et al.*, Origin of the Breit-Wigner-Fano lineshape of the tangential G -band feature of metallic carbon nanotubes. *Phys. Rev. B.* **63**, 187 (2001), doi:10.1103/PhysRevB.63.155414.
171. A. Gaur, M. Shim, Substrate-enhanced O<sub>2</sub> adsorption and complexity in the Raman G -band spectra of individual metallic carbon nanotubes. *Phys. Rev. B.* **78** (2008), doi:10.1103/PhysRevB.78.125422.
172. L. Ding *et al.*, Direct observation of the strong interaction between carbon nanotubes and quartz substrate. *Nano Res.* **2**, 903–910 (2009), doi:10.1007/s12274-009-9093-9.
173. X. Li, Y. Jia, J. Dong, Y. Kawazoe, Resonant Raman spectroscopy of deformed single-walled carbon nanotubes under both torsional and tensile strain. *Phys. Rev. B.* **81**, 137 (2010), doi:10.1103/PhysRevB.81.195439.

174. S. B. Cronin *et al.*, Resonant Raman spectroscopy of individual metallic and semiconducting single-wall carbon nanotubes under uniaxial strain. *Phys. Rev. B.* **72** (2005), doi:10.1103/PhysRevB.72.035425.
175. Z. Liu, J. Zhang, B. Gao, Raman spectroscopy of strained single-walled carbon nanotubes. *Chemical communications (Cambridge, England)*, 6902–6918 (2009), doi:10.1039/b914588e.
176. Y. Zhang *et al.*, Raman Spectra Variation of Partially Suspended Individual Single-Walled Carbon Nanotubes. *J. Phys. Chem. C.* **111**, 1983–1987 (2007), doi:10.1021/jp065973l.
177. Y. Zhang, J. Zhang, H. Son, J. Kong, Z. Liu, Substrate-induced Raman frequency variation for single-walled carbon nanotubes. *Journal of the American Chemical Society.* **127**, 17156–17157 (2005), doi:10.1021/ja056793c.
178. A. C. Ferrari *et al.*, Raman spectrum of graphene and graphene layers. *Physical review letters.* **97**, 187401 (2006), doi:10.1103/PhysRevLett.97.187401.
179. K. Yazda *et al.*, Voltage-activated transport of ions through single-walled carbon nanotubes. *Nanoscale.* **9**, 11976–11986 (2017), doi:10.1039/c7nr02976d.
180. P. T. Araujo *et al.*, Third and fourth optical transitions in semiconducting carbon nanotubes. *Physical review letters.* **98**, 67401 (2007), doi:10.1103/PhysRevLett.98.067401.
181. A. Jorio, R. Saito, Raman spectroscopy for carbon nanotube applications. *Journal of Applied Physics.* **129**, 21102 (2021), doi:10.1063/5.0030809.
182. Open Source Computer Vision, *Object Detection, Image processing* (available at [https://docs.opencv.org/4.5.2/df/dfb/group\\_\\_imgproc\\_\\_object.html#gga3a7850640f1fe1f58fe91a2d7583695dac6677e2af5e0fae82cc5339bfaef5038](https://docs.opencv.org/4.5.2/df/dfb/group__imgproc__object.html#gga3a7850640f1fe1f58fe91a2d7583695dac6677e2af5e0fae82cc5339bfaef5038)).
183. Open Source Computer Vision, *Template Matching* (available at [https://docs.opencv.org/4.5.2/d4/dc6/tutorial\\_py\\_template\\_matching.html](https://docs.opencv.org/4.5.2/d4/dc6/tutorial_py_template_matching.html)).
184. D. B. Goldman, Vignette and exposure calibration and compensation. *IEEE transactions on pattern analysis and machine intelligence.* **32**, 2276–2288 (2010), doi:10.1109/TPAMI.2010.55.
185. T. Peng *et al.*, A BaSiC tool for background and shading correction of optical microscopy images. *Nature communications.* **8**, 14836 (2017), doi:10.1038/ncomms14836.
186. J. C. Russ, *The Image Processing Handbook* (2006), doi:10.1201/9780203881095.
187. D. Tomazevic, B. Likar, F. Pernus, Comparative evaluation of retrospective shading correction methods. *Journal of microscopy.* **208**, 212–223 (2002), doi:10.1046/j.1365-2818.2002.01079.x.
188. E. O. Brigham, *The fast Fourier transform and its applications* (Prentice-Hall, Inc, 1988).
189. P. Heckbert, *Fourier transforms and the fast Fourier transform (FFT) algorithm* (1995).
190. B. Wang, D. M. Rose, A. A. Farag, E. J. Delp, *Local estimation of Gaussian-based edge enhancement filters using Fourier analysis, 1993 IEEE International Conference on Acoustics,*

*Speech, and Signal Processing, April 27-30, 1993, Minneapolis Convention Center, Minneapolis, Minnesota* (Institute of Electrical and Electronics Engineers, New York, N.Y, Piscataway, N.J, 1993).

191. P. Sharma, A. Singh, Era of deep neural networks: A review, 1–5 (2017), doi:10.1109/ICCCNT.2017.8203938.
192. R. T. Birge, The Calculation of Errors by the Method of Least Squares. *Phys. Rev.* **40**, 207–227 (1932), doi:10.1103/PhysRev.40.207.
193. S. S. Haykin, *Neural networks, A comprehensive foundation / Simon Haykin* (Prentice Hall; London : Prentice-Hall International, Upper Saddle River, N.J., ed. 2, 2004).
194. S. Ruder, An overview of gradient descent optimization algorithms. *arXiv preprint arXiv:1609.04747* (2016).
195. D. P. Mandic, A Generalized Normalized Gradient Descent Algorithm. *IEEE Signal Process. Lett.* **11**, 115–118 (2004), doi:10.1109/LSP.2003.821649.
196. I. Goodfellow, Y. Bengio, A. Courville, *Deep learning* (MIT press, 2016).
197. K. Jarrett, K. Kavukcuoglu, M. A. Ranzato, Y. LeCun, *What is the best multi-stage architecture for object recognition?*, Kyoto, Japan, 29 September - 2 October 2009 (IEEE, Piscataway, NJ, 2009).
198. *Rectified linear units improve restricted boltzmann machines* (2010).
199. R. Rojas, *Neural networks, A systematic introduction / Raúl Rojas ; foreword by Jerome Feldman* (Springer-Verlag, Berlin, London, 1996).
200. John S. Denker *et al.*, Eds., *Neural Network Recognizer for Hand-Written Zip Code Digits* (Citeseer, 1989).
201. *Mask r-cnn* (2017).
202. *Feature pyramid networks for object detection* (2017).
203. M. Hossin, M.N. Sulaiman, A Review on Evaluation Metrics for Data Classification Evaluations. *IJDKP.* **5**, 1–11 (2015), doi:10.5121/ijdkp.2015.5201.
204. W. Zhiqiang, L. Jun, A review of object detection based on convolutional neural network, 11104–11109, doi:10.23919/ChiCC.2017.8029130.
205. Facebook AI Research Lab (FAIR), *Pytorch* (available at <https://pytorch.org/>).
206. *Deep residual learning for image recognition* (2016).
207. T.-Y. Lin *et al.*, Microsoft COCO: Common Objects in Context. **8693**, 740–755, doi:10.1007/978-3-319-10602-1\_48.
208. T. George Karimpanal, R. Bouffanais, Self-organizing maps for storage and transfer of knowledge in reinforcement learning. *Adaptive Behavior.* **27**, 111–126 (2019), doi:10.1177/1059712318818568.

209. O. Ronneberger, P. Fischer, T. Brox, in *Medical Image Computing and Computer-Assisted Intervention – MICCAI 2015*, N. Navab, J. Hornegger, W. M. Wells, A. F. Frangi, Eds. (Springer International Publishing, Cham, 2015), vol. **9351**, pp. 234–241.
210. C. Shorten, T. M. Khoshgoftaar, A survey on Image Data Augmentation for Deep Learning. *J Big Data*. **6**, 1106 (2019), doi:10.1186/s40537-019-0197-0.
211. Google, *Colaboratory* (available at <https://colab.research.google.com/notebooks/intro.ipynb>).
212. Paper With Code, *Benchmark of neural network for object detection (2021)* (available at <https://paperswithcode.com/sota/real-time-object-detection-on-coco>).
213. H. W. Kuhn, The Hungarian method for the assignment problem. *Naval Research Logistics*. **2**, 83–97 (1955), doi:10.1002/nav.3800020109.
214. R. E. Kalman, A New Approach to Linear Filtering and Prediction Problems. *Journal of Basic Engineering*. **82**, 35–45 (1960), doi:10.1115/1.3662552.
215. A. Bewley, Z. Ge, L. Ott, F. Ramos, B. Upcroft, in *2016 IEEE International Conference on Image Processing (ICIP)* (IEEE, 25.09.2016 - 28.09.2016), pp. 3464–3468.
216. G. Chen *et al.*, The relationship between the growth rate and the lifetime in carbon nanotube synthesis. *Nanoscale*. **7**, 8873–8878 (2015), doi:10.1039/c5nr01125f.
217. Z. Zhu *et al.*, Rate-selected growth of ultrapure semiconducting carbon nanotube arrays. *Nature communications*. **10**, 4467 (2019), doi:10.1038/s41467-019-12519-5.
218. C. T. Wirth, C. Zhang, G. Zhong, S. Hofmann, J. Robertson, Diffusion- and reaction-limited growth of carbon nanotube forests. *ACS nano*. **3**, 3560–3566 (2009), doi:10.1021/nn900613e.
219. G. de Souza, N. M. Balzaretto, N. R. Marcílio, O. W. Perez-Lopez, Decomposition of Ethanol Over Ni-Al Catalysts: Effect of Copper Addition. *Procedia Engineering*. **42**, 335–345 (2012), doi:10.1016/j.proeng.2012.07.425.
220. R. Sivaramakrishnan *et al.*, Rate constants for the thermal decomposition of ethanol and its bimolecular reactions with OH and D: reflected shock tube and theoretical studies. *The journal of physical chemistry. A*. **114**, 9425–9439 (2010), doi:10.1021/jp104759d.
221. V. Jourdain, C. Bichara, Current understanding of the growth of carbon nanotubes in catalytic chemical vapour deposition. *Carbon*. **58**, 2–39 (2013), doi:10.1016/j.carbon.2013.02.046.
222. K. Bartsch, K. Biedermann, T. Gemming, A. Leonhardt, On the diffusion-controlled growth of multiwalled carbon nanotubes. *Journal of Applied Physics*. **97**, 114301 (2005), doi:10.1063/1.1922067.

223. A. A. Puretzky, D. B. Geohegan, S. Jesse, I. N. Ivanov, G. Eres, In situ measurements and modeling of carbon nanotube array growth kinetics during chemical vapor deposition. *Appl. Phys. A*. **81**, 223–240 (2005), doi:10.1007/s00339-005-3256-7.
224. Dogterom, Leibler, Physical aspects of the growth and regulation of microtubule structures. *Physical review letters*. **70**, 1347–1350 (1993), doi:10.1103/PhysRevLett.70.1347.
225. T. Mitchison, M. Kirschner, Dynamic instability of microtubule growth. *Nature*. **312**, 237–242 (1984), doi:10.1038/312237a0.
226. Y.-C. Chou *et al.*, Atomic-scale variability and control of III-V nanowire growth kinetics. *Science (New York, N.Y.)*. **343**, 281–284 (2014), doi:10.1126/science.1244623.
227. K. W. Schwarz, J. Tersoff, S. Kodambaka, F. M. Ross, Jumping-catalyst dynamics in nanowire growth. *Physical review letters*. **113**, 55501 (2014), doi:10.1103/PhysRevLett.113.055501.
228. S. H. Oh *et al.*, Oscillatory mass transport in vapor-liquid-solid growth of sapphire nanowires. *Science (New York, N.Y.)*. **330**, 489–493 (2010), doi:10.1126/science.1190596.
229. S. Mazzucco *et al.*, Direct evidence of active and inactive phases of Fe catalyst nanoparticles for carbon nanotube formation. *Journal of Catalysis*. **319**, 54–60 (2014), doi:10.1016/j.jcat.2014.07.023.
230. C. T. Wirth *et al.*, The Phase of Iron Catalyst Nanoparticles during Carbon Nanotube Growth. *Chem. Mater.* **24**, 4633–4640 (2012), doi:10.1021/cm301402g.
231. H.-Y. Chao *et al.*, A structure and activity relationship for single-walled carbon nanotube growth confirmed by in situ observations and modeling. *Nanoscale*. **12**, 21923–21931 (2020), doi:10.1039/D0NR05916A.

### **Short abstract in English**

The use of carbon nanotubes with predetermined structure and properties is a promising direction for the development of electronic and optical devices. However, in order to develop methods for obtaining such tubes, it is first necessary to understand how their growth and especially their kinetics depends on their structure.

To address this question, we used an original optical setup to obtain videos of individual nanotube growth during synthesis. Specialized tools were also developed for processing these videos and extracting the kinetics, which made it possible to increase both the speed of analysis and its quality.

It was found that the growth rate of a CNT is constant during growth for about half of cases, but that they can stochastically change to faster or slower ones, as well as switch between growth and shrinkage in the other half of cases. Moreover, we found an inverse relationship between lifetime and growth rate. This inverse relationship is still observed when temperature and pressure are changed. Our results show that the current growth models need to be revised to account for these fluctuations.

**Key words:** In-situ imaging, CVD, Raman, microscopy, optics, CNT, kinetics

### **Résumé court en français**

L'utilisation de nanotubes de carbone ayant une structure et des propriétés prédéterminées est une voie prometteuse pour le développement de dispositifs électroniques et optiques. Cependant, afin de développer des méthodes pour obtenir de tels tubes, il est d'abord nécessaire de comprendre comment leur croissance dépend de leur structure.

Pour répondre à cette question, nous avons utilisé une configuration unique pour obtenir des vidéos de la croissance des nanotubes pendant la synthèse. Des outils spécialisés ont également été développés pour traiter ces vidéos et extraire la cinétique, ce qui a permis d'augmenter à la fois la vitesse d'analyse et sa qualité.

Nous avons constaté que le taux de croissance d'un NTC est constant pendant la croissance pour environ la moitié des cas, mais qu'il peut changer de façon stochastique pour devenir plus rapide ou plus lent, ainsi que passer de la croissance au rétrécissement dans l'autre moitié des cas. De plus, nous avons trouvé une relation inverse entre la durée de vie et le taux de croissance. Cette relation inverse est toujours observée lorsque la température et la pression sont modifiées.

Ces résultats montrent que les modèles de croissance actuels doivent être révisés pour intégrer ces fluctuations.

**Mots clés :** Imagerie in-situ, CVD, Raman, microscopie, optique, NTC, cinétique